

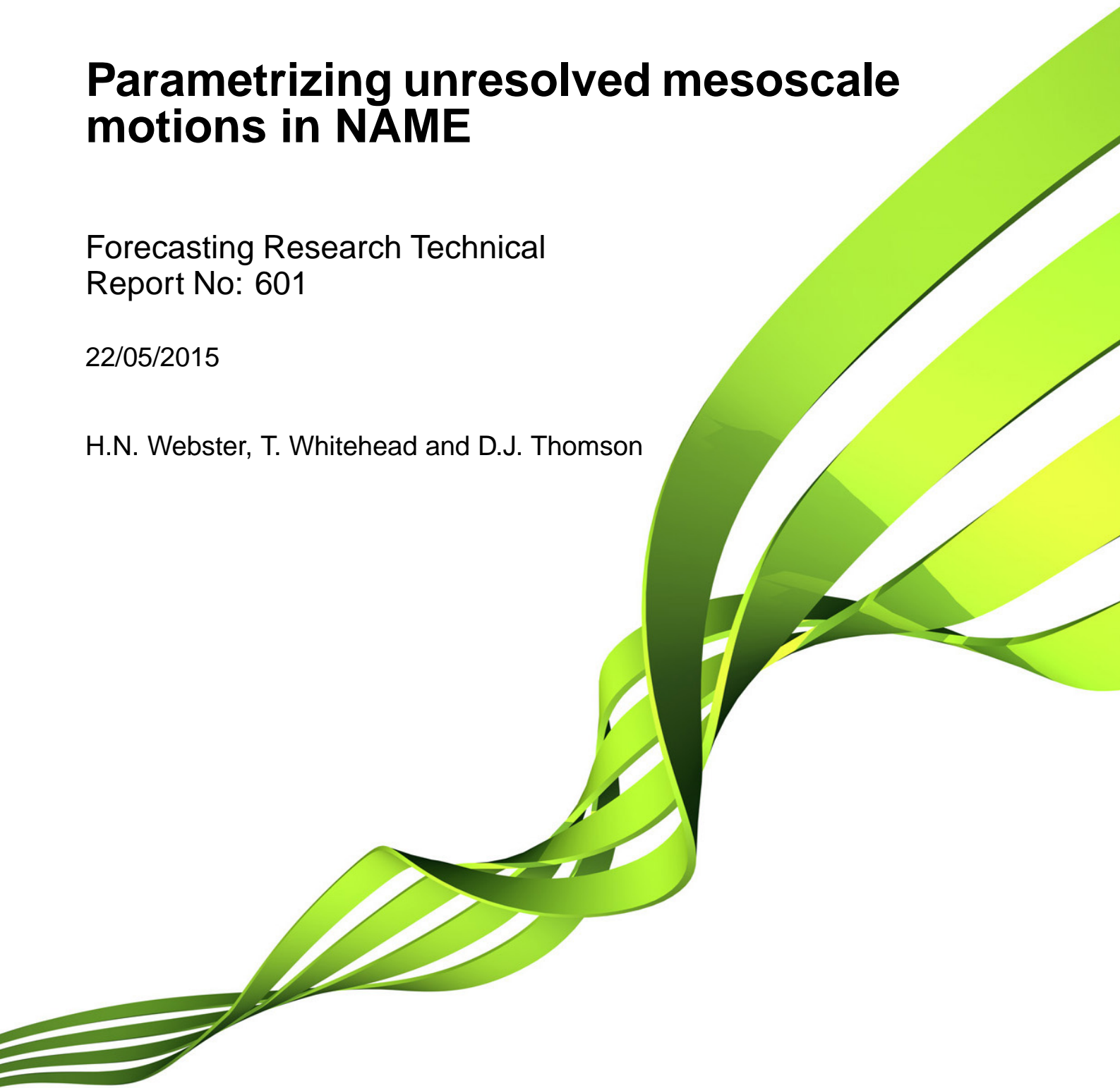
**Met Office**

# **Parametrizing unresolved mesoscale motions in NAME**

Forecasting Research Technical  
Report No: 601

22/05/2015

H.N. Webster, T. Whitehead and D.J. Thomson



## Contents

|          |   |            |
|----------|---|------------|
| <b>1</b> | <b>Plume meandering</b>   | <b>4</b>   |
| <b>2</b> | <b>Parametrization of unresolved mesoscale motions</b>  | <b>4</b>   |
| <b>3</b> | <b>Parametrizations of mesoscale motions in the literature</b>                                    | <b>6</b>   |
| 3.1      | The history of the parametrization of unresolved mesoscale motions in NAME . . . .                | 10         |
| 3.2      | Parametrizations of unresolved mesoscale motions in other atmospheric dispersion models . . . . . | 11         |
| 3.2.1    | FLEXPART . . . . .  | 11         |
| 3.2.2    | ADMS . . . . .  | 12         |
| <b>4</b> | <b>Spectra of resolved motions</b>  | <b>12</b>  |
| <b>5</b> | <b>Boundary layer motions</b>   | <b>15</b>  |
| 5.1      | Understanding spectral curve discrepancies at low frequencies . . . . .                           | 16         |
| 5.2      | Spectra and missing variance calculations . . . . .   | 17         |
| 5.2.1    | Determining the point of divergence . . . . .   | 23         |
| 5.2.2    | Calculating Lagrangian timescales . . . . .   | 24         |
| 5.2.3    | Calculating appropriate $\sigma_u$ values . . . . .   | 33         |
| 5.3      | Diffusivities . . . . .   | 37         |
| 5.4      | Recommended boundary layer parametrization of unresolved mesoscale motions .                      | 37         |
| <b>6</b> | <b>Free troposphere motions</b>   | <b>40</b>  |
| 6.1      | Wind profiler data . . . . .  | 41         |
| <b>7</b> | <b>Validation of the parametrization of unresolved mesoscale motions</b>                          | <b>53</b>  |
| 7.1      | Intercomparison of plume spread predicted using NWP data of differing resolutions .               | 53         |
| 7.2      | The 2010 eruption of Eyjafjallajökull . . . . .   | 57         |
| <b>8</b> | <b>Conclusions</b>  | <b>60</b>  |
| <b>A</b> | <b>Boundary layer scaling factors used with NWP winds for years 1998 - 2008</b>                   | <b>62</b>  |
| <b>B</b> | <b>Boundary layer spectral plots generated using observed and NWP winds</b>                       | <b>64</b>  |
| <b>C</b> | <b>Boundary layer fractional difference plots generated using observed and NWP winds</b>          | <b>78</b>  |
| <b>D</b> | <b>Boundary layer difference plots generated using observed and NWP winds</b>                     | <b>92</b>  |
| <b>E</b> | <b>Boundary layer correlation plots generated using observed and NWP winds</b>                    | <b>104</b> |
| <b>F</b> | <b>Free tropospheric spectral plots</b>   | <b>118</b> |

---

|  |            |
|--|------------|
| <b>G Free tropospheric fractional difference plots</b> | <b>122</b> |
| <b>H Free tropospheric correlation plots</b>           | <b>126</b> |

---

### **Abstract**

The Met Office's atmospheric dispersion model, NAME (Numerical Atmospheric-dispersion Modelling Environment), includes a parametrization for plume spread due to unresolved mesoscale motions. These motions are generally not resolved by input Numerical Weather Prediction (NWP) data used to drive NAME but they are larger in size than the three-dimensional turbulent motions represented by turbulence parametrizations. Neglecting the effect of these two-dimensional unresolved mesoscale motions has been shown to underpredict plume spread and overpredict concentrations within the plume.

We begin this report by presenting evidence and observations from the literature of these two-dimensional atmospheric motions. Parametrizations used in other atmospheric dispersion models are summarised and the evolution of the parametrization in NAME described.

With the advancement of science and increases in computing power, there has been significant progress in Numerical Weather Prediction modelling, with high resolution simulations with horizontal spatial resolutions of the order of a few kilometres now routinely being conducted. This high resolution NWP data is expected to resolve smaller scale atmospheric motions than previously possible and hence there was a growing risk that motions of certain scales were both represented in NWP data as resolved motions and included in NAME's parametrization of unresolved mesoscale motions. This suggested that the parametrization of unresolved mesoscale motions in NAME should depend on the resolution of the input NWP data.

Spectral analysis of NWP data and boundary layer wind observations is used to assess the mesoscale motions unresolved by the NWP model. Appropriate velocity variances and Lagrangian timescales for the unresolved mesoscale motions are found by calculating the missing variance in the energy spectra and analysing correlation functions. A strong dependence on the resolution of the NWP data is seen, with the lower resolution global models (both in time and space) having more unresolved mesoscale motions which results in larger velocity variances and Lagrangian timescales. A revised parametrization of unresolved mesoscale motions based on the NWP resolution is proposed for NAME and its effect assessed in simulations of plume spread.

As well as analysing boundary layer data, spectral analysis of free tropospheric wind profiler observations and NWP data is used to assess the free tropospheric mesoscale motions unresolved by the NWP model. This spectral analysis suggests larger velocity variances are appropriate in the free troposphere. The overall diffusivity has a large amount of uncertainty but is similar to that obtained in the boundary layer.

## 1 Plume meandering

Large variations in wind direction have been observed in stable light wind conditions (see section 3 for further details). This variation in wind direction is due to two-dimensional horizontal eddies which are not suppressed by vertical stability forces. These mesoscale eddies are often attributed to gravity waves, terrain interactions with the flow, mesoscale rolls and cell patterns in the synoptic flow or surface inhomogeneities [12]. The effect of atmospheric motions of these scales on plumes is usually recognised as, at least relatively close to the source, a slow meandering of the plume, in which the instantaneous plume may be thin but over a time period of an hour or more may meander over a wide angle. Plume meandering moves the plume around as a whole and does not disperse the plume or affect its internal structure. Observed concentrations in regions of meandering plumes are often characterised by periods of zero concentrations interspersed by periods of relatively high concentrations. Hourly averaged plumes are considerably wider and have lower concentrations than observed within the instantaneous plume. These mesoscale motions which cause plume meandering near to source can, however, result in plume diffusion further downwind when the width of the plume has, due to diffusion by small-scale turbulent eddies, increased to be comparable in size to the mesoscale eddies.

## 2 Parametrization of unresolved mesoscale motions

These two-dimensional mesoscale motions are particularly relevant in stable light wind conditions when they are the dominant cause of lateral spread of a plume. However, these motions are usually neither resolved by the meteorological data used to drive atmospheric dispersion models nor are they covered by parametrizations of small-scale three-dimensional turbulent motions. It has been shown that neglecting these intermediate scale motions leads to underestimation of plume spread [9] and overestimation of air concentrations [17]. Indeed Kristensen et al. [16] suggest that estimates of mean concentrations can be at least factors of 4 - 6 too high if these motions are not taken into account. It is important, therefore, to parametrize these unresolved motions within atmospheric dispersion models. Within the Met Office's Numerical Atmospheric-dispersion Modelling Environment (NAME), the parametrization of these mesoscale motions has been known historically as the meander parametrization. The use of the term 'meander' to refer to the atmospheric motions as well as the meandering plume behaviour has led to much confusion. Consequently we try here to reserve 'meander' purely for the plume behaviour and refer to the motions as unresolved mesoscale motions.

The parametrization of unresolved mesoscale motions is intended to represent diffusion by motions in the intermediate frequency range between the motions resolved by the input meteorological data and small-scale three-dimensional turbulent eddies. However, in reality, turbulent diffusion cannot be split into well defined spatial scales corresponding to diffusion by resolved motions, unre-

solved mesoscale motions and turbulent fluctuations. The input meteorological data for atmospheric dispersion models commonly comes from Numerical Weather Prediction (NWP) models which are increasingly being conducted at higher resolutions. According to Maryon [18], the scale of motions resolved by the input NWP data is mainly constrained by the temporal resolution, which tends to be coarse in comparison to the spatial resolution. For input wind fields with a time resolution of  $\Delta T_f$ , the highest frequency motions which can be resolved are those of period  $2\Delta T_f$  (although this is complicated by the fact that, for low frequency but instantaneous data from the NWP model, the higher frequencies resolved by the NWP model will be aliased to lower frequencies rather than discarded). Furthermore, it is often not explicitly stated in the literature for which scales the turbulence parametrizations have been developed [31]. The result of all of this is an intermediate frequency range between the resolved and turbulent motions which is not well defined and which is dependent on the input meteorological data and perhaps even the turbulence parametrization chosen.

The simple solution adopted in NAME is to treat the unresolved mesoscale motions and turbulent motions as additive and independent parts. At short range, NAME model particles are advected each time-step using

$$\mathbf{x}_{t+\Delta t} = \mathbf{x}_t + [\bar{\mathbf{u}} + \mathbf{u}' + \mathbf{u}'_m] \Delta t,$$

where  $\mathbf{x}_t$  is the particle position at time  $t$ ,  $\bar{\mathbf{u}}$  is the mean wind velocity taken from the input meteorological data,  $\mathbf{u}'$  is the turbulent velocity component,  $\mathbf{u}'_m$  is the unresolved mesoscale wind component and  $\Delta t$  is the time-step. The unresolved mesoscale wind components are modelled within NAME using random walk techniques analogous to those used to model random turbulent motion. The unresolved components  $\mathbf{u}'$  and  $\mathbf{u}'_m$  are assumed to be independent. The unresolved mesoscale wind components are calculated using a velocity memory scheme

$$\mathbf{u}'_{m,t+\Delta t} = \mathbf{u}'_{m,t} \left( 1 - \frac{\Delta t}{\tau_{u,m}} \right) + \left( \frac{2\sigma_{u,m}^2 \Delta t}{\tau_{u,m}} \right)^{1/2} \mathbf{r}_t,$$

where  $\mathbf{u}'_{m,t}$  are the unresolved mesoscale velocity components at time  $t$ ,  $\sigma_{u,m}^2$  is the velocity variance of the unresolved mesoscale motions,  $\tau_{u,m}$  is the Lagrangian timescale of the unresolved mesoscale motions and  $\mathbf{r}_t$  is a vector of independent random Gaussian variables of zero mean and unit variance. At long range NAME model particles are advected each time-step using

$$\mathbf{x}_{t+\Delta t} = \mathbf{x}_t + \bar{\mathbf{u}}\Delta t + \mathbf{x}' + \mathbf{x}'_m$$

where  $\mathbf{x}'$  is an increment to the particle position due to turbulence and  $\mathbf{x}'_m$  is an increment to the particle position due to unresolved mesoscale motions. The increments  $\mathbf{x}'$  and  $\mathbf{x}'_m$  are assumed to be independent and are calculated using a simple diffusive scheme. The particle position increment due to unresolved mesoscale motions is calculated from

$$\mathbf{x}'_m = \sqrt{2K_{u,m} \Delta t} \mathbf{r}_t,$$

where  $K_{u,m}$  is damped near to source ( $K_{u,m} = \sigma_{u,m}^2 \tau_{u,m} \left(1 - \exp\left(\frac{-t}{\tau_{u,m}}\right)\right)$ ,  $t$  is travel time) to improve prediction when  $t < \tau_{u,m}$ . The unresolved mesoscale motions are two-dimensional horizontal motions (i.e.,  $z'_m = 0$  at long range and  $w'_m = 0$  at short range – here,  $w'_m$  is interpreted as rate of change of height above ground).

The question regarding appropriate values for the velocity variances and Lagrangian timescales of unresolved mesoscale motions remains. Opinion on this has changed over the years with different values being adopted in NAME at different points in time (see section 3.1 for a discussion of the historical values used). We seek to address this question more thoroughly in this report, with the expectation that appropriate values may vary as the intermediate frequency range changes with different input NWP meteorological data.

### 3 Parametrizations of mesoscale motions in the literature

We start by reviewing the literature on meandering plumes in light wind, stable conditions and, in particular, summarise observations of the variability in wind direction and lateral wind speed. We also describe the different parametrizations used in atmospheric dispersion models to represent the effects of these unresolved mesoscale motions, including a description of the evolution of the parametrization used in NAME.

Hanna [12] states that there is much evidence in the literature for the presence of mesoscale lateral motions in the stable nighttime boundary layer. These motions are often attributed to gravity waves and boundary layer vortices over flat terrain or in coastal regions, or to terrain induced vortices [8]. Gravity waves with periods typically between 3 and 30 minutes can be observed in the free atmosphere and in the boundary layer [8]. Longitudinal eddies with a horizontal axis can result in plume meandering. For example, Raynor and Hayes [26] describe plume meandering due to roll eddies in coastal regions. Scorer [29] proposed that vortices with horizontal axes could form in the wake of quasi two-dimensional ridges. Vortices with a horizontal axis are much confined under stable conditions. For eddies with a vertical axis, motion is mainly restricted to horizontal planes and hence such eddies are not affected in the same way by stability forces. These quasi-horizontal mesoscale motions, with periods from about 30 minutes to 4 hours, can persist for a long time in situations with stable stratification. Their origin is not always clear, though vortex shedding in the wake of hills is one possible mechanism. Horizontal mesoscale motions may exist in the stable boundary layer even in the absence of vortex shedding by obstacles. So-called vortical modes are believed to be produced by the collapse of three-dimensional turbulent regions, with transformation of energy into horizontal motions. One possible mechanism of the origin of these vortical modes could be wave breaking due to Kelvin-Helmholtz instability in shear layers. Mesoscale motions may also be due to variations in cloud cover and land use / soil properties leading to differential heating / cooling. Furthermore some mesoscale motions will have no local forcing, being simply the high frequency tail of the large scale atmospheric energy spectrum.

Similarity theory, which applies adequately to boundary layer turbulent motions during unstable and neutral conditions, does not apply to lateral motions in stable conditions when two-dimensional mesoscale motions dominate. In these conditions the lateral turbulence intensity ( $\sigma_v/u$ ) has been shown to be a function of the wind speed ( $u$ ) and of hour-to-hour variations in wind direction [12]. Hanna [12] states that the lateral turbulence intensity is related, during stable conditions, to the standard deviation of wind direction fluctuations ( $\sigma_\theta$ ) by the formula,

$$\tan \sigma_\theta = \sigma_v/u.$$

At Porton, UK, Smith and Abbott [30] observed that  $\sigma_\theta$  increased at night as winds became light. The standard deviation of the lateral wind velocity ( $\sigma_v$ ) was relatively insensitive to both wind speed and stability and was found to have a constant value of  $0.3 \text{ m s}^{-1}$  for all wind speeds in stable conditions. At a complex terrain site in California, Hanna [10] found similarly that a constant value for  $\sigma_v$ , independent of wind speed, was appropriate during nighttime conditions. However, a larger value for  $\sigma_v$  of about  $1 \text{ m s}^{-1}$  was found at this site and attributed to lateral eddies induced by the terrain. For an overwater diffusion experiment performed off the Californian coast, Schacher et al. [27] found that  $\sigma_\theta$  was large and variable during stable conditions. Here a representative  $\sigma_v$  value of about  $0.5 \text{ m s}^{-1}$  was found by Hanna [12] to be appropriate. Schacher et al. [27] attribute their observations of large variability in wind direction to local mesoscale eddies caused by sea breeze interactions with the coastal mountains or flow around the channel islands.

In his paper, Hanna [12] analyses data from a number of overnight experiments of 8-hour duration at Cinder Cone Butte in Idaho, USA during October 1980. Cinder Cone Butte is an isolated 100 m symmetrical hill located on a flat plain in the Snake River Basin, although the siting of equipment and the tracer release location were such that results can be assumed to be obtained over flat terrain. During tracer gas release experiments, considerable lateral meandering of the plume was often observed. Cross-sections of the plume obtained from lidar illustrate meandering of the plume centroid. Analysis of anemometer data at heights of 40 m and 80 m found evidence of mesoscale eddies with periods of between 10 minutes and several hours. Hanna [12] calculates the time period at which maximum turbulent energy occurs ( $T_{max}$ ) using both an autocorrelogram method, based on the time lag when the autocorrelogram first drops to  $e^{-1}$ , and a spectral method, based on the maximum of the product of the frequency and spectra. (These methods are described further and used in section 5.2.2 of this report.)  $T_{max}$  values calculated by Hanna [12], from data from 17 experiments, range from approximately 1 to 4 hours with a median of 2 hours. Hourly averaged<sup>1</sup>  $\sigma_v$  values are  $\sim 0.5 \text{ m s}^{-1}$  during average nighttime conditions over the Snake River Plain in Idaho. This value lies within the range  $0.3$  to  $1.0 \text{ m s}^{-1}$  reported elsewhere. Hanna [12, 13] provides evidence that

<sup>1</sup>Note that the averaging time is important with larger variation expected over longer averaging times



his formula for wind direction variability over time periods of one hour, namely

$$\frac{\sigma_v}{u} = \tan \sigma_\theta = \frac{0.5 \text{ m s}^{-1}}{u},$$

is valid over all types of terrain with the large values of  $\sigma_\theta$  over complex terrain being due to lower wind speeds. He notes, however, that, for individual sites,  $\sigma_v$  values typically exhibit a scatter of about  $\pm 0.3 \text{ m s}^{-1}$  about the  $\sigma_v \sim 0.5 \text{ m s}^{-1}$  relationship.

Over longer time periods of several hours larger scale meso- and synoptic-scale eddies contribute to variation in the wind direction. Moore [20, 21] proposed parametrizations of wind variability over a range of time periods up to 24 hours. Moore's parametrizations have been widely used in dispersion modelling in the UK (e.g., in the short range models R91 [5] and ADMS [3]). Davies and Thomson [6] studied wind direction variability over time periods of one hour and over longer time periods up to 12 hours using surface site observations from the Meteorological Research Unit (MRU) at Cardington (Bedfordshire, UK) and then compared their results against various parametrizations. Wind data for the period from February 1988 until December 1990, and observed at a height of 21 m above ground, was used. Data was recorded at a frequency of 1 Hz. Hourly averages of the wind direction variability ( $\sigma_\theta$ ) and lateral velocity variability ( $\sigma_v$ ) were compared against the parametrizations proposed by Hanna [12]

$$\sigma_\theta \simeq \frac{\sigma_v}{u} \simeq \frac{0.5 \text{ m s}^{-1}}{u}, \quad (1)$$

and by Joffre and Laurila [15]

$$\begin{aligned} \sigma_\theta &\simeq \frac{0.32}{u}, & \text{for } u \leq 5 \text{ m s}^{-1}, \\ \sigma_\theta &\simeq 0.065, & \text{for } u > 5 \text{ m s}^{-1}. \end{aligned}$$

Joffre and Laurila [15] obtained their results from an experiment conducted over sea ice in the Bothnian Bay in April 1979. For low wind speeds, the parametrizations of Hanna [12, 13] and of Joffre and Laurila [15] agree well with hourly average observations at Cardington. For wind speeds above  $5 \text{ m s}^{-1}$ , the Joffre and Laurila value of 0.065 for  $\sigma_\theta$  appears too low when compared against observations from Cardington: the data suggests a larger value of 0.11 for  $\sigma_\theta$ . Davies and Thomson [6] show that the difference between the value of  $\sigma_\theta$  observed at Cardington and the parametrization of Joffre and Laurila [15] at high wind speeds can be partly attributed to differences in the roughness length and in the observation height at the two sites. Davies and Thomson [6] express the wind direction variability as two independent terms: one due to short term boundary layer turbulence and the other due to wind direction unsteadiness. Using Hanna's parametrization (equation (1)) for the latter, the agreement with the hourly averaged observed wind direction variability at Cardington is good for all wind speeds. As the averaging time increases, however, so too does the component of the wind direction variability due to wind direction unsteadiness. The short range dispersion models

ADMS and R91 represent this component using the following Moore parametrization for  $\sigma_\theta$ ,

$$\sigma_\theta = 0.065 \left( \frac{7}{u_{10m}} T_A \right)^{1/2},$$

where  $T_A$  is the averaging time in hours and  $u_{10m}$  is the magnitude of the average 10 m wind velocity over the same period. Using this formula for the component due to wind direction unsteadiness, the wind direction variability is under-predicted at low wind speeds when compared to Cardington observations averaged over 1, 3, 6 and 12 hours. This under-prediction is greatest for hourly averaged data, with the best agreement in comparisons with the 12 hourly averaged data. Davies and Thomson [6] present a formula for the total variability due to wind direction unsteadiness and turbulence of the form

$$\sigma_\theta = \left[ \left( \frac{\sigma_{turb}}{u} \right)^2 + \left( \frac{0.5 \text{ m s}^{-1}}{u} \right)^2 \right]^{1/2} T_A^{1/4},$$

where  $\sigma_{turb}$  is an estimate of the turbulent lateral velocity standard deviation, from which we can estimate the contribution due to wind direction unsteadiness as

$$\sigma_\theta = \frac{0.5 \text{ m s}^{-1}}{u} T_A^{1/4}.$$

This is an extension of Hanna's parametrization for longer averaging times and agrees better with observations at Cardington. It is more appropriate, however, to fit a formula where the power of  $T_A$  does not apply to  $\sigma_{turb}$ , i.e.,

$$\sigma_\theta = \left[ \left( \frac{\sigma_{turb}}{u} \right)^2 + \left( \frac{0.5 \text{ m s}^{-1}}{u} T_A^p \right)^2 \right]^{1/2}.$$

This form fits well with  $p = 1/3$  (see figure 1) suggesting the following formula for the variability due to wind direction unsteadiness,

$$\sigma_\theta = \frac{0.5 \text{ m s}^{-1}}{u} T_A^{1/3}.$$

Anfossi et al. [1] analysed hourly wind observations from two sites: one in complex terrain and one in a rather flat area. They found that mesoscale motions exist in all meteorological conditions regardless of the stability or wind speed. Their analysis indicates that mesoscale motions also lead to a modification of the autocorrelation function of the horizontal wind components such that an oscillatory behaviour and negative lobes occur. Anfossi et al. [1] also note that since mesoscale motions are generally detected everywhere in low wind conditions, they cannot be simply associated with the presence of orography and / or terrain inhomogeneities, although this may well play a part in the process. Since the traditional explanations of the presence of mesoscale motions relate only to the stable boundary layer, Anfossi et al. [1] prefer that additional explanations might need to be provided. Oettl et al. [22] conclude from analytical considerations and numerical simulations that small perturbations in the flow which introduce horizontal gradients in the velocity are sufficient to

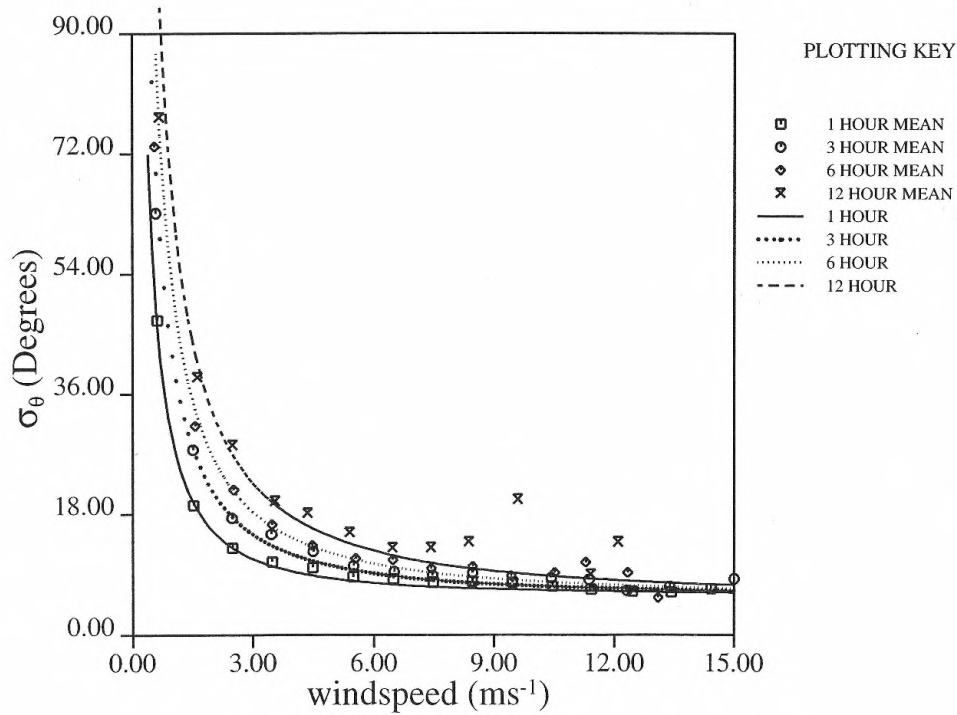


Figure 1: Figure 5b from Davies and Thomson [6], with the curves replaced by  $\sigma_\theta = \left[ (\sigma_{turb}/u)^2 + \left( (0.5 \text{ m s}^{-1}/u) T_A^{1/3} \right)^2 \right]^{1/2}$ , with the lateral turbulent velocity standard deviation estimated in the same way as in [6].

initiate mesoscale motions. They state that there appears to be no need for specific mechanisms such as gravity waves and / or particular stability conditions.

### 3.1 The history of the parametrization of unresolved mesoscale motions in NAME

Comparisons with other models and with data from the ETEX experiment highlighted that early versions of NAME were tending to over-predict air concentrations [17]. This was due to the absence of a parametrization of unresolved mesoscale motions. An initial parametrization of unresolved mesoscale motions was designed for NAME based on a Moore-type formula [20, 21], with horizontal velocity variances determined from 10 minute mean surface wind observations over the period 1988 - 1990 from the MRU (Cardington) site. At the time of the construction of this parametrization, global Numerical Weather Prediction data used as input to NAME had temporal and spatial resolutions of 90 km and 6-hourly, respectively. The highest resolution limited area NWP model had a spatial resolution of 16 km with hourly fields. The original NAME parametrization of velocity variances of unresolved mesoscale motions ( $\sigma_{u,m}^2$ ) had the following Moore-type form

$$\sigma_{u,m}^2 = 2 c_m u_{10} \Delta T_f, \quad (2)$$

where  $c_m$  is a constant,  $u_{10}$  is the mean 10 m wind and  $\Delta T_f$  is the time interval of the input Numerical Weather Prediction data, in hours. The parametrization of unresolved mesoscale motions also required a suitable timescale ( $\tau_{u,m}$ ) which was obtained by calculating a variance-weighted mean value of the periods over the range of motions of interest. Spectral analysis of the Cardington wind data gave the suggested values in table 1 for  $\sigma_{u,m}^2$ ,  $\tau_{u,m}$  and  $c_m$ , where  $c_m$  is determined from the monthly mean wind strength and cross-wind velocity variances. These velocity variances and Lagrangian timescales were used in NAME for the parametrization of unresolved mesoscale motions [19]. The parametrization was, however, only applied within the boundary layer, with the wind component (or the increment to the particle position) due to unresolved mesoscale motions set to zero above the boundary layer.

|                  | $\Delta T_f = 6$ hrs | $\Delta T_f = 3$ hrs | $\Delta T_f = 1$ hr |
|------------------|----------------------|----------------------|---------------------|
| $\sigma_{u,m}^2$ | 1.199                | 0.7380               | 0.2972              |
| $\tau_{u,m}$     | 266.6                | 171.2                | 67.2                |
| $c_m$            | 0.0209               | 0.0260               | 0.0319              |

Table 1: Velocity variances ( $\sigma_{u,m}^2$  in  $\text{m}^2 \text{s}^{-2}$ ), Lagrangian timescales ( $\tau_{u,m}$  in s) and inferred values of  $c_m$  in equation (2) obtained by Maryon [17] from spectral analysis of surface wind data from Cardington.

Some time later, changes were made to use Hanna's value of  $0.5 \text{ m s}^{-1}$  for the velocity variance and a Lagrangian timescale of 2 hours was adopted. In addition, the parametrization of unresolved mesoscale motions was applied throughout the atmosphere, and not just within the boundary layer. Following an initial spectral analysis of Numerical Weather Prediction input data conducted in 2005 [33], the  $\sigma_{u,m}$  value and the Lagrangian timescale value to be used with NWP data were increased to  $\sigma_{u,m} = 0.8 \text{ m s}^{-1}$  and 4 hours. The values to be used with single site data remained unchanged and based on Hanna's value, reflecting the belief that hourly meteorological observations would contain more information on sub two-hourly fluctuations.

It is now our belief, however, that a Lagrangian timescale of 4 hours is a little too large for unresolved mesoscale motions. Further discussion of this issue appears later in this document.

## 3.2 Parametrizations of unresolved mesoscale motions in other atmospheric dispersion models

### 3.2.1 FLEXPART

The Lagrangian dispersion model FLEXPART assumes, in a similar way to NAME, that unresolved turbulence and mesoscale motions are independent components of the total wind and both can be parametrized using a Langevin type equation [31]. FLEXPART assumes that the variance observed at the grid scale provides some information on its subgrid variance. The standard deviation of the

unresolved mesoscale motions is set to a fraction (`turbmesoscale`) of the standard deviation of the wind at the 16 grid points surrounding the particle's position in space and time. Currently this fraction is set to 0.16 [32] although previous model documentation suggests that `turbmesoscale` was set to 0.5 in earlier versions of FLEXPART [31]. The corresponding timescale is taken as half the time interval of the input meteorological data, based on the assumption that linear interpolation between the grid points can recover half the subgrid variability.

### 3.2.2 ADMS

Following Moore [21], ADMS [4] represents lateral spread in terms of two independent components: one due to boundary layer turbulence and the other due to wind direction unsteadiness. The component due to wind direction unsteadiness is based on local wind field measurements of  $\sigma_\theta$ , if available, or, if not, calculated using the formula developed by Moore [21]

$$\sigma_\theta = 0.065 \left( \frac{7}{u_{10m}} T_A \right)^{1/2},$$

where  $T_A$  is the required averaging time (in hours) and  $u_{10m}$  is the average 10 m wind speed over the same period. Moore's formula is considered to be a generic model for the UK and to be valid for averaging times up to 24 hours.

## 4 Spectra of resolved motions

In reviewing the parametrization of unresolved mesoscale motions in NAME it is a good idea to study the resolved motions in the input meteorological data, in order to gain some understanding of the missing motions that need to be parametrized. NAME primarily uses input meteorological data from the Met Office's NWP model, the Unified Model (MetUM). The global version of the MetUM has, over the years, been run at increasingly higher spatial resolution. In addition, various limited area versions, covering different geographical regions, have existed and these have also been run at increasingly higher spatial resolutions. Table 2 summarises the NWP data used in this study and illustrates the increase in resolution over time.

Energy spectra of the resolved motions were generated from time-series of NWP wind components ( $u$  and  $v$ ). The spectra obtained from NWP data were compared to the spectra obtained from observational data. A discrete Fourier transform

$$u_m = \sum_{q=-(N/2-1)}^{N/2} A_q \cos\left(\frac{2\pi qm}{N}\right) + \sum_{q=-(N/2-1)}^{N/2-1} B_q \sin\left(\frac{2\pi qm}{N}\right), \quad (3)$$

was calculated using the IDL fast Fourier transform routine, where  $u_m$  is the time-series of wind

| Year | NWP model configurations<br>(temporal sampling interval, spatial resolution) |   |   |
|------|--|---|---|
|      | MetUM  |   | ECMWF   |
|      | global model   | limited area model  | global model  |
| 1998 |  | <b>Regional</b><br><i>UMV3R</i><br>(3 hrs, 50 km)   | <b>ERAInt</b><br><i>ECMWF ERAInt Regional</i><br>(3 hrs, 80 km) |
| 2000 | <b>Global</b><br><i>UMHR</i><br>(3 hrs, 60 km)                               | <b>Mesoscale</b><br><i>UMHM</i><br>(3 hrs, 12 km)   | <b>ERAInt</b><br><i>ECMWF ERAInt Regional</i><br>(3 hrs, 80 km) |
| 2001 | <b>Global</b><br><i>UMH2001R</i><br>(3 hrs, 60 km)                           | <b>Mesoscale</b><br><i>UMH2001M</i><br>(1 hr, 12 km)  | <b>ERAInt</b><br><i>ECMWF ERAInt Regional</i><br>(3 hrs, 80 km) |
| 2004 | <b>Global</b><br><i>UM5R</i><br>(3 hrs, 60 km)                               | <b>Mesoscale</b><br><i>UM5M</i><br>(1 hr, 12 km)  | <b>ERAInt</b><br><i>ECMWF ERAInt Regional</i><br>(3 hrs, 80 km) |
| 2006 | <b>Global</b><br><i>UM6G</i><br>(3 hrs, 40 km)                               | <b>Mesoscale</b><br><i>UM5M</i><br>(1 hr, 12 km)  | <b>ERAInt</b><br><i>ECMWF ERAInt Regional</i><br>(3 hrs, 80 km) |
| 2008 | <b>Global</b><br><i>UM6G</i><br>(3 hrs, 40 km)                               | <b>NAE</b><br><i>UM6REGNAE</i><br>(1 hr, 12 km)<br><br><b>4km</b><br><i>UM4kmMk3_L50</i><br>(1 hr, 4 km)  | <b>ERAInt</b><br><i>ECMWF ERAInt Regional</i><br>(3 hrs, 80 km) |
| 2012 | <b>Global</b><br><i>UMG_Mk6_L59pp</i><br>(3 hrs, 25 km)                      | <b>NAE</b><br><i>UMNAE_Mk3_L42Rpp</i><br>(1 hr, 12 km)<br><br><b>4km</b><br><i>UM4kmMk3_L50</i><br>(1 hr, 4 km)<br><br><b>UKV</b><br><i>UM1p5km_Mk1_L57pp</i><br>(1 hr, 1.5 km) |   |

Table 2: Temporal and spatial resolution of the NWP data used in this study. Spatial resolutions are approximate values for mid-latitudes and the names by which these data sources are known within NAME (UMV3R etc.) are also noted.

components ( $u$  or  $v$ ),  $q$  is the wavenumber,  $A_q$  and  $B_q$  are the Fourier components,

$$\begin{aligned} A_q &= \frac{1}{N} \sum_{n=1}^N u_n \cos\left(\frac{2\pi qn}{N}\right), & q = \pm 1, \pm 2, \dots, \pm\left(\frac{N}{2} - 1\right) \\ B_q &= \frac{1}{N} \sum_{n=1}^N u_n \sin\left(\frac{2\pi qn}{N}\right), & q = \pm 1, \pm 2, \dots, \pm\left(\frac{N}{2} - 1\right) \\ A_0 &= \frac{1}{N} \sum_{n=1}^N u_n, \\ A_{N/2} &= \frac{1}{N} \sum_{n=1}^N u_n \cos(n\pi), \end{aligned}$$

and  $N$  is the number of data points in the time-series. If  $\Delta t$  is the time interval between successive observations ( $u_{m+1}$  and  $u_m$ ),  $m = t/\Delta t$ , where  $t$  is the time since the start of the observation series. The frequency  $f$  is given by  $f = |q| / (N\Delta t)$  and the highest frequency represented is  $f = 1 / (2\Delta t)$ . The Fourier components satisfy the relation  $A_{-q} = A_q$  and  $B_{-q} = -B_q$  and hence equation (3) can also be written as

$$u_m = A_0 + 2 \sum_{q=1}^{N/2-1} \left( A_q \cos\left(\frac{2\pi qm}{N}\right) + B_q \sin\left(\frac{2\pi qm}{N}\right) \right) + A_{N/2} \cos(\pi m).$$

The total variance is given by

$$\langle (u_m - \langle u_m \rangle)^2 \rangle = \langle u_m^2 \rangle - \langle u_m \rangle^2 = \sum_{q=1}^{N/2-1} 2(A_q^2 + B_q^2) + A_{N/2}^2.$$

The variance at each wavenumber is multiplied by  $N\Delta t$  to get the variance density (variance per unit change in frequency)

$$\phi\left(f = \frac{|q|}{N\Delta t}\right) = \phi_q = \begin{cases} 2(A_q^2 + B_q^2) \times N\Delta t, & q = 1, \dots, N/2 - 1, \\ A_{N/2}^2 \times N\Delta t, & q = N/2, \end{cases} \quad (4)$$

which satisfies

$$\int_0^\infty \phi(f) df \approx \sum_{f=1/(N\Delta t)}^{1/(2\Delta t)} \phi(f) \Delta f = \sum_{q=1}^{N/2} \phi_q \frac{1}{N\Delta t} = \text{total variance}.$$

The area under the variance spectral density curve ( $f > 0$ ) equates to the total variance. The raw spectral curve is noisy and hence a block averaging method is applied, in which the number of data values to be averaged increases by approximately a factor of 4/3 from one block to the next (i.e., the frequency boundaries of the blocks increase by roughly a factor of 4/3 between blocks).

## 5 Boundary layer motions

Hourly averaged and hourly spot (in reality, 10 minute mean) wind observations at a height of 10 m agl (above ground level) at Heathrow (51.48°N, 0.45°W), Wattisham (52.12°N, 0.96°E) and Aviemore (57.21°N, 3.83°W) have been obtained from the Met Office's observations archive (the MetDB) for the selected years 1998, 2000, 2001, 2004, 2006, 2008 and 2012. Wattisham is located in a flat rural area and Aviemore represents a rural area of complex terrain. Heathrow was chosen as a consistent and reliable observing site. Linear interpolation in time was employed, however, to replace missing data values from any of the sites. In general, missing values account for a small proportion of the observations (less than 2% in most cases) but can, on specific occasions, represent a larger fraction (for example, 8% of hourly mean wind speed observations at Heathrow are missing during 2006). Wind observations from the Met Office's Meteorological Research Unit (MRU) at Cardington (52.10°N, 0.42°W) were also obtained. Data from the surface site instrumentation at Cardington are processed and logged at a range of time intervals and observing heights (see table 3). NWP data were also retrieved at the locations and heights of the observations and linearly interpolated, if necessary, to match the time resolution of the observations.

| Year | Observing heights (m agl) | Time interval (min) |
|------|---------------------------|---------------------|
| 1998 | 4, 10                     | 17.5                |
| 2000 | 4, 10                     | 17.5                |
| 2001 | 4, 10, 45                 | 17.5                |
| 2004 | 4, 10, 25, 50             | 17.5                |
| 2006 | 10, 25, 50                | 30, 10, 5, 1        |
| 2008 | 10, 25, 50                | 30, 10, 5, 1        |
| 2012 | 2, 10, 25, 50             | 30, 10, 5, 1        |

Table 3: Heights and time intervals of Cardington surface site observations.

An example plot of the average of the spectra of  $u$  and  $v$  wind components obtained from both observations and NWP data is shown in figure 2. There is very good agreement between the spectra generated from hourly mean and hourly spot observations at a height of 10 m except at high frequencies when the spectra generated using hourly spot observations has a larger variance. This indicates that the hourly spot observations capture more information concerning higher-frequency motions. Due to the sampling rate (1 hour for Wattisham observations), aliasing of high frequency fluctuations occurs, resulting in the representation of these eddies as lower frequency motions in the spectral curve.

As expected, the spectra generated from NWP data contain less energy at high frequencies



than the spectra generated from observational data. The purpose of the NAME parametrization of unresolved mesoscale motions is to represent the effect of these sub-scale motions which are missing from the input NWP data and which are not captured by the turbulence parametrization.

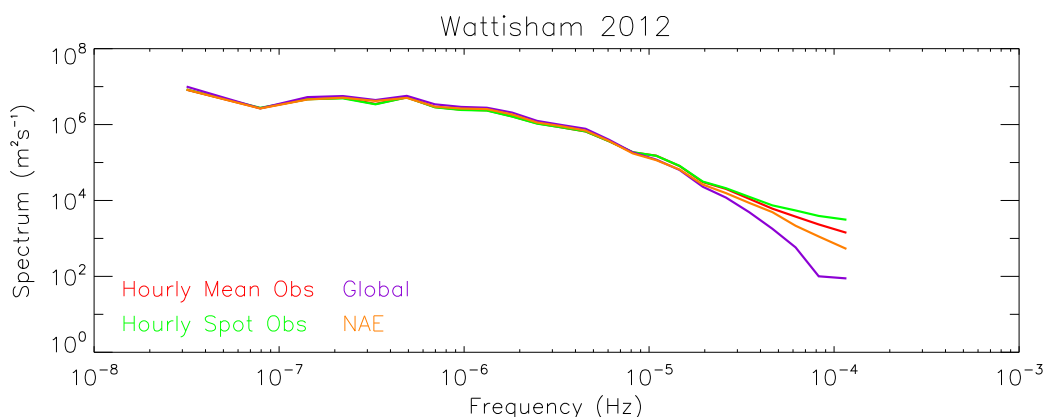


Figure 2: Wattisham spectra at a height of 10 m agl generated from 2012 observations (hourly mean and hourly spot) and MetUM data (global and NAE).

## 5.1 Understanding spectral curve discrepancies at low frequencies

Whilst most spectra (generated from observations and NWP data) agree well at low frequencies (see figure 2), there are occasions when a significant discrepancy exists at low frequencies and the spectral curve appears to have been noticeably translated up or down (see, for example, figure 3). We show that this discrepancy can be explained by differences in roughness lengths ( $z_0$ ). Smaller (larger) roughness lengths will lead, in a NWP model, to higher (lower) wind speeds within the boundary layer and hence to a shift upwards (downwards) in the spectral curve.

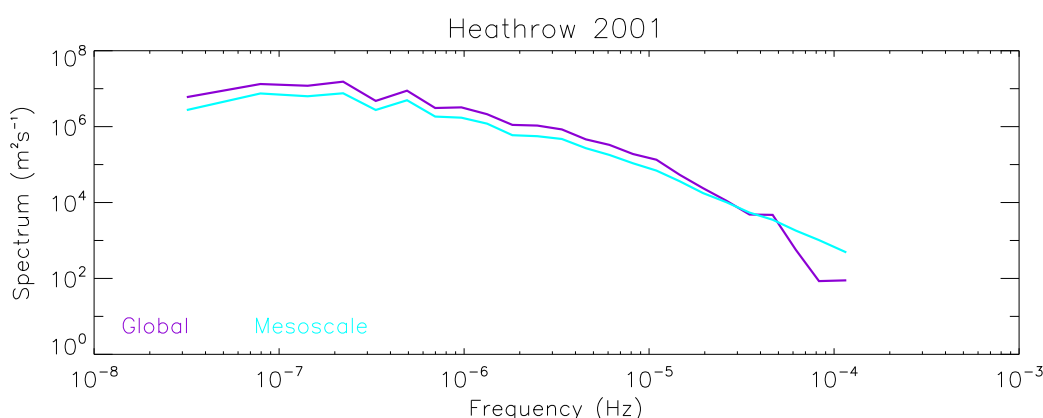


Figure 3: Heathrow spectra at a height of 10 m agl generated from 2001 global and mesoscale MetUM data and showing poor agreement at low frequencies.

For a steady-state horizontally-homogeneous neutral barotropic flow over a level surface of uni-

form roughness,

$$\begin{aligned}\frac{u_g}{u_*} &= \frac{1}{k} \ln \left( \frac{u_*}{f z_0} \right) - \frac{1}{k} A, \\ \frac{v_g}{u_*} &= -\frac{1}{k} B,\end{aligned}$$

where  $A$  and  $B$  are universal constants,  $\mathbf{u}_g = (u_g, v_g)$  is the geostrophic wind,  $u_*$  is the friction velocity,  $f$  is the Coriolis parameter and  $k$  is von Kármán's constant. Using  $A = 1.3$  and  $B = 4.4$  (Hess and Garratt's [14] best estimates for middle and high latitudes) we have

$$\frac{|\mathbf{u}_g|}{u_*} = \frac{1}{k} \left[ \left( \ln \left( \frac{u_*}{f z_0} \right) \right)^2 - 2.6 \ln \left( \frac{u_*}{f z_0} \right) + 21.05 \right]^{1/2}. \quad (5)$$

Assuming a typical value for  $\mathbf{u}_g$  ( $|\mathbf{u}_g| = 5.0 \text{ m s}^{-1}$ ), we can solve equation (5) numerically to yield  $u_*$ . We can then assume a neutral wind profile,

$$u = \frac{u_*}{k} \ln \left( \frac{z}{z_0} \right),$$

to obtain a typical 10 m wind. This procedure can be repeated using a different roughness length value to obtain a typical 10 m wind for this roughness length. From these two 10 m wind values the ratio of wind speeds for two roughness lengths can be estimated. For example, based on a mesoscale MetUM roughness length of 0.52 m and a global MetUM roughness length of 0.014 m at Heathrow during 2001, a scaling factor of 0.61 will scale the global MetUM winds to the mesoscale roughness length. Figure 4 shows the Heathrow 2001 spectra generated from the global MetUM winds scaled by a factor of 0.61 and the spectra generated from the mesoscale MetUM winds. It can be seen that the discrepancy in figure 3 between the global and mesoscale MetUM spectra at low frequencies can be more than accounted for by differences in the NWP model roughness lengths.

## 5.2 Spectra and missing variance calculations

To eliminate such discrepancies in the spectra at low frequencies, the NWP wind components are henceforth multiplied by a scaling factor chosen by fitting the NWP spectra by eye to the observed spectra at low frequencies. As well as accounting for  $z_0$  differences this will correct for any anemometer calibration inaccuracies. The scaling factors used with 2012 data at various locations and heights are given in table 4. Those used at Aviemore differ significantly from 1.0 and perhaps reflect the complex terrain of this location. Scaling factors for the other years studied are given in appendix A.

Figures 5 to 7 show the spectra generated from (scaled) NWP data and observations for 2012. Spectral plots for other years studied are given in appendix B. At Aviemore, Heathrow and Wat-

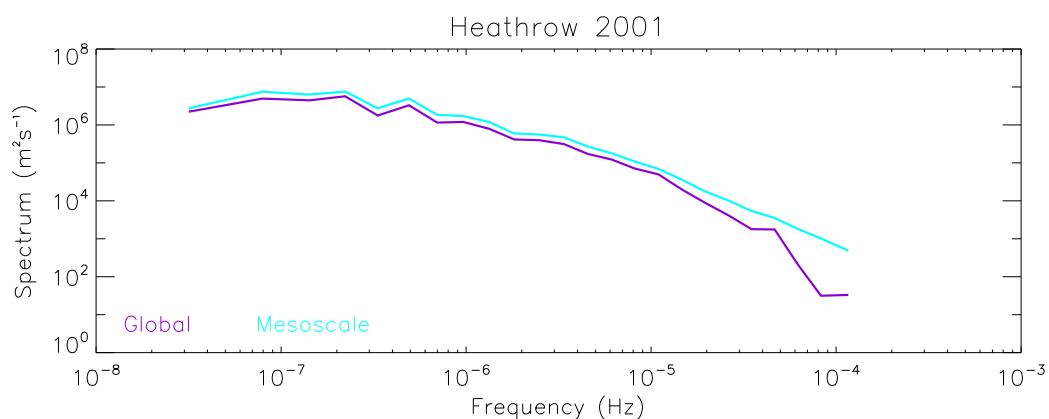


Figure 4: Heathrow spectra at a height of 10 m agl generated from (scaled) global and mesoscale MetUM winds during 2001. The global NWP winds have been modified to account for differences in roughness lengths at Heathrow between the global MetUM and the mesoscale MetUM.

| Location              | Global (25 km) | NAE (12 km) | 4 km | UKV (1.5 km) |
|-----------------------|----------------|-------------|------|--------------|
| Aviemore (10 m agl)   | 0.55           | 0.58        | 0.9  | 0.55         |
| Heathrow (10 m agl)   | 1.06           | 1.11        | 1.09 | 1.11         |
| Wattisham (10 m agl)  | 0.95           | 1.0         | 1.0  | 1.0          |
| Cardington (2 m agl)  | 1.1            | 1.1         | 1.32 | 1.32         |
| Cardington (10 m agl) | 0.9            | 0.9         | 1.1  | 1.1          |
| Cardington (25 m agl) | 0.85           | 0.85        | 1.0  | 1.0          |
| Cardington (50 m agl) | 0.85           | 0.85        | 0.98 | 0.98         |

Table 4: Scaling factors applied to NWP winds from 2012

tisham we focus on the hourly spot observations since these capture more higher frequency motions than the hourly mean observations. The higher time resolution of the observations at Cardington enable the spectra to be calculated out to higher frequencies. All NWP spectra diverge from the observed spectra at the upper frequency end, showing that the NWP models do not fully capture motions of these frequencies. The resolution of the NWP model has a noticeable impact on the motions captured at the higher frequency end, with less variance here in the spectral curve for the lower resolution models. The temporal and the spatial resolution of the NWP model are both important. There is, however, very little difference between the 4km model spectra and the UKV model spectra suggesting that the NWP time resolution may be the limiting factor for these models. The variation in the missing variance between the different NWP models is in line with the belief that the parametrization of unresolved mesoscale motions will depend on the NWP model used.

We note that, as well as aliasing affecting the observational spectra when the sampling rate doesn't match the averaging time (e.g., 1 hour vs 10 minutes for the hourly spot winds), it also affects the NWP spectra when the NWP model sampling rate is less frequent than the effective averaging time of the data (the latter being perhaps of order the NWP model's internal time step or grid length divided by a typical velocity). One would not expect the reduction of the sampling rate relative to the effective averaging time to reduce the variance, but any subsequent interpolation of the model data to match the sampling rate of the observations (such as is done within NAME and in our comparisons here) will reduce the variance. This is likely to be the main process by which the frequency at which the model data is stored influences the missing variance. (In fact this leads to the conclusion that, for 3 hourly NWP data for example, the meteorological errors are bigger and the meteorological variability is smaller at intermediate times (e.g., 1000 and 1100 UTC) than at NWP data times (e.g., 0900 and 1200 UTC). Furthermore, the missing variance ought perhaps to be bigger at intermediate times than at NWP data times. In addition the resolved eddies which are aliased to lower frequencies might perhaps be more effective than they should be in causing dispersion because of their longer life time, although this is offset by the fact that, although the Eulerian timescale of these eddies is increased, the Lagrangian timescale might not be. However we do not consider these subtle effects further here.)

To calculate the missing variance, the area between the two spectral curves is determined over a frequency range from a lower to an upper value. The lower point of the frequency range is given by the point of divergence of the NWP spectra from the observed spectra. (Section 5.2.1 discusses how this point of divergence is determined.) The upper point of the frequency range is the high frequency end of the spectral curves or the frequency which the turbulence parametrizations cover, if it is deemed to be lower. This upper frequency point is therefore both subjective and dependent on the time resolution of the observations. The most frequent observations used here are 10 minute observations from Cardington, resulting in  $8.3 \times 10^{-4}$  Hz being the highest frequency in the spectral curves (motions with periods of 20 minutes). Motions of such frequencies may possibly overlap with the frequencies covered by the turbulence parametrizations, particularly in convective condi-

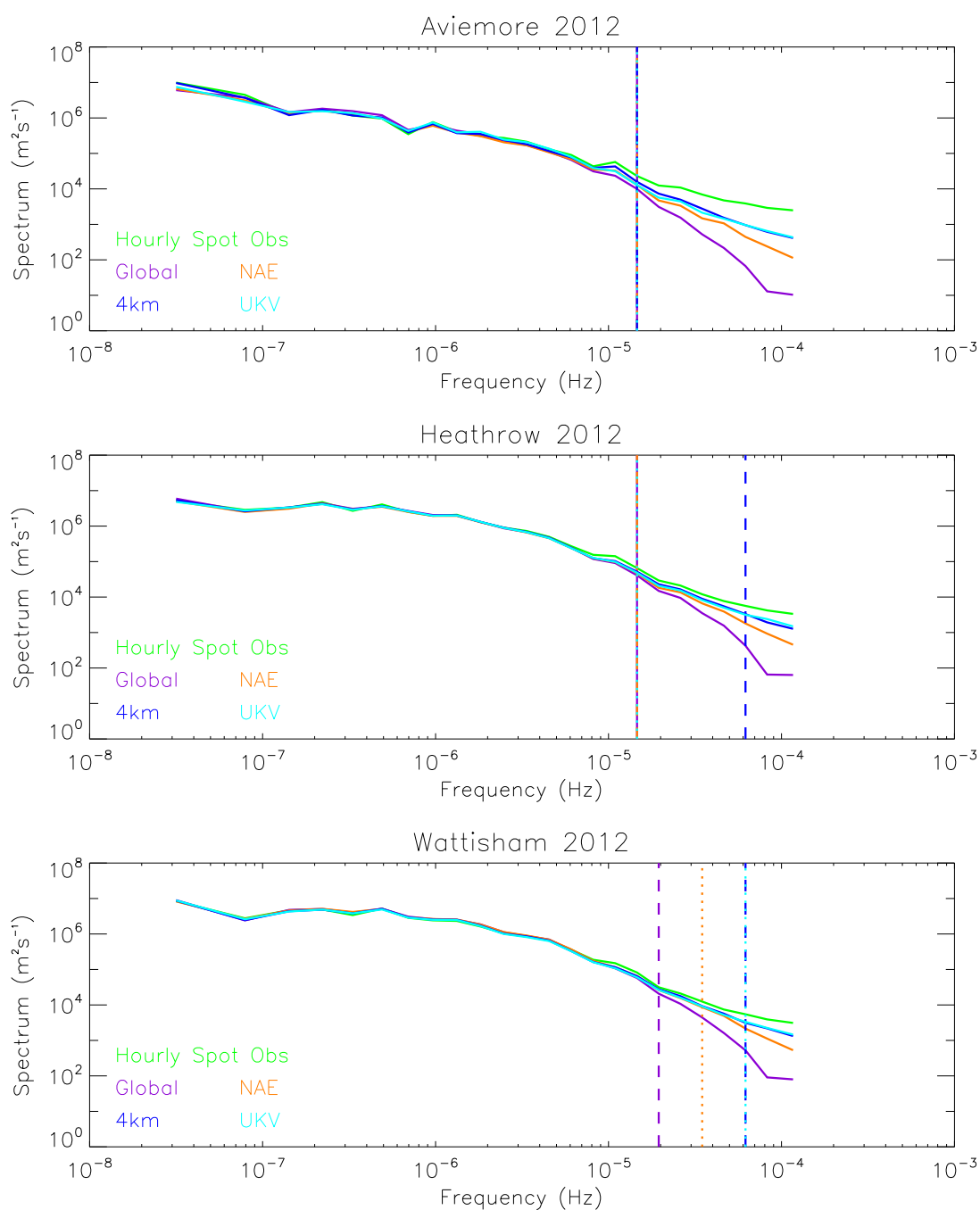


Figure 5: Aviemore, Heathrow and Wattisham spectra at a height of 10 m agl generated from 2012 observations (hourly spot) and MetUM data (global (25 km, 3 hourly), NAE (12 km, hourly), 4km (4 km, hourly) and UKV (1.5 km, hourly)). The dashed and dotted vertical lines indicate the frequency at which the NWP spectra diverge from the observational spectra.

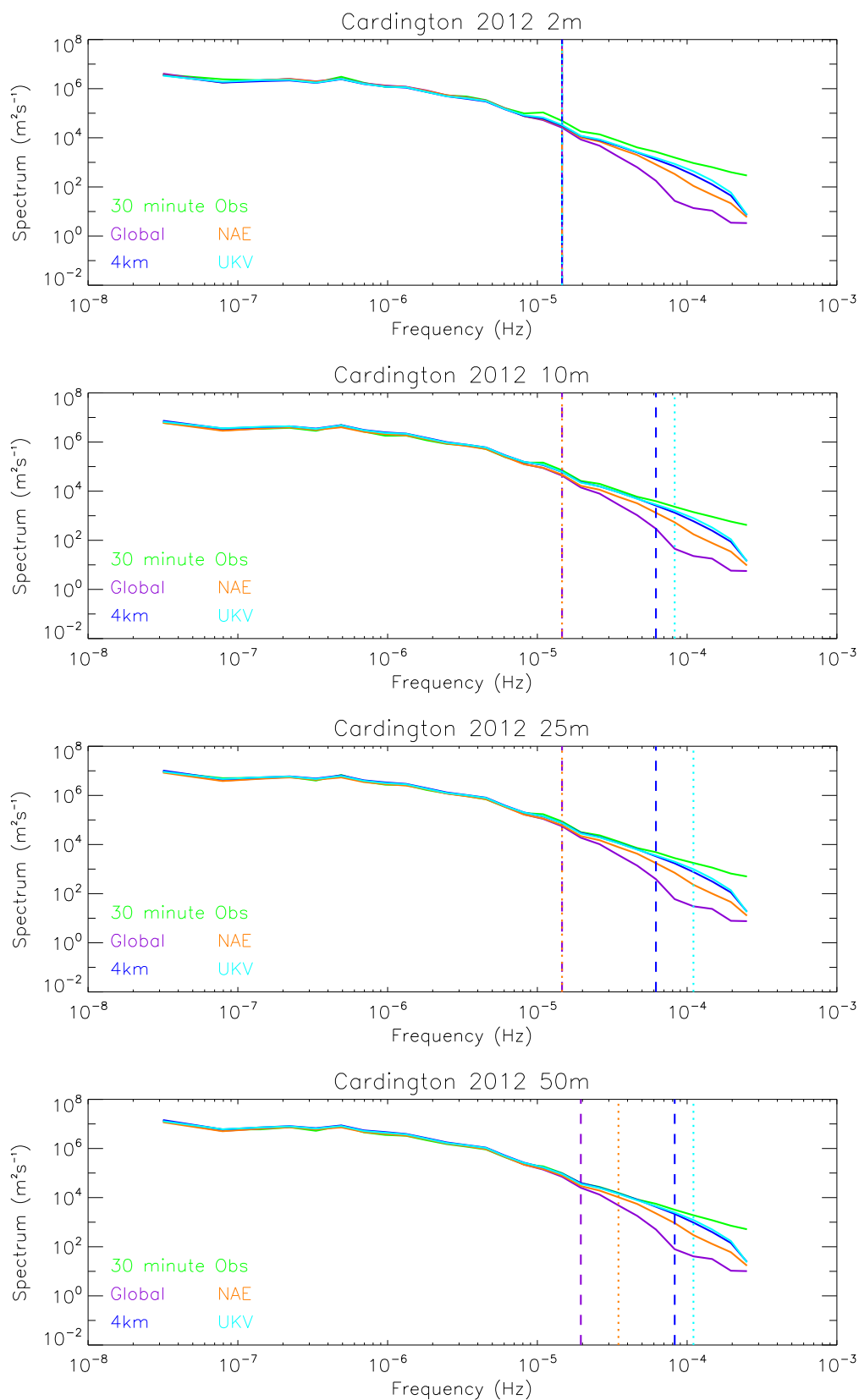


Figure 6: Cardington spectra at heights of 2 m, 10 m, 25 m and 50 m agl generated from 2012 observations (30 minute) and MetUM data (global (25 km, 3 hourly), NAE (12 km, hourly), 4km (4 km, hourly) and UKV (1.5 km, hourly)). The dashed and dotted vertical lines indicate the frequency at which the NWP spectra diverge from the observational spectra.

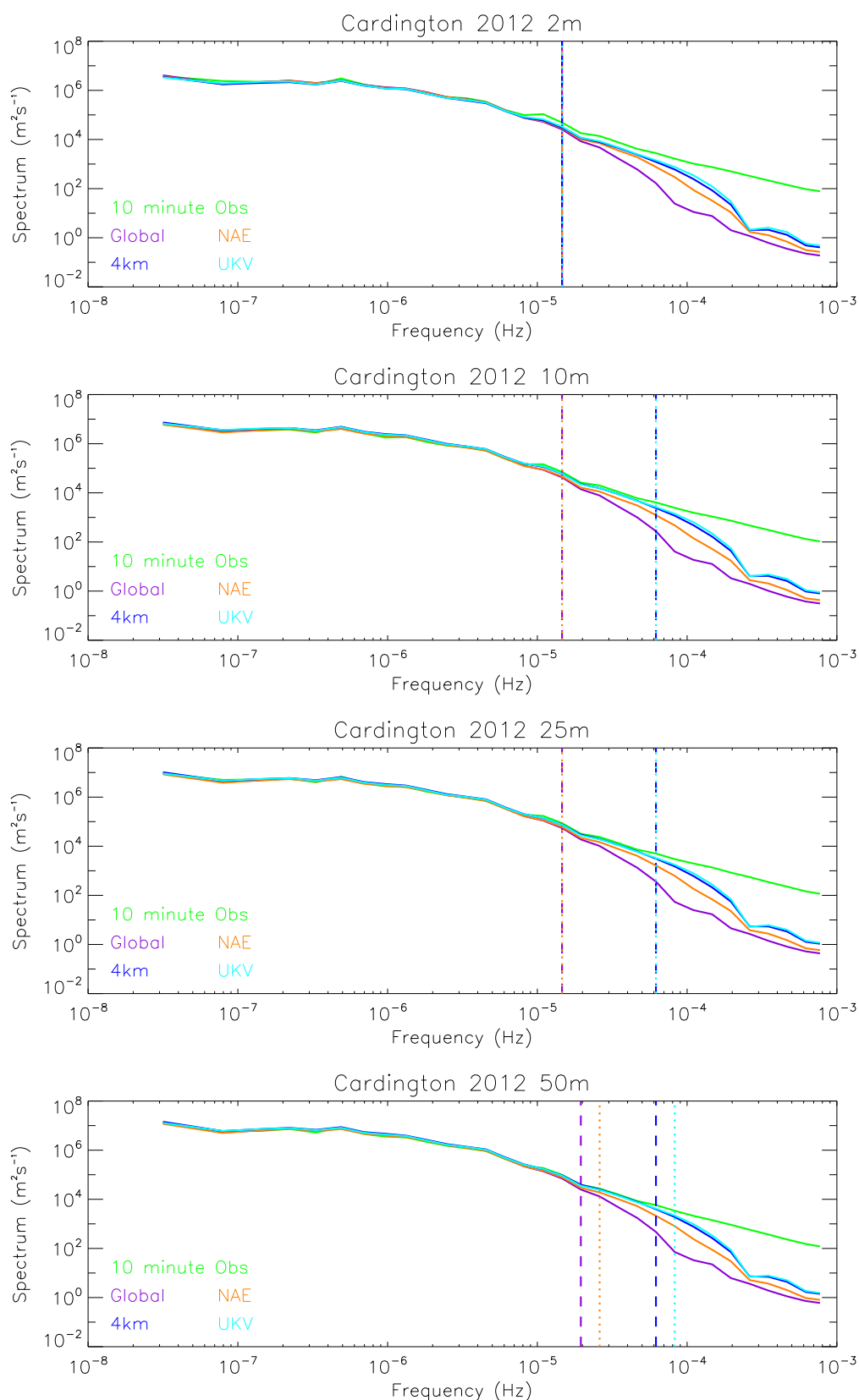


Figure 7: Cardington spectra at heights of 2 m, 10 m, 25 m and 50 m agl generated from 2012 observations (10 minute) and MetUM data (global (25 km, 3 hourly), NAE (12 km, hourly), 4km (4 km, hourly) and UKV (1.5 km, hourly)). The dashed and dotted vertical lines indicate the frequency at which the NWP spectra diverge from the observational spectra.

tions. On the other hand, the lowest frequency observations used here are hourly values, equating to a lower highest frequency in the spectral curve of  $1.4 \times 10^{-4}$  Hz (motions with periods of two hours). For hourly averaged wind observations, for example, there may be atmospheric motions with periods less than two hours which are neither captured by the missing variance calculation (because they are not resolved by the observations or equivalently are at higher frequencies than the spectra extend) nor represented in the turbulence parametrization. However, for the hourly spot observed winds (in reality, 10 minute averages at hourly intervals) which we focus on here, the variance in the observations will be similar to the variance in observations with a 10 minute frequency, with the highest frequencies being represented as lower frequency motions in the spectral curve due to aliasing. Hence, these higher frequency atmospheric motions which, on first glance might be thought to be excluded from the missing variance calculation, are included except for the part aliased to below the divergence point. There is also still the question of whether the observations include a contribution from turbulent motions. Fortunately, however, the area between the observed and NWP spectral curves is not strongly influenced by the upper frequency point (note the use of a log scale on the spectral plots and refer to table 5 which assesses the sensitivity to the upper frequency cut-off point), suggesting that one should not be overly concerned with the finer details of this point. Hence, in the calculation of the missing variance (the area between the observed and NWP spectral curves) the upper frequency point is taken as the upper frequency end of the spectral curve in each case.

| MetUM  | Upper frequency ( $10^{-4}$ Hz) |      |      |      |      |      |      |
|--------|---------------------------------|------|------|------|------|------|------|
|        | 1.68                            | 2.23 | 2.99 | 3.98 | 5.31 | 7.08 | 8.33 |
| Global | 0.64                            | 0.69 | 0.72 | 0.75 | 0.78 | 0.80 | 0.81 |
| NAE    | 0.50                            | 0.54 | 0.57 | 0.60 | 0.63 | 0.65 | 0.67 |
| 4 km   | 0.13                            | 0.17 | 0.21 | 0.24 | 0.26 | 0.29 | 0.30 |
| UKV    | 0.12                            | 0.15 | 0.19 | 0.22 | 0.24 | 0.27 | 0.29 |

Table 5: The area (in  $\text{m}^2 \text{s}^{-2}$ ) between the observed spectra (generated from 10 minute observations at a height of 10 m agl at Cardington during 2012) and the MetUM spectra from the point of divergence block to various upper frequencies.

### 5.2.1 Determining the point of divergence

The point of divergence of the NWP spectral curve from the observed spectral curve is determined from the difference between the (block averaged) modelled and observational spectra (normalised by the observational spectra) and equating where this fractional difference exceeds a threshold (taken here to be 30% of the observed spectra). There is some noise at low frequencies in the results of this difference calculation so we restrict the point of divergence to frequencies higher



than those where the spectral curves appear to diverge (around a period of 24 hours). Figures 8 to 10 show plots of the fractional difference between the observed and modelled spectra for 2012. Fractional difference plots for other years can be found in appendix C. It can be seen that there is a steep increase in the fractional difference at frequencies around  $10^{-5}$  Hz representing diurnal motions with periods of around 24 hours. The dashed and dotted vertical lines in figures 8 to 10 denote the frequency where the modelled and observed spectra differ by 30%. It can be seen that the determined point of divergence is strongly dependent on the arbitrary choice of the 30% threshold and a different threshold would, in some cases, result in a significantly different point of divergence. However, in general the lowest divergence frequency occurs for the lowest resolution NWP model (global) and the highest divergence frequency occurs for the highest resolution NWP model (UKV). Table 6 gives the frequency of the point of divergence (the block-average frequency of the first block to exceed a 30% difference, excluding any exceedances of the 30% limit at low frequencies) for 2012 data for different locations and different MetUM models, identified using this method and a threshold of 30%.

| Location              | Point of divergence frequency (Hz)<br>(Block average) |                        |                       |                         |
|-----------------------|---|------------------------|-----------------------|-------------------------|
|                       | Global<br>(25 km, 3 hourly)                           | NAE<br>(12 km, hourly) | 4km<br>(4 km, hourly) | UKV<br>(1.5 km, hourly) |
| Aviemore (10 m agl)   | $1.09 \times 10^{-5}$                                 | $1.09 \times 10^{-5}$  | $1.46 \times 10^{-5}$ | $1.09 \times 10^{-5}$   |
| Heathrow (10 m agl)   | $1.09 \times 10^{-5}$                                 | $1.09 \times 10^{-5}$  | $6.19 \times 10^{-5}$ | $1.09 \times 10^{-5}$   |
| Wattisham (10 m agl)  | $1.95 \times 10^{-5}$                                 | $3.48 \times 10^{-5}$  | $6.19 \times 10^{-5}$ | $6.19 \times 10^{-5}$   |
| Cardington (2 m agl)  | $1.09 \times 10^{-5}$                                 | $1.09 \times 10^{-5}$  | $1.09 \times 10^{-5}$ | $1.09 \times 10^{-5}$   |
| Cardington (10 m agl) | $1.09 \times 10^{-5}$                                 | $1.09 \times 10^{-5}$  | $6.19 \times 10^{-5}$ | $6.19 \times 10^{-5}$   |
| Cardington (25 m agl) | $1.09 \times 10^{-5}$                                 | $1.09 \times 10^{-5}$  | $6.19 \times 10^{-5}$ | $6.19 \times 10^{-5}$   |
| Cardington (50 m agl) | $1.95 \times 10^{-5}$                                 | $2.61 \times 10^{-5}$  | $6.19 \times 10^{-5}$ | $8.26 \times 10^{-5}$   |

Table 6: The point of divergence (in Hz) of the 2012 MetUM spectra from the observed spectra, given by the frequency at which the fractional difference exceeds 30% (see the dashed and dotted vertical lines in figures 8 and 10). The points of divergence are given for the hourly spot observations at Aviemore, Heathrow and Wattisham and for the 10 minute observations at Cardington.

### 5.2.2 Calculating Lagrangian timescales

Consider the discrete correlation function,

$$R_m = \frac{1}{N} \sum_n u_n u_{m+n},$$

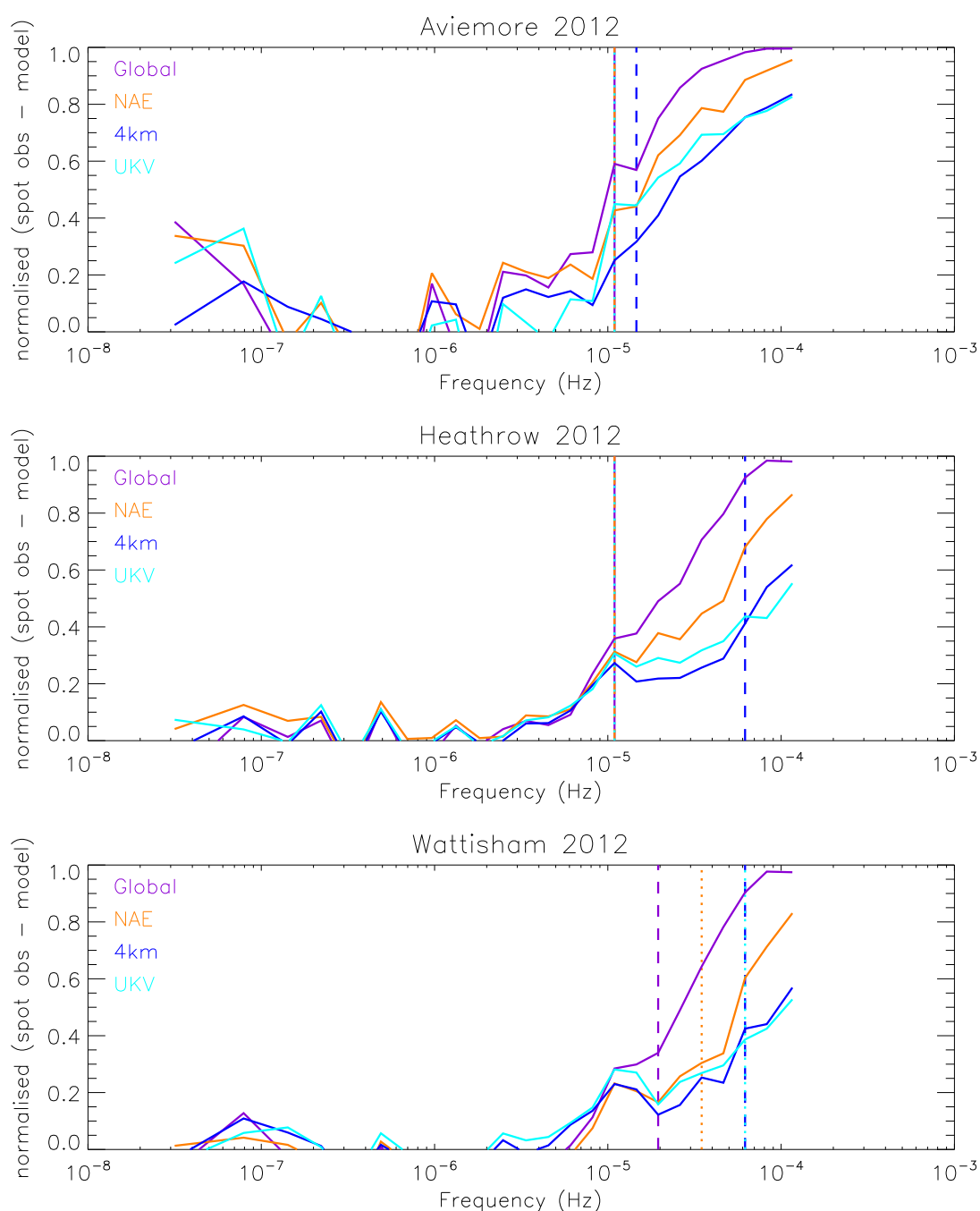


Figure 8: Fractional difference in the Aviemore, Heathrow and Wattisham spectra at a height of 10 m agl generated from 2012 hourly spot observations and MetUM data (global (25 km, 3 hourly), NAE (12 km, hourly), 4km (4 km, hourly) and UKV (1.5 km, hourly)). The dashed and dotted vertical lines denote the frequency at which the difference between the modelled and observed spectra exceeds 30%.

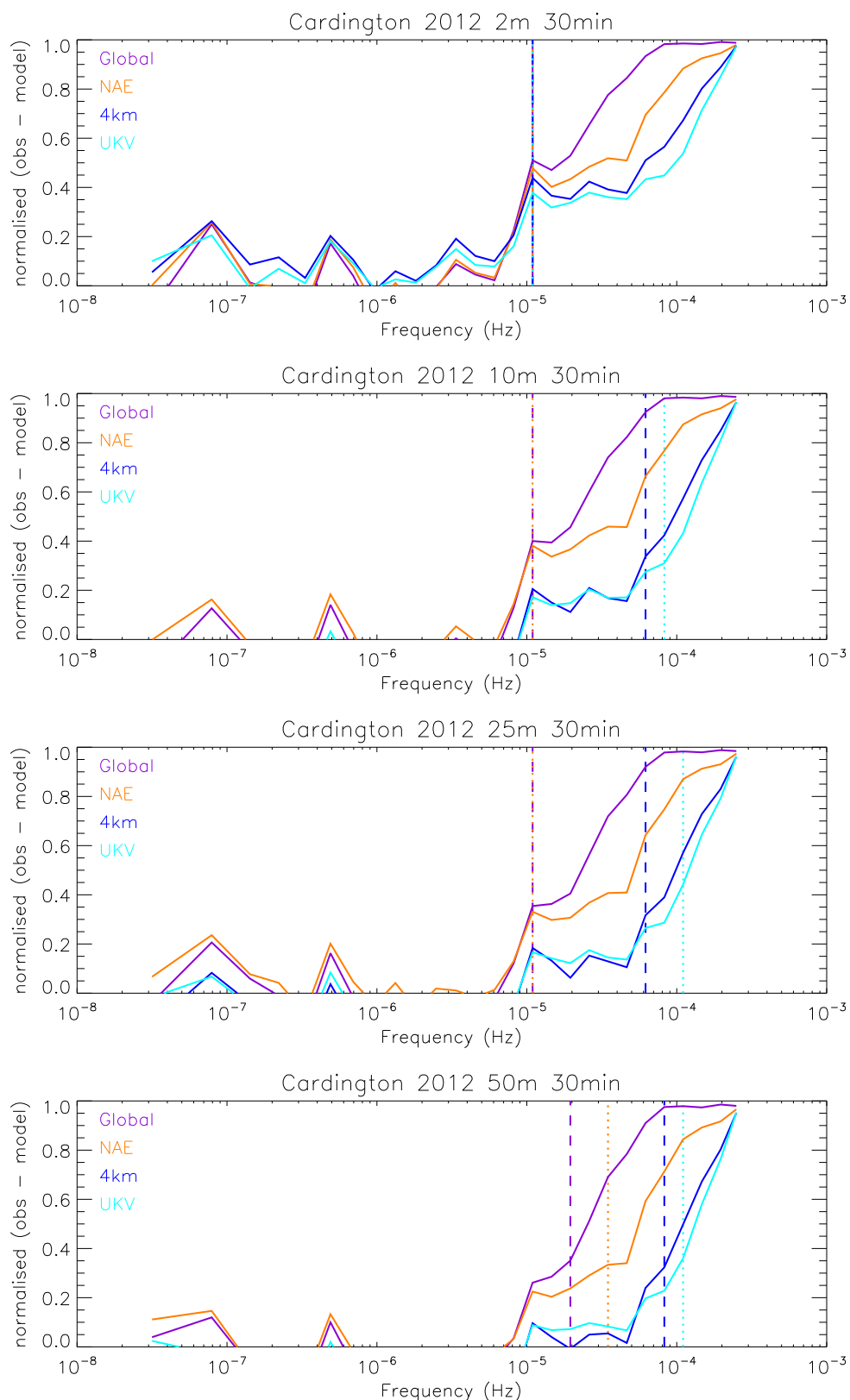


Figure 9: Fractional difference in the Cardington spectra at heights of 2 m, 10 m, 25 m and 50 m agl generated from 2012 observations (30 minute) and MetUM data (global (25 km, 3 hourly), NAE (12 km, hourly), 4km (4 km, hourly) and UKV (1.5 km, hourly)). The dashed and dotted vertical lines denote the frequency at which the difference between the modelled and observed spectra exceeds 30%.

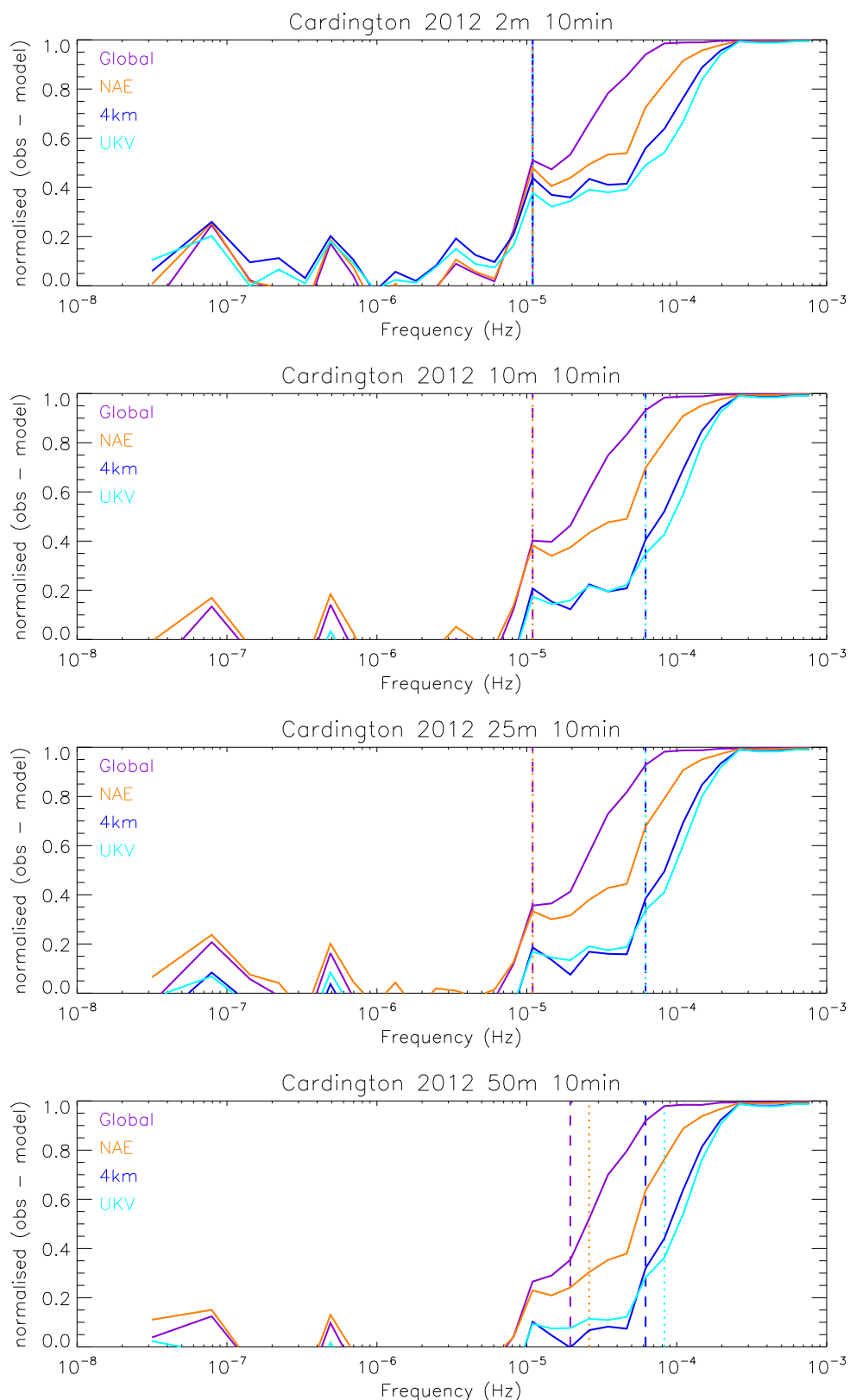


Figure 10: Fractional difference in the Cardington spectra at heights of 2 m, 10 m, 25 m and 50 m agl generated from 2012 observations (10 minute) and MetUM data (global (25 km, 3 hourly), NAE (12 km, hourly), 4km (4 km, hourly) and UKV (1.5 km, hourly)). The dashed and dotted vertical lines denote the frequency at which the difference between the modelled and observed spectra exceeds 30%.

between two observations, time  $t = m\Delta t$  apart. Treating  $R_m$  as periodic with period  $N$ ,  $R_m$  can be decomposed into Fourier analysis components and written as

$$R_m = \sum_{q=-(N/2-1)}^{N/2} S_q \cos\left(\frac{2\pi qm}{N}\right) + \sum_{q=-(N/2-1)}^{N/2-1} T_q \sin\left(\frac{2\pi qm}{N}\right).$$

One can prove using equation (3), the Fourier decomposition of  $u_m$ , that

$$\begin{aligned} S_q &= A_q^2 + B_q^2, & \forall q, \\ T_q &= 0, & \forall q. \end{aligned}$$

The Fourier component  $S_q$  satisfies the relation  $S_{-q} = S_q$  and hence

$$R_m = A_0^2 + \sum_{q=1}^{N/2-1} 2(A_q^2 + B_q^2) \cos\left(\frac{2\pi qm}{N}\right) + A_{N/2}^2 \cos(\pi m).$$

Using the definition of the variance density ( $\phi$ ) and assuming that the observations have zero mean (by preprocessing the raw data to remove the mean, if necessary),  $R_m$  can be written as

$$R_m = \sum_{q=1}^{N/2} \phi\left(\frac{q}{N\Delta t}\right) \frac{1}{N\Delta t} \cos\left(\frac{2\pi qt}{N\Delta t}\right),$$

where  $t = m\Delta t$ . Taking the continuous limit when  $\Delta t \rightarrow 0$  and  $N \rightarrow \infty$  one obtains the following expression for the correlation ( $R(t)$ ) between  $u$  at two times ( $s$  and  $s + t$ , time  $t$  apart),

$$R(t) = \overline{u(s)u(s+t)} = \int_0^\infty \phi(f) \cos(2\pi ft) df.$$

The inverse Fourier transform gives

$$\phi(f) = 4 \operatorname{Re} \left\{ \int_0^\infty R(t) \exp(-2\pi i ft) dt \right\}.$$

We can use the above analysis to calculate the correlation function from spectra. However, the integral of the correlation function cannot be used to compute an integral timescale since the correlation function with these periodicity assumptions has zero integral. Hence we consider other methods of estimating the integral timescale.

To begin we consider the spectral peak. Assuming the correlation function takes the form

$$R(t) = \sigma_u^2 \exp\left(\frac{-t}{\tau}\right), \quad (6)$$

where  $\tau$  is the integral timescale, we obtain

$$\phi(f) = 4\sigma_u^2 \operatorname{Re} \left\{ \int_0^\infty \exp\left(\frac{-t}{\tau}\right) \exp(-2\pi i f t) dt \right\} = \frac{4\sigma_u^2 \tau}{1 + 4\pi^2 f^2 \tau^2}.$$

The function  $f\phi = 4\sigma_u^2 f\tau/(1 + 4\pi^2 f^2 \tau^2)$  has a maximum at a frequency  $f = f_{max} = 1/(2\pi\tau)$  and hence the timescale  $\tau$  is given by  $\tau = 1/(2\pi f_{max})$ . Plotting the function  $f\phi$  (frequency multiplied by spectra) and determining the maximum can therefore give some insight into the appropriate value for the Lagrangian timescale.

Figures 11 and 12 show plots of the difference between the  $f\phi$  functions for observations and for MetUM data at a height of 10 m agl for 2012. The corresponding plots for other years can be found in appendix D. These plots consistently show a peak in  $f\phi$  at a block averaged frequency of  $1.09 \times 10^{-5}$  Hz, indicating that most energy is missing in the MetUM at motions with periods of about a day (i.e., diurnal motions which are not fully represented in the MetUM). This is consistent with the sudden increase in the fractional difference seen in figures 8 to 10 at this frequency. This peak in  $f\phi$  is also present, but less pronounced, using data at a height of 50 m agl at Cardington (see figure 13 for 2012; plots for data at a height of 50 m agl from other years are not presented). Gupta et al. [9] plotted spectral intensity ( $\text{m}^2 \text{s}^{-2}$ ) of observed winds and showed a similar peak in the spectral energy near the diurnal period which decayed with observation height and had its greatest amplitude just above the surface. At the latitude of Gupta's observations (Tennessee, USA), the inertial period ( $2\pi/f$ , where  $f$  is the Coriolis parameter) is about 20 hours and close to the diurnal period. Hence Gupta et al. [9] refer to this peak as the diurnal-inertial period. At UK latitudes, however, the inertial period is somewhat less ( $\sim 14$  hours) so it seems unlikely that the spectral peak observed here is related to the inertial period. It should be noted too that Gupta et al. [9] present spectral energy curves of observed winds whereas here we present the difference between observed and modelled spectral energy curves.

A diurnal variation in boundary layer wind biases is a well known problem in NWP models (see figure 7 of Brown et al. [2]) and one that is in itself important to seek improvements to. Diurnal motions are, however, not considered to be within the scales of unresolved mesoscale motions we are seeking to parametrize here. To exclude these diurnal motions from the parametrization of unresolved mesoscale motions we force the point of divergence of the modelled spectra from the observed spectra to be at a higher frequency than that corresponding to diurnal motions, moving the point of divergence as necessary from that determined by a 30% difference between the modelled and observed spectra by imposing a lower limit on the frequency ( $f = 1.25 \times 10^{-5}$  Hz). (Note that the points of divergence indicated by dashed and dotted vertical lines in the spectral plots in figures 5 to 7 are determined in this way.)

Having disregarded the diurnal peak in the  $f\phi$  functions in figures 11 and 12 and with no obvious secondary peak in the difference spectra, we investigate another method for determining a timescale for the unresolved mesoscale motions. Equation (6) indicates that a timescale can be

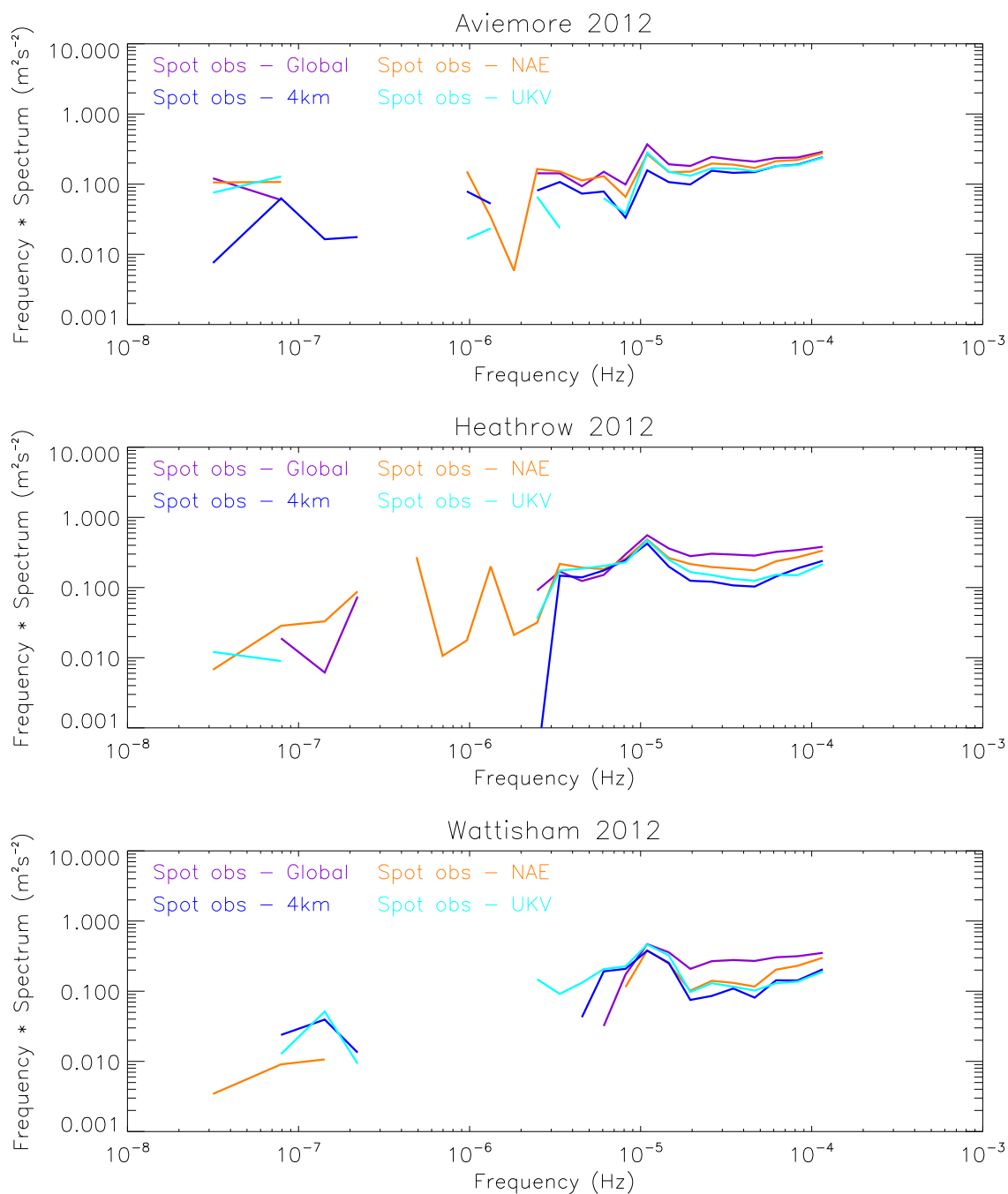


Figure 11: Difference in the observed and modelled spectra at a height of 10 m agl at Aviemore, Heathrow and Wattisham generated from 2012 hourly spot observations and MetUM data (global (25 km, 3 hourly), NAE (12 km, hourly), 4km (4 km, hourly) and UKV (1.5 km, hourly)).

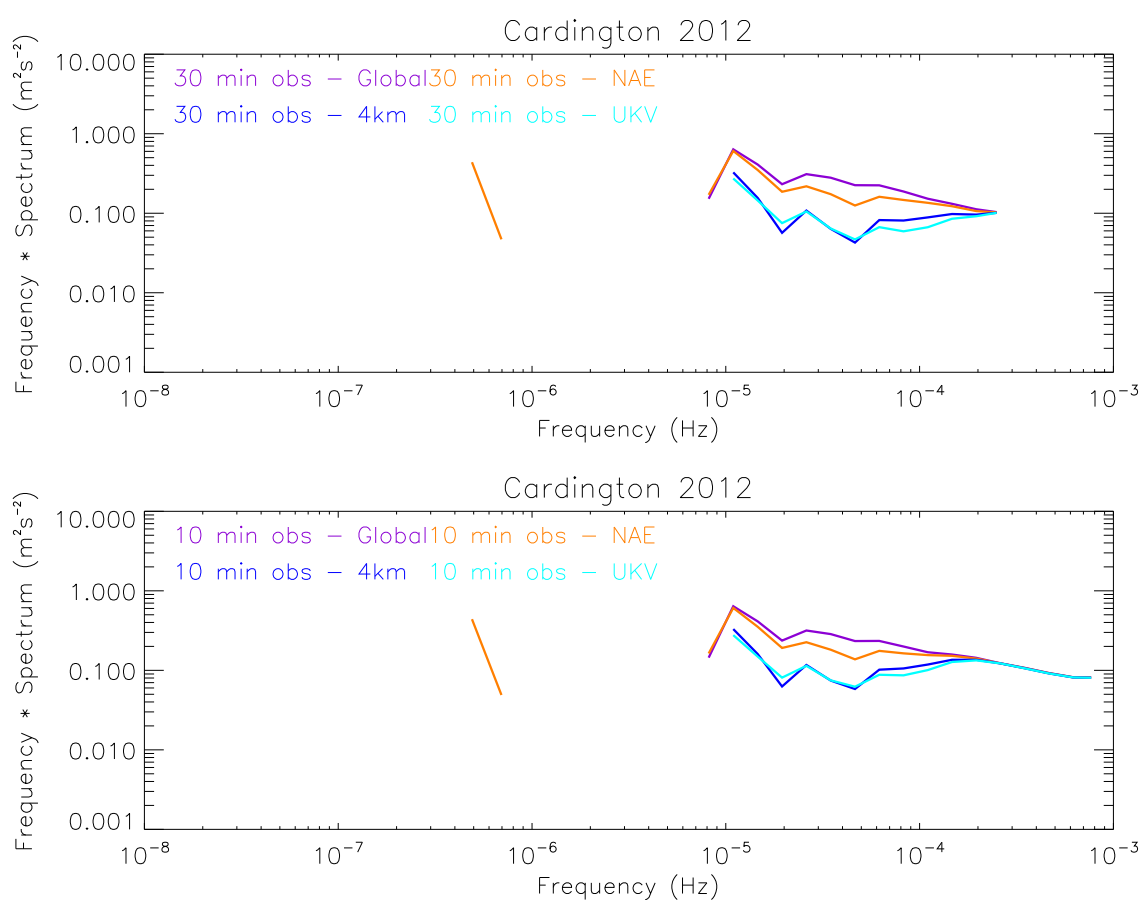


Figure 12: Difference in the observed and modelled spectra at a height of 10 m agl at Cardington generated from 2012 observations (30 minute and 10 minute) and MetUM data (global (25 km, 3 hourly), NAE (12 km, hourly), 4km (4 km, hourly) and UKV (1.5 km, hourly)).



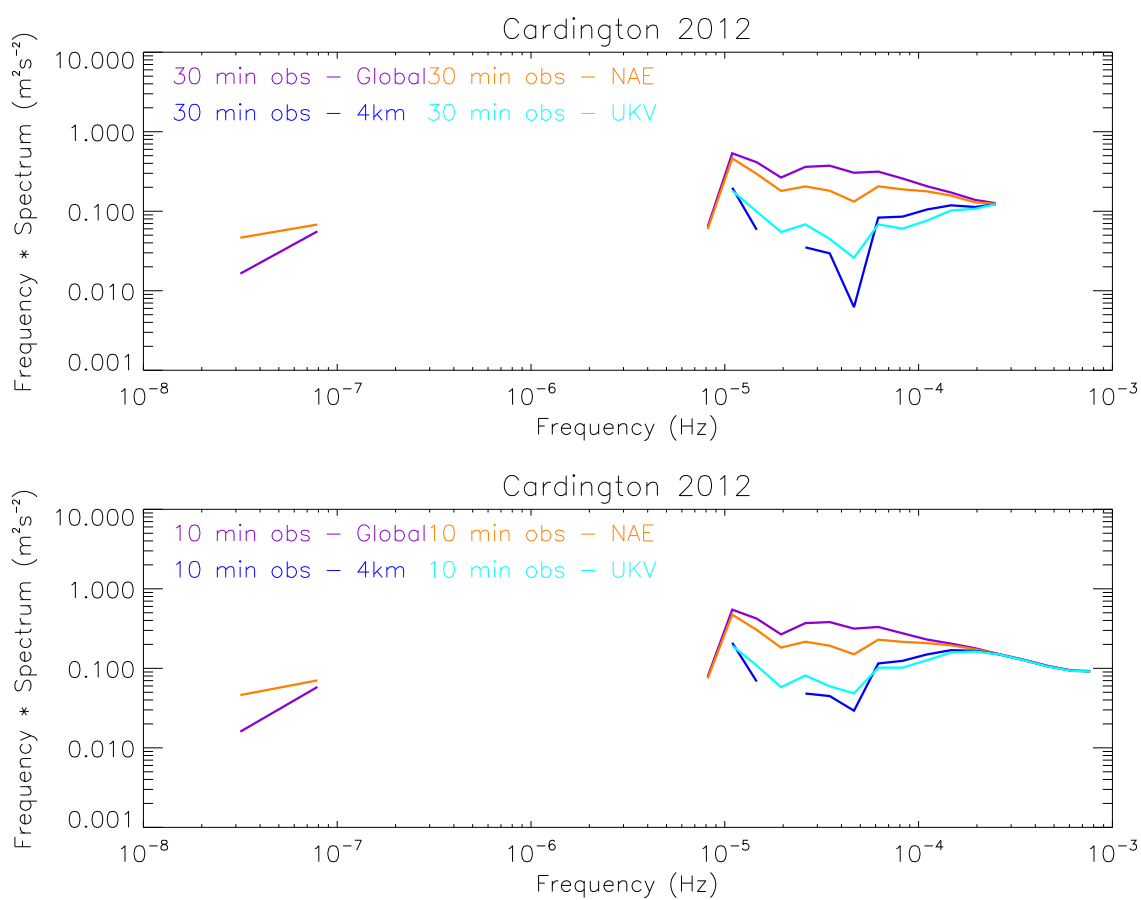


Figure 13: Difference in the observed and modelled spectra at a height of 50 m agl at Cardington generated from 2012 observations (30 minute and 10 minute) and MetUM data (global (25 km, 3 hourly), NAE (12 km, hourly), 4km (4 km, hourly) and UKV (1.5 km, hourly)).

found using the time at which the normalised correlation falls to  $e^{-1}$ . We note that the zero integral of the correlation function implies a negative lobe, potentially quite a large one if the data period is short (with significant energy on periods comparable to the data period). This may be part of the explanation for Anfossi's oscillatory correlation function [1].

A fast Fourier transform is applied to the observed and NWP time-series of wind components. The energy spectra ( $A_q^2 + B_q^2$ ) is calculated from the Fourier components ( $A_q$  and  $B_q$ ) for  $q = 0, \pm 1, \pm 2, \dots, \pm(N/2 - 1), N/2$  and filtered to remove the low frequency motions by setting  $A_q^2 + B_q^2$  to zero for wavenumbers  $q = 0, \pm 1, \pm 2, \dots, \pm(D - 1)$ , where  $f = D/(N\Delta t)$  is the block averaged frequency at which the modelled spectra is deemed to diverge from the observed spectra (including, here, the imposition of the lower limit on the frequency of the point of divergence to exclude diurnal motions). (Recall that the energy spectra ( $A_q^2 + B_q^2$ ) is the real Fourier component of the correlation function  $R_m$ .) The difference between the filtered spectra obtained from observations and from NWP model data is calculated and an inverse Fourier transform ( $F^{-1}$ ) applied to this difference to give the correlation function ( $R_m$ ) for the unresolved motions only. Plotting  $R_m$  against  $t = m\Delta t$ ,  $m = 0, \dots, N - 1$ , one can determine a timescale for the missing motions from the time at which the correlation first falls to  $e^{-1}$  of its original value ( $R_0$ ). The velocity variances ( $\sigma_u^2$ ) can also be determined from this method and are given by the initial value of the correlation function ( $R_0$ ).

Figures 14 - 16 show the correlation functions (normalised by the variance) for the motions corresponding to the missing energy in the 2012 NWP spectra. The correlation functions for the other years studied are given in appendix E. In general, the higher resolution NWP models have the smallest predicted timescales for the missing energy, in agreement with the higher frequencies for the point of divergence. The timescale determined by this correlation method, using wind data at a fixed point in space, is an Eulerian timescale ( $\tau_E$ ); the Lagrangian timescale ( $\tau_L$ ) is generally larger than the Eulerian timescale. Pasquill and Smith [24] and Hanna [11] discuss the relationship between Eulerian and Lagrangian timescales. Theory suggests that  $\tau_L/\tau_E \propto u/\sigma_u$ . However, for simplicity (and because our approach only gives a single value of  $\tau_E$  rather than one which can vary with wind speed) we choose to use  $\tau_L/\tau_E = \beta$ , where  $\beta$  is a constant value. There is some scatter in  $\beta$  obtained from observations [11]. Here we use  $\beta = 3$  to determine a Lagrangian timescale from the calculated Eulerian timescale, noting, however, that there is some uncertainty in this  $\beta$  value.

### 5.2.3 Calculating appropriate $\sigma_u$ values

The missing variance was obtained by calculating the area between the observed spectra and the NWP spectra from the point of divergence up to the high frequency end of the spectral curves (see figures 5 to 7). Recall that the high frequency end of the spectra depends on the time resolution of the observations. The point of divergence is indicated by the dotted and dashed vertical lines in figures 5 to 7. Table 7 summarises the  $\sigma_u$  values for different NWP model resolutions, acquired by computing the square root of the missing variance. The mean values are obtained by calculating the mean of the missing variance over the different locations and years studied. The range is given

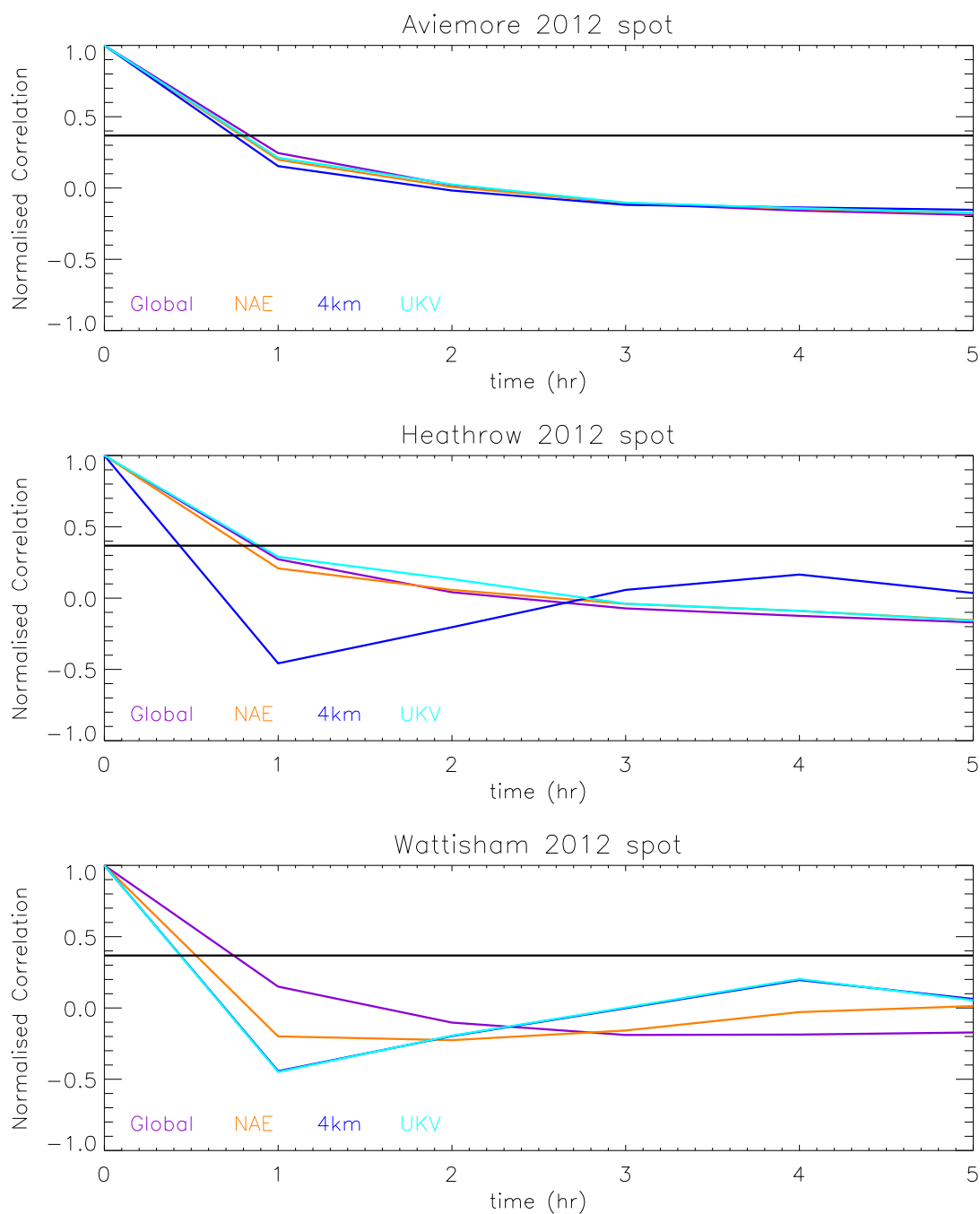


Figure 14: Normalised correlation functions for the unresolved mesoscale motions at a height of 10 m agl at Aviemoire, Heathrow and Wattisham, generated from 2012 observations (hourly spot) and MetUM data (global (25 km, 3 hourly), NAE (12 km, hourly), 4km (4 km, hourly) and UKV (1.5 km, hourly)). The  $1/e$  line (shown in black) is used to determine the timescale.

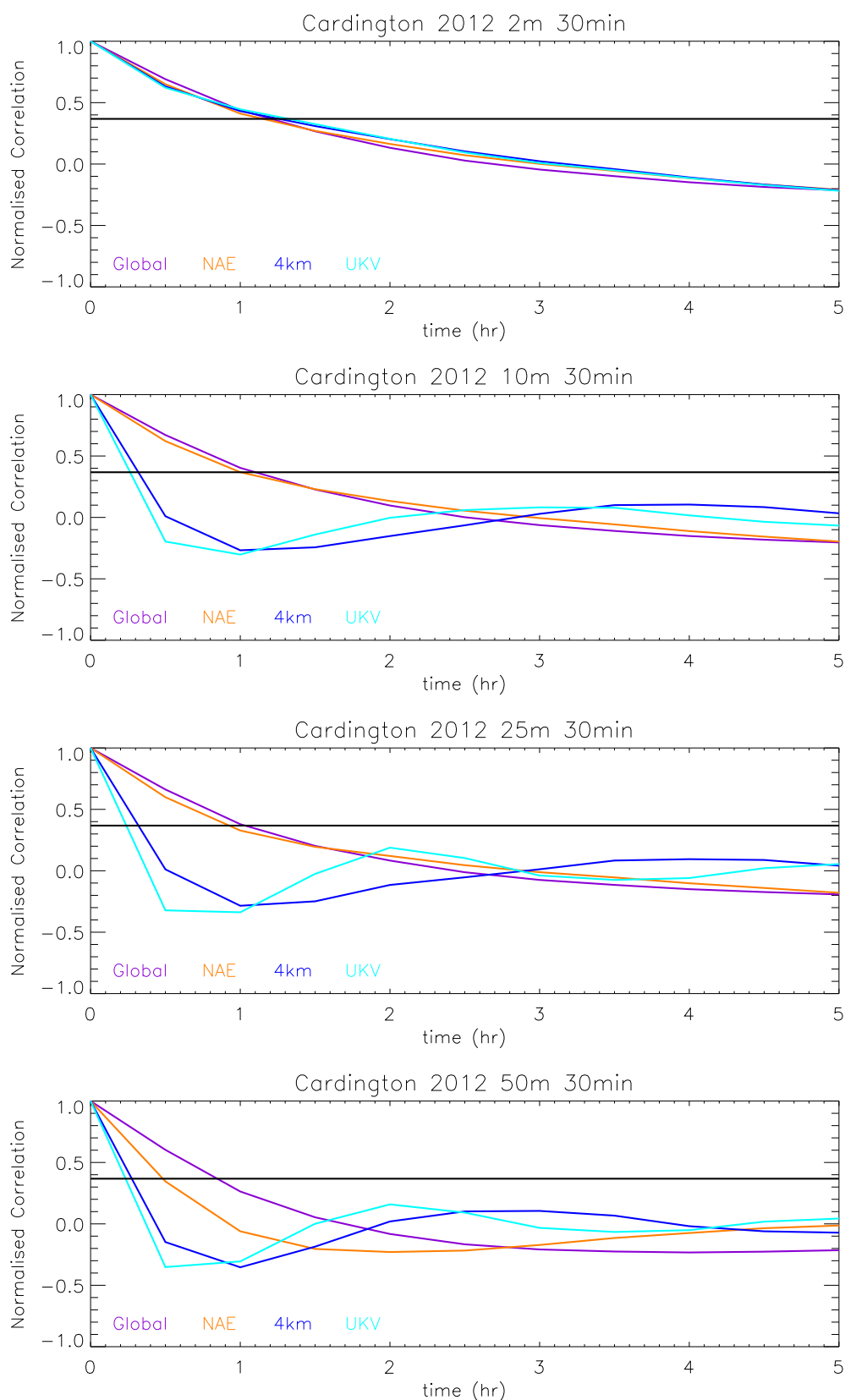


Figure 15: Normalised correlation functions for the unresolved mesoscale motions at heights of 2 m, 10 m, 25 m and 50 m agl at Cardington, generated from 2012 observations (30 minute) and MetUM data (global (25 km, 3 hourly), NAE (12 km, hourly), 4km (4 km, hourly) and UKV (1.5 km, hourly)). The  $1/e$  line (shown in black) is used to determine the timescale.

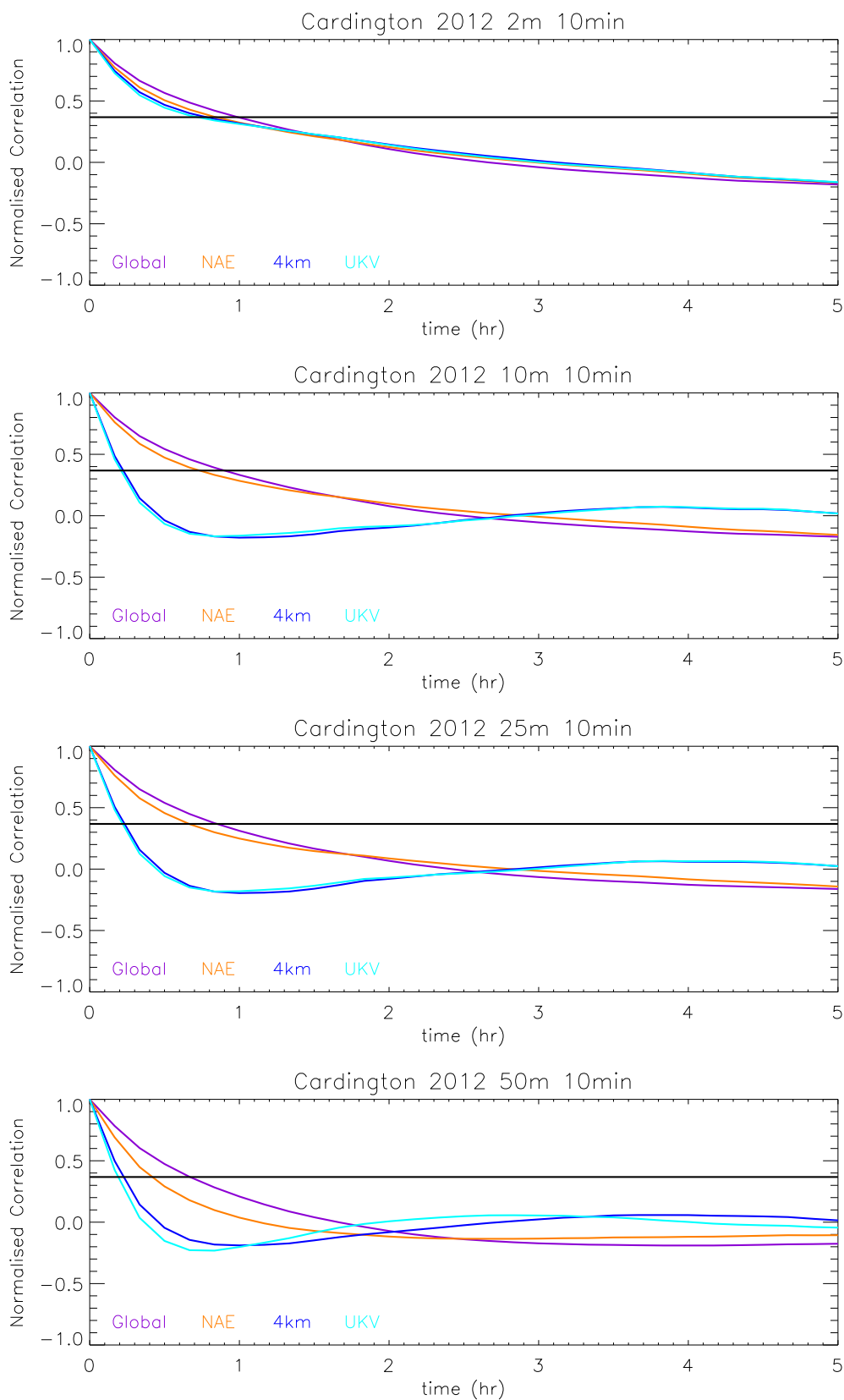


Figure 16: Normalised correlation functions for the unresolved mesoscale motions at heights of 2 m, 10 m, 25 m and 50 m agl at Cardington, generated from 2012 observations (10 minute) and MetUM data (global (25 km, 3 hourly), NAE (12 km, hourly), 4km (4 km, hourly) and UKV (1.5 km, hourly)). The  $1/e$  line (shown in black) is used to determine the timescale.

by the minimum and maximum values over the different locations and / or years. Note that a large (or small) range in  $\sigma_u$  is mainly due to many (or few) locations and years studied for that NWP model resolution (see table 2) and hence should not be interpreted as indicating large (or small) uncertainty in the  $\sigma_u$  values. Where only one missing variance calculation is available, no range is given. We observe that the  $\sigma_u$  values calculated from 30 minute observations at Cardington are similar to or slightly lower than the values obtained from the hourly spot observations at the three other sites. The  $\sigma_u$  values obtained from the older 17.5 minute observations at Cardington are similar to the values obtained from the hourly spot observations elsewhere, whereas the values obtained using the high resolution 10 minute observations at Cardington are slightly higher than the values from the hourly spot data. We also note that the  $\sigma_u$  values decrease with increasing resolution of the NWP model. Recommended values suitable for use with current NWP data, and based on the values in table 7, are given in table 9 below.

### 5.3 Diffusivities

Appropriate diffusivities ( $K_u$ ) are determined from the velocity variances (obtained from calculating the missing variance in the energy spectra) and the Lagrangian timescales (obtained from the correlation functions) using  $K_u = \sigma_u^2 \tau_u = 3\sigma_u^2 \tau_E$  and are given in table 8. The mean values are the mean diffusivities over the different years and locations studied. A range from the minimum to the maximum diffusivities is given when more than one diffusivity is available. In some cases, there is a wide range of diffusivities. Nonetheless, it can be seen that smaller diffusivities are appropriate for use with high resolution NWP data. The diffusivity value used to parametrize unresolved mesoscale motions in NAME prior to this study (namely,  $K_u \sim 9000 \text{ m}^2 \text{ s}^{-1}$ ) is appropriate for low resolution NWP data (i.e., for meteorological fields available every 3 hours (or less frequently) and with gridpoints with a horizontal spacing of 40-50 km or coarser). However, smaller diffusivities are suggested here for use with higher (spatial or temporal) resolution NWP data.

### 5.4 Recommended boundary layer parametrization of unresolved mesoscale motions

One can see from tables 7 and 8 that there is obviously some uncertainty in the appropriate parameters to be used with different resolution NWP data in the parametrization of unresolved mesoscale motions in NAME. Table 9, however, provides some guidance of suggested parameter values which can be implemented simply. In most cases, NAME is run using the cheap long-range diffusive scheme and hence the key quantity for the parametrization is the overall horizontal diffusivity. As a result of this work, the appropriate  $\sigma_u$  and  $\tau_u$  parameters (table 9) for the parametrization of unresolved mesoscale motions are now specified in the NWP met definition file. The user can, however, easily modify these parameters by specifying alternative values in the NAME input file. It is heartening to note that the ECMWF ERA Interim parameters in tables 7 and 8 are in keeping with the

| Model                      | Aviemore, Heathrow & Wattisham |      |             | Cardington                   |                      |   |
|----------------------------|--------------------------------|------|-------------|------------------------------|----------------------|---|
|                            | Obs                            | Mean | Range       | Obs                          | Mean                 | Range                                     |
| ERAInt<br>(80 km, 3 hrs)   | 1 hr                           | 0.96 | 0.83 - 1.11 | 30 min<br>17.5 min<br>10 min | 0.92<br>1.01<br>0.99 | 0.91 - 0.92<br>0.98 - 1.05<br>0.99 - 1.00 |
| Global<br>(60 km, 3 hrs)   | 1 hr                           | 0.90 | 0.79 - 0.97 | 17.5 min                     | 0.98                 | 0.97 - 0.99                               |
| Regional<br>(50 km, 3 hrs) | 1 hr                           | 1.02 | 0.84 - 1.11 | 17.5 min                     | 1.05                 |   |
| Global<br>(40 km, 3 hrs)   | 1 hr                           | 0.89 | 0.81 - 0.93 | 30 min<br>10 min             | 0.88<br>0.96         | 0.88 - 0.88<br>0.96 - 0.96                |
| Global<br>(25 km, 3 hrs)   | 1 hr                           | 0.80 | 0.74 - 0.88 | 30 min<br>10 min             | 0.82<br>0.90         |   |
| Mesoscale<br>(12 km, 3 hr) | 1 hr                           | 0.87 | 0.77 - 0.99 | 17.5 min                     | 0.96                 |   |
| Mesoscale<br>(12 km, 1 hr) | 1 hr                           | 0.69 | 0.44 - 0.84 | 30 min<br>17.5 min<br>10 min | 0.71<br>0.92<br>0.81 | 0.91 - 0.94                               |
| NAE<br>(12 km, 1 hr)       | 1 hr                           | 0.69 | 0.56 - 0.76 | 30 min<br>10 min             | 0.65<br>0.76         | 0.58 - 0.72<br>0.70 - 0.82                |
| 4km<br>(4 km, 1 hr)        | 1 hr                           | 0.51 | 0.40 - 0.62 | 30 min<br>10 min             | 0.45<br>0.60         | 0.39 - 0.50<br>0.55 - 0.65                |
| UKV<br>(1.5 km, 1 hr)      | 1 hr                           | 0.57 | 0.39 - 0.65 | 30 min<br>10 min             | 0.33<br>0.53         |   |

Table 7: A summary of  $\sigma_u$  values (in  $\text{m s}^{-1}$ ) obtained by calculating the missing variance in the NWP spectra obtained using data at a height of 10 m agl. The hourly spot observations are used at Aviemore, Heathrow and Wattisham.

| Model                      | Aviemore, Heathrow & Wattisham |       |              | Cardington                   |                         |   |
|----------------------------|--------------------------------|-------|--------------|------------------------------|-------------------------|---|
|                            | Obs                            | Mean  | Range        | Obs                          | Mean                    | Range   |
| ERAInt<br>(80 km, 3 hrs)   | 1 hr                           | 9951  | 6163 - 16882 | 30 min<br>17.5 min<br>10 min | 11132<br>11736<br>11310 | 10878 - 11386<br>10534 - 12826<br>10847 - 11773 |
| Global<br>(60 km, 3 hrs)   | 1 hr                           | 8045  | 5882 - 11037 | 17.5 min                     | 10854                   | 9724 - 11812                                    |
| Regional<br>(50 km, 3 hrs) | 1 hr                           | 11765 | 7414 - 16165 | 17.5 min                     | 12777                   |   |
| Global<br>(40 km, 3 hrs)   | 1 hr                           | 7558  | 5977 - 8613  | 30 min<br>10 min             | 9545<br>9798            | 9291 - 9800<br>9631 - 9965                      |
| Global<br>(25 km, 3 hrs)   | 1 hr                           | 5694  | 4905 - 7245  | 30 min<br>10 min             | 7855<br>7911            |   |
| Mesoscale<br>(12 km, 3 hr) | 1 hr                           | 6667  | 5350 - 9023  | 17.5 min                     | 9466                    |   |
| Mesoscale<br>(12 km, 1 hr) | 1 hr                           | 3813  | 852 - 6381   | 30 min<br>17.5 min<br>10 min | 4995<br>9763<br>4629    | 9087 - 10439                                    |
| NAE<br>(12 km, 1 hr)       | 1 hr                           | 3740  | 1783 - 4947  | 30 min<br>10 min             | 3662<br>3622            | 1837 - 5486<br>1966 - 5279                      |
| 4km<br>(4 km, 1 hr)        | 1 hr                           | 1763  | 752 - 3131   | 30 min<br>10 min             | 880<br>1130             | 537 - 1222<br>753 - 1508                        |
| UKV<br>(1.5 km, 1 hr)      | 1 hr                           | 2728  | 701 - 3873   | 30 min<br>10 min             | 312<br>658              |   |

Table 8: A summary of horizontal diffusivity values ( $K_u$  in  $\text{m}^2 \text{s}^{-1}$ ) obtained from the velocity variances and Lagrangian timescales ( $K_u = \sigma_u^2 \tau_u$ ) at 10 m agl. The hourly spot observations are used at Aviemore, Heathrow and Wattisham.



MetUM parameters (namely, they are similar to, if a bit larger than, the older global MetUM parameters as expected, due to ERA Interim having a similar but slightly coarser resolution). This suggests that, in general, the results here can be assumed to be transferable and appropriate parameters can be selected for use with NWP data from other centres based on the spatial and temporal resolution of the data.

| Model / Resolution           | Recommended values                 |                 |  |
|------------------------------|------------------------------------|-----------------|--|
|                              | $\sigma_u$<br>(m s <sup>-1</sup> ) | $\tau_u$<br>(s) | $K_u$<br>(m <sup>2</sup> s <sup>-1</sup> ) |
| Global / >60 km, 3-hourly    | 0.95                               | 10000           | 9000                                       |
| Global / ~40 km, 3-hourly    | 0.9                                | 10000           | 8000                                       |
| Global / ~20 km, 3-hourly    | 0.8                                | 10000           | 7000                                       |
| Mesoscale / ~10 km, 3-hourly | 0.8                                | 10000           | 7000                                       |
| Mesoscale / ~10 km, hourly   | 0.7                                | 8000            | 4000                                       |
| 4km or UKV / ≤ 4 km, hourly  | 0.55                               | 6500            | 2000                                       |

Table 9: Recommended parameter values for the parametrization of unresolved mesoscale motions based on NWP model resolution.

## 6 Free troposphere motions

As mentioned earlier there has been a significant change over time in NAME's parametrization of unresolved mesoscale motions in the free troposphere. Initially, unresolved mesoscale motions were not represented in NAME in the free troposphere. However, since these early versions of NAME, the parametrization used within the boundary layer has been adopted. This indecision, or change of view, reflects, in some way, a lack of observations from the free troposphere on which to put the parametrization on a firm basis. In comparison to the boundary layer, mesoscale motions in the free troposphere are not well understood.

It is a non-trivial exercise to obtain good, reliable and frequent wind observations over a significant period of time in the free troposphere. Even instrumentation on tall towers (such as the 200 m Cabauw tower in The Netherlands) do not consistently measure above the boundary layer. Radiosondes provide atmospheric profile data but only infrequently (often twice a day) and furthermore they are advected downwind, and hence do not give observations at a fixed location. Free tropospheric wind data (Atmospheric Motion Vectors (AMVs)) can be derived from satellite data by tracking tracers (usually clouds or water vapour) through a sequence of images. Whilst this can result in some cases in hourly data, the location and height (in pressure) of observations is variable and determined by the cloud location and cloud top. Furthermore, the resolution is relatively coarse

with significant spatial and temporal averaging. In addition, the data can have rather complicated error characteristics. This suggests that satellite-derived wind data is not well suited to the spectral analysis conducted here. Wind data determined from wind profilers, however, results in high temporal resolution data at fixed locations, measured at fixed heights and is therefore well suited to the type of spectral analysis considered here.

## 6.1 Wind profiler data

A number of authors have studied the accuracy of horizontal winds measured by wind profilers. Further studies comparing wind profiler observations to model analyses have also been conducted. Pauley et al. [25] compared wind profiler observations to operational regional analyses at a site in Illinois. Schafer et al. [28] studied the differences between wind profiler measurements and model winds (from the NCEP-NCAR reanalysis) at locations in the tropical Pacific which is a region with few observations. Both studies showed that assimilation of wind profiler observations resulted in an improvement to the model analyses.

Wind profilers are designed to detect the motion of the air due to refractive index irregularities (Bragg scattering) [7]. Data can, however, be contaminated by competing motion from objects in the air such as birds and, more importantly, hydrometeors (Rayleigh scattering). The wind data utilised here is obtained from a network of wind profilers around the UK: Aberystwyth (52.424°N, 4.005°W), Camborne (50.219°N, 5.327°W), Douglas, Isle of Man (54.107°N, 4.553°W), Dunkeswell (50.860°N, 3.240°W), South Uist (57.254°N, 7.375°W) and Wattisham (52.124°N, 0.956°E). Data at each location is available at fixed heights above mean sea level and time averaged at either 15 or 30 minute intervals. There are some differences between the instrumentation at the various sites.

The wind profilers at Camborne, Douglas, Dunkeswell and Wattisham are all Vaisala LAP3000 wind profilers with an antenna array about 5 m across. These operate at either 1290 or 915 MHz and routinely measure up to heights of around 3 km. They are capable of measuring up to around 3 km in 'normal' clear sky conditions, as long as the atmosphere is sufficiently moist. If the atmosphere is dry, then the returned power is lower and this can result in layers of missing data or a reduction in the maximum measurable altitude. Because of their operating frequency, they are significantly affected by scattering from hydrometeors, but otherwise measure scattering from the air. Thick clouds produce strong scattering at the wind profiler's operating frequency and, as a result, under these conditions the wind profilers are capable of producing data up to approximately 8 km.

The wind profiler at South Uist is a 64 MHz LAP12000 system, designed to measure up to around 12 km under any conditions, although it currently rarely reaches that height. The South Uist wind profiler is a powerful array comprising a field of 144 antennas, each 2 m high and the array is about 40 m across. The operating frequency is too low for the wind profiler to be affected by rainfall unless it is very heavy, so it generally only yields returns from the air. The profiler is affected by areas of dry air and certain types of flow which result in low returns, so gaps are sometimes seen

in the data.

The wind profiler array at Aberystwyth is larger still with 400 antennas, each about 4 m tall with a total array width of 110 m. This gives a maximum measurable altitude of around 20 km, although it is typically only used up to 16 km. It operates at 46.5 MHz, so it is even less likely to be affected by rainfall than the wind profiler at South Uist. When it is, however, it tends to mask the clear-air returns (resulting in gaps in the data) rather than contaminating them with scattering from the precipitation. It is a much more powerful array - the most powerful in the UK, so it rarely suffers from gaps in the data.

The Aberystwyth and South Uist wind profilers consistently report data above the boundary layer so we focus on the results from these two wind profilers (although results from the other wind profilers at lower heights are presented in appendices F, G and H). Wind data for the year from March 2012 until February 2013, at a range of heights above the boundary layer, were obtained and the energy spectra calculated. Data from the Aberystwyth and South Uist wind profilers are available at 30 minute intervals. Figures 17 and 18 compare the calculated spectra at a range of heights at Aberystwyth and South Uist, respectively, using wind profiler observations and MetUM NWP data. The spectra from observations and from NWP data agree remarkably well at low frequencies. Hence no scaling is required, in contrast to what was often the case within the boundary layer, to ensure that the observed and NWP spectra agreed well at low frequencies. The surface roughness has minimal effect within the free troposphere so this is to be expected and further strengthens the reasoning for scaling the NWP spectra within the boundary layer. There is more energy in motions of all frequencies in the free troposphere compared to boundary layer motions (note the difference in the vertical axis values between figures 17 and 18 and figures 5 to 7) which is consistent with higher wind speeds in the free troposphere. In addition, figures 17 and 18 show that the NWP spectra begin to diverge from the observations spectra at a higher frequency (compare table 10 with table 6). We see also that the NAE and UKV spectra (both from hourly resolution NWP data) are very similar but both differ significantly from the global spectra (from three-hourly resolution NWP data), which diverges from the observed spectra at a lower frequency and has noticeably more missing energy. This suggests that the time resolution of the NWP data is the limiting factor here in representing the higher frequency motions in the free troposphere.

The point of divergence of the NWP spectra from the observed spectral curve is determined using the same method as before, by equating the frequency at which the normalised difference between the modelled and observed spectra exceeds a threshold value of 30%. The fractional differences between the observed and NWP spectra at selected heights at Aberystwyth and South Uist are shown in figures 19 and 20, respectively. (The fractional difference plots for the other wind profiler sites are given in appendix G.) The points of divergence for the different NWP models are indicated by the dashed and dotted vertical lines in figures 17 - 20 and the frequencies are given in table 10. In general, the point of divergence of the UKV spectra is similar to that of the NAE spectra, due to the similarities between these spectral curves. However some differences do exist

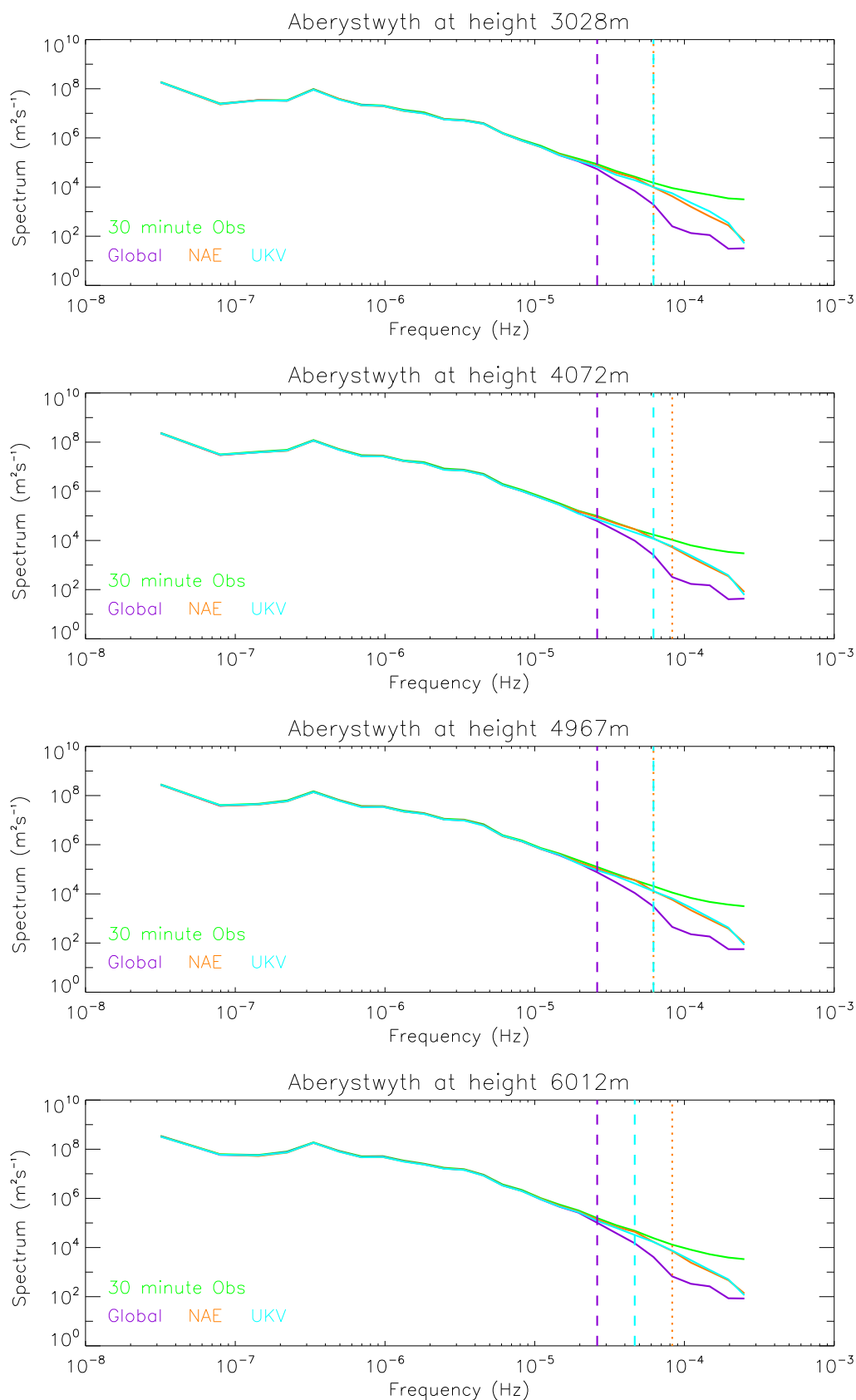


Figure 17: Free tropospheric spectra at various heights at Aberystwyth generated from wind profiler observations (30 minute mean) and MetUM data (global (25 km, 3 hourly), NAE (12 km, hourly) and UKV (1.5 km, hourly)).

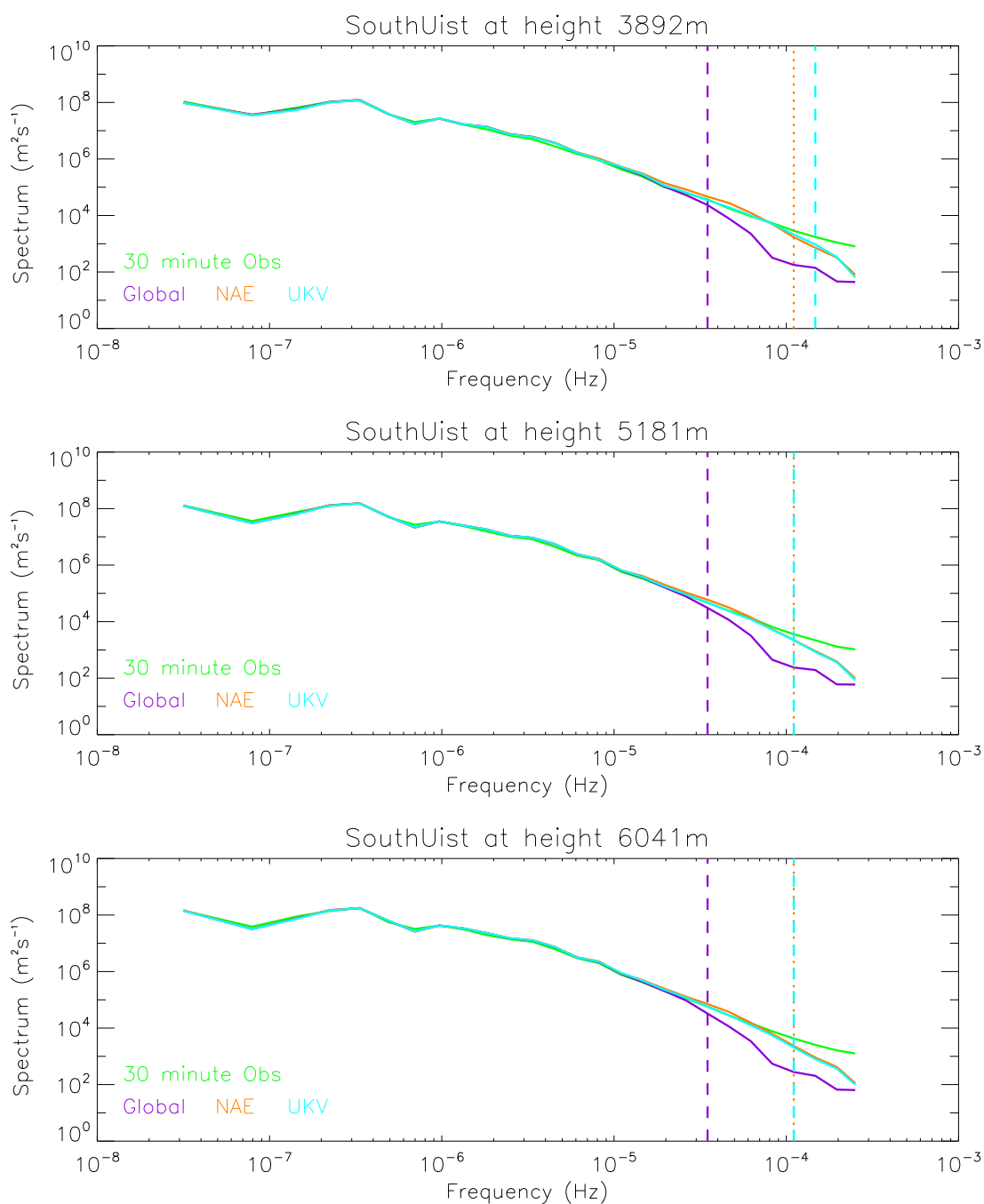


Figure 18: Free tropospheric spectra at various heights at South Uist generated from wind profiler observations (30 minute mean) and MetUM data (global (25 km, 3 hourly), NAE (12 km, hourly) and UKV (1.5 km, hourly)).

which highlights the sensitivity of this method to the threshold value. At a height of 6012 m at Aberystwyth, the point of divergence of the UKV spectra occurs at a significantly lower frequency than the point of divergence of the NAE spectra, despite the similarities between the NAE and UKV spectra. The fractional difference between the observed and UKV spectra at 6012 m at Aberystwyth just exceeds the 30% threshold at the frequency of the determined point of divergence. At higher frequencies the rate of increase of the fractional difference between the observed and the UKV spectra is initially slow allowing the NAE fractional difference curve to catch up.

The missing variance in the NWP free tropospheric spectra is calculated from the determined point of divergence to the upper frequency end of the spectra. Table 11 gives the  $\sigma_u$  values, for different model resolutions of NWP models, obtained by taking the square root of the missing variance. As expected, and as seen within the boundary layer, there is more missing energy in the global spectra than in the higher resolution NAE and UKV models. The missing energy in the NAE and UKV models is similar, particularly where a similar point of divergence has been determined. In general, for a particular NWP model, the missing energy is similar at various free tropospheric heights at any one wind profiler location but there is significant variation in the missing energy between different locations (cf. Aberystwyth with South Uist). The data from South Uist has more missing observations than the data from Aberystwyth, but investigations show that this fact cannot explain the lower missing energy values. These differences between results from different wind profiler sites are not really understood but it is possible that they may be due to different instrumentation or that results may be affected by calibration errors. A summary of the  $\sigma_u$  values obtained from calculating the missing energy in the free tropospheric spectra is given in tables 12 and 13. The mean values are obtained from the mean variances over the different wind profiler locations and observation heights studied.

Figures 21 and 22 show the correlation functions (normalised by the variance) for the motions corresponding to the missing energy in the free tropospheric NWP spectra at various heights at Aberystwyth and South Uist. (The correlation functions for the other wind profiler locations studied are given in appendix H.) As before, the time taken for the normalised correlation function to fall to  $1/e$  gives an Eulerian timescale which is used to determine an appropriate Lagrangian timescale. The largest timescales are predicted for use with the 3 hourly global NWP data. The similarities between the missing motions in the NAE and UKV data (both hourly) are also seen in the correlation functions, with similar timescales predicted.

Horizontal diffusivities are obtained from the velocity variances (calculated from the missing variance in the energy spectra) and the Lagrangian timescales (calculated from the correlation functions) using  $K_u = \sigma_u^2 \tau_L$ . Within the boundary layer, a Lagrangian timescale ( $\tau_L$ ) was obtained from the Eulerian timescale ( $\tau_E$ ) using  $\tau_L = \beta \tau_E$  and assuming  $\beta = 3$ . The timescales  $\tau_L$  and  $\tau_E$  satisfy  $\tau_L/\tau_E \propto u/\sigma_u$  and an analysis of observations in the boundary layer and in the free troposphere indicates that  $u/\sigma_u$  can be larger in the free troposphere by approximately a factor of 3. However, given the significant uncertainty surrounding the free tropospheric parameters and

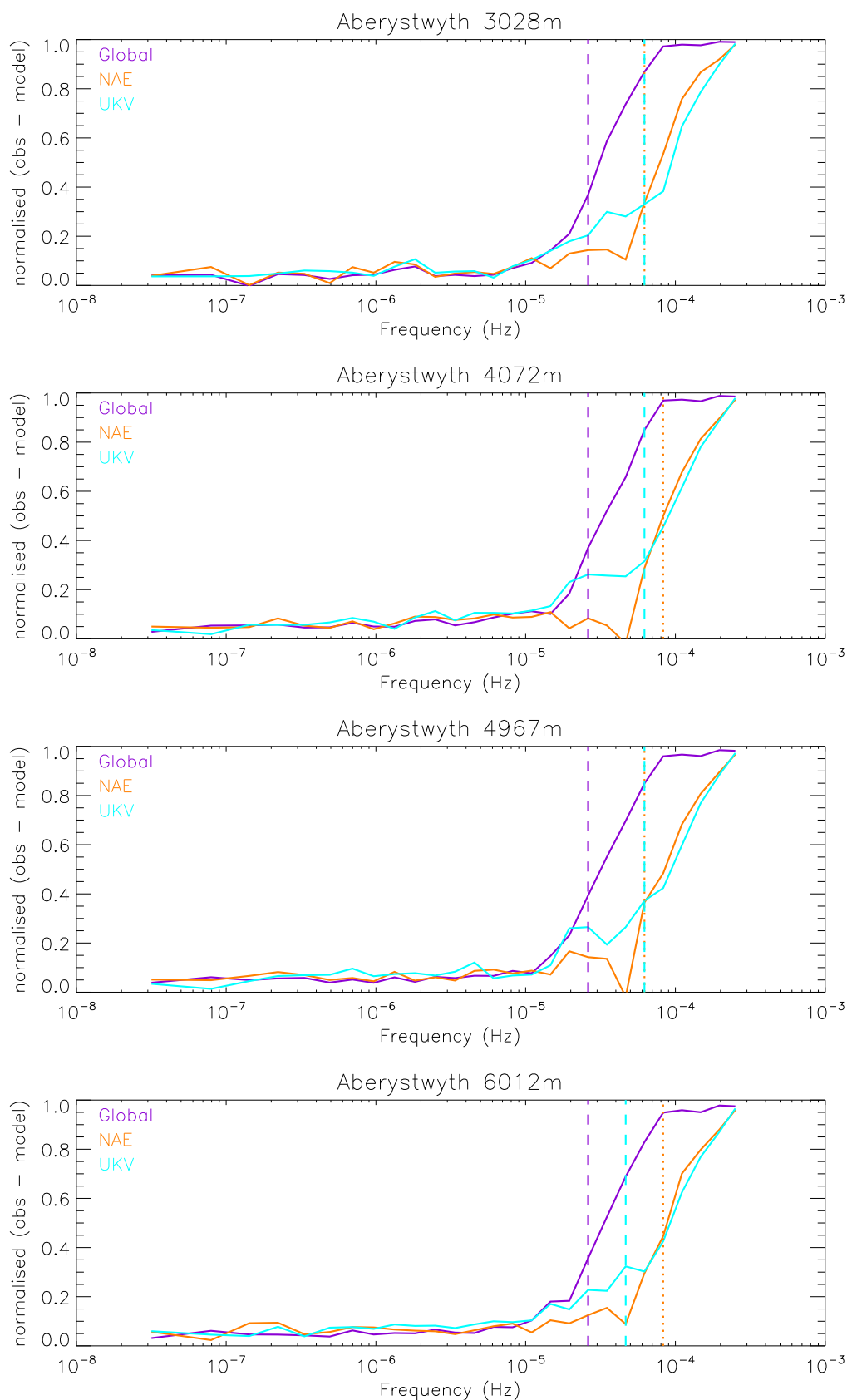


Figure 19: Fractional difference between the observed and NWP spectra at various heights in the free troposphere at Aberystwyth generated from 30 minute wind profiler observations and MetUM data (global (25 km, 3 hourly), NAE (12 km, hourly) and UKV (1.5 km, hourly)).

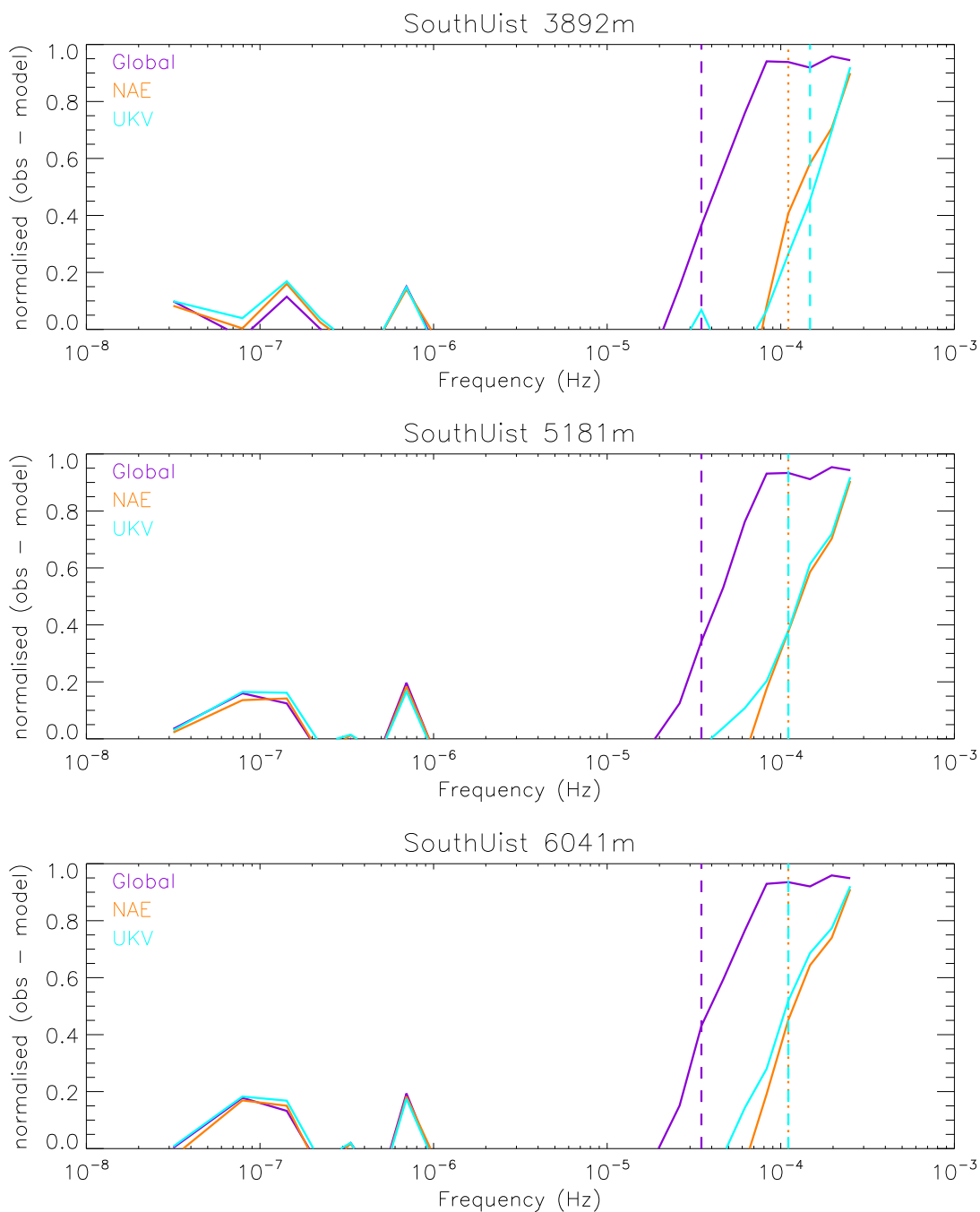


Figure 20: Fractional difference between the observed and NWP spectra at various heights in the free troposphere at South Uist generated from 30 minute wind profiler observations and MetUM data (global (25 km, 3 hourly), NAE (12 km, hourly) and UKV (1.5 km, hourly)).



| Location    | Time <sup>†</sup><br>(mins) | Height<br>(m) | Point of divergence frequency (Hz) |                        |                        |
|-------------|-----------------------------|---------------|------------------------------------|------------------------|------------------------|
|             |                             |               | Global                             | NAE                    | UKV                    |
| Aberystwyth | 30                          | 3028          | $2.613 \times 10^{-5}$             | $6.209 \times 10^{-5}$ | $6.209 \times 10^{-5}$ |
|             |                             | 4072          | $2.613 \times 10^{-5}$             | $8.283 \times 10^{-5}$ | $6.209 \times 10^{-5}$ |
|             |                             | 4967          | $2.613 \times 10^{-5}$             | $6.209 \times 10^{-5}$ | $6.209 \times 10^{-5}$ |
|             |                             | 6012          | $2.613 \times 10^{-5}$             | $8.283 \times 10^{-5}$ | $4.653 \times 10^{-5}$ |
| South Uist  | 30                          | 3892          | $3.488 \times 10^{-5}$             | $1.105 \times 10^{-4}$ | $1.474 \times 10^{-4}$ |
|             |                             | 5181          | $3.488 \times 10^{-5}$             | $1.105 \times 10^{-4}$ | $1.105 \times 10^{-4}$ |
|             |                             | 6041          | $3.488 \times 10^{-5}$             | $1.105 \times 10^{-4}$ | $1.105 \times 10^{-4}$ |
| Camborne    | 15                          | 2297          | $2.613 \times 10^{-5}$             | $8.283 \times 10^{-5}$ | $6.209 \times 10^{-5}$ |
|             |                             | 2707          | $2.613 \times 10^{-5}$             | $8.283 \times 10^{-5}$ | $8.283 \times 10^{-5}$ |
|             | 30                          | 2297          | $3.488 \times 10^{-5}$             | $1.105 \times 10^{-4}$ | $1.474 \times 10^{-4}$ |
|             |                             | 2707          | $3.488 \times 10^{-5}$             | $1.105 \times 10^{-4}$ | $1.474 \times 10^{-4}$ |
| Douglas     | 15                          | 2351          | $2.613 \times 10^{-5}$             | $6.209 \times 10^{-5}$ | $3.488 \times 10^{-5}$ |
|             |                             | 2740          | $2.613 \times 10^{-5}$             | $6.209 \times 10^{-5}$ | $6.209 \times 10^{-5}$ |
|             | 30                          | 2351          | $2.613 \times 10^{-5}$             | $8.283 \times 10^{-5}$ | $1.105 \times 10^{-4}$ |
|             |                             | 2740          | $2.613 \times 10^{-5}$             | $8.283 \times 10^{-5}$ | $1.105 \times 10^{-4}$ |
| Dunkeswell  | 15                          | 2239          | $1.956 \times 10^{-5}$             | $6.209 \times 10^{-5}$ | $3.488 \times 10^{-5}$ |
|             |                             | 2649          | $2.613 \times 10^{-5}$             | $6.209 \times 10^{-5}$ | $6.209 \times 10^{-5}$ |
|             | 30                          | 2239          | $1.956 \times 10^{-5}$             | $8.283 \times 10^{-5}$ | $1.105 \times 10^{-4}$ |
|             |                             | 2649          | $2.613 \times 10^{-5}$             | $8.283 \times 10^{-5}$ | $1.105 \times 10^{-4}$ |
| Wattisham   | 15                          | 2278          | $3.488 \times 10^{-5}$             | $6.209 \times 10^{-5}$ | $8.283 \times 10^{-5}$ |
|             |                             | 2688          | $3.488 \times 10^{-5}$             | $6.209 \times 10^{-5}$ | $6.209 \times 10^{-5}$ |
|             | 30                          | 2278          | $3.488 \times 10^{-5}$             | $8.283 \times 10^{-5}$ | $1.105 \times 10^{-4}$ |
|             |                             | 2688          | $3.488 \times 10^{-5}$             | $8.283 \times 10^{-5}$ | $1.105 \times 10^{-4}$ |

Table 10: The points of divergence (in Hz) of the MetUM spectra from the observed spectra, calculated as the point at which the fractional difference exceeds 30% (see the vertical lines in figures 17 - 20 and in the figures in appendices F and G). <sup>†</sup>The time resolution of the wind profiler observations.

| Location    | Time <sup>†</sup><br>(mins) | Height<br>(m) | $\sigma_u$ (m s <sup>-1</sup> ) |       |       |
|-------------|-----------------------------|---------------|---------------------------------|-------|-------|
|             |                             |               | Global                          | NAE   | UKV   |
| Aberystwyth | 30                          | 3028          | 1.40                            | 0.938 | 0.896 |
|             |                             | 4072          | 1.42                            | 0.861 | 0.898 |
|             |                             | 4967          | 1.55                            | 0.956 | 0.935 |
|             |                             | 6012          | 1.67                            | 0.929 | 1.08  |
| South Uist  | 30                          | 3892          | 0.876                           | 0.402 | 0.340 |
|             |                             | 5181          | 0.984                           | 0.445 | 0.450 |
|             |                             | 6041          | 1.10                            | 0.509 | 0.526 |
| Camborne    | 15                          | 2297          | 1.34                            | 0.840 | 0.850 |
|             |                             | 2707          | 1.34                            | 0.840 | 0.792 |
|             | 30                          | 2297          | 0.986                           | 0.450 | 0.367 |
|             |                             | 2707          | 0.955                           | 0.433 | 0.335 |
| Douglas     | 15                          | 2351          | 1.40                            | 0.955 | 1.03  |
|             |                             | 2740          | 1.33                            | 0.900 | 0.822 |
|             | 30                          | 2351          | 1.19                            | 0.647 | 0.540 |
|             |                             | 2740          | 1.10                            | 0.615 | 0.512 |
| Dunkeswell  | 15                          | 2239          | 1.50                            | 0.961 | 1.04  |
|             |                             | 2649          | 1.39                            | 0.929 | 0.896 |
|             | 30                          | 2239          | 1.34                            | 0.689 | 0.587 |
|             |                             | 2649          | 1.22                            | 0.650 | 0.551 |
| Wattisham   | 15                          | 2278          | 1.21                            | 0.863 | 0.776 |
|             |                             | 2688          | 1.19                            | 0.847 | 0.802 |
|             | 30                          | 2278          | 1.10                            | 0.657 | 0.543 |
|             |                             | 2688          | 1.09                            | 0.640 | 0.530 |

Table 11: Values of  $\sigma_u$  (in m s<sup>-1</sup>) obtained by calculating the missing variance in the free tropospheric NWP spectra. <sup>†</sup>The time resolution of the wind profiler observations.

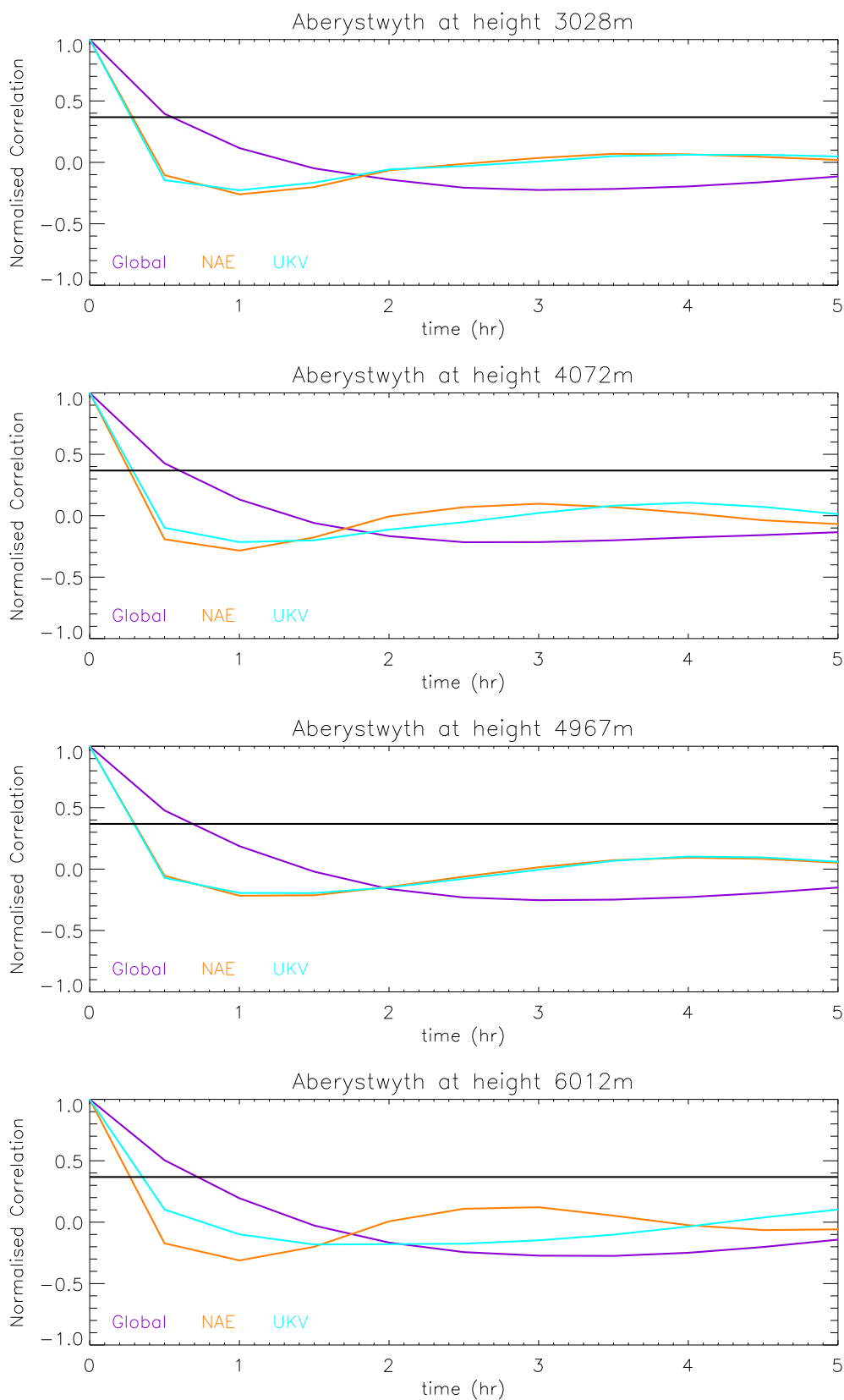


Figure 21: Normalised correlation functions for the unresolved mesoscale motions at various heights at Aberystwyth, generated from wind profiler observations (30 minute) and MetUM data (global (25 km, 3 hourly), NAE (12 km, hourly) and UKV (1.5 km, hourly)). The  $1/e$  line (shown in black) is used to determine the timescale.

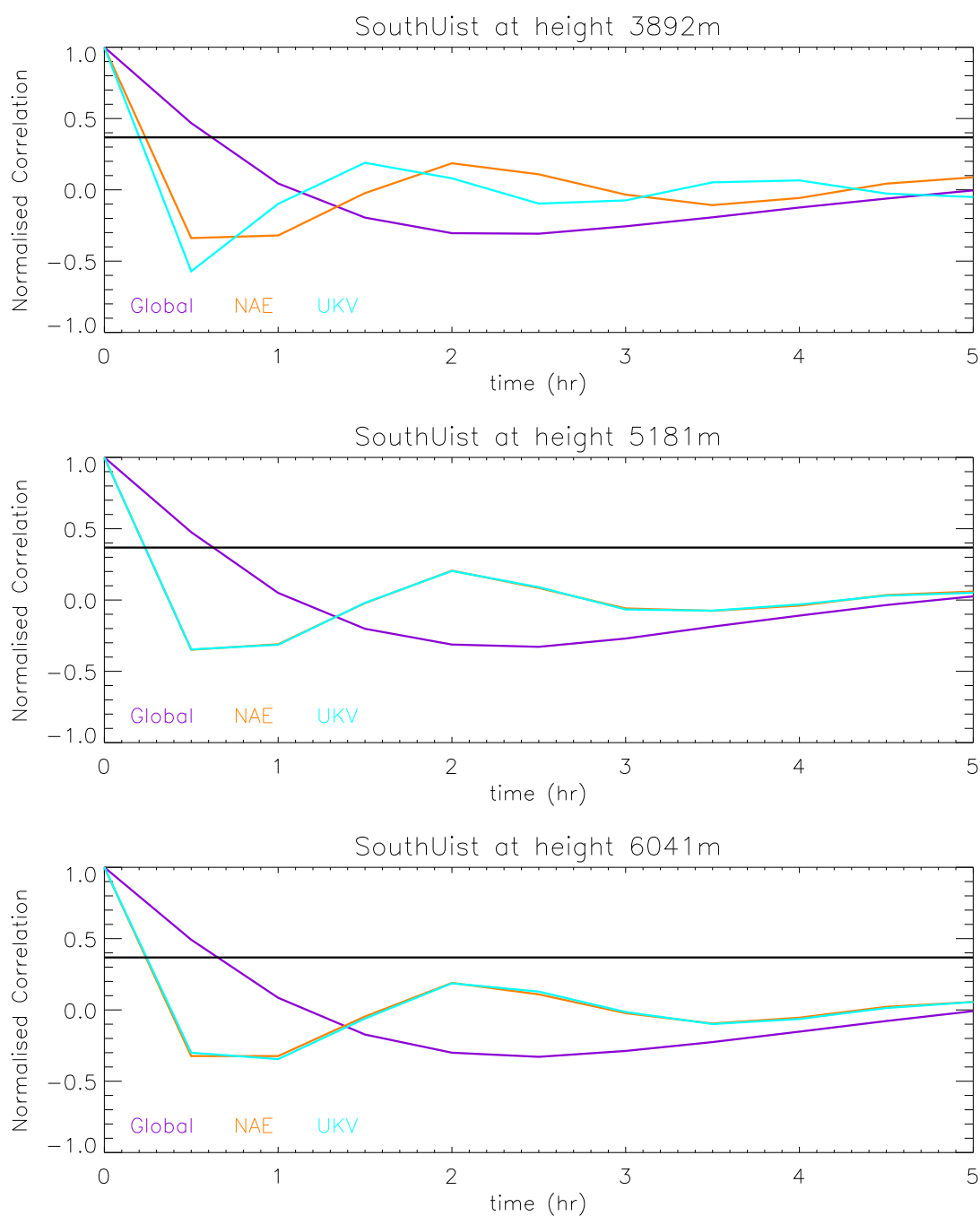


Figure 22: Normalised correlation functions for the unresolved mesoscale motions at various heights at South Uist, generated from wind profiler observations (30 minute) and MetUM data (global (25 km, 3 hourly), NAE (12 km, hourly) and UKV (1.5 km, hourly)). The  $1/e$  line (shown in black) is used to determine the timescale.

the simplicity of adopting the same approach throughout, we continue to use  $\tau_L = \beta \tau_E$  where  $\beta = 3$  within the free troposphere. A summary of the calculated diffusivities is given in tables 12 and 13. The mean and range (minimum to maximum) values are obtained over the different wind profiler locations and observing heights studied. As was the case for the study of missing motions in the NWP data in the boundary layer, a wide range of diffusivities is obtained which is, in this case, due primarily to the differences seen between different wind profiler locations. The diffusivity values recommended for use within the boundary layer (see table 9) lie within the free tropospheric ranges given in tables 12 and 13, except in the case of the NAE model. In the free troposphere, the parametrization of missing motions in the NAE model is much more similar to the parametrization of missing motions in the UKV model, than a similar comparison made within the boundary layer. This would be expected given the similarities seen between the NAE and UKV in the free tropospheric energy spectra and correlation functions. The range of NAE diffusivity values obtained from data within the boundary layer do, however, overlap to some degree the range of NAE diffusivity values obtained from data within the free troposphere. If we increase the free tropospheric diffusivities by a factor of 3 to reflect a possible increase in  $\tau_L/\tau_E$  (based on the indication that  $u/\sigma_u$  can be larger in the free troposphere by approximately a factor of 3), then the NAE free tropospheric values agree quite well with the boundary layer values. The global and UKV free tropospheric values are then somewhat larger than the corresponding boundary layer values, although with a wide range which is not inconsistent with the boundary layer values. Given the uncertainty in the diffusivities it is proposed, for simplicity, that the recommended boundary layer diffusivities (see table 9) be applied throughout.

| NWP model                | $\sigma_u$ |               | $K_u$ |              |
|--------------------------|------------|---------------|-------|--------------|
|                          | Mean       | Range         | Mean  | Range        |
| Global<br>(25 km, 3 hrs) | 1.22       | 0.876 - 1.67  | 10620 | 5248 - 22102 |
| NAE<br>(12 km, 1 hr)     | 0.680      | 0.402 - 0.957 | 1338  | 407 - 2963   |
| UKV<br>(1.5 km, 1 hr)    | 0.647      | 0.335 - 1.08  | 1259  | 243 - 4614   |

Table 12: A summary of  $\sigma_u$  values (in  $\text{m s}^{-1}$ ) and  $K_u$  values (in  $\text{m}^2 \text{s}^{-1}$ ) based on 30 minute wind profiler observations.

| NWP model                | $\sigma_u$ |               | $K_u$ |             |
|--------------------------|------------|---------------|-------|-------------|
|                          | Mean       | Range         | Mean  | Range       |
| Global<br>(25 km, 3 hrs) | 1.34       | 1.19 - 1.50   | 3844  | 2554 - 5696 |
| NAE<br>(12 km, 1 hr)     | 0.893      | 0.840 - 0.961 | 2293  | 1652 - 2789 |
| UKV<br>(1.5 km, 1 hr)    | 0.882      | 0.776 - 1.04  | 2403  | 1469 - 4233 |

Table 13: A summary of  $\sigma_u$  values (in  $\text{m s}^{-1}$ ) and  $K_u$  values (in  $\text{m}^2 \text{s}^{-1}$ ) based on 15 minute wind profiler observations.

## 7 Validation of the parametrization of unresolved mesoscale motions

Validating NAME's parametrization of unresolved mesoscale motions is a difficult, but important, matter. It is likely that a better picture will evolve over time as the parametrization is used for a range of different NAME simulations. Furthermore, when comparing against plume dispersion observations, some excess diffusion may be seen as preferable to account for errors in the spatial position of the plume and to smooth out features which are not reliably predictable. Nonetheless, some validation should be attempted here. We present the results from two validation exercises. The first is a hypothetical study which compares predicted plume spread in light wind conditions, using input NWP meteorological data of differing resolutions. In the second exercise we use observations from the 2010 eruption of Eyjafjallajökull to validate the parametrization of unresolved mesoscale motions in NAME for global MetUM data (25 km horizontal spatial resolution). Further validation and testing of the parametrization would, however, give a more thorough understanding and increase confidence.

### 7.1 Intercomparison of plume spread predicted using NWP data of differing resolutions

Aside from the parametrization of unresolved mesoscale motions, there are other reasons why plume spread may vary between simulations conducted using input NWP data of differing resolutions. Firstly, differences in the representation of the meteorological situation will exist between the various NWP models. Variations in the plume spread downwind may be due to differences in the wind speed, changes in wind direction over time and varying amounts of wind shear and small scale turbulence. Secondly, some scales of motions will be resolved in the higher resolution NWP models but parametrized, and hence treated statistically, in lower resolution NWP models. The predicted

plume spread may therefore be less, using the higher resolution NWP models, than that obtained using the lower resolution NWP models, since NAME represents an ensemble of realisations of the unresolved parametrized motions. These differences will be more evident for small averaging times (and also at short ranges when the eddies are causing plume meandering rather than plume diffusion) and hence the averaging time for the validation is chosen to be larger than the estimated timescale of the unresolved motions.

A light wind period was chosen and a continuous release of an inert tracer, from a hypothetical point source at a height of 10 m above ground in a flat rural area, was simulated using MetUM data of various resolutions: Global (25 km, 3 hourly), NAE (12 km, hourly), 4km (4 km, hourly) and UKV (1.5 km, hourly). Six-hourly-averaged predicted plumes were compared.

The first test case modelled a 10 m agl release from Wattisham (52.12°N, 0.96°E) from 1600 UTC on 05/02/2012 until 0400 UTC on 07/02/2012. At the source, mean 10 m wind speeds during the first 18 hours of this period were 0.9 m s<sup>-1</sup> (global), 1.5 m s<sup>-1</sup> (NAE), 1.4 m s<sup>-1</sup> (4km) and 1.3 m s<sup>-1</sup> (UKV) and ranged from 0.4 to 1.6 m s<sup>-1</sup> (global), from 0.4 to 2.3 m s<sup>-1</sup> (NAE), from 0.6 to 2.4 m s<sup>-1</sup> (4km) and from 0.3 to 1.8 m s<sup>-1</sup> (UKV). Forecast winds, therefore, differed between the MetUM models of various resolutions with, the strongest winds forecast by the NAE model and the lightest winds forecast in the global model. Figure 23 shows the six-hourly-averaged plumes from 0400 UTC to 1000 UTC on 06/02/2012, forecast using global, NAE, 4km and UKV input meteorological data. Simulations were conducted using a parametrization of unresolved mesoscale motions based on the diffusivity values given in table 9, namely 7000 m<sup>2</sup> s<sup>-1</sup> (global), 4000 m<sup>2</sup> s<sup>-1</sup> (NAE) and 2000 m<sup>2</sup> s<sup>-1</sup> (4km and UKV).

There are noticeable differences in the predicted plumes. The larger wind speeds in the NAE model result in a narrower plume which is transported further downwind during the first 18 hours. The global and NAE model winds are consistently from a south-southwesterly direction for the majority of the simulation. Conversely the 4km and UKV model winds fluctuate over different directions, and this variation in the wind direction contributes to additional spread in the predicted plume. Given these differences in the MetUM winds, it is difficult to compare the plume widths and conclude the appropriateness of the parametrization of unresolved mesoscale motions in each case. Nonetheless, nothing appears untoward in the predicted plumes.

The second test case models a 10 m agl release from Wattisham (52.12°N, 0.96°E) from 2300 UTC on 20/01/2013 until 0600 UTC on 22/01/2013. For all MetUM models, the 10 m NWP wind had a northerly component for the first few hours changing to have a southerly component thereafter. Mean 10 m wind speeds during the first 13 hours of the release were 1.4 m s<sup>-1</sup> (global and NAE), 1.8 m s<sup>-1</sup> (4km) and 1.6 m s<sup>-1</sup> (UKV) and ranged from 0.4 to 2.2 m s<sup>-1</sup> (global), 0.3 to 2.9 m s<sup>-1</sup> (NAE), 0.5 to 2.9 m s<sup>-1</sup> (4km) and 0.5 to 2.8 m s<sup>-1</sup> (UKV). In this case wind speeds were higher in the 4km and UKV models than in the global and NAE MetUM. Figure 24 shows the six-hourly-averaged plumes from 0600 UTC to 1200 UTC on 21/01/2013, forecast using global, NAE, 4km and UKV input meteorological data.

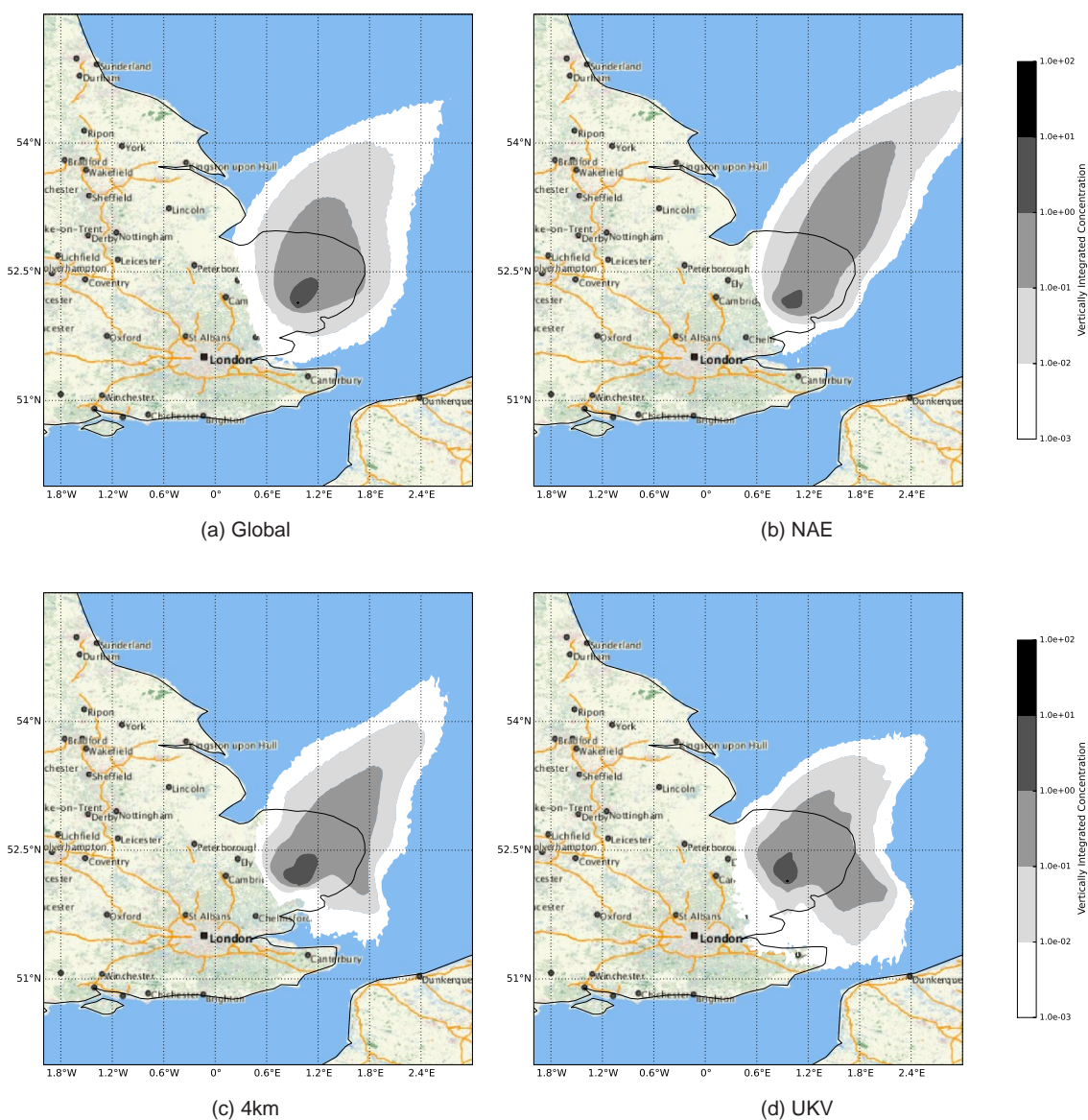


Figure 23: A comparison of six-hourly-averaged NAME predicted plumes using global, NAE, 4km and UKV input MetUM data, for the period 0400 UTC to 1000 UTC on 06/02/2012.



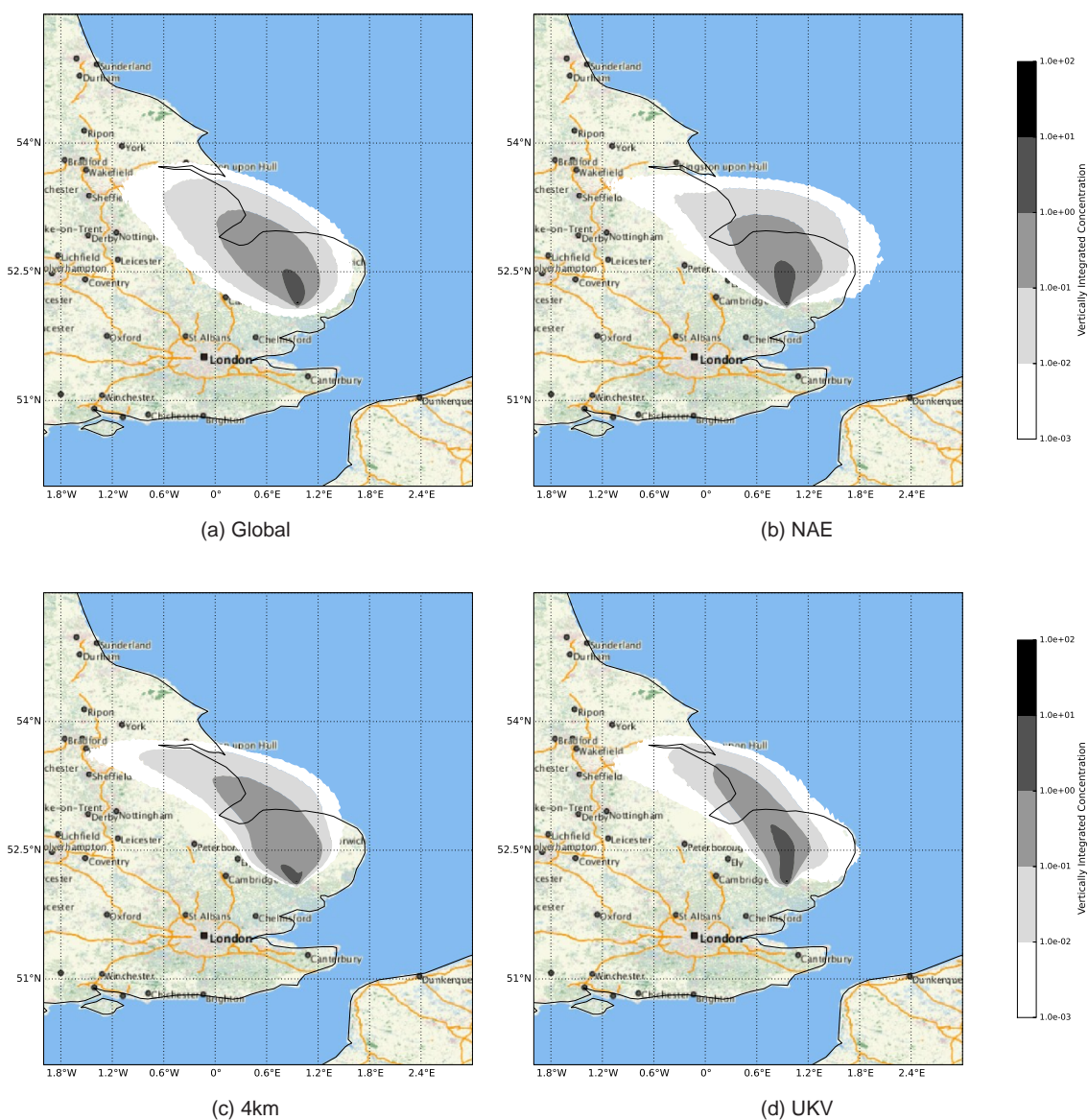


Figure 24: A comparison of six-hourly-averaged NAME predicted plumes using global, NAE, 4km and UKV input MetUM data, for the period 0600 UTC to 1200 UTC on 21/01/2013.

In contrast to the first test case, the UKV simulation has the least plume spread and the NAE simulation has the largest plume spread. The NAE model had the greatest variation in (hour-to-hour) wind direction and wind speed over the simulation period which played a key role in the lateral spread of the predicted plume. Conversely, the global and UKV models have smaller hour-to-hour variations in the wind direction. This, coupled with the relatively large wind speeds, resulted in the UKV simulation predicting the least lateral plume spread.

For these two test cases, no one particular simulation consistently produces the least or greatest lateral plume spread; as well as the parametrization of unresolved mesoscale motions, the NWP model's representation of the meteorological situation also plays a role in the spread of the plume. This is as it should be; consistently large or small amounts of lateral plume spread would suggest that the parametrization of unresolved mesoscale motions was overdone or insufficient.

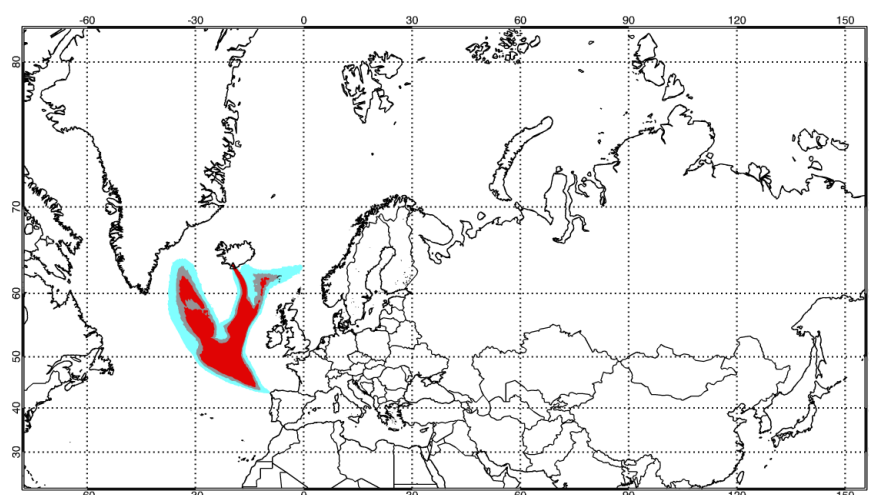
## 7.2 The 2010 eruption of Eyjafjallajökull

Webster et al. [34] compared peak ash concentrations, predicted using NAME, against observations obtained by ground-based and research aircraft instrumentation during the 2010 eruption of Eyjafjallajökull, Iceland. Despite the difficulties and uncertainties involved, NAME exhibited skill in predicting ash concentrations. The level of agreement between modelled and observed values was assessed.

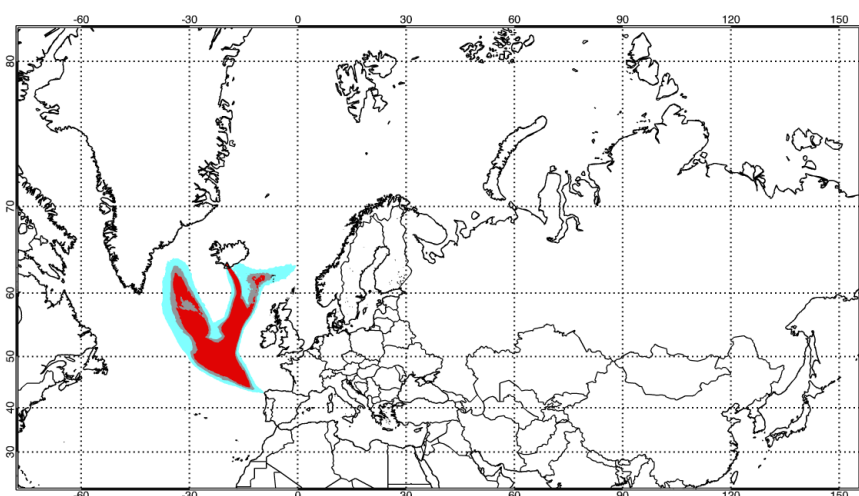
The ash forecasting method presented by Webster et al. [34] employed NAME and input NWP data from the global MetUM (3 hourly fields with a horizontal spatial resolution of 25 km). The parametrization of unresolved mesoscale motions, in the form discussed at the end of section 3.1, was used, with a horizontal diffusivity of about  $9000 \text{ m}^2 \text{ s}^{-1}$ . Here we repeat the original validation exercise using a revised parametrization with a horizontal diffusivity value of  $7000 \text{ m}^2 \text{ s}^{-1}$ .

Figure 25 shows an example six-hourly ash concentration field obtained using the original and revised parametrizations. Differences between the ash clouds predicted using the original and revised parametrizations of unresolved mesoscale motions are minor. This is probably due to the fact that, not only are the differences in horizontal diffusivities between the revised and original parametrizations relatively small (a larger difference may be seen for simulations using the higher resolution input NWP data), unresolved mesoscale motions may not be the dominant transport and/or dispersion component here. The revisions to the parametrization of unresolved motions would not have changed the guidance issued or the predictions of the Eyjafjallajökull ash cloud, and this is, to some extent, reassuring.

Figure 26 compares model predicted peak ash concentrations with observations for the three schemes studied by Webster et al. [34] and the original and revised parametrization. Whilst some differences between results from the original and revised parametrizations can be seen in the scatter plots, these differences are minor and do not alter the findings of Webster et al. [34]. Table 14 assesses the level of agreement between the observations and model predictions. Again, we see



(a) Original



(b) Revised

Figure 25: Six-hourly averaged ash concentrations predicted by NAME using (a) the original parametrization of unresolved mesoscale motions and (b) the revised parametrization.

that the changes to the parametrization of unresolved mesoscale motions have had a minor effect on predicted ash cloud concentrations.

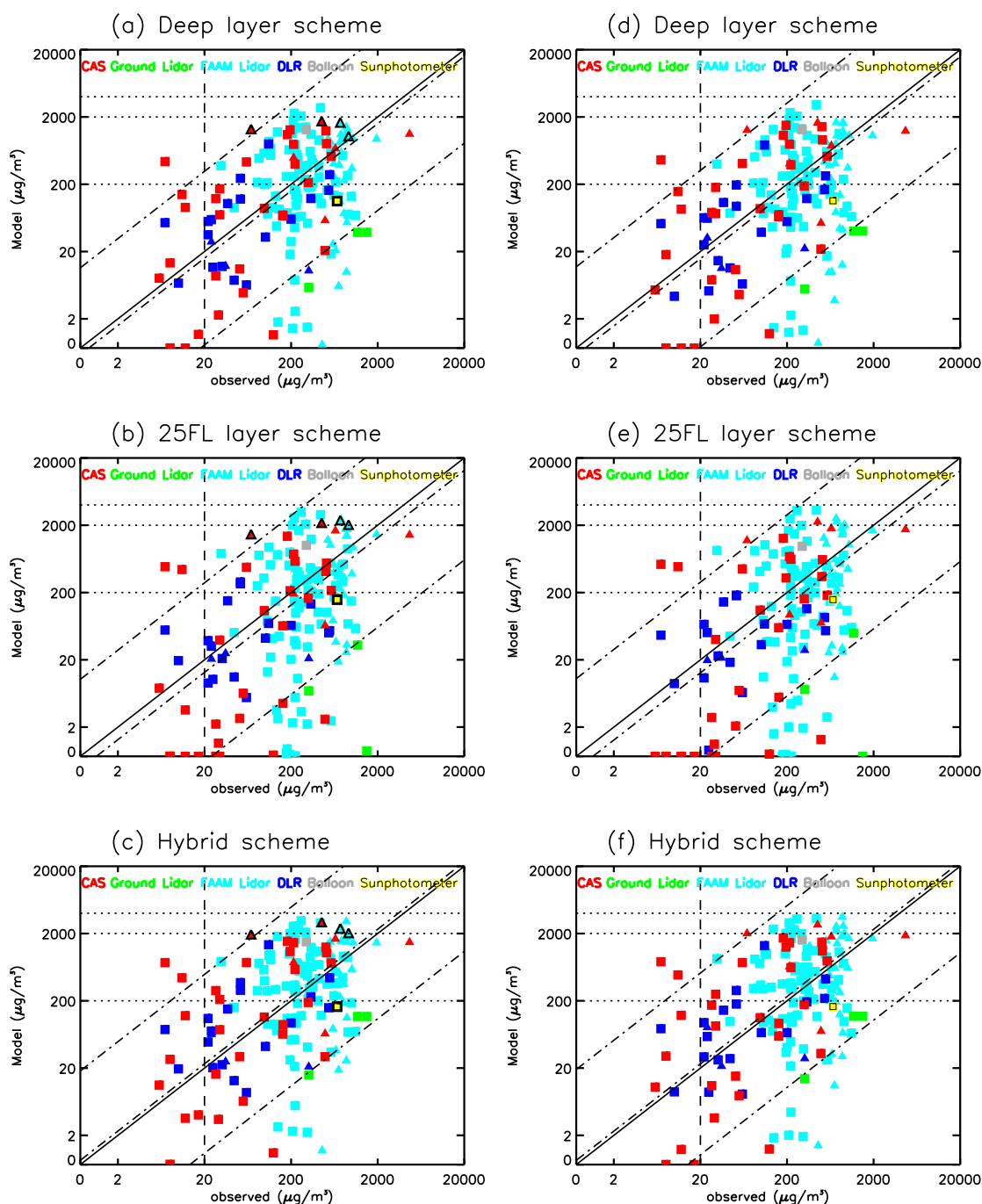


Figure 26: Modelled peak concentrations (obtained using three ash forecasting schemes) versus the peak observed concentrations. Scatter plots (a), (b) and (c) are taken from figure 5 in Webster et al. [34] and are obtained using the original parametrization of unresolved mesoscale motions. Scatter plots (d), (e) and (f) are obtained using a revised horizontal diffusivity value of  $7000 \text{ m}^2 \text{ s}^{-1}$  for the unresolved mesoscale motions. Squares denote observations below FL200 and triangles denote observations between FL200 and FL350. The colour of the square or triangle is used here to denote the observation type. See Webster et al. [34] for further details.

| Model scheme | Parametrization       | Percentage in agreement           | Percentage of overpredictions     | Percentage of underpredictions    |
|--------------|-----------------------|-----------------------------------|-----------------------------------|-----------------------------------|
| Deep layer   | Original <sup>‡</sup> | 33 <sup>§</sup> , 61 <sup>†</sup> | 28 <sup>§</sup> , 16 <sup>†</sup> | 39 <sup>§</sup> , 23 <sup>†</sup> |
|              | Revised               | 34 <sup>§</sup> , 63 <sup>†</sup> | 26 <sup>§</sup> , 15 <sup>†</sup> | 40 <sup>§</sup> , 22 <sup>†</sup> |
| 25FL layer   | Original <sup>‡</sup> | 30 <sup>§</sup> , 75 <sup>†</sup> | 23 <sup>§</sup> , 3 <sup>†</sup>  | 48 <sup>§</sup> , 22 <sup>†</sup> |
|              | Revised               | 27 <sup>§</sup> , 75 <sup>†</sup> | 24 <sup>§</sup> , 3 <sup>†</sup>  | 49 <sup>§</sup> , 22 <sup>†</sup> |
| Hybrid       | Original <sup>‡</sup> | 29 <sup>§</sup> , 66 <sup>†</sup> | 42 <sup>§</sup> , 20 <sup>†</sup> | 29 <sup>§</sup> , 14 <sup>†</sup> |
|              | Revised               | 29 <sup>§</sup> , 65 <sup>†</sup> | 41 <sup>§</sup> , 20 <sup>†</sup> | 30 <sup>§</sup> , 14 <sup>†</sup> |

Table 14: Statistical comparison between model predictions and observations using both the original and revised parametrization of unresolved mesoscale motions. <sup>‡</sup>taken from table 3 of Webster et al. [34]. <sup>§</sup>Agreement assessed using a factor of 2 uncertainty in the observations but no model uncertainty. <sup>†</sup>Agreement assessed using a factor of 2 uncertainty in the observations and positional uncertainty in the model predictions.

## 8 Conclusions

In this report spectral analysis has been used to compare NWP and observed winds. This analysis has enabled certain statistics of the atmospheric motions which are missing in the NWP data to be determined. A parametrization of unresolved mesoscale motions is proposed, taking account of the scales of, and the variance in, these missing motions.

Despite some uncertainty resulting from variations between results at different observing sites and from different time periods, there is strong evidence to suggest that the parametrization of unresolved mesoscale motions should depend on the resolution of the NWP data, with high time resolution data from recent high resolution NWP models resolving motions with smaller scales than coarser NWP models. The default parametrization used in NAME prior to this study had a horizontal diffusivity value of  $K_u = 9000 \text{ m}^2 \text{ s}^{-1}$  ( $\sigma_u = 0.8 \text{ m s}^{-1}$ ,  $\tau_u = 14400 \text{ s}$ ) and this has been shown to be appropriate for use with low resolution NWP data with 3-hourly fields and horizontal spatial resolutions of approximately 60 km. Smaller diffusivities should, however, be used with recent higher resolution NWP data:  $K_u \sim 7000 \text{ m}^2 \text{ s}^{-1}$  ( $\sigma_u = 0.8 \text{ m s}^{-1}$ ,  $\tau_u = 10000 \text{ s}$ ) for 3-hourly data with a horizontal spatial resolution of approximately 20 km,  $K_u \sim 4000 \text{ m}^2 \text{ s}^{-1}$  ( $\sigma_u = 0.7 \text{ m s}^{-1}$ ,  $\tau_u = 8000 \text{ s}$ ) for hourly data with a horizontal spatial resolution of approximately 10 km, and  $K_u \sim 2000 \text{ m}^2 \text{ s}^{-1}$  ( $\sigma_u = 0.55 \text{ m s}^{-1}$ ,  $\tau_u = 6500 \text{ s}$ ) for hourly data with a horizontal spatial resolution of a few kilometres.

In the free troposphere there is a large variation between results from different wind profiler sites which is not understood. This leads to significant uncertainty in the determined timescales and variances of the missing motions in the NWP data. Within the free troposphere, temporal resolution seems to be the main restricting factor, with hourly NWP data of differing horizontal

spatial resolutions giving similar results. Overall the missing motions in the free troposphere have more variance, indicative of higher wind speeds aloft. The resulting diffusivities are, however, not too dissimilar to those obtained in the boundary layer.

Based on the uncertainties involved and the benefits of a simple scheme which is spatially homogeneous, typical diffusivities are recommended for NAME's parametrization of unresolved mesoscale motions. Appropriate diffusivities (velocity variances and Lagrangian timescales) should be chosen based on the temporal and spatial resolution of the input NWP data. Results presented here use both MetUM data, from the Met Office, and ECMWF data but are thought to be applicable to NWP data of similar resolutions from other centres. Validation of the parametrization is difficult but the attempts in this report have not revealed any issues of concern. A more thorough understanding of the performance of the scheme will be gained over time by routinely using the parametrization in a wide range of simulations.

## **Acknowledgements**

Use of observational data from the following sources is acknowledged: Met Office surface site observations, MRU Cardington surface site observations and Met Office wind profiler data. The authors are grateful to the following teams and individuals within the Met Office for data provision, advice and assistance: Weather Analytics for provision of the Met Office surface site data, MRU and Gabriel Rooney for provision of MRU Cardington surface site data and for assistance and advice, Bruce Wright for assistance in accessing the wind profiler data, David Edwards for helpful discussions and advice on wind profilers.

## A Boundary layer scaling factors used with NWP winds for years 1998 - 2008

| Location          | ERAInt (80 km) | Global (40 km) | NAE (12 km) | 4 km |
|-------------------|----------------|----------------|-------------|------|
| Aviemore (10 m)   | 0.57           | 0.85           | 0.75        | 1.2  |
| Heathrow (10 m)   | 0.92           | 1.02           | 1.17        | 1.15 |
| Wattisham (10 m)  | 0.77           | 0.94           | 1.0         | 1.0  |
| Cardington (10 m) | 0.93           | 0.99           | 0.99        | 1.08 |
| Cardington (25 m) | 0.91           | 0.9            | 0.9         | 1.0  |
| Cardington (50 m) | 0.88           | 0.85           | 0.85        | 0.95 |

Table 15: Scaling factors applied to 2008 NWP winds

| Location          | ERAInt (80 km) | Global (40 km) | Mesoscale (12 km) |
|-------------------|----------------|----------------|-------------------|
| Aviemore (10 m)   | 0.67           | 1.0            | 1.15              |
| Heathrow (10 m)   | 0.91           | 0.9            | 1.18              |
| Wattisham (10 m)  | 0.77           | 0.9            | 1.05              |
| Cardington (10 m) | 0.92           | 0.88           | 1.02              |
| Cardington (25 m) | 0.92           | 0.83           | 0.97              |
| Cardington (50 m) | 0.9            | 0.83           | 0.95              |

Table 16: Scaling factors applied to 2006 NWP winds

| Location          | ERAInt (80 km) | Global (60 km) | Mesoscale (12 km) |
|-------------------|----------------|----------------|-------------------|
| Aviemore (10 m)   | 0.6            | 0.93           | 1.15              |
| Heathrow (10 m)   | 0.93           | 0.9            | 1.2               |
| Wattisham (10 m)  | 0.78           | 0.9            | 1.1               |
| Cardington (4 m)  | 1.16           | 0.91           | 1.12              |
| Cardington (10 m) | 0.86           | 0.8            | 0.97              |

Table 17: Scaling factors applied to 2004 NWP winds

| Location          | ERAInt (80 km) | Global (60 km) | Mesoscale (12 km) |
|-------------------|----------------|----------------|-------------------|
| Aviemore (10 m)   | 0.68           | 0.87           | 1.28              |
| Heathrow (10 m)   | 0.85           | 0.78           | 1.06              |
| Wattisham (10 m)  | 0.79           | 0.82           | 1.08              |
| Cardington (4 m)  | 1.22           | 0.91           | 1.22              |
| Cardington (10 m) | 0.85           | 0.75           | 0.93              |

Table 18: Scaling factors applied to 2001 NWP winds

| Location          | ERAInt (80 km) | Global (60 km) | Mesoscale (12 km) |
|-------------------|----------------|----------------|-------------------|
| Aviemore (10 m)   | 0.7            | 0.89           | 1.25              |
| Heathrow (10 m)   | 0.83           | 0.75           | 1.12              |
| Wattisham (10 m)  | 0.87           | 0.89           | 1.1               |
| Cardington (4 m)  | 1.16           | 0.85           | 1.12              |
| Cardington (10 m) | 0.84           | 0.75           | 0.89              |

Table 19: Scaling factors applied to 2000 NWP winds

| Location          | ERAInt (80 km) | Regional (50 km) |
|-------------------|----------------|------------------|
| Aviemore (10 m)   | 0.8            | 0.86             |
| Heathrow (10 m)   | 0.69           | 0.65             |
| Wattisham (10 m)  | 0.86           | 0.9              |
| Cardington (4 m)  | 1.14           | 1.02             |
| Cardington (10 m) | 0.83           | 0.77             |

Table 20: Scaling factors applied to 1998 NWP winds



## B Boundary layer spectral plots generated using observed and NWP winds

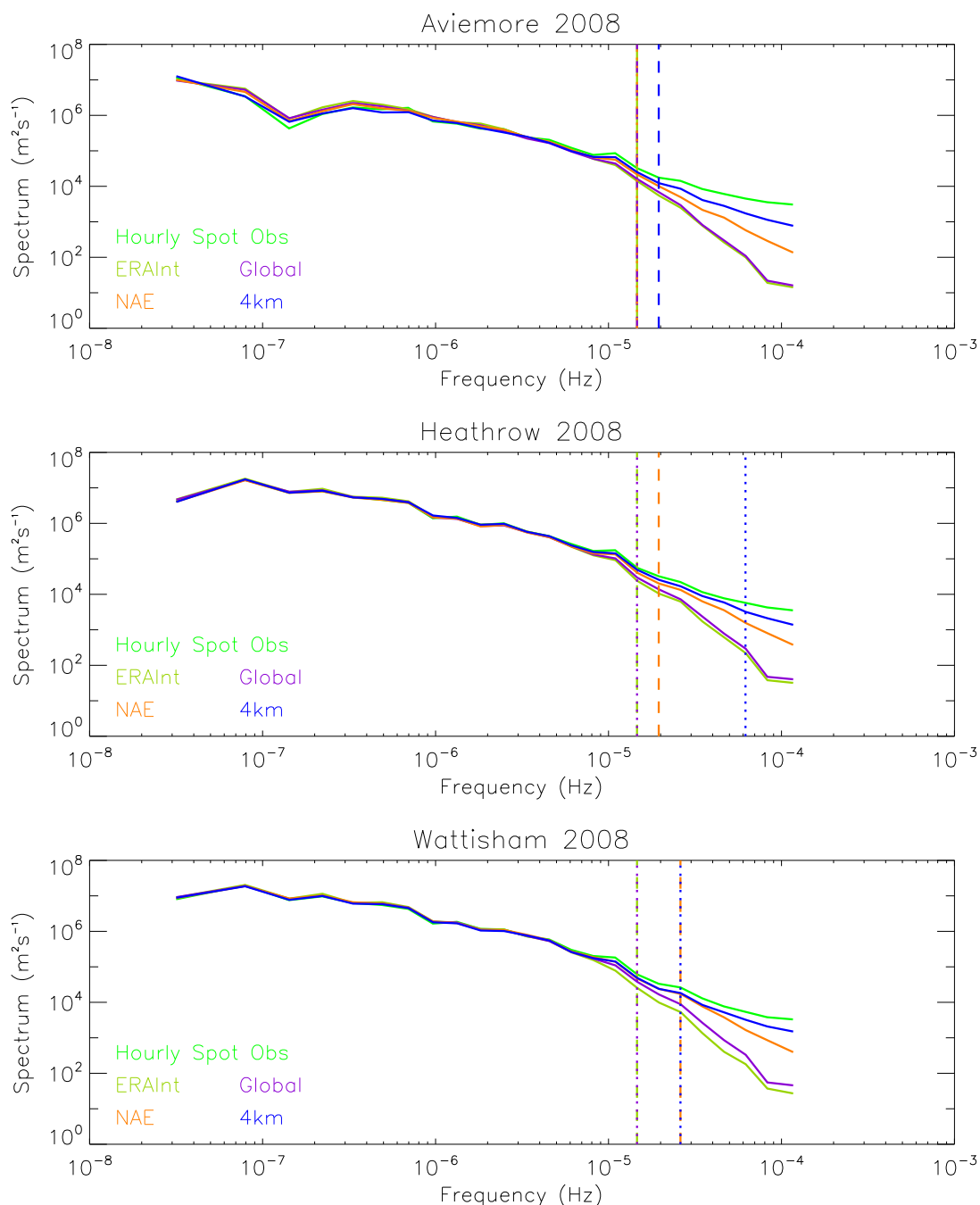


Figure 27: Aviemore, Heathrow and Wattisham spectra at a height of 10 m agl generated from 2008 observations (hourly spot), MetUM data (global (40 km, 3 hourly), NAE (12 km, hourly) and 4km (4 km, hourly)) and ECMWF ERA Interim data (80 km, 3hourly).

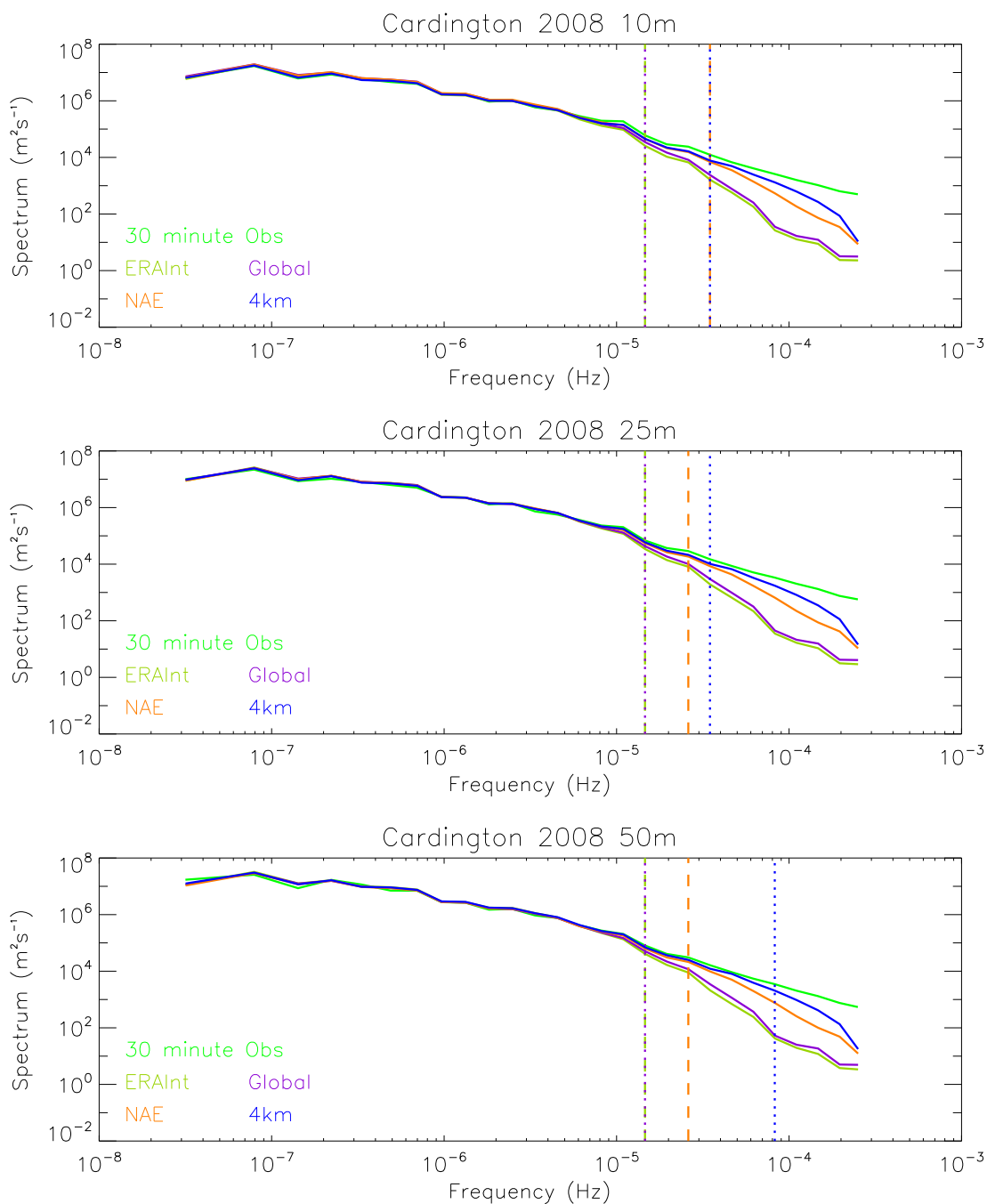


Figure 28: Cardington spectra at heights of 10 m, 25 m and 50 m agl generated from 2008 observations (30 minute), MetUM data (global (40 km, 3 hourly), NAE (12 km, hourly) and 4km (4 km, hourly)) and ECMWF ERA Interim data (80 km, 3 hourly).

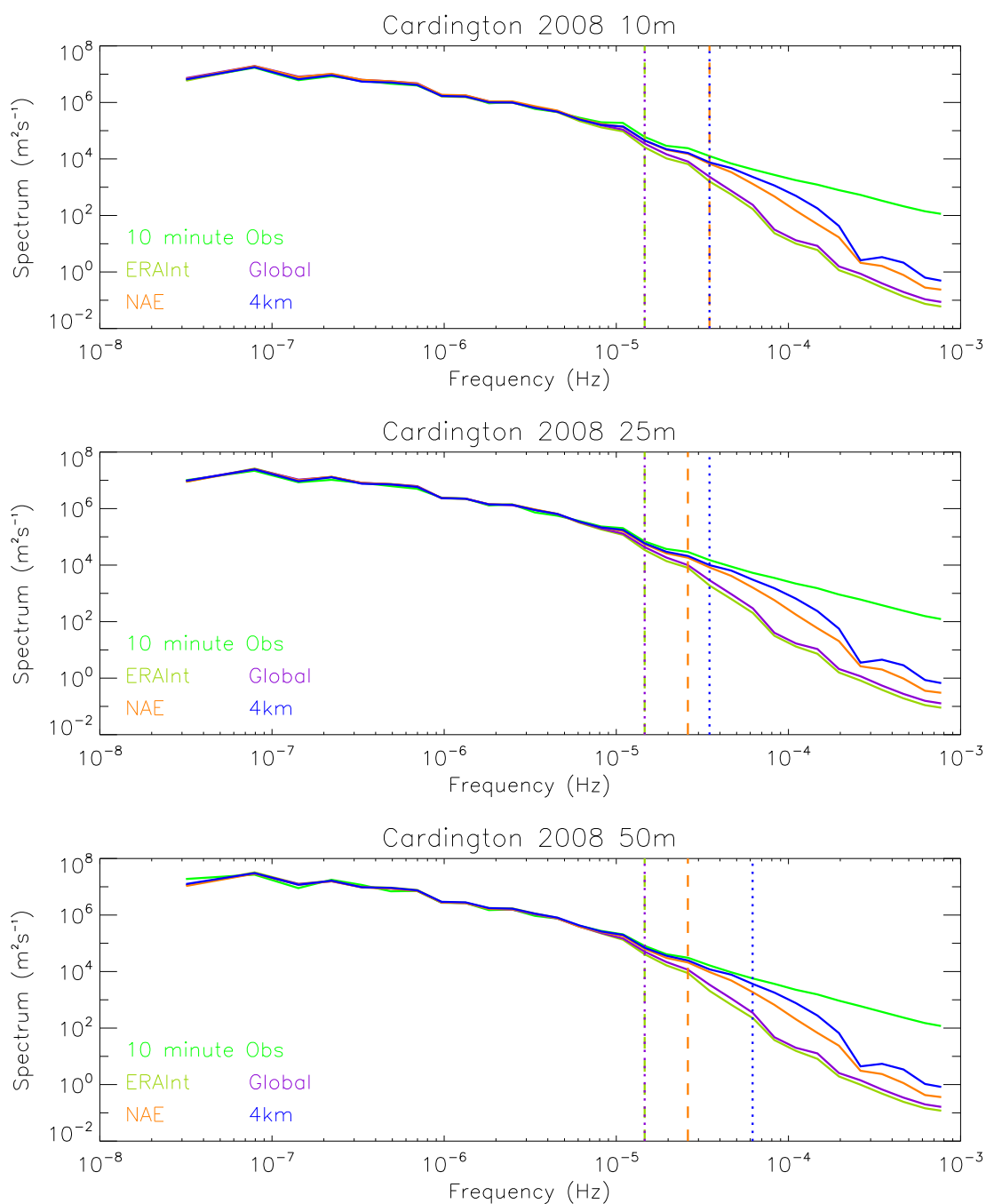


Figure 29: Cardington spectra at heights of 10 m, 25 m and 50 m agl generated from 2008 observations (10 minute), MetUM data (global (40 km, 3 hourly), NAE (12 km, hourly) and 4km (4 km, hourly)) and ECMWF ERA Interim data (80 km, 3 hourly).

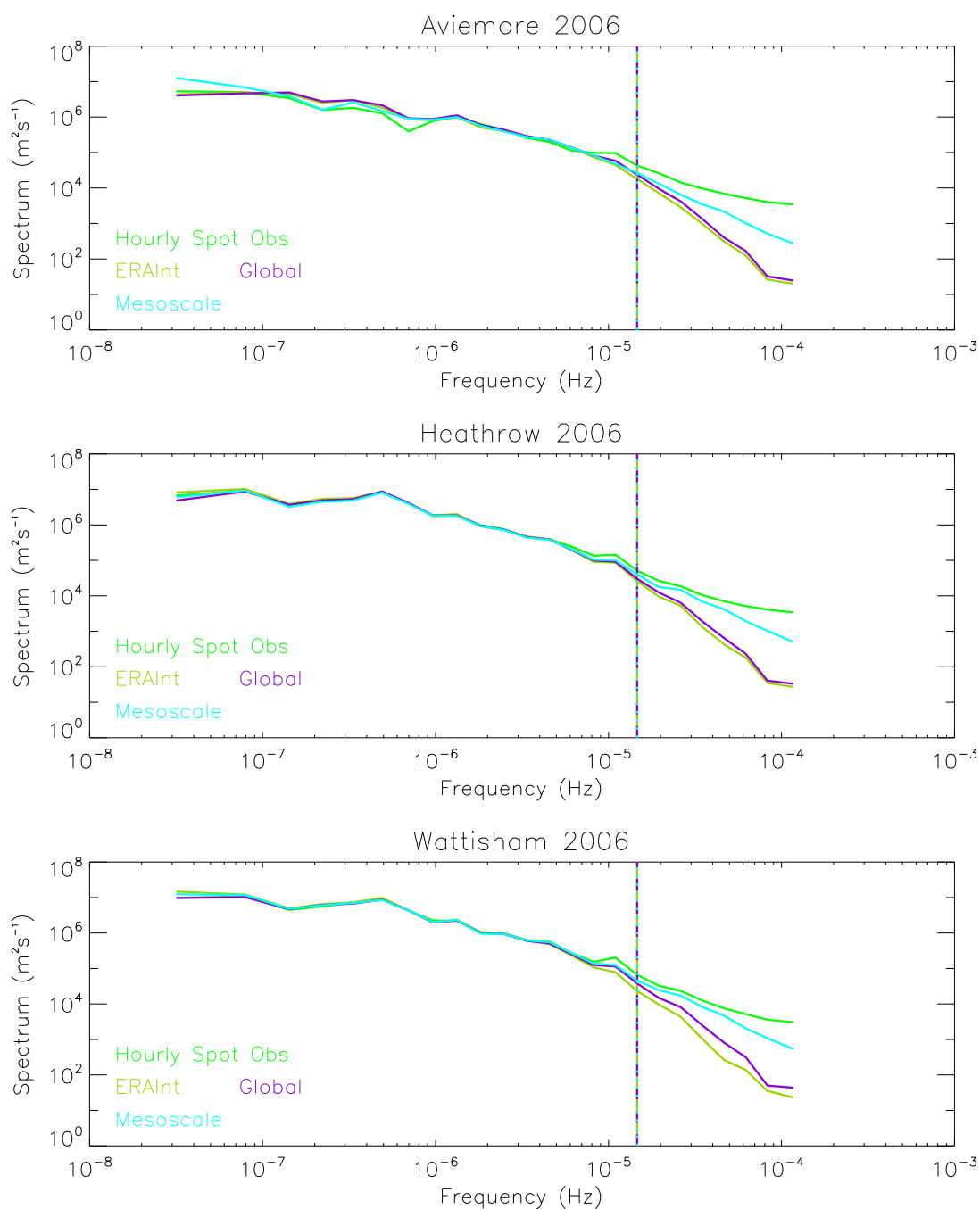


Figure 30: Aviemore, Heathrow and Wattisham spectra at a height of 10 m agl generated from 2006 observations (hourly spot), MetUM data (global (40 km, 3 hourly) and mesoscale (12 km, hourly)) and ECMWF ERA Interim data (80 km, 3 hourly).

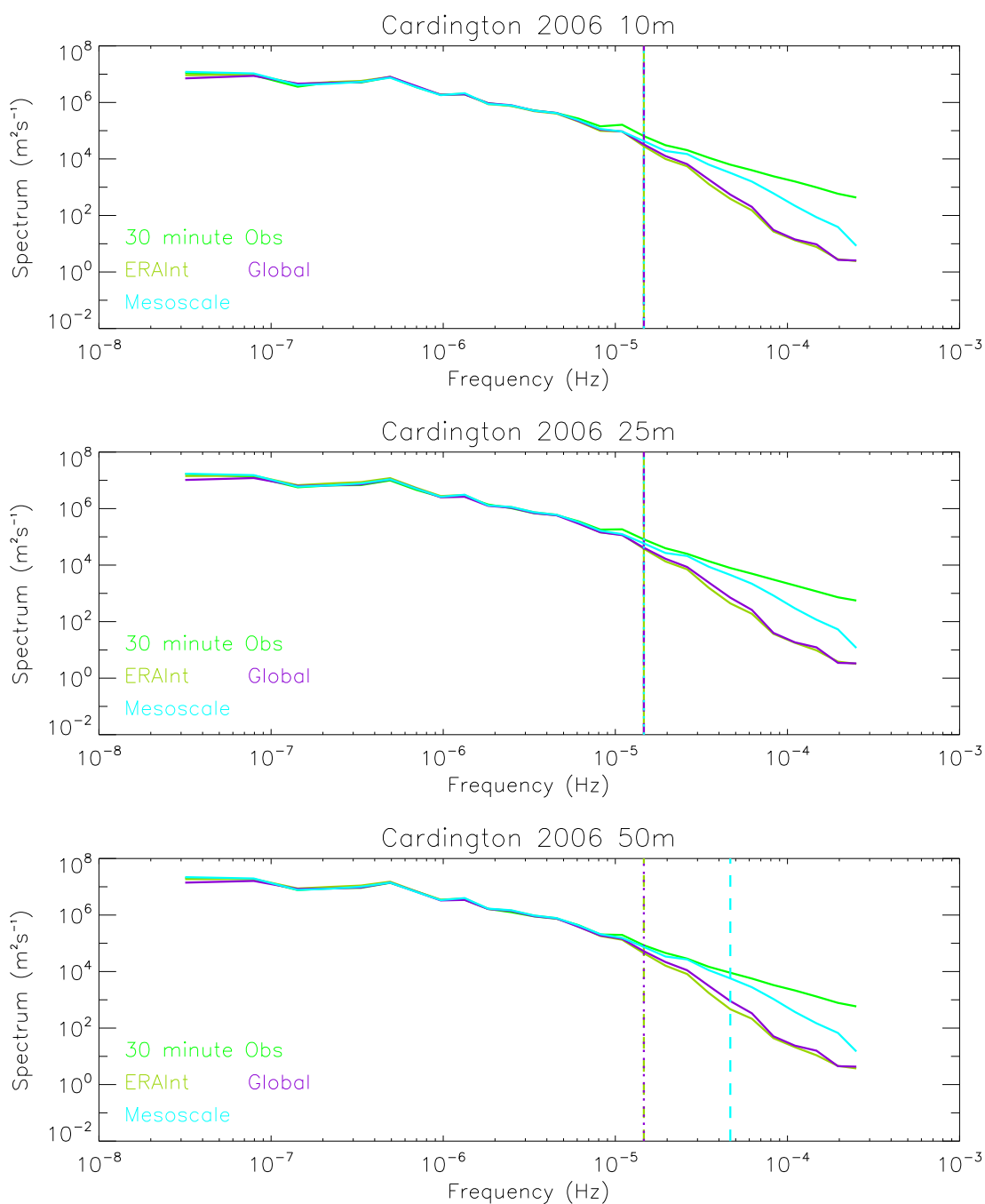


Figure 31: Cardington spectra at heights of 10 m, 25 m and 50 m agl generated from 2006 observations (30 minute), MetUM data (global (40 km, 3 hourly) and mesoscale (12 km, hourly)) and ECMWF ERA Interim data (80 km, 3 hourly).

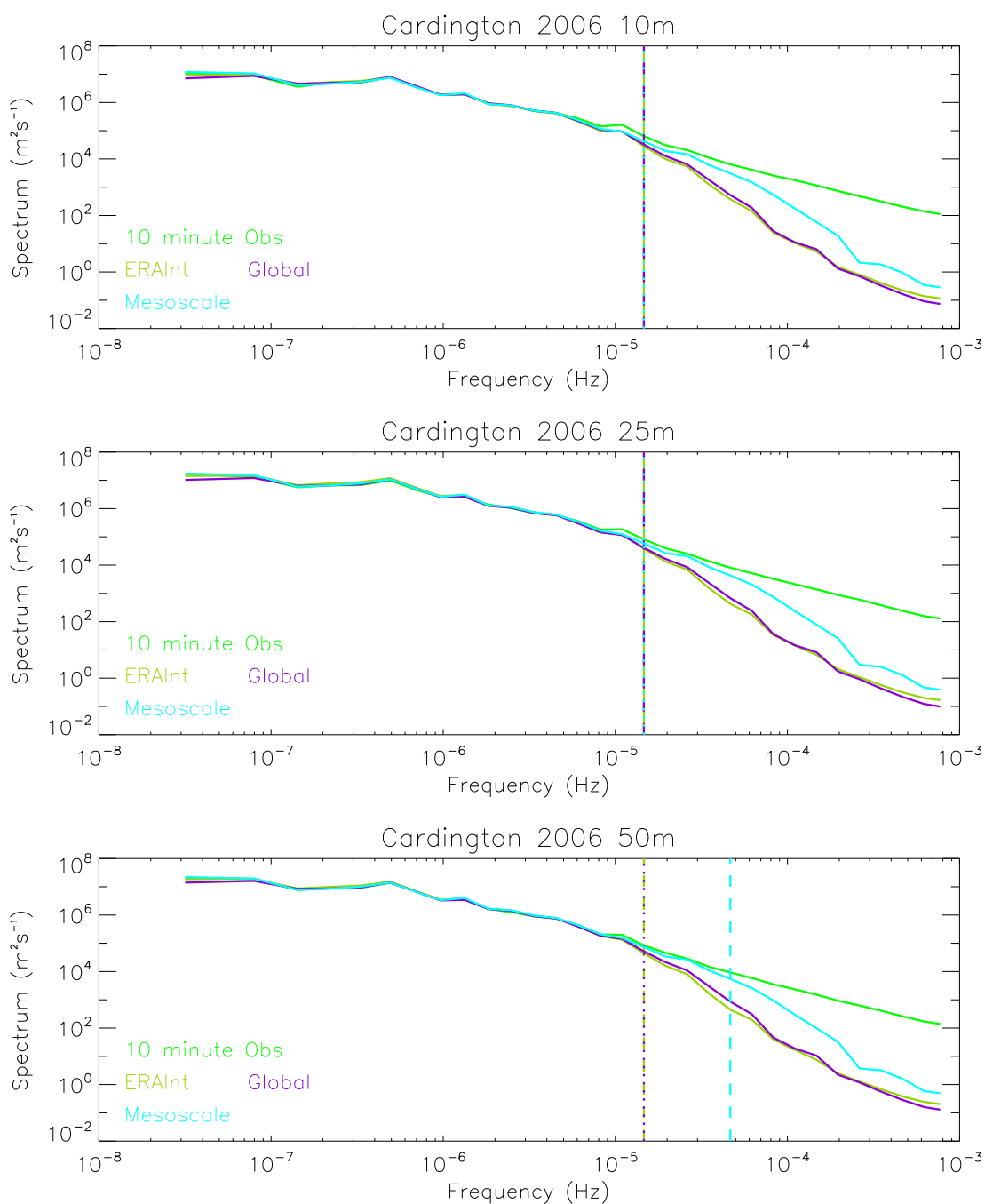


Figure 32: Cardington spectra at heights of 10 m, 25 m and 50 m agl generated from 2006 observations (10 minute), MetUM data (global (40 km, 3 hourly) and mesoscale (12 km, hourly)) and ECMWF ERA Interim data (80 km, 3 hourly).

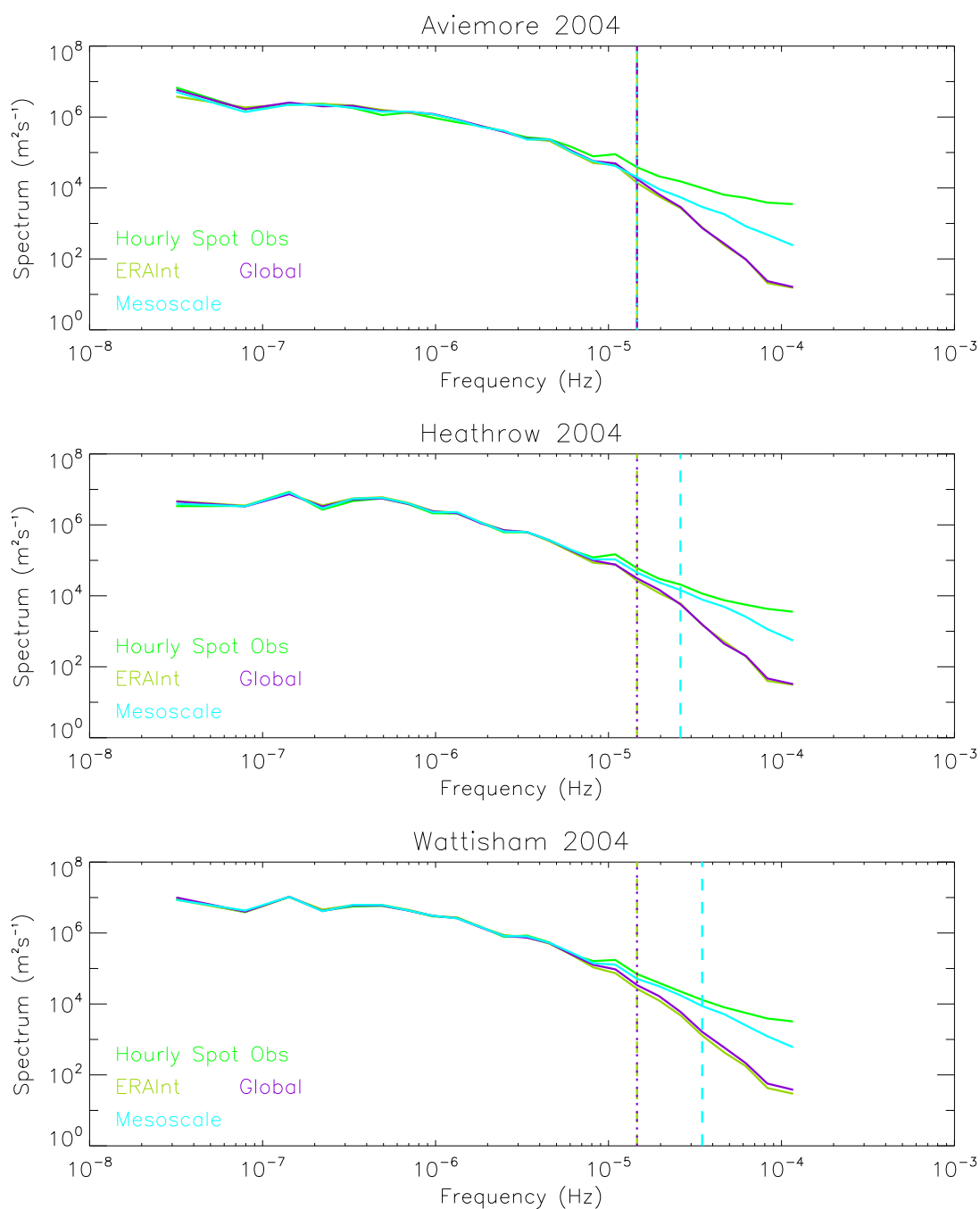


Figure 33: Aviemore, Heathrow and Wattisham spectra at a height of 10 m agl generated from 2004 observations (hourly spot), MetUM data (global (60 km, 3 hourly) and mesoscale (12 km, hourly)) and ECMWF ERA Interim data (80 km, 3 hourly).

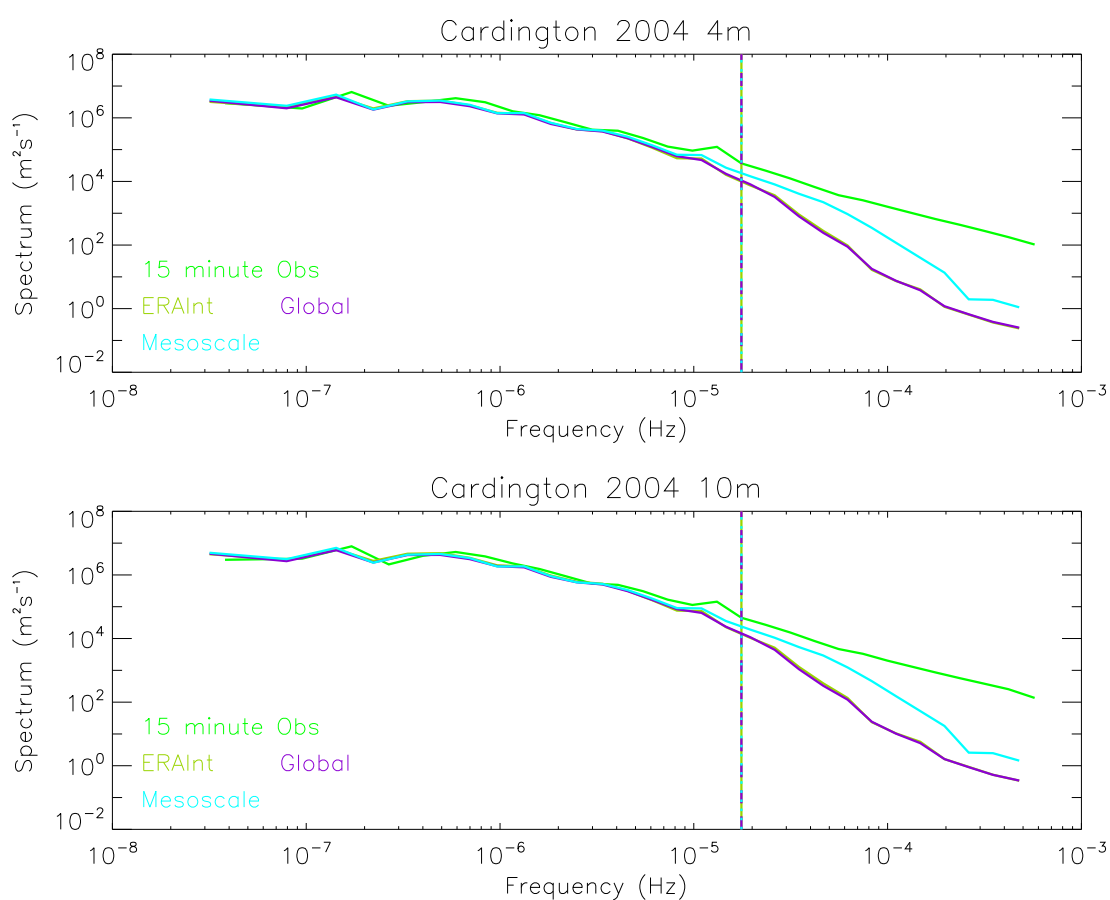


Figure 34: Cardington spectra at heights of 4 m and 10 m agl generated from 2004 observations (17.5 minute), MetUM data (global (60 km, 3 hourly) and mesoscale (12 km, hourly)) and ECMWF ERA Interim data (80 km, 3 hourly).



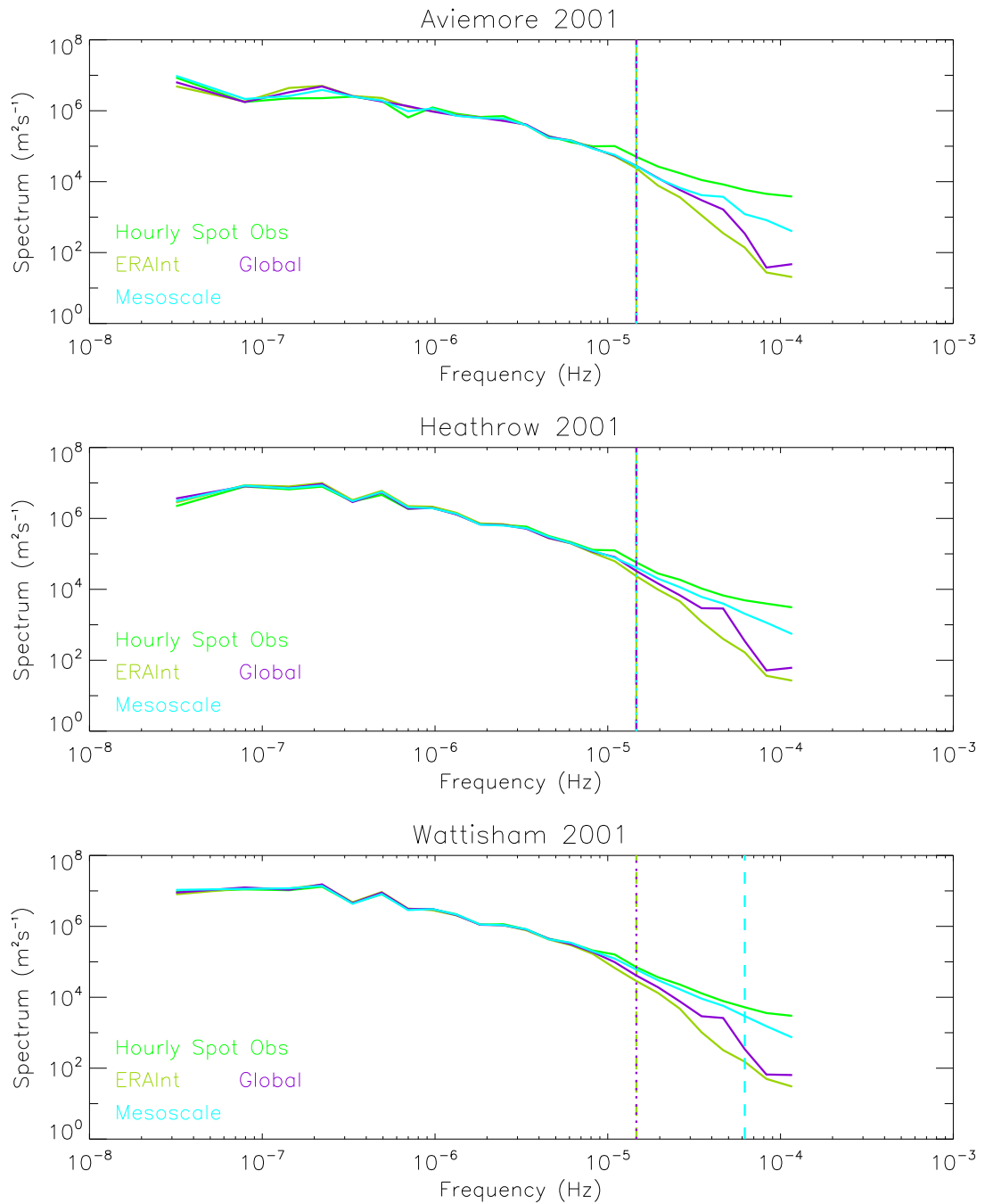


Figure 35: Aviemore, Heathrow and Wattisham spectra at a height of 10 m agl generated from 2001 observations (hourly spot), MetUM data (global (60 km, 3 hourly) and mesoscale (12 km, hourly)) and ECMWF ERA Interim data (80 km, 3 hourly).

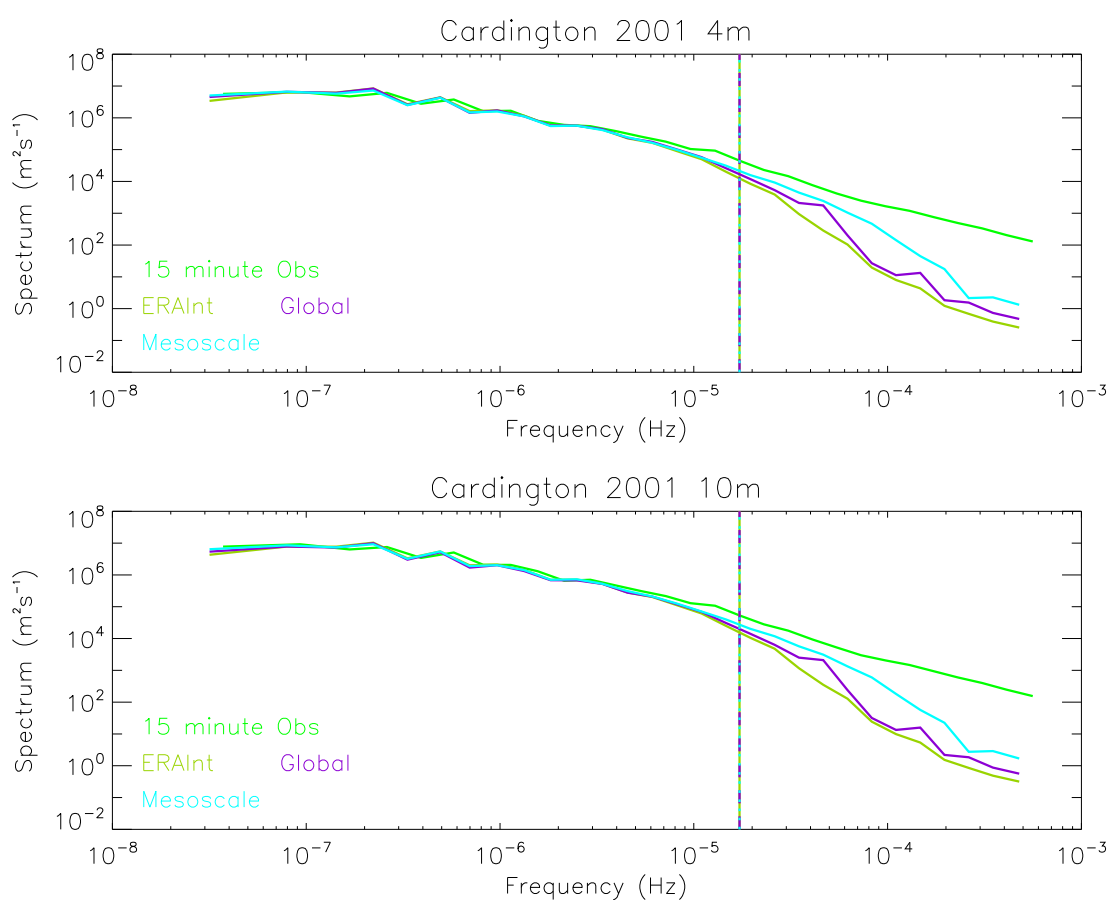


Figure 36: Cardington spectra at heights of 4 m and 10 m agl generated from 2001 observations (17.5 minute), MetUM data (global (60 km, 3 hourly) and mesoscale (12 km, hourly)) and ECMWF ERA Interim data (80 km, 3 hourly).

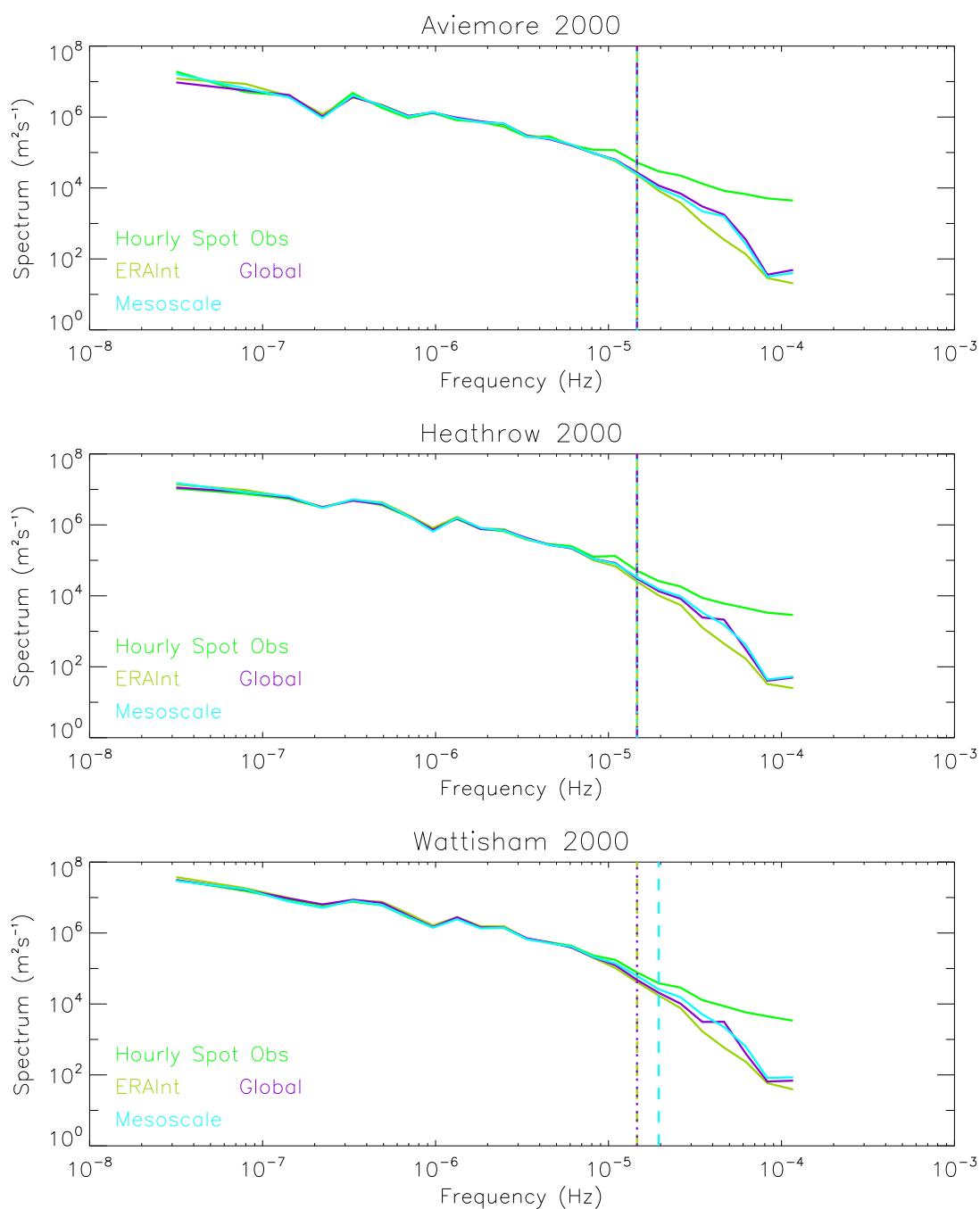


Figure 37: Aviemore, Heathrow and Wattisham spectra at a height of 10 m agl generated from 2000 observations (hourly spot), MetUM data (global (60 km, 3 hourly) and mesoscale (12 km, 3 hourly)) and ECMWF ERA Interim data (80 km, 3 hourly).

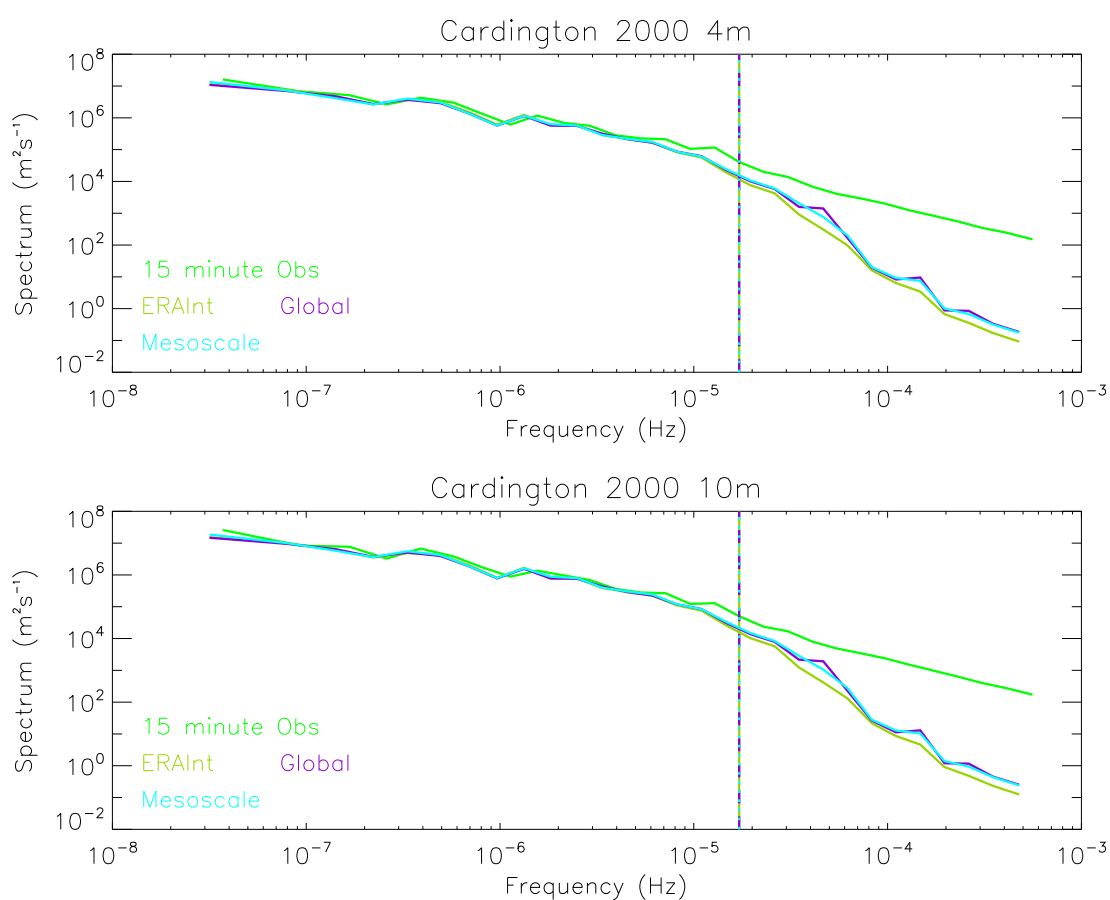


Figure 38: Cardington spectra at heights of 4 m and 10 m agl generated from 2000 observations (17.5 minute), MetUM data (global (60 km, 3 hourly) and mesoscale (12 km, 3 hourly)) and ECMWF ERA Interim data (80 km, 3 hourly).

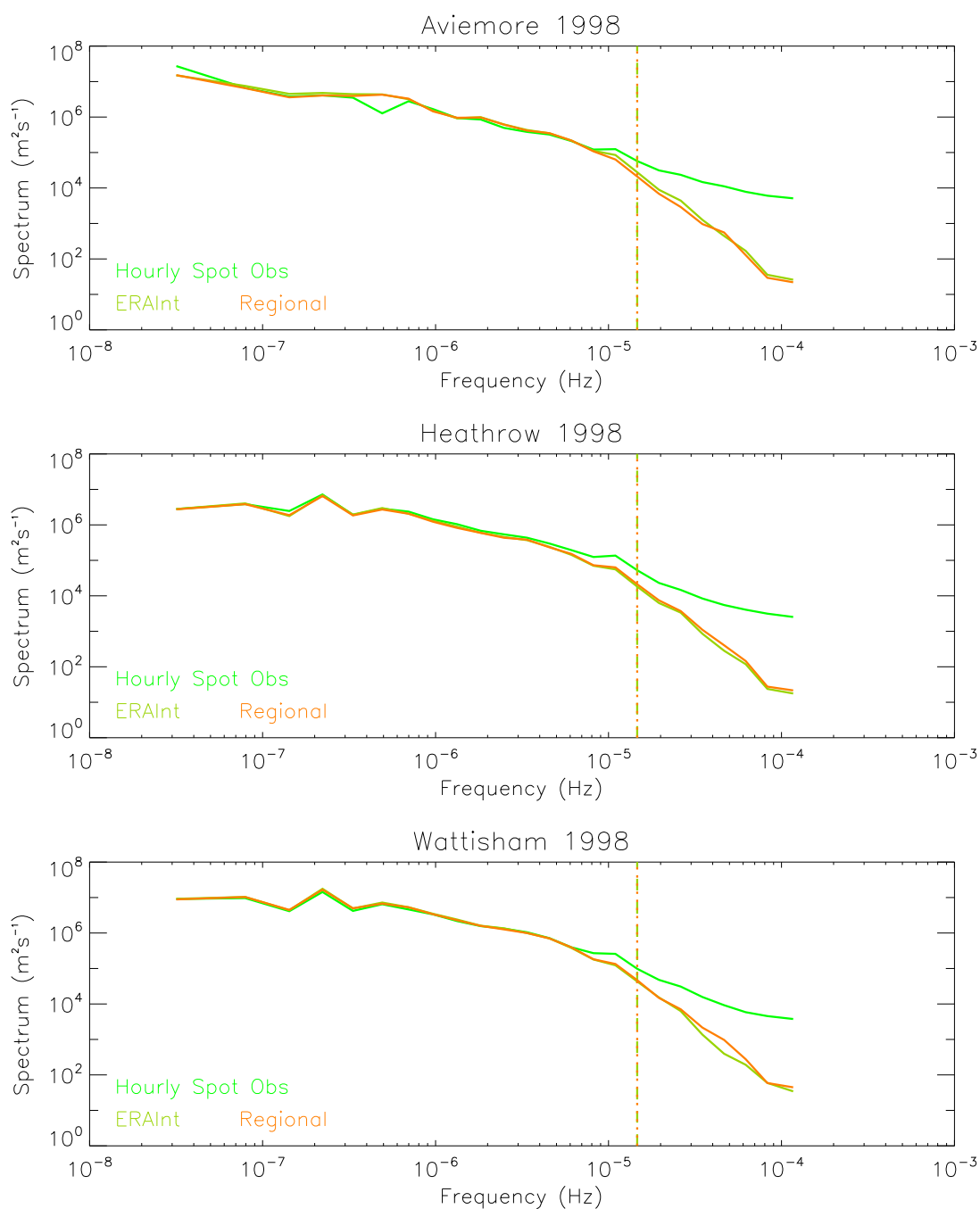


Figure 39: Aviemore, Heathrow and Wattisham spectra at a height of 10 m agl generated from 1998 observations (hourly spot), regional MetUM data (50 km, 3 hourly) and ECMWF ERA Interim data (80 km, 3 hourly).

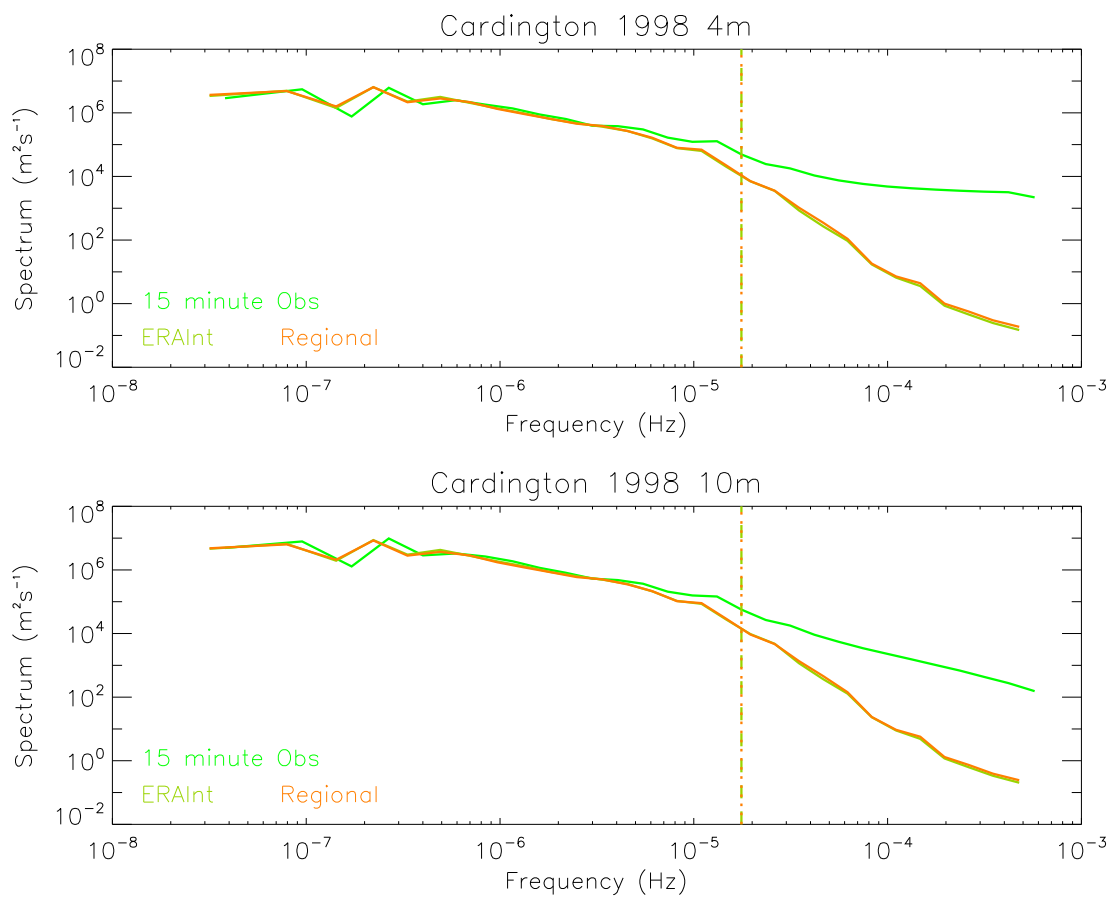


Figure 40: Cardington spectra at heights of 4 m and 10 m agl generated from 1998 observations (17.5 minute), regional MetUM data (50 km, 3 hourly) and ECMWF ERA Interim data (80 km, 3 hourly).

## C Boundary layer fractional difference plots generated using observed and NWP winds

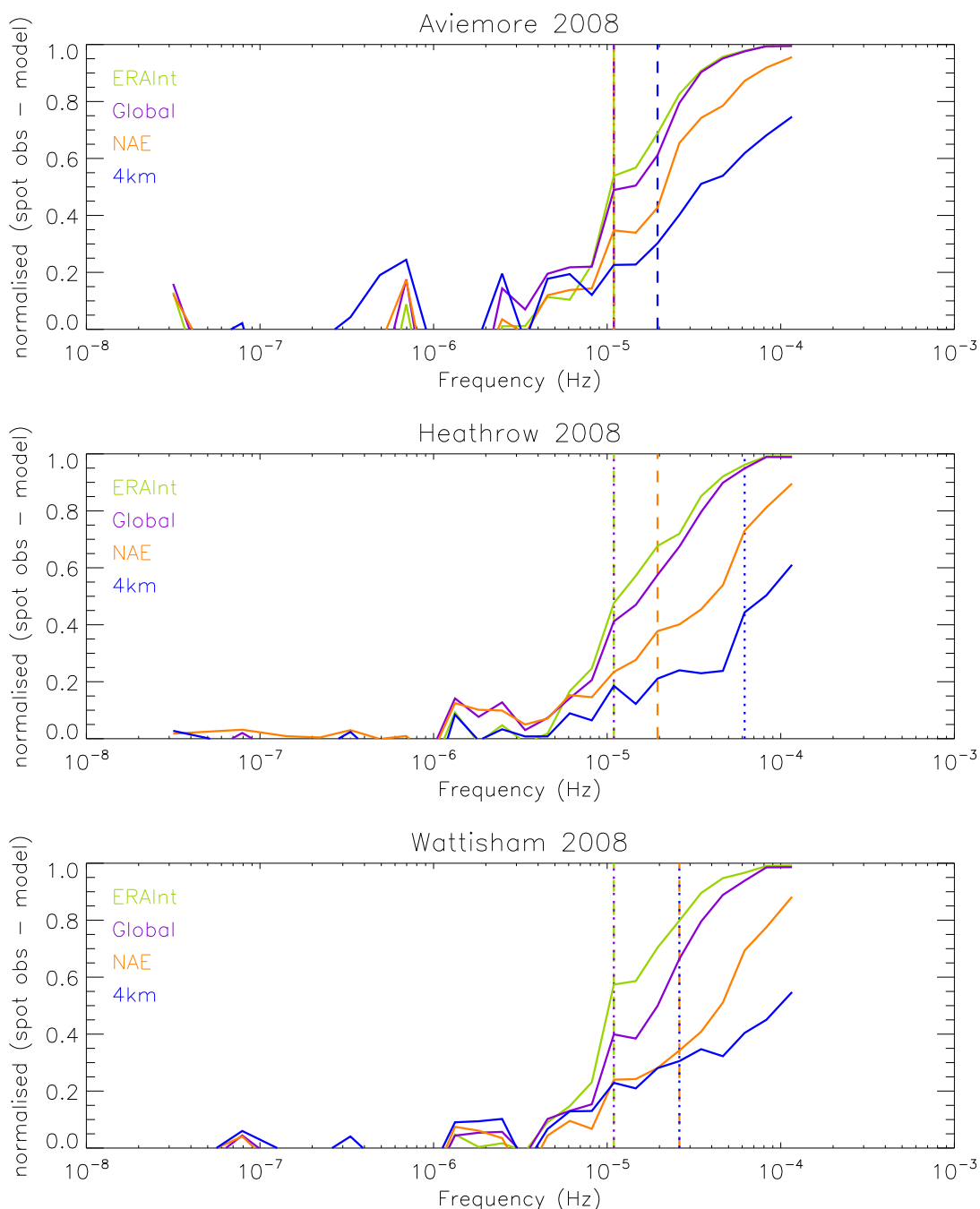


Figure 41: Fractional difference in the Aviemore, Heathrow and Wattisham spectra at a height of 10 m agl generated from 2008 hourly spot observations, MetUM data (global (40 km, 3 hourly), NAE (12 km, hourly) and 4km (4 km, hourly)) and ECMWF ERA Interim data (80 km, 3 hourly). The dashed and dotted vertical lines denote the frequency at which the difference between the modelled and observed spectra exceeds 30%.

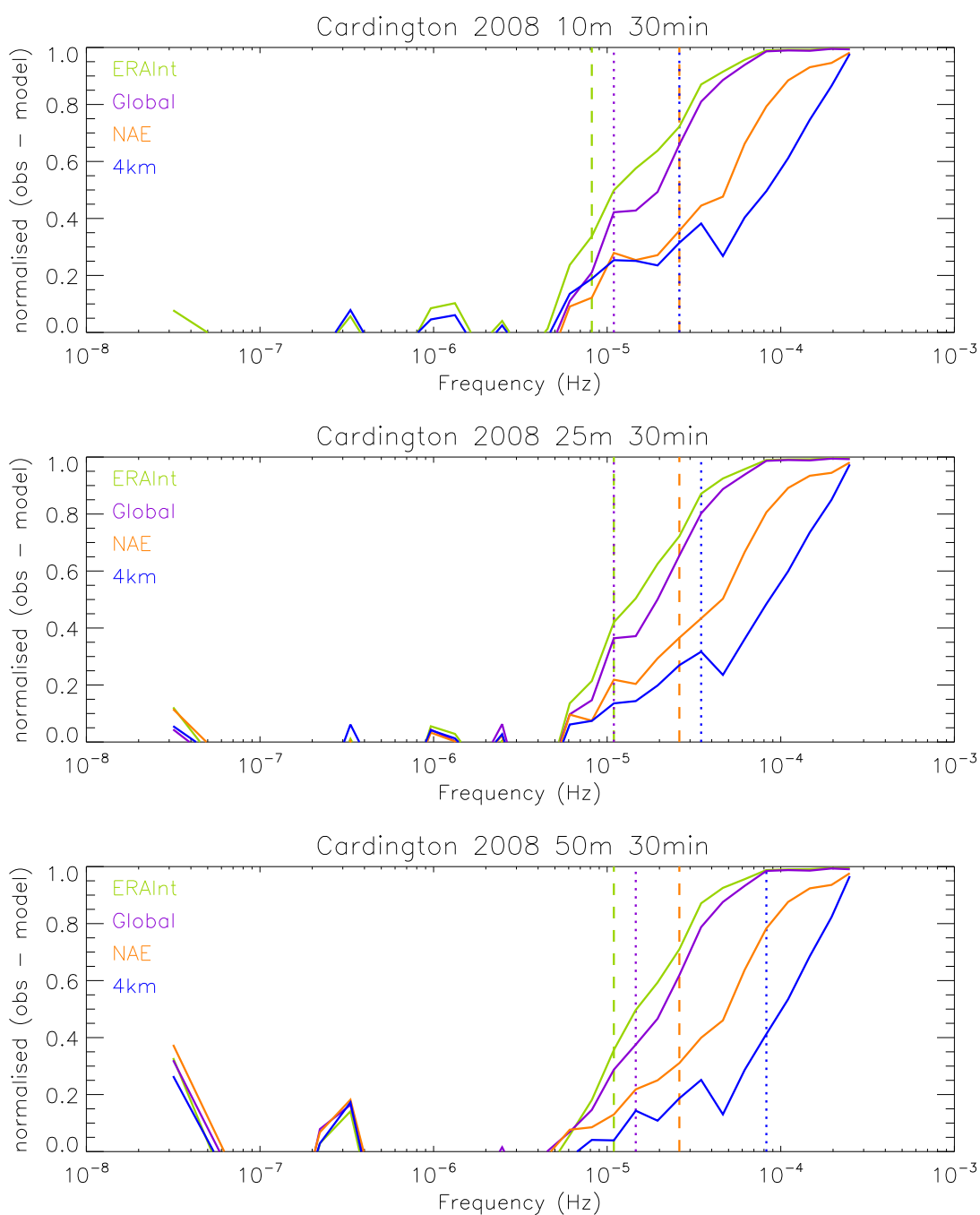


Figure 42: Fractional difference in the Cardington spectra at heights of 10 m, 25 m and 50 m agl generated from 2008 observations (30 minute), MetUM data (global (40 km, 3 hourly), NAE (12 km, hourly) and 4km (4 km, hourly)) and ECMWF ERA Interim data (80 km, 3 hourly). The dashed and dotted vertical lines denote the frequency at which the difference between the modelled and observed spectra exceeds 30%.



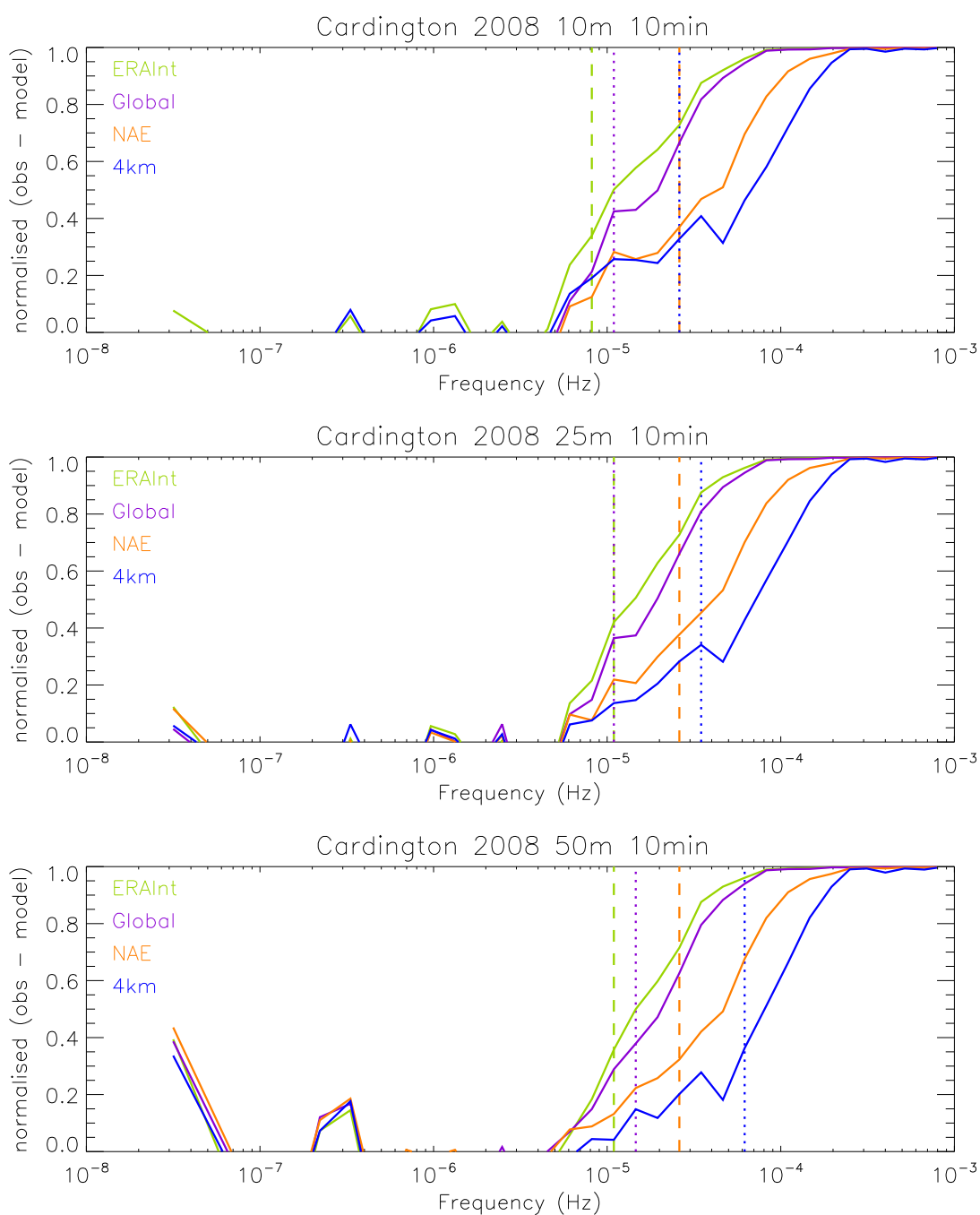


Figure 43: Fractional difference in the Cardington spectra at heights of 10 m, 25 m and 50 m agl generated from 2008 observations (10 minute), MetUM data (global (40 km, 3 hourly), NAE (12 km, hourly) and 4km (4 km, hourly)) and ECMWF ERA Interim data (80 km, 3 hourly). The dashed and dotted vertical lines denote the frequency at which the difference between the modelled and observed spectra exceeds 30%.

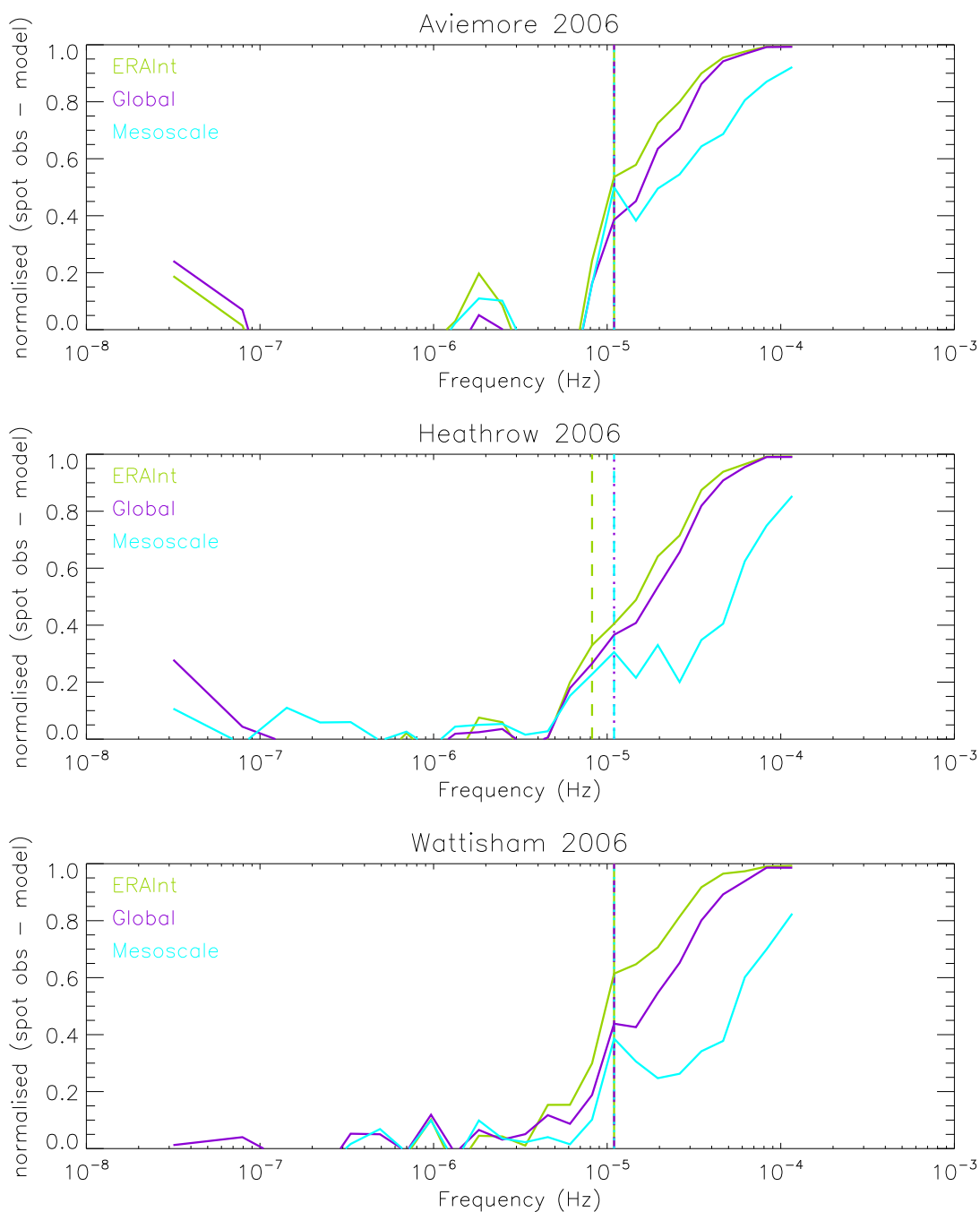


Figure 44: Fractional difference in the Aviemore, Heathrow and Wattisham spectra at a height of 10 m agl generated from 2006 hourly spot observations, MetUM data (global (40 km, 3 hourly) and mesoscale (12 km, hourly)) and ECMWF ERA Interim data (80 km, 3 hourly). The dashed and dotted vertical lines denote the frequency at which the difference between the modelled and observed spectra exceeds 30%.

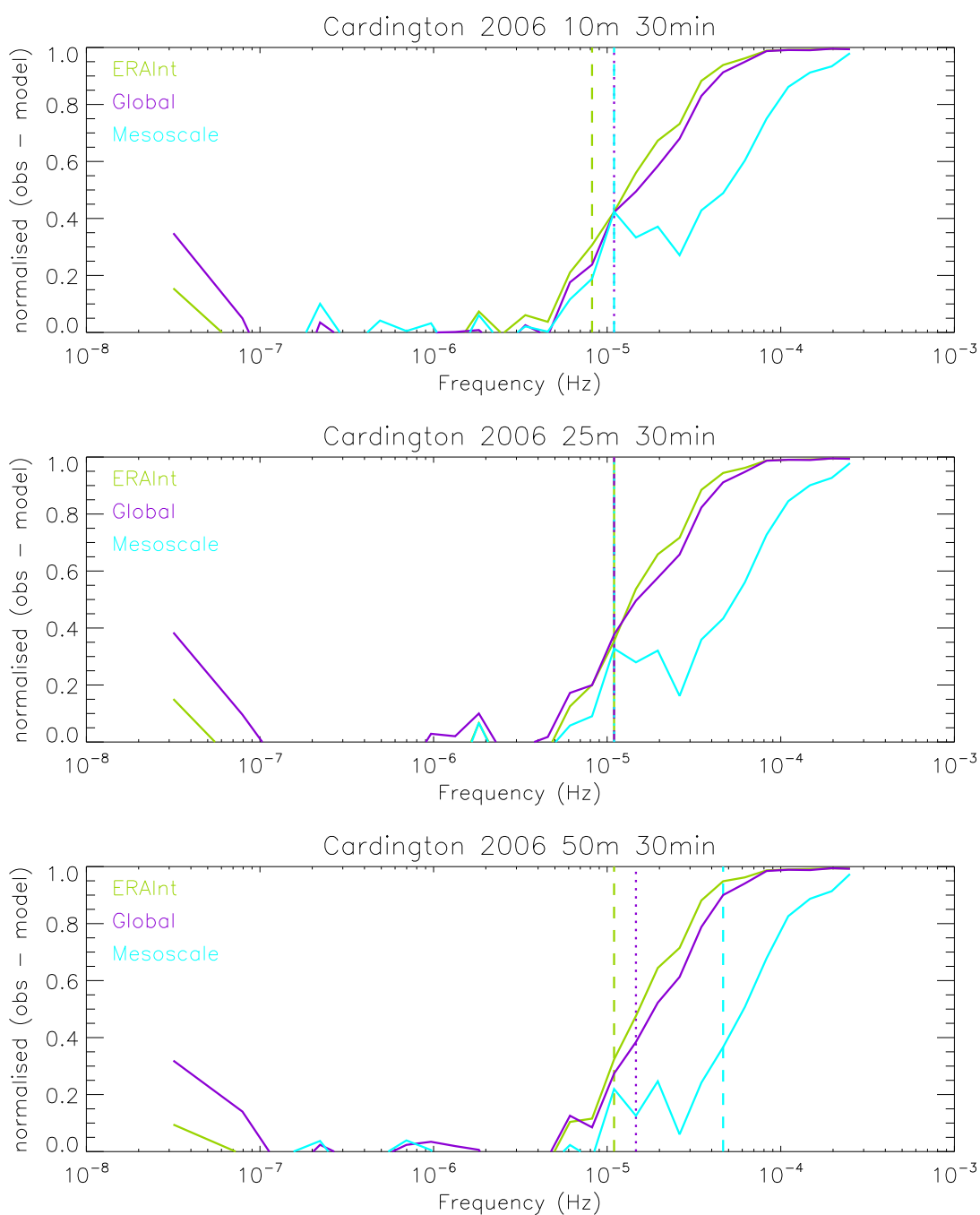


Figure 45: Fractional difference in the Cardington spectra at heights of 10 m, 25 m and 50 m agl generated from 2006 observations (30 minute), MetUM data (global (40 km, 3 hourly) and mesoscale (12 km, hourly)) and ECMWF ERA Interim data (80 km, 3 hourly). The dashed and dotted vertical lines denote the frequency at which the difference between the modelled and observed spectra exceeds 30%.

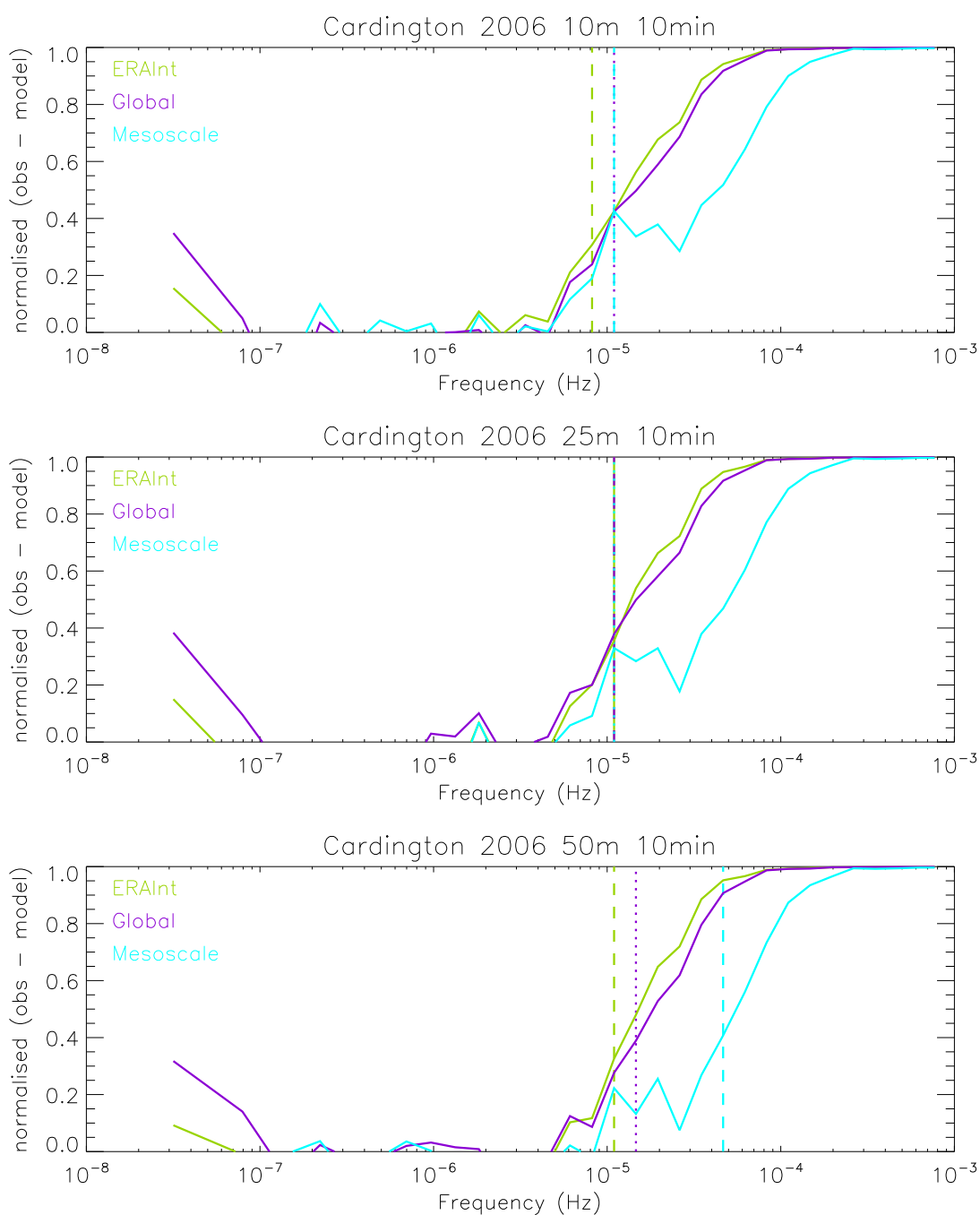


Figure 46: Fractional difference in the Cardington spectra at heights of 10 m, 25 m and 50 m agl generated from 2006 observations (10 minute), MetUM data (global (40 km, 3 hourly) and mesoscale (12 km, hourly)) and ECMWF ERA Interim data (80 km, 3 hourly). The dashed and dotted vertical lines denote the frequency at which the difference between the modelled and observed spectra exceeds 30%.

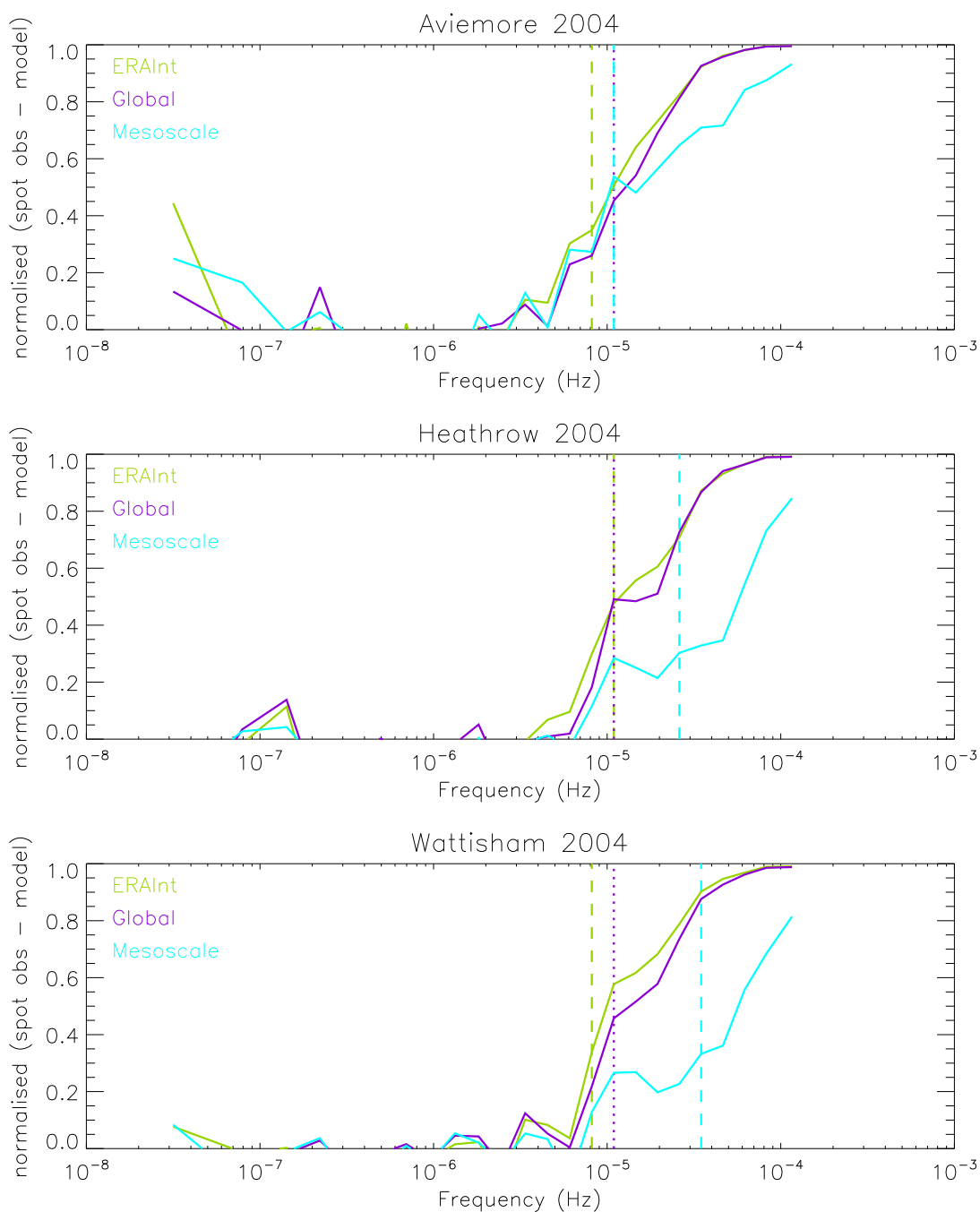


Figure 47: Fractional difference in the Aviemore, Heathrow and Wattisham spectra at a height of 10 m agl generated from 2004 hourly spot observations, MetUM data (global (60 km, 3 hourly) and mesoscale (12 km, hourly)) and ECMWF ERA Interim data (80 km, 3 hourly). The dashed and dotted vertical lines denote the frequency at which the difference between the modelled and observed spectra exceeds 30%.

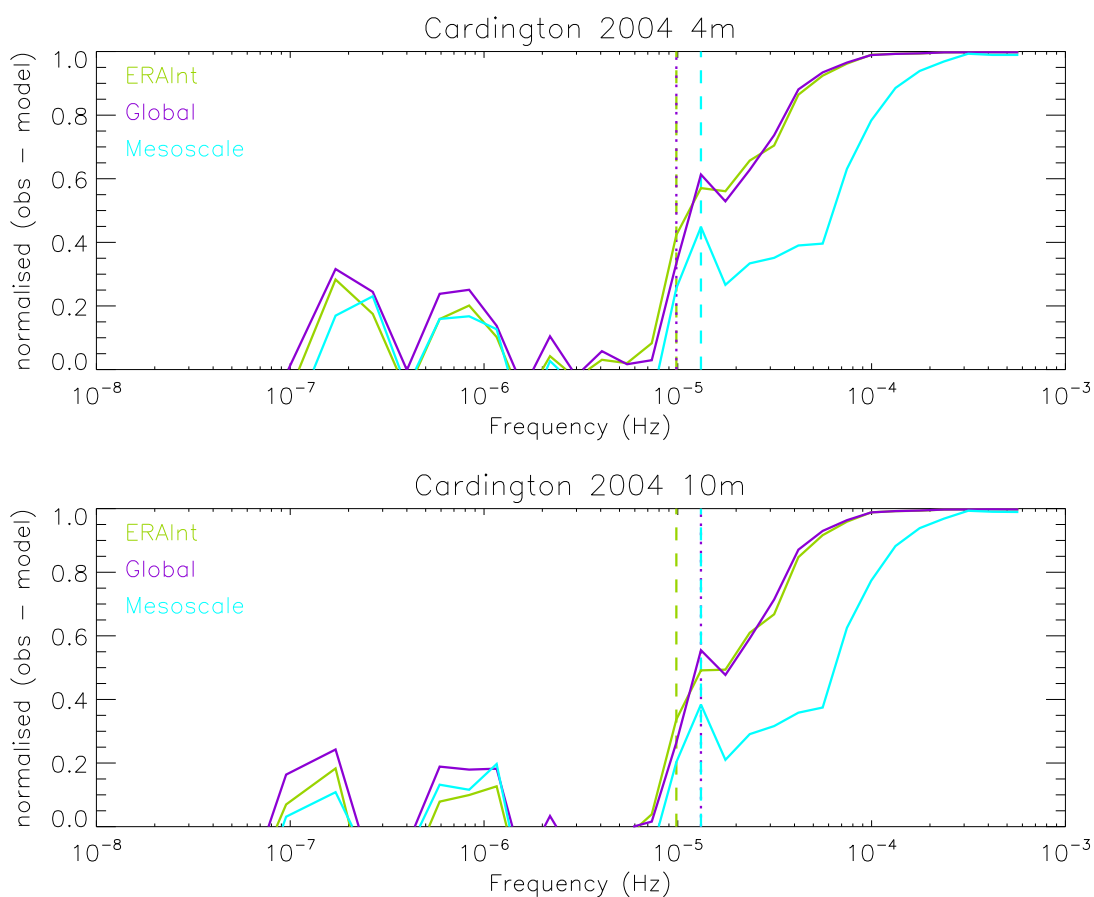


Figure 48: Fractional difference in the Cardington spectra at heights of 4 m and 10 m agl generated from 2004 observations (17.5 minute), MetUM data (global (60 km, 3 hourly) and mesoscale (12 km, hourly)) and ECMWF ERA Interim data (80 km, 3 hourly). The dashed and dotted vertical lines denote the frequency at which the difference between the modelled and observed spectra exceeds 30%.

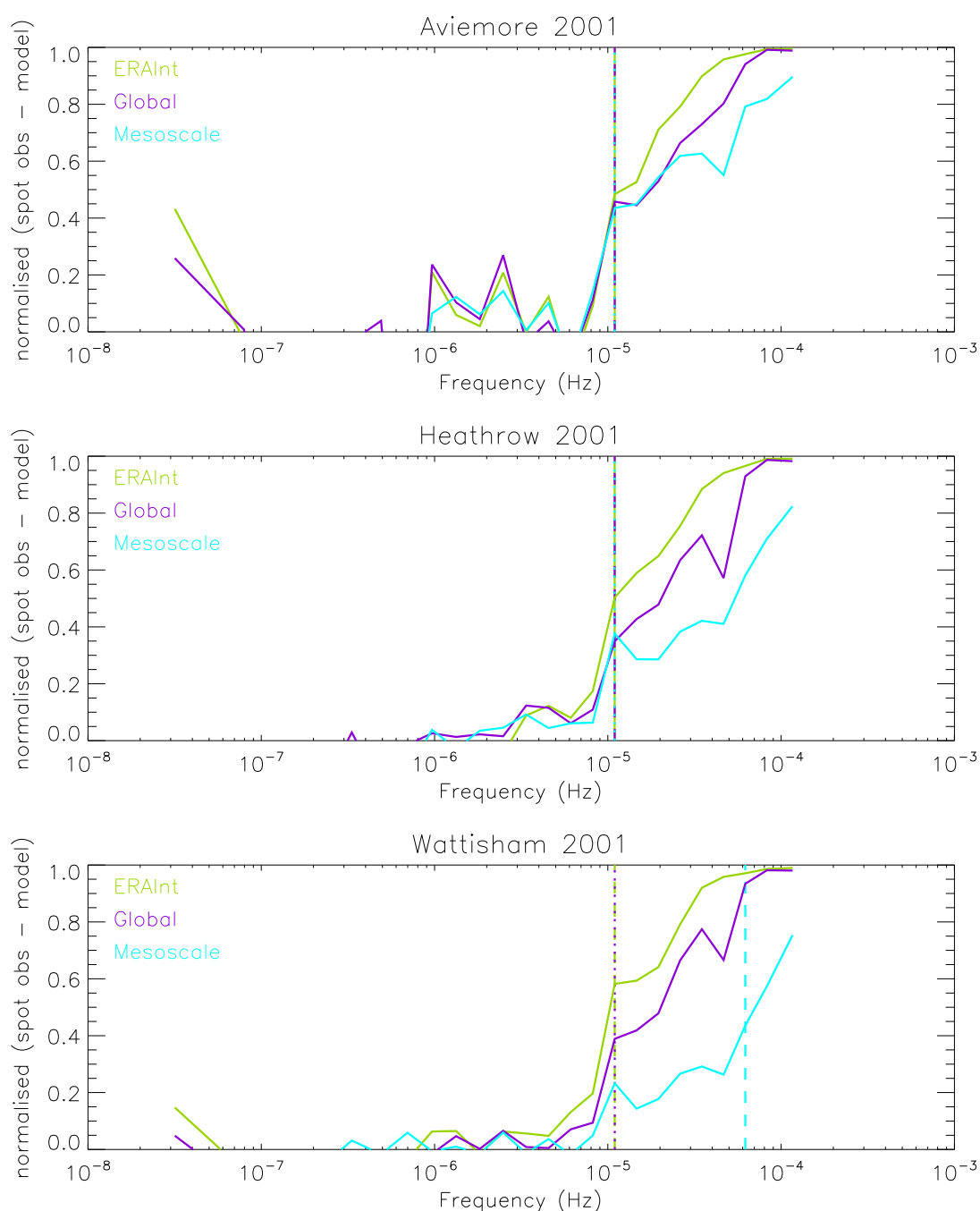


Figure 49: Fractional difference in the Aviemore, Heathrow and Wattisham spectra at a height of 10 m agl generated from 2001 hourly spot observations, MetUM data (global (60 km, 3 hourly) and mesoscale (12 km, hourly)) and ECMWF ERA Interim data (80 km, 3 hourly). The dashed and dotted vertical lines denote the frequency at which the difference between the modelled and observed spectra exceeds 30%.

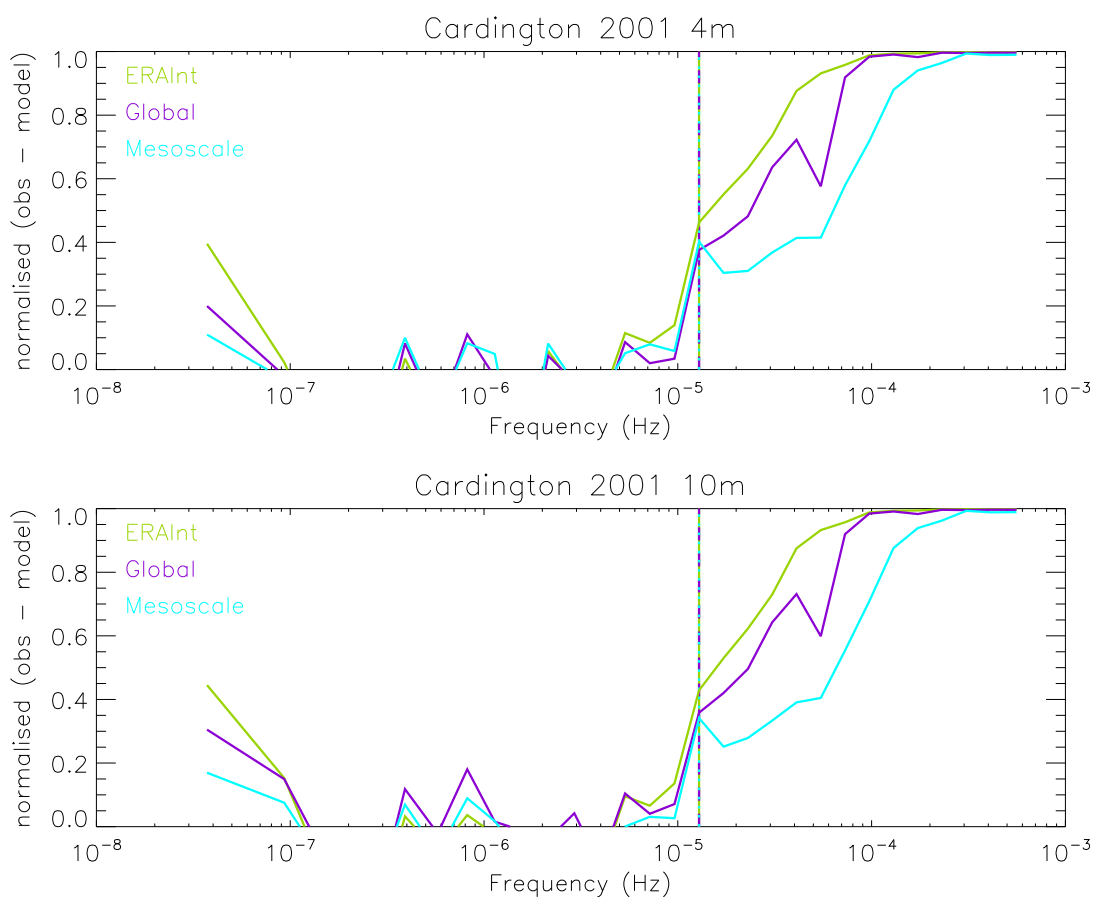


Figure 50: Fractional difference in the Cardington spectra at heights of 4 m and 10 m agl generated from 2001 observations (17.5 minute), MetUM data (global (60 km, 3 hourly) and mesoscale (12 km, hourly)) and ECMWF ERA Interim data (80 km, 3 hourly). The dashed and dotted vertical lines denote the frequency at which the difference between the modelled and observed spectra exceeds 30%.



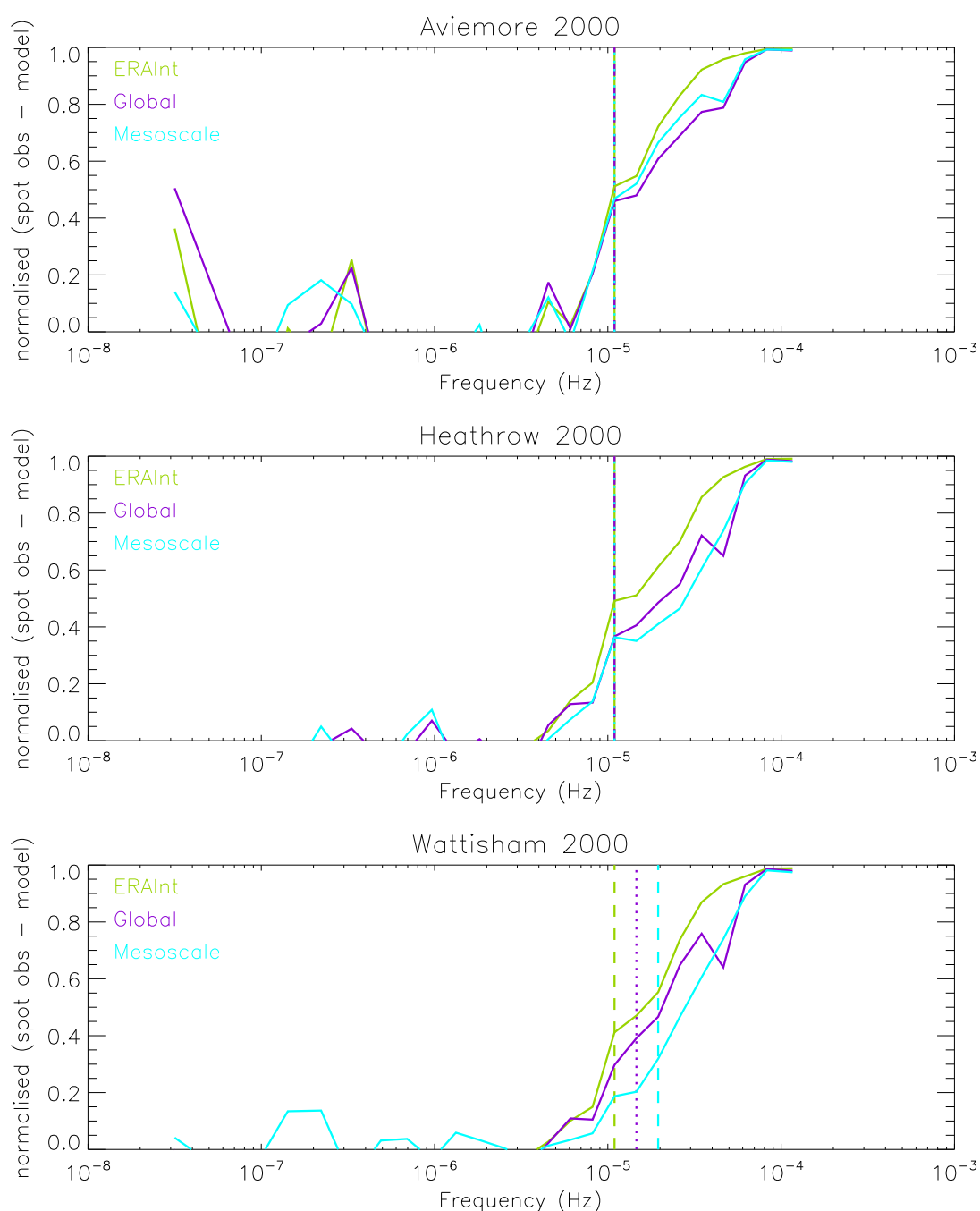


Figure 51: Fractional difference in the Aviemore, Heathrow and Wattisham spectra at a height of 10 m agl generated from 2000 hourly spot observations, MetUM data (global (60 km, 3 hourly) and mesoscale (12 km, 3 hourly)) and ECMWF ERA Interim data (80 km, 3 hourly). The dashed and dotted vertical lines denote the frequency at which the difference between the modelled and observed spectra exceeds 30%.

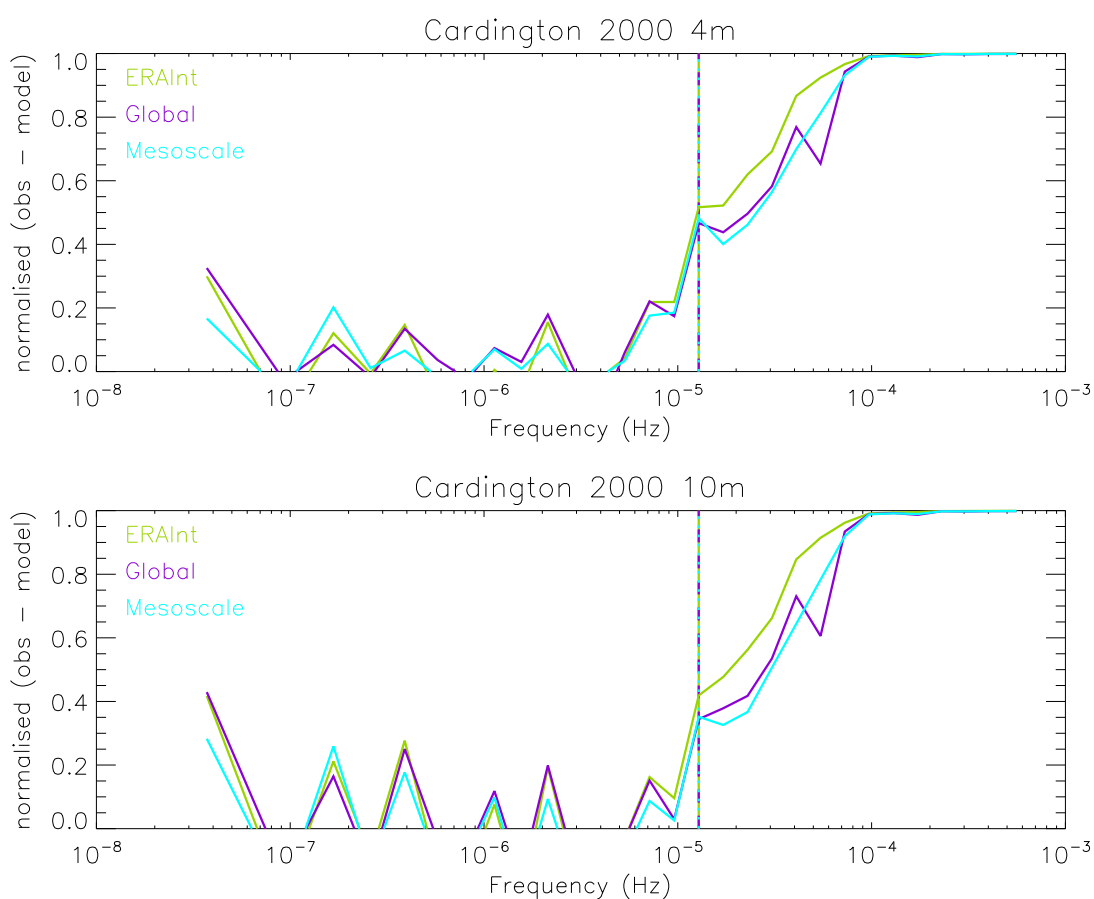


Figure 52: Fractional difference in the Cardington spectra at heights of 4 m and 10 m agl generated from 2000 observations (17.5 minute), MetUM data (global (60 km, 3 hourly) and mesoscale (12 km, 3 hourly)) and ECMWF ERA Interim data (80 km, 3 hourly). The dashed and dotted vertical lines denote the frequency at which the difference between the modelled and observed spectra exceeds 30%.

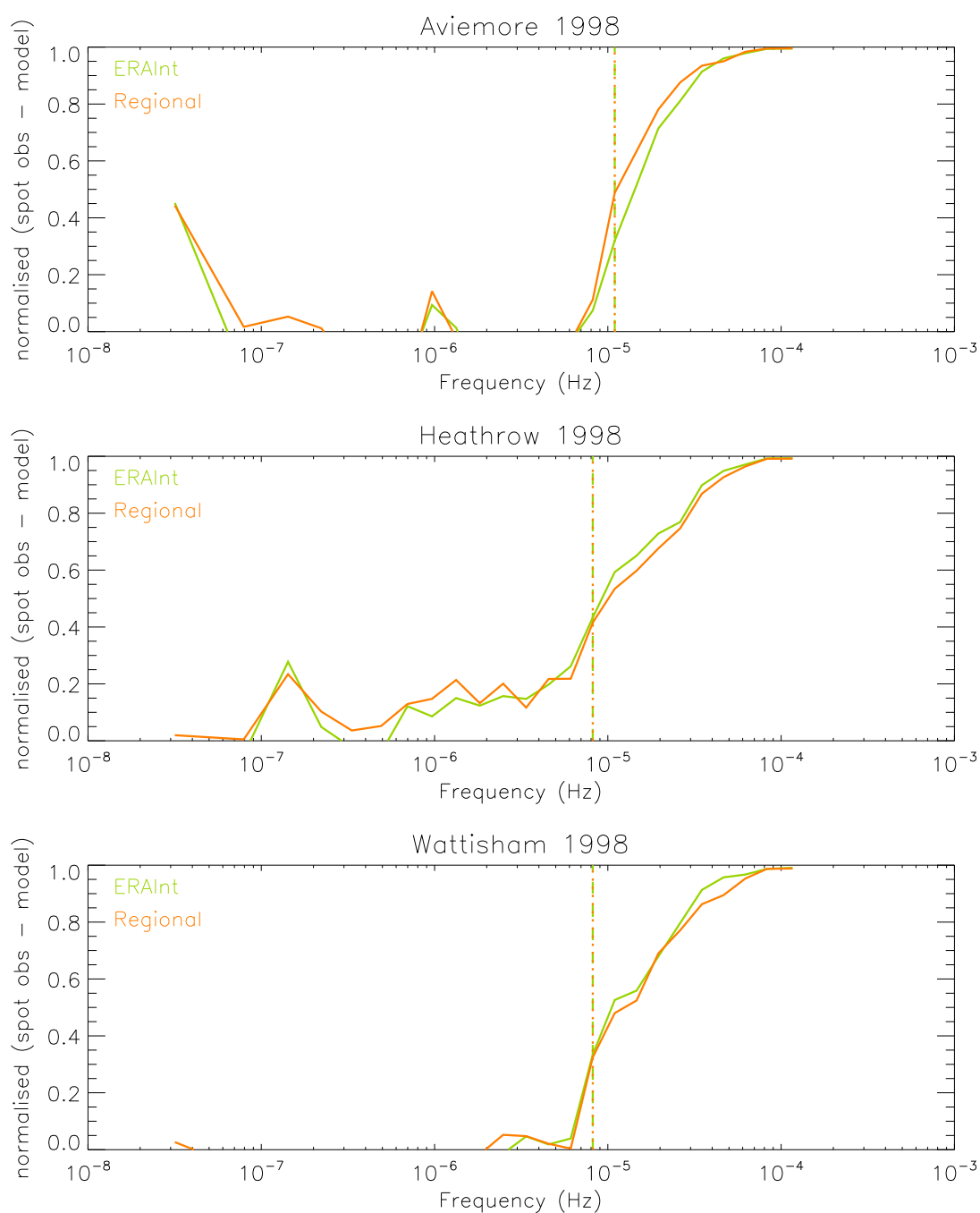


Figure 53: Fractional difference in the Aviemore, Heathrow and Wattisham spectra at a height of 10 m agl generated from 1998 hourly spot observations, regional MetUM data (50 km, 3 hourly) and ECMWF ERA Interim data (80 km, 3 hourly). The dashed and dotted vertical lines denote the frequency at which the difference between the modelled and observed spectra exceeds 30%.

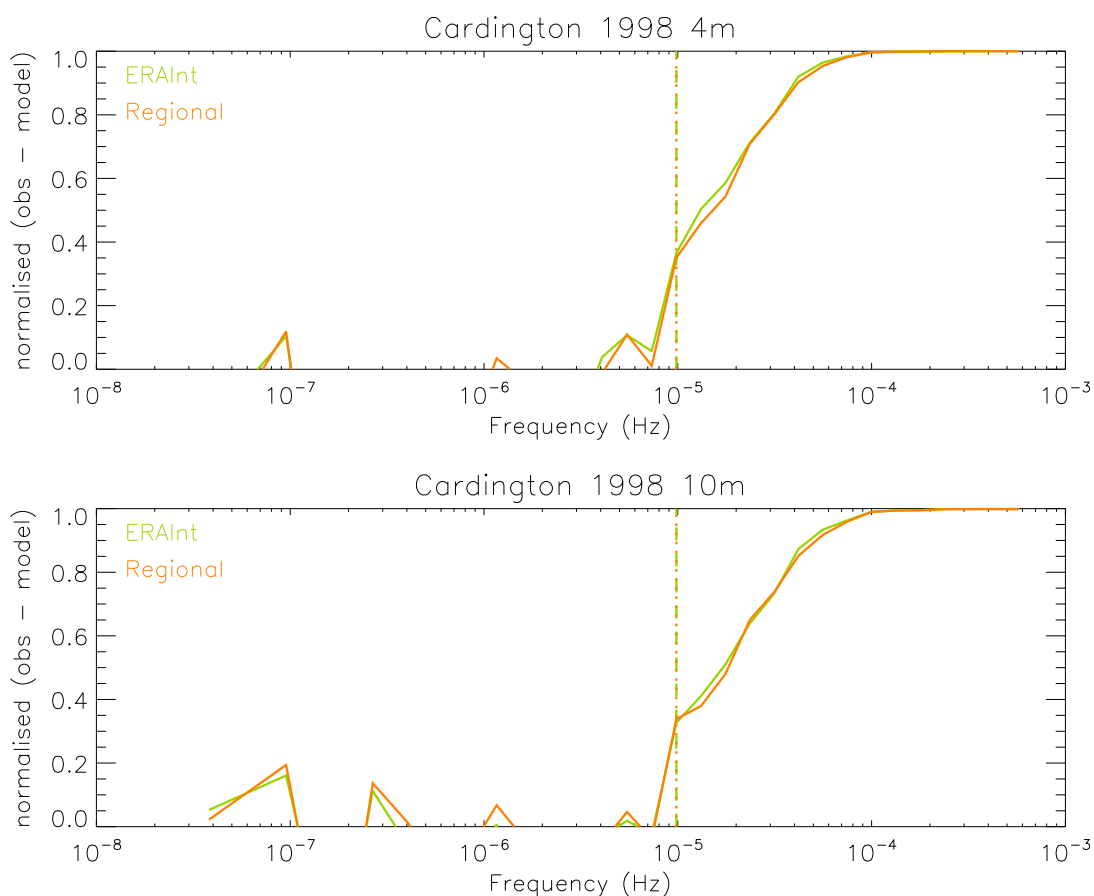


Figure 54: Fractional difference in the Cardington spectra at heights of 4 m and 10 m agl generated from 1998 observations (17.5 minute), regional MetUM data (50 km, 3 hourly) and ECMWF ERA Interim data (80 km, 3 hourly). The dashed and dotted vertical lines denote the frequency at which the difference between the modelled and observed spectra exceeds 30%.

## D Boundary layer difference plots generated using observed and NWP winds

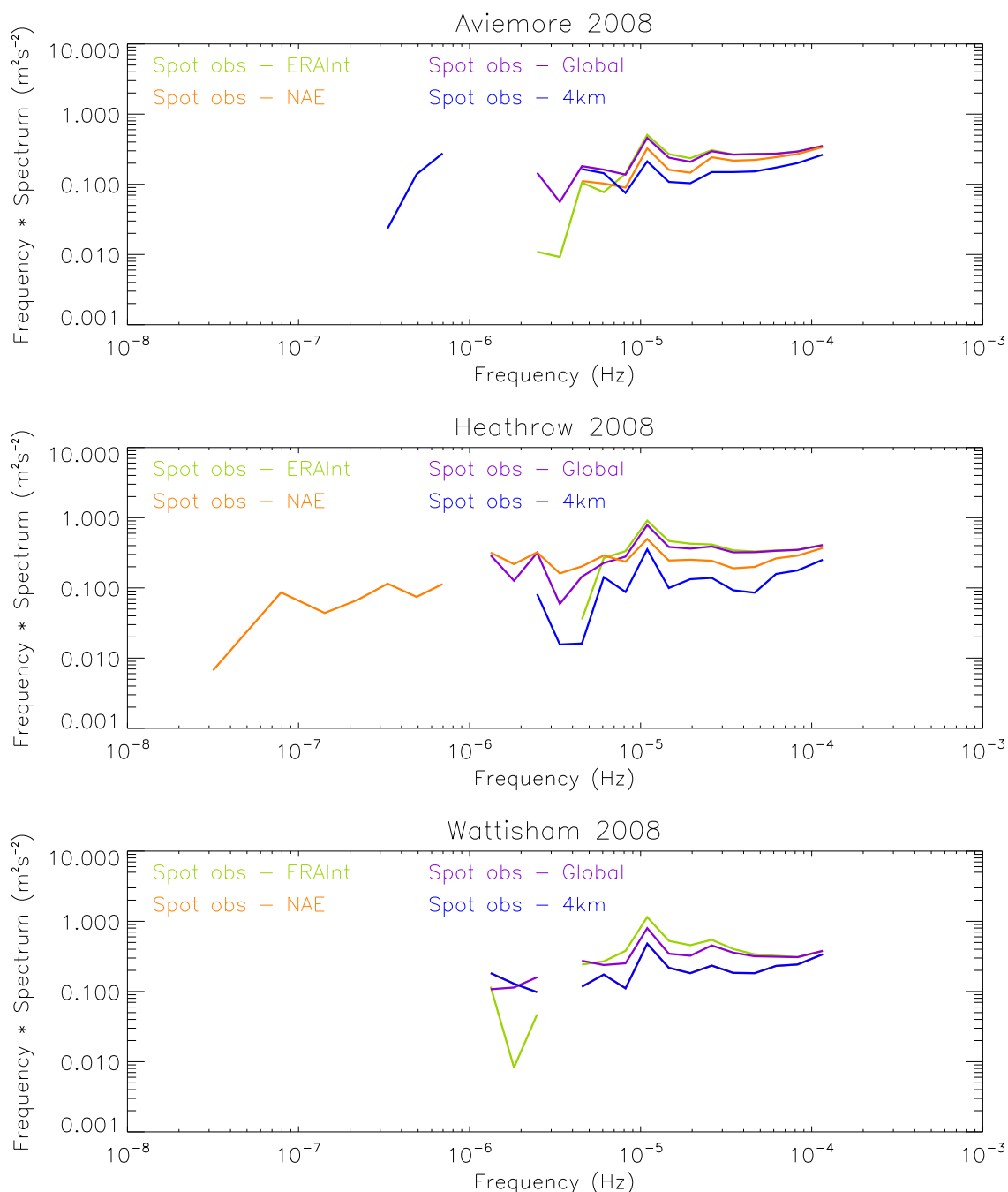


Figure 55: Difference in the observed and modelled spectra at a height of 10 m agl at Aviemore, Heathrow and Wattisham generated from 2008 hourly spot observations, MetUM data (global (40 km, 3 hourly), NAE (12 km, hourly) and 4km (4 km, hourly)) and ECMWF ERA Interim data (80 km, 3 hourly).

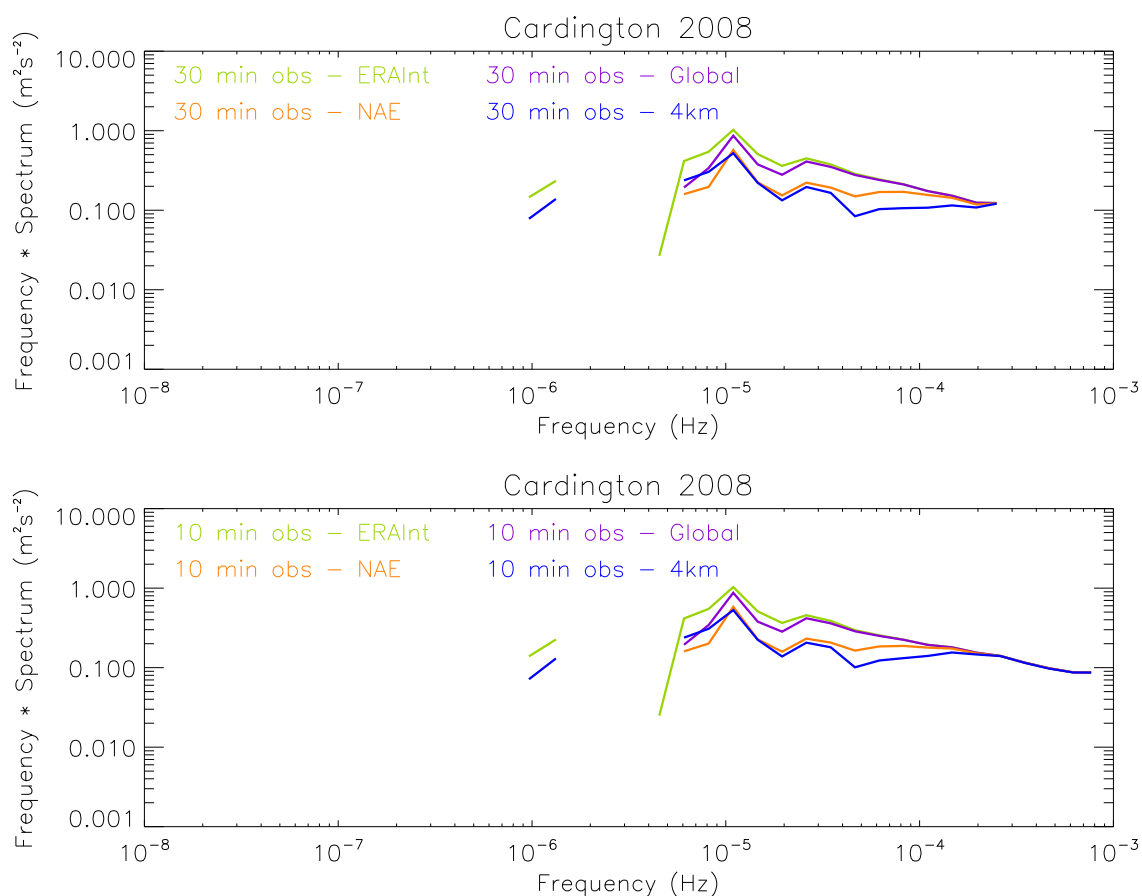


Figure 56: Difference in the observed and modelled spectra at a height of 10 m agl at Cardington generated from 2008 observations (30 minute and 10 minute), MetUM data (global (40 km, 3 hourly), NAE (12 km, hourly) and 4km (4 km, hourly)) and ECMWF ERA Interim data (80 km, 3 hourly).

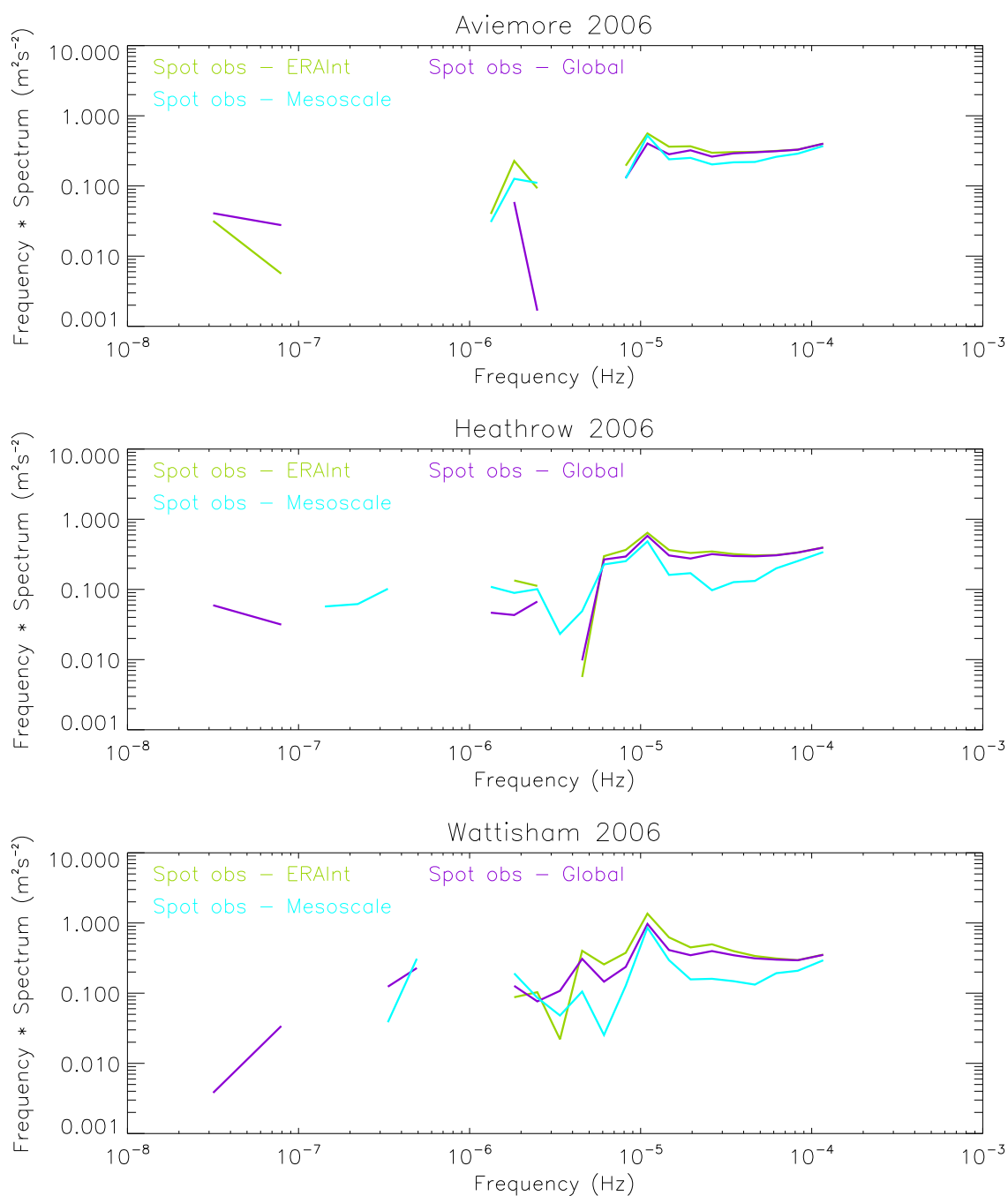


Figure 57: Difference in the observed and modelled spectra at a height of 10 m agl at Aviemore, Heathrow and Wattisham generated from 2006 hourly spot observations, MetUM data (global (40 km, 3 hourly) and mesoscale (12 km, hourly)) and ECMWF ERA Interim data (80 km, 3 hourly).

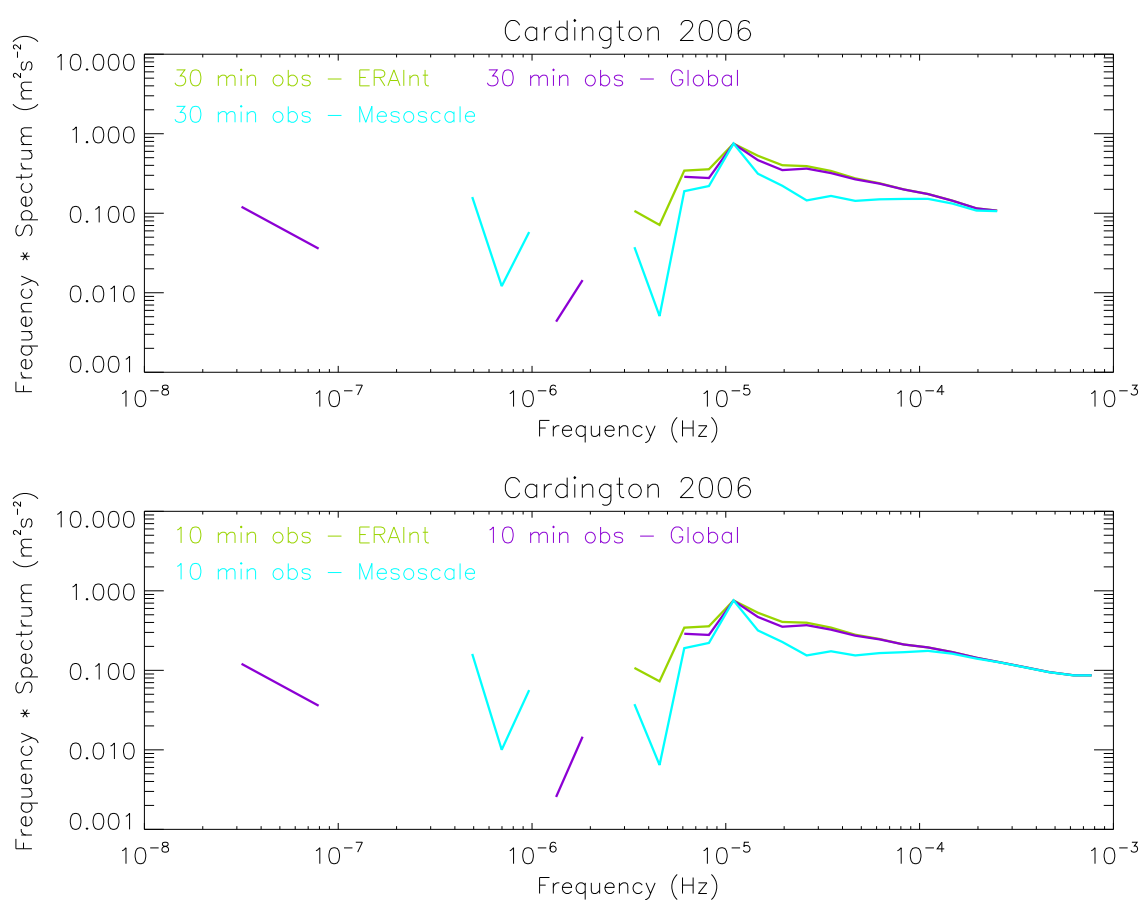


Figure 58: Difference in the observed and modelled spectra at a height of 10 m agl at Cardington generated from 2006 observations (30 minute and 10 minute), MetUM data (global (40 km, 3 hourly) and mesoscale (12 km, hourly)) and ECMWF ERA Interim data (80 km, 3 hourly).



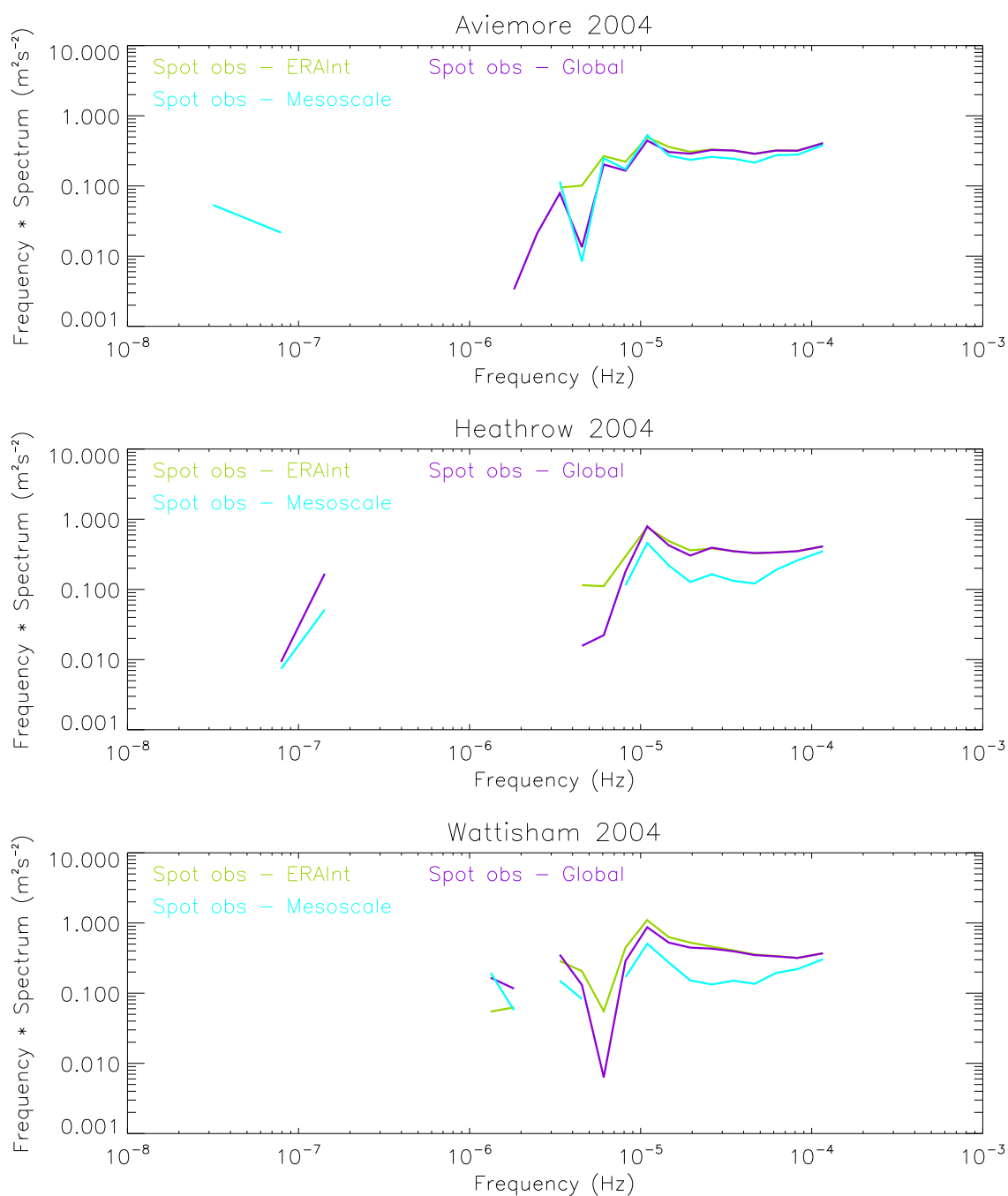


Figure 59: Difference in the observed and modelled spectra at a height of 10 m agl at Aviemore, Heathrow and Wattisham generated from 2004 hourly spot observations, MetUM data (global (60 km, 3 hourly) and mesoscale (12 km, hourly)) and ECMWF ERA Interim data (80 km, 3 hourly).

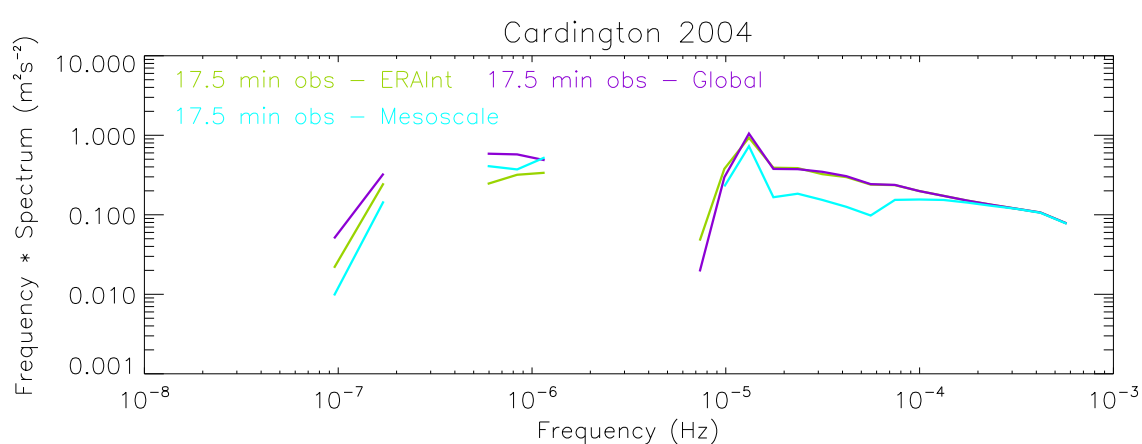


Figure 60: Difference in the observed and modelled spectra at a height of 10 m agl at Cardington generated from 2004 observations (17.5 minute), MetUM data (global (60 km, 3 hourly) and mesoscale (12 km, hourly)) and ECMWF ERA Interim data (80 km, 3 hourly).

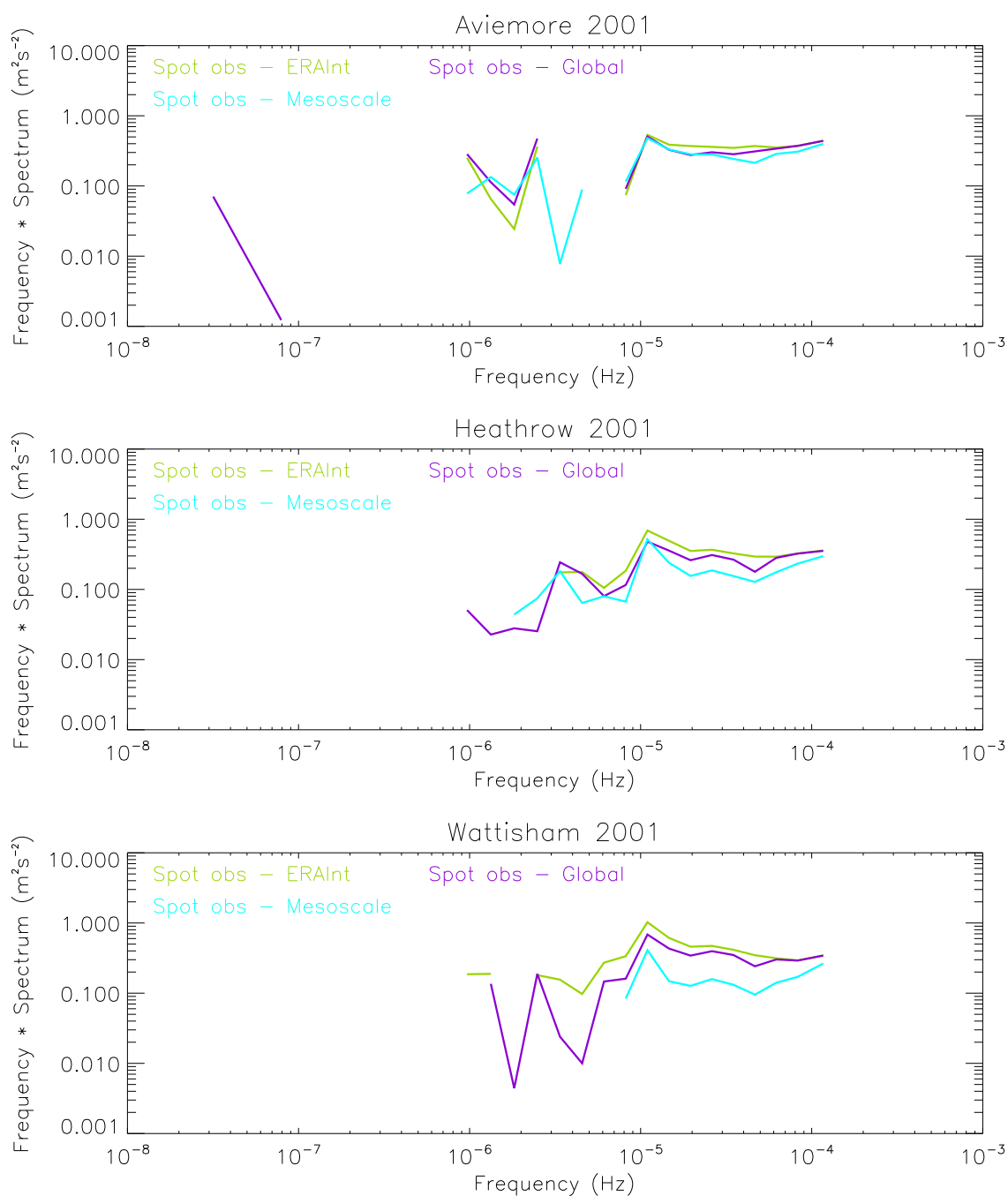


Figure 61: Difference in the observed and modelled spectra at a height of 10 m agl at Aviemoire, Heathrow and Wattisham generated from 2001 hourly spot observations, MetUM data (global (60 km, 3 hourly) and mesoscale (12 km, hourly)) and ECMWF ERA Interim data (80 km, 3 hourly).

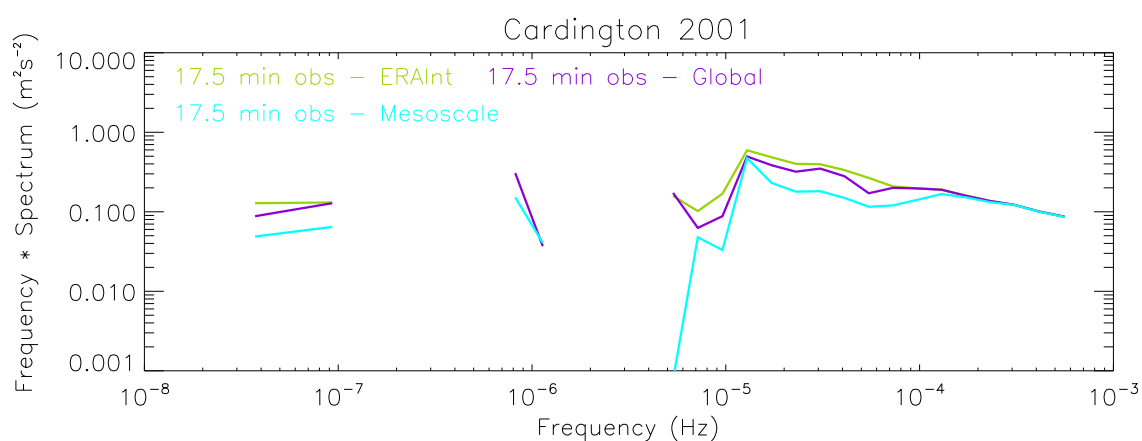


Figure 62: Difference in the observed and modelled spectra at a height of 10 m agl at Cardington generated from 2001 observations (17.5 minute), MetUM data (global (60 km, 3 hourly) and mesoscale (12 km, hourly)) and ECMWF ERA Interim data (80 km, 3 hourly).

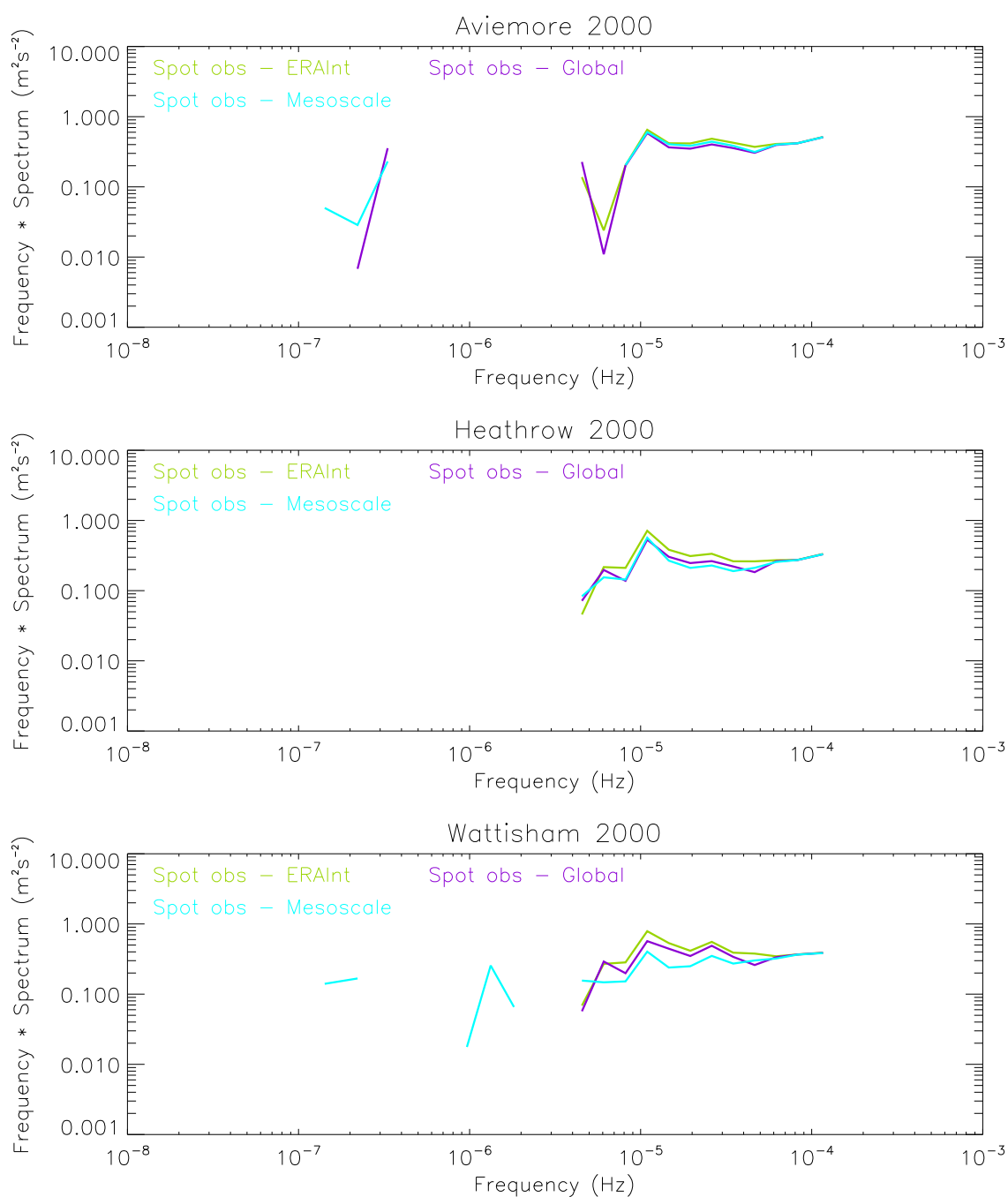


Figure 63: Difference in the observed and modelled spectra at a height of 10 m agl at Aviemore, Heathrow and Wattisham generated from 2000 hourly spot observations, MetUM data (global (60 km, 3 hourly) and mesoscale (12 km, 3 hourly)) and ECMWF ERA Interim data (80 km, 3 hourly).

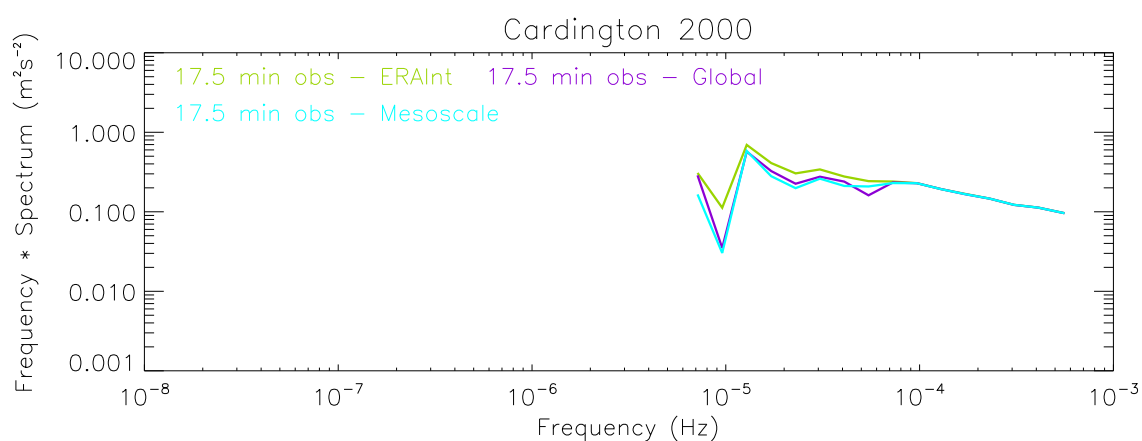


Figure 64: Difference in the observed and modelled spectra at a height of 10 m agl at Cardington generated from 2000 observations (17.5 minute), MetUM data (global (60 km, 3 hourly) and mesoscale (12 km, 3 hourly)) and ECMWF ERA Interim data (80 km, 3 hourly).

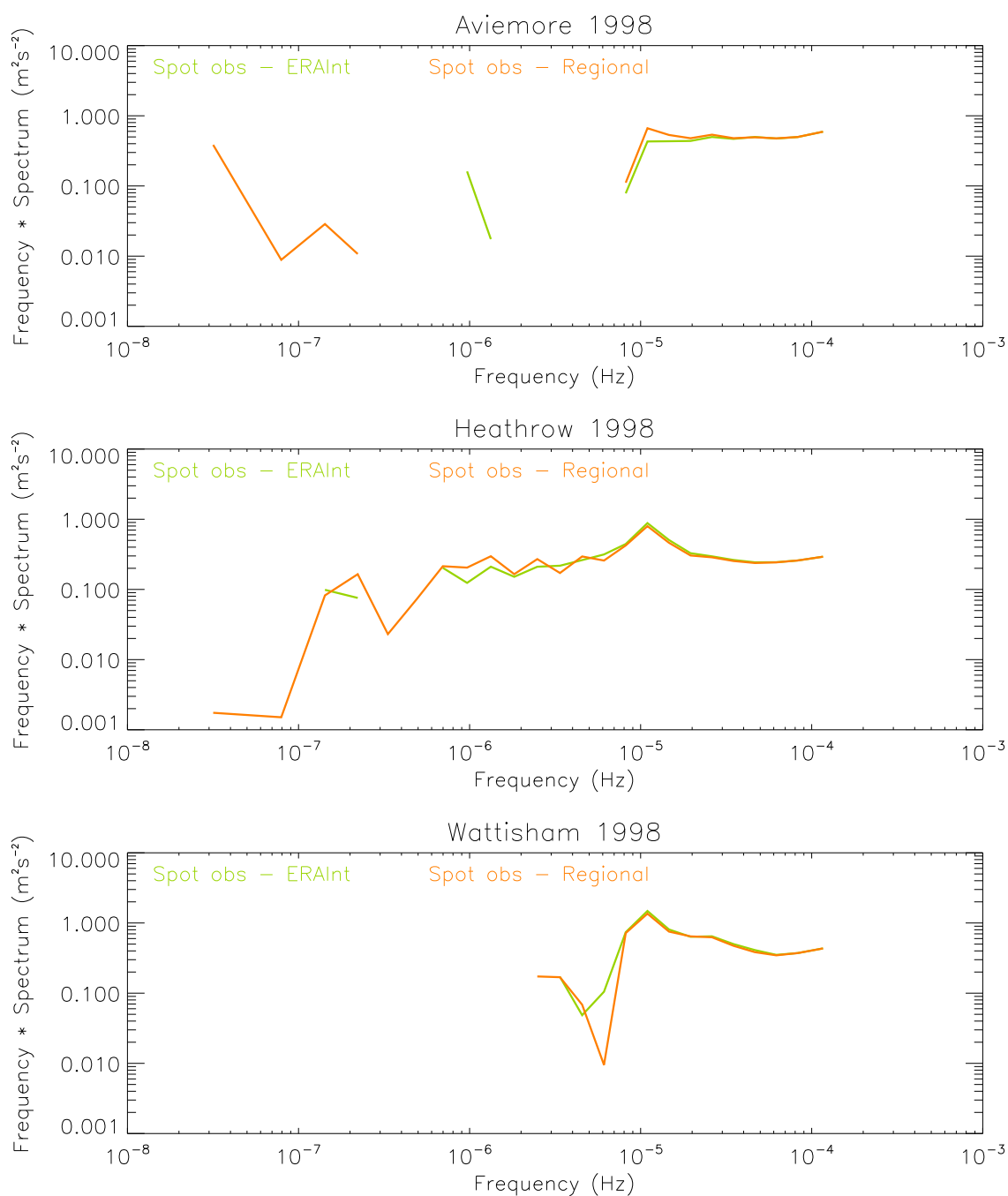


Figure 65: Difference in the observed and modelled spectra at a height of 10 m agl at Aviemoire, Heathrow and Wattisham generated from 1998 hourly spot observations, regional MetUM data (50 km, 3 hourly) and ECMWF ERA Interim data (80 km, 3 hourly).

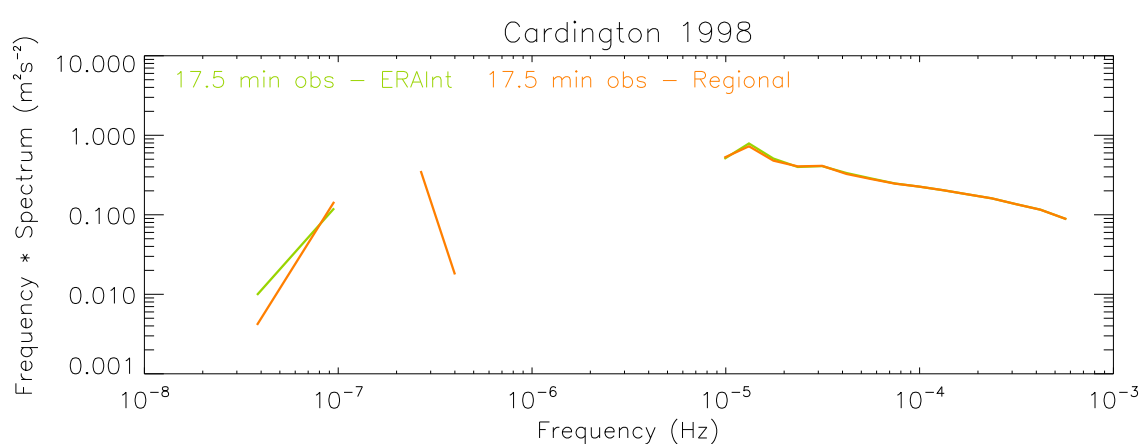


Figure 66: Difference in the observed and modelled spectra at a height of 10 m agl at Cardington generated from 1998 observations (17.5 minute), regional MetUM data (50 km, 3 hourly) and ECMWF ERA Interim data (80 km, 3 hourly).



## E Boundary layer correlation plots generated using observed and NWP winds

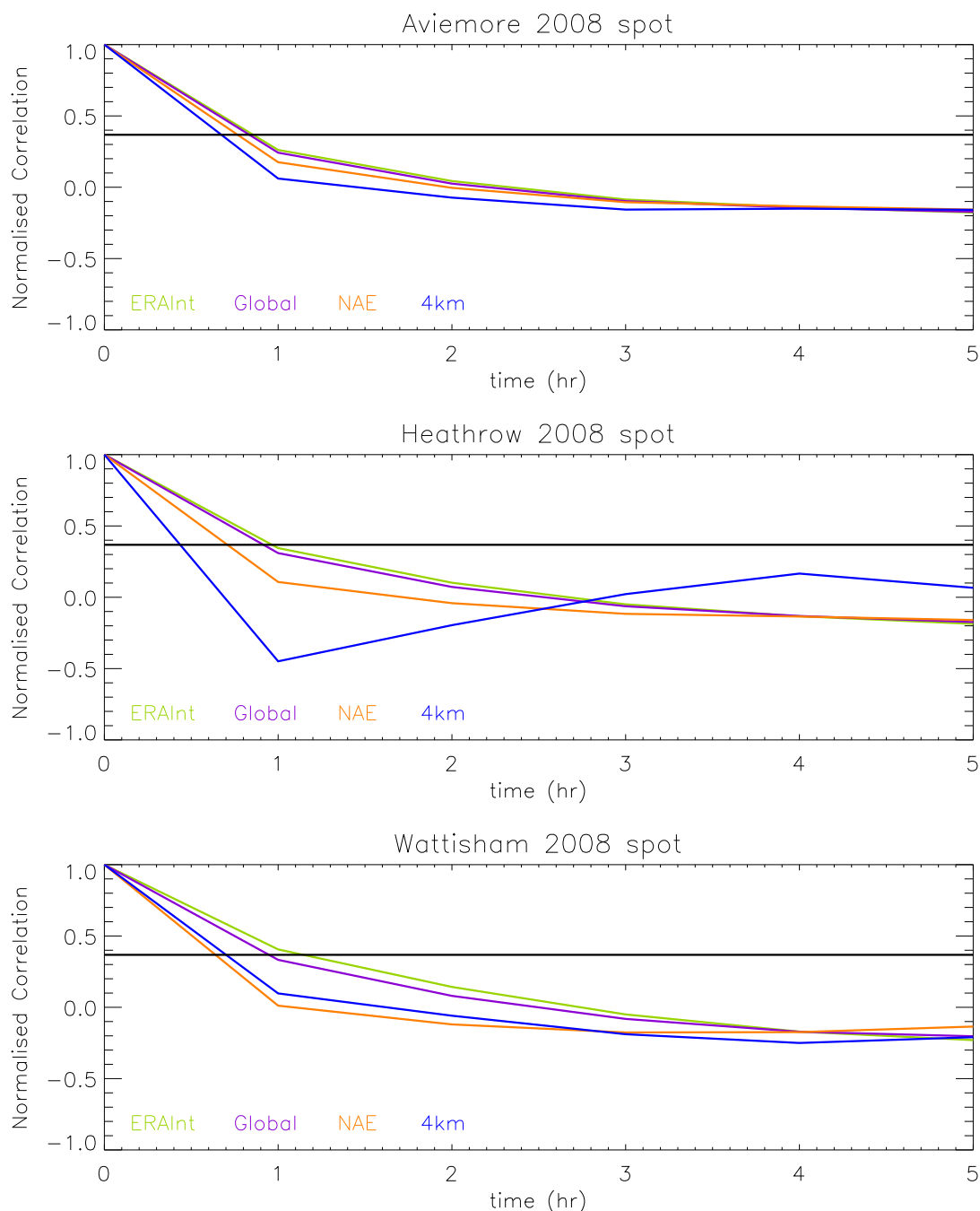


Figure 67: Normalised correlation functions for the unresolved mesoscale motions at a height of 10 m agl at Aviemoire, Heathrow and Wattisham, generated from 2008 observations (hourly spot), MetUM data (global (40 km, 3 hourly), NAE (12 km, hourly) and 4km (4 km, hourly)) and ECMWF ERA Interim data (80 km, 3 hourly). The  $1/e$  line (shown in black) is used to determine the timescale.

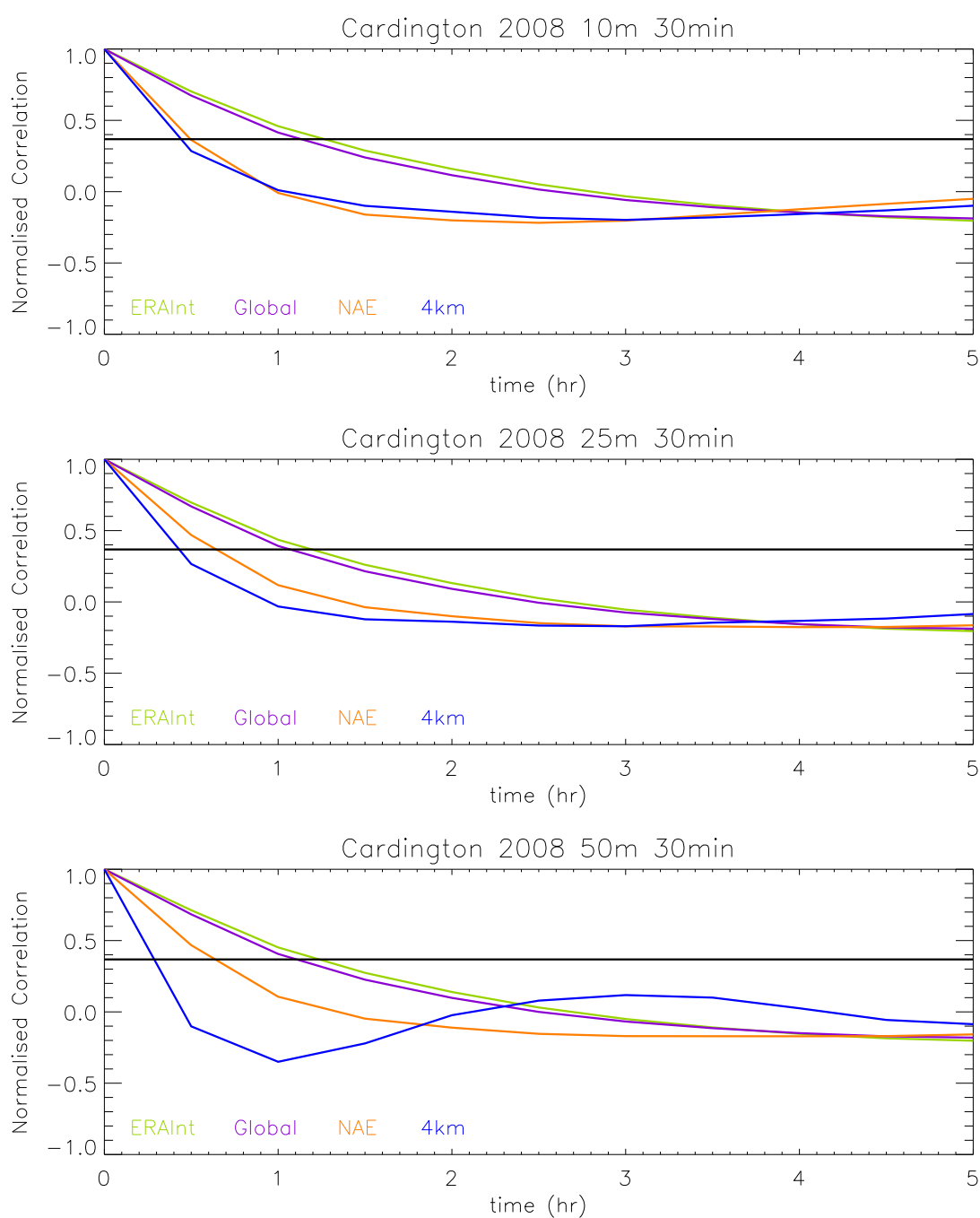


Figure 68: Normalised correlation functions for the unresolved mesoscale motions at heights of 10 m, 25 m and 50 m agl at Cardington, generated from 2008 observations (30 minute), MetUM data (global (40 km, 3 hourly), NAE (12 km, hourly) and 4km (4 km, hourly)) and ECMWF ERA Interim data (80 km, 3 hourly). The  $1/e$  line (shown in black) is used to determine the timescale.

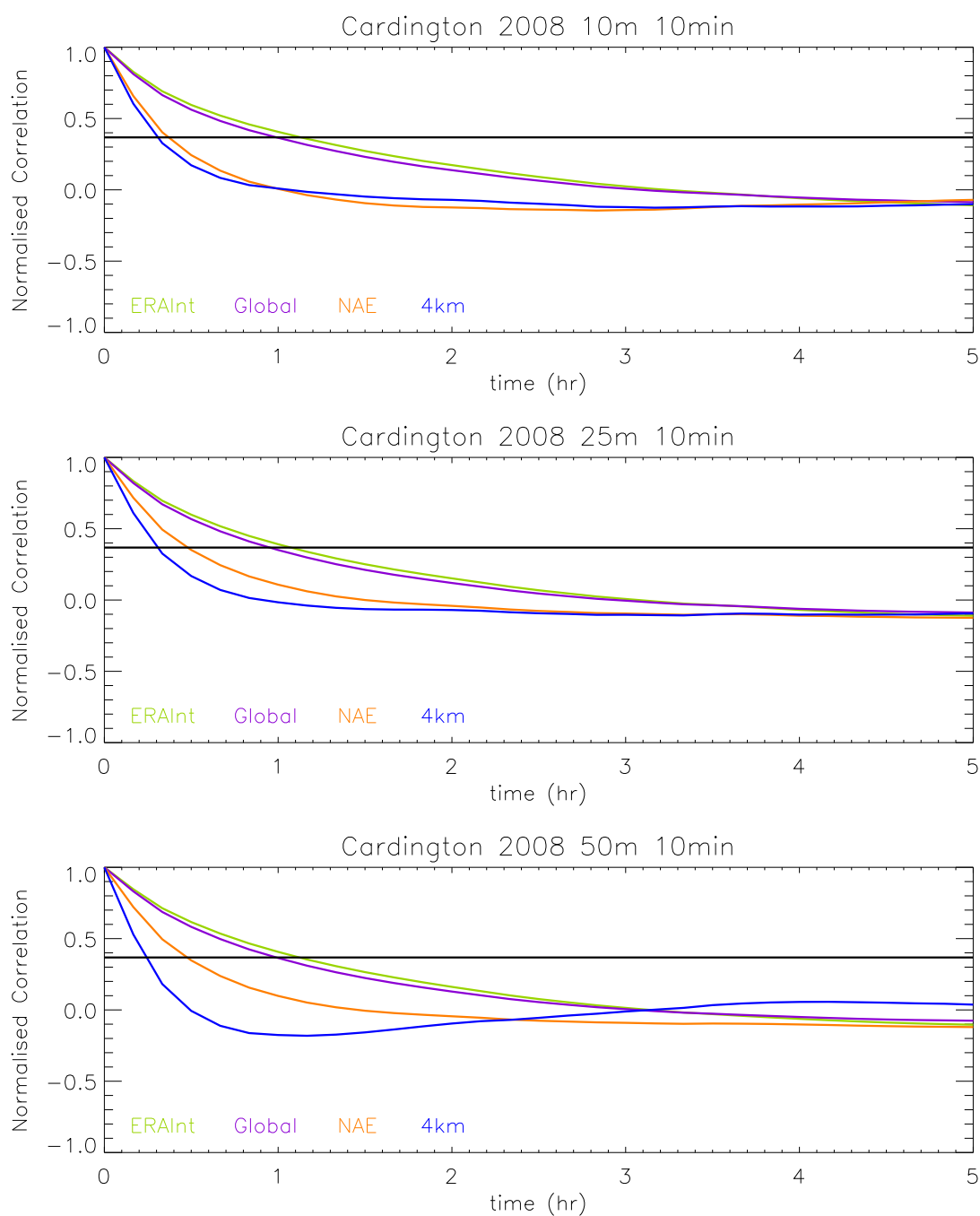


Figure 69: Normalised correlation functions for the unresolved mesoscale motions at heights of 10 m, 25 m and 50 m agl at Cardington, generated from 2008 observations (10 minute), MetUM data (global (40 km, 3 hourly), NAE (12 km, hourly) and 4km (4 km, hourly)) and ECMWF ERA Interim data (80 km, 3 hourly). The  $1/e$  line (shown in black) is used to determine the timescale.

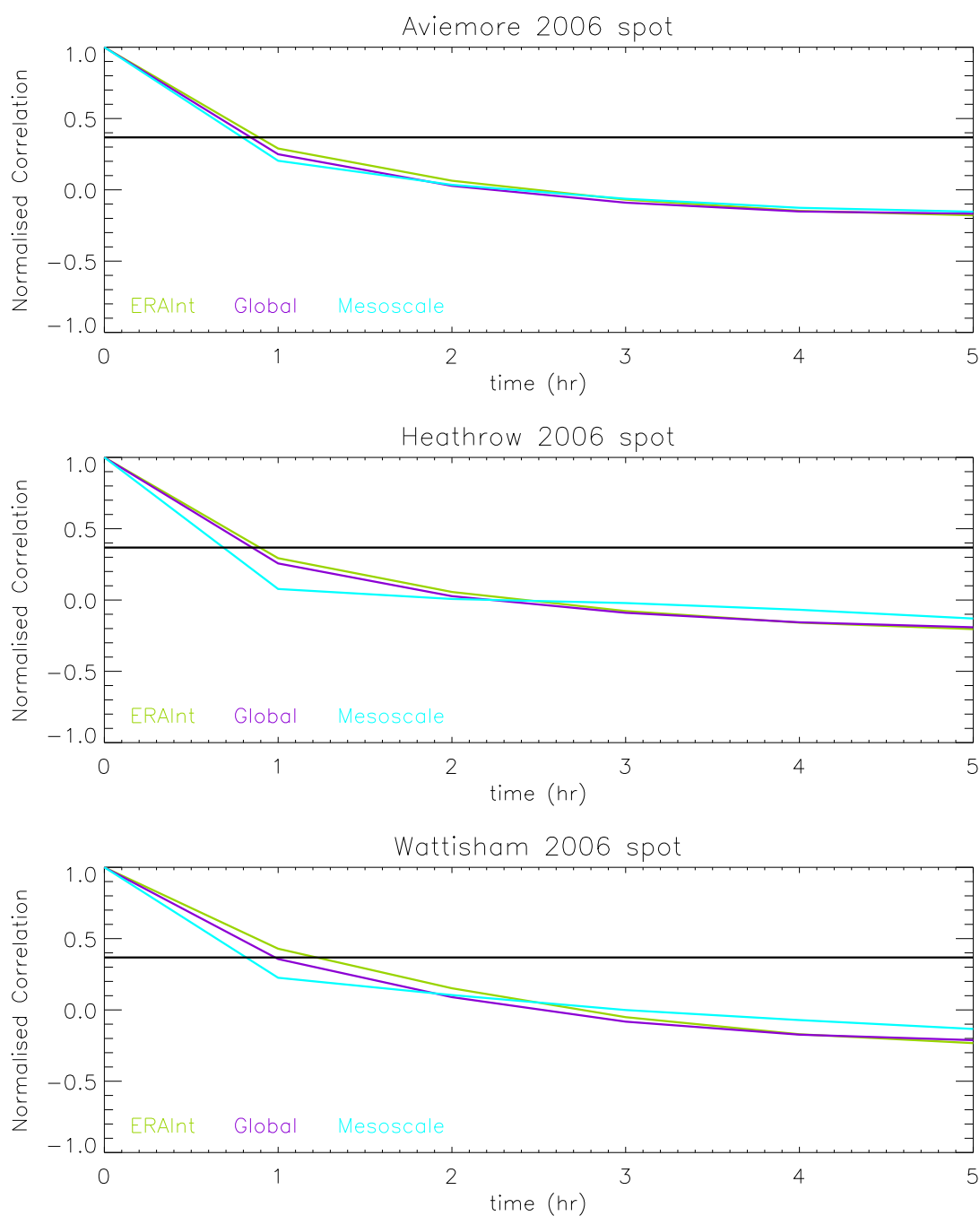


Figure 70: Normalised correlation functions for the unresolved mesoscale motions at a height of 10 m agl at Aviemoire, Heathrow and Wattisham, generated from 2006 observations (hourly spot), MetUM data (global (40 km, 3 hourly) and mesoscale (12 km, hourly)) and ECMWF ERA Interim data (80 km, 3 hourly). The  $1/e$  line (shown in black) is used to determine the timescale.

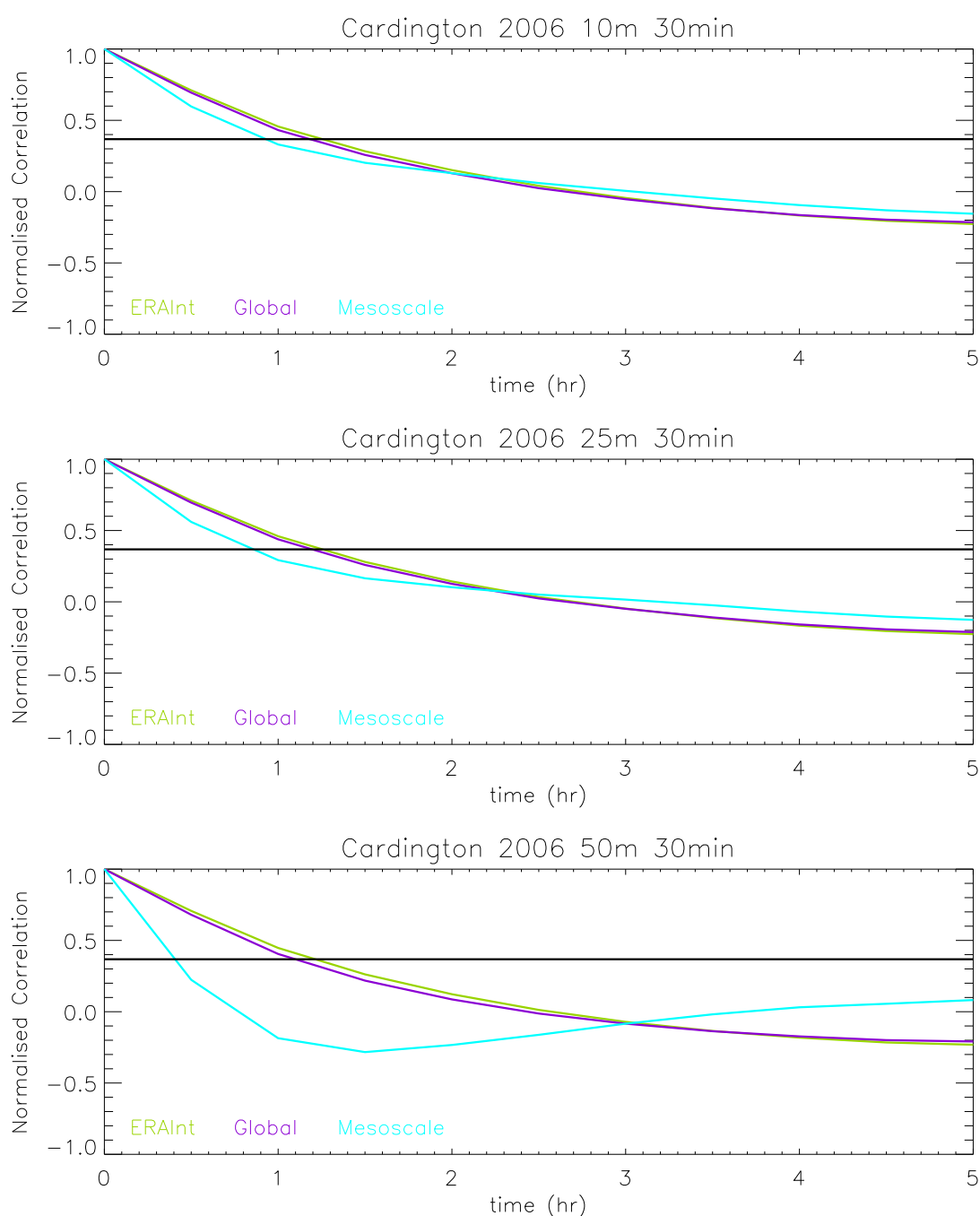


Figure 71: Normalised correlation functions for the unresolved mesoscale motions at heights of 10 m, 25 m and 50 m agl at Cardington, generated from 2006 observations (30 minute), MetUM data (global (40 km, 3 hourly) and mesoscale (12 km, hourly)) and ECMWF ERA Interim data (80 km, 3 hourly). The  $1/e$  line (shown in black) is used to determine the timescale.

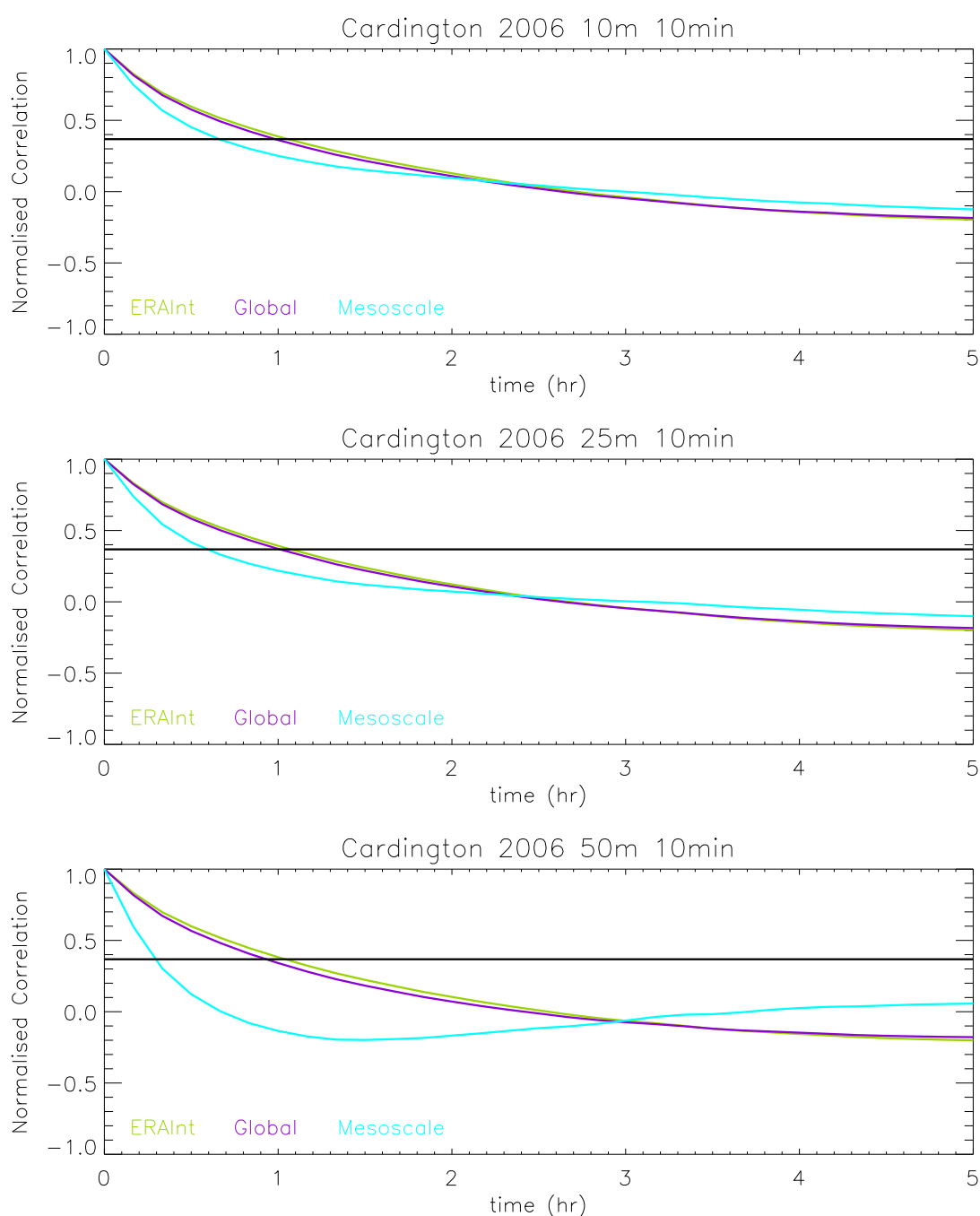


Figure 72: Normalised correlation functions for the unresolved mesoscale motions at heights of 10 m, 25 m and 50 m agl at Cardington, generated from 2006 observations (10 minute), MetUM data (global (40 km, 3 hourly) and mesoscale (12 km, hourly)) and ECMWF ERA Interim data (80 km, 3 hourly). The  $1/e$  line (shown in black) is used to determine the timescale.

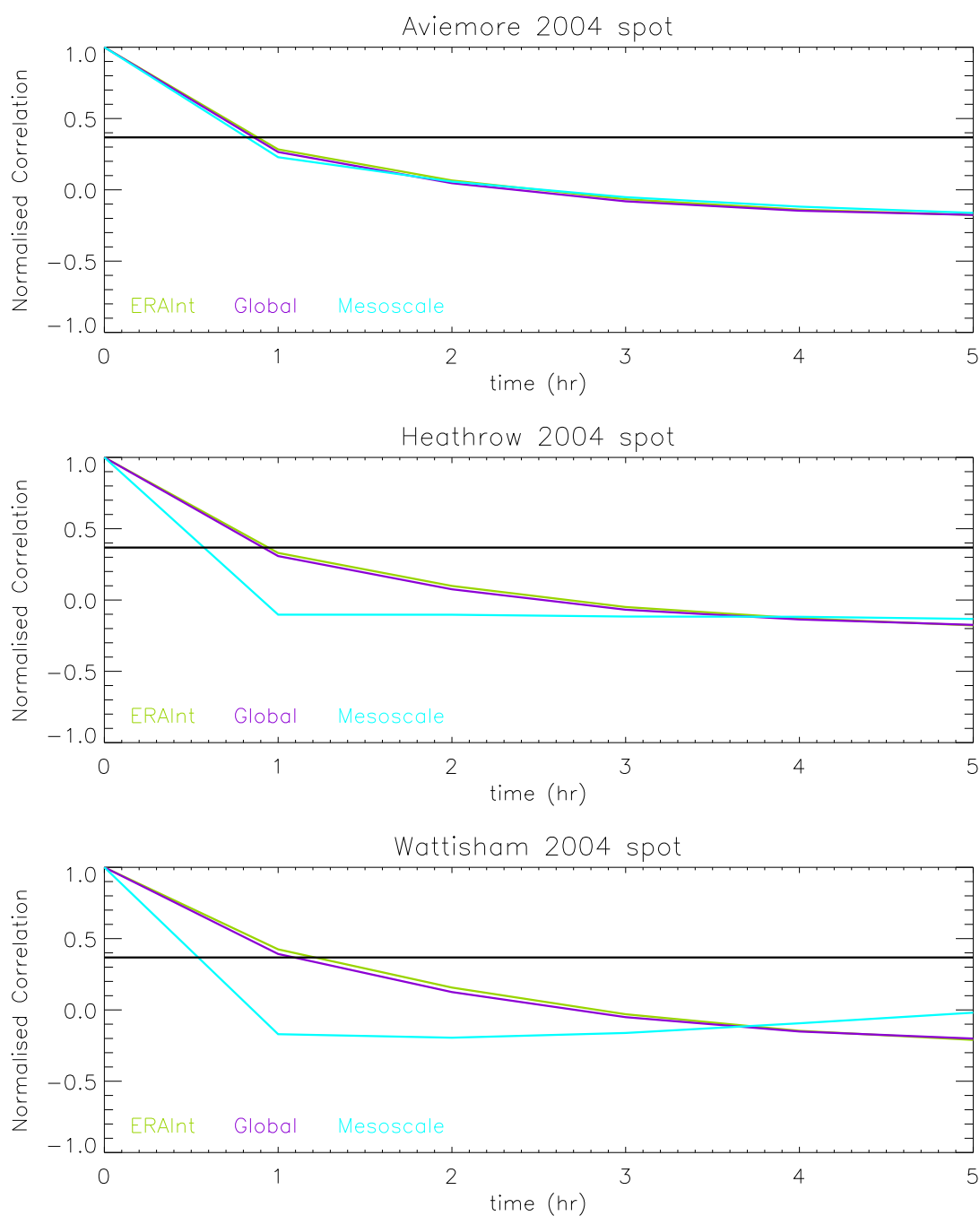


Figure 73: Normalised correlation functions for the unresolved mesoscale motions at a height of 10 m agl at Aviemoire, Heathrow and Wattisham, generated from 2004 observations (hourly spot), MetUM data (global (60 km, 3 hourly) and mesoscale (12 km, hourly)) and ECMWF ERA Interim data (80 km, 3 hourly). The  $1/e$  line (shown in black) is used to determine the timescale.

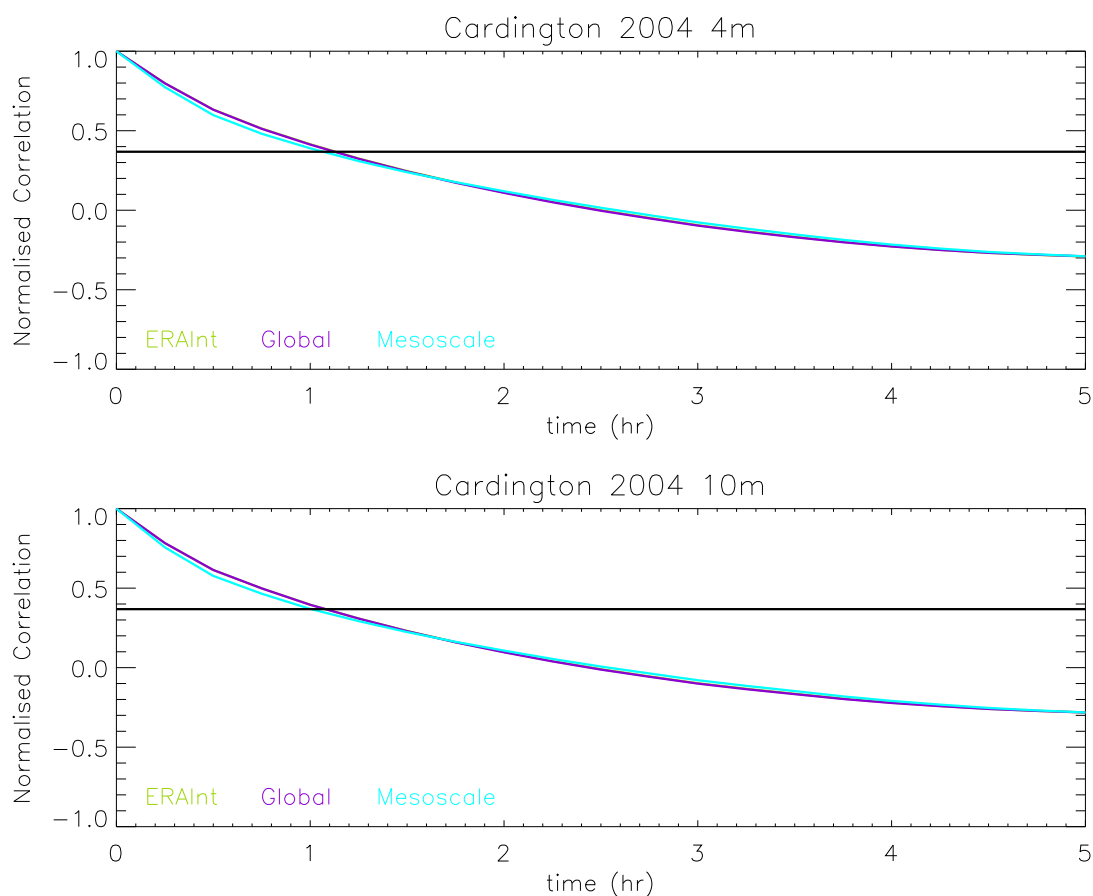


Figure 74: Normalised correlation functions for the unresolved mesoscale motions at heights of 4 m and 10 m agl at Cardington, generated from 2004 observations (17.5 minute), MetUM data (global (60 km, 3 hourly) and mesoscale (12 km, hourly)) and ECMWF ERA Interim data (80 km, 3 hourly). The  $1/e$  line (shown in black) is used to determine the timescale.



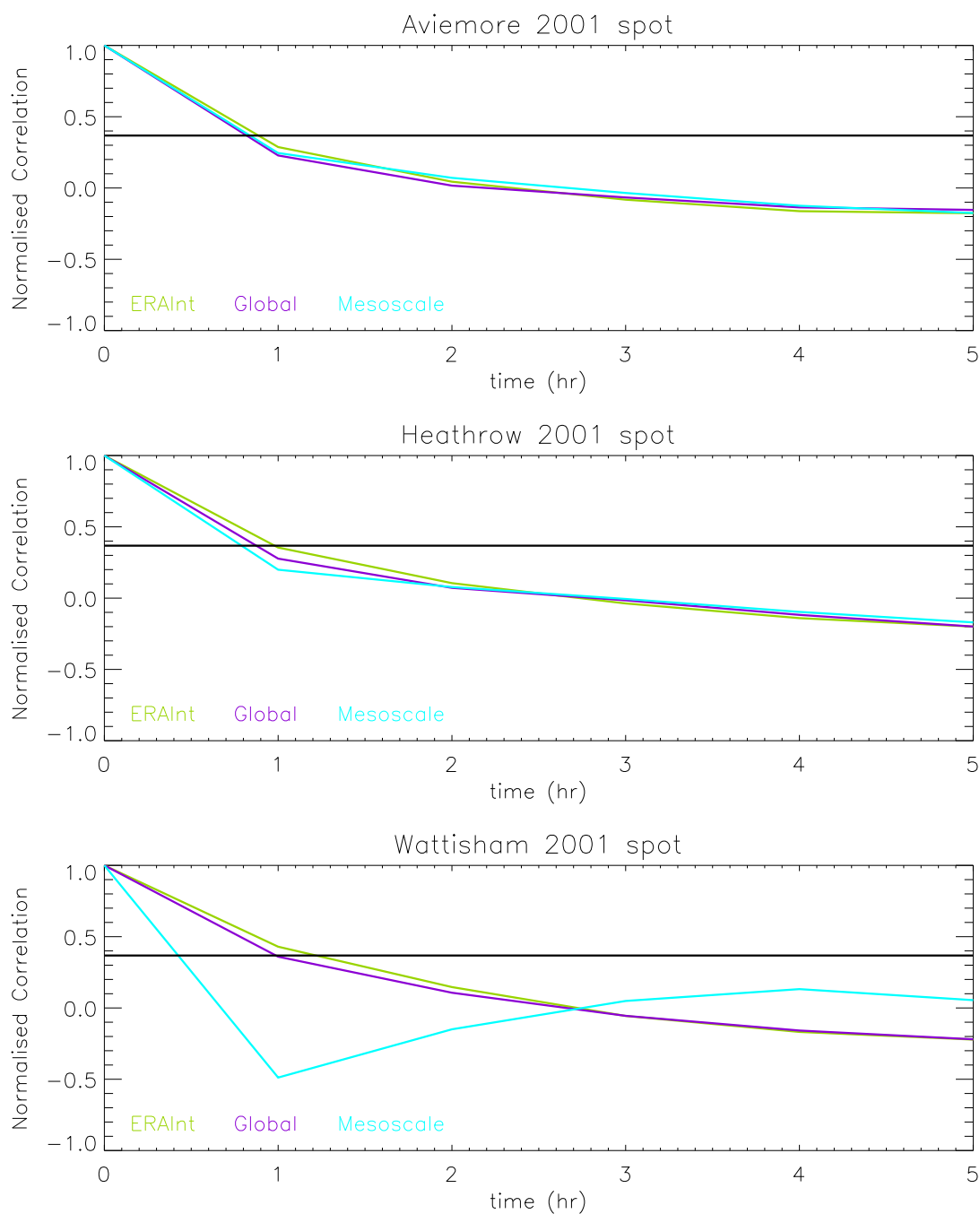


Figure 75: Normalised correlation functions for the unresolved mesoscale motions at a height of 10 m agl at Aviemoire, Heathrow and Wattisham, generated from 2001 observations (hourly spot), MetUM data (global (60 km, 3 hourly) and mesoscale (12 km, hourly)) and ECMWF ERA Interim data (80 km, 3 hourly). The  $1/e$  line (shown in black) is used to determine the timescale.

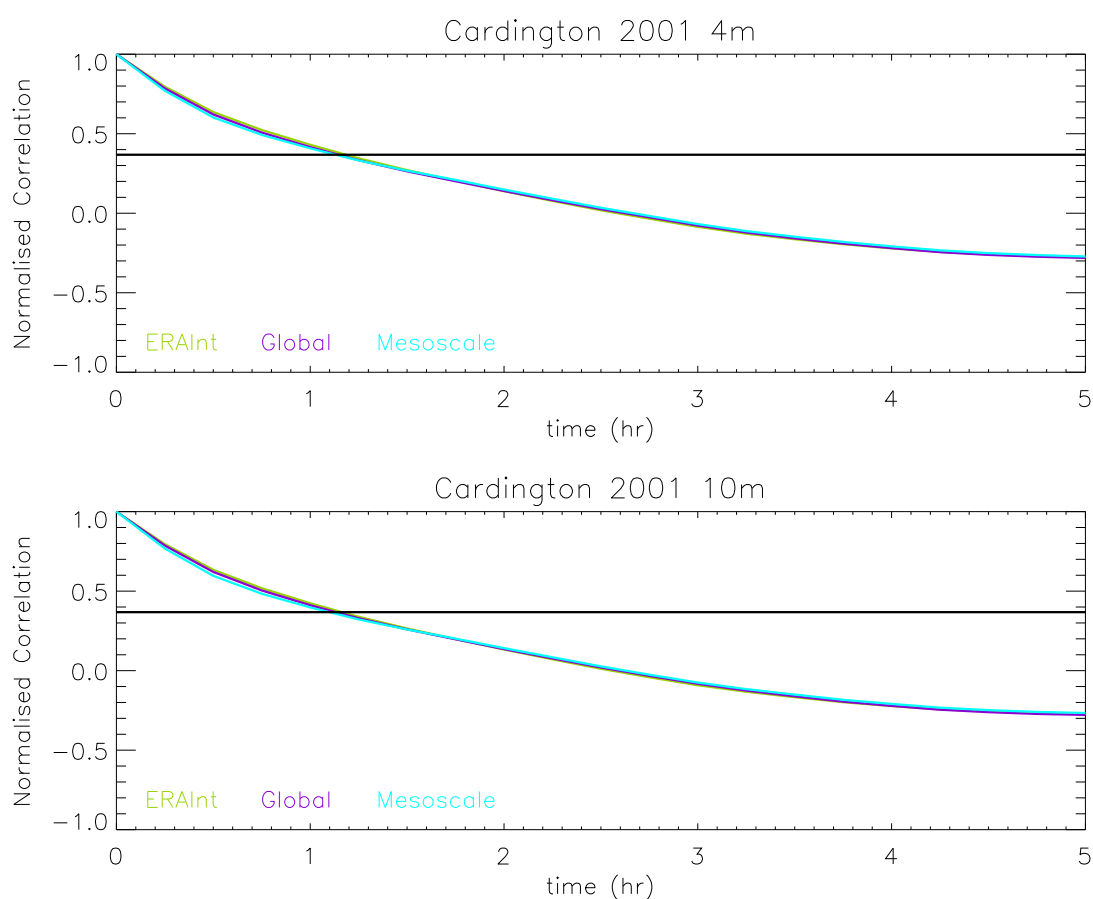


Figure 76: Normalised correlation functions for the unresolved mesoscale motions at heights of 4 m and 10 m agl at Cardington, generated from 2001 observations (17.5 minute), MetUM data (global (60 km, 3 hourly) and mesoscale (12 km, hourly)) and ECMWF ERA Interim data (80 km, 3 hourly). The  $1/e$  line (shown in black) is used to determine the timescale.

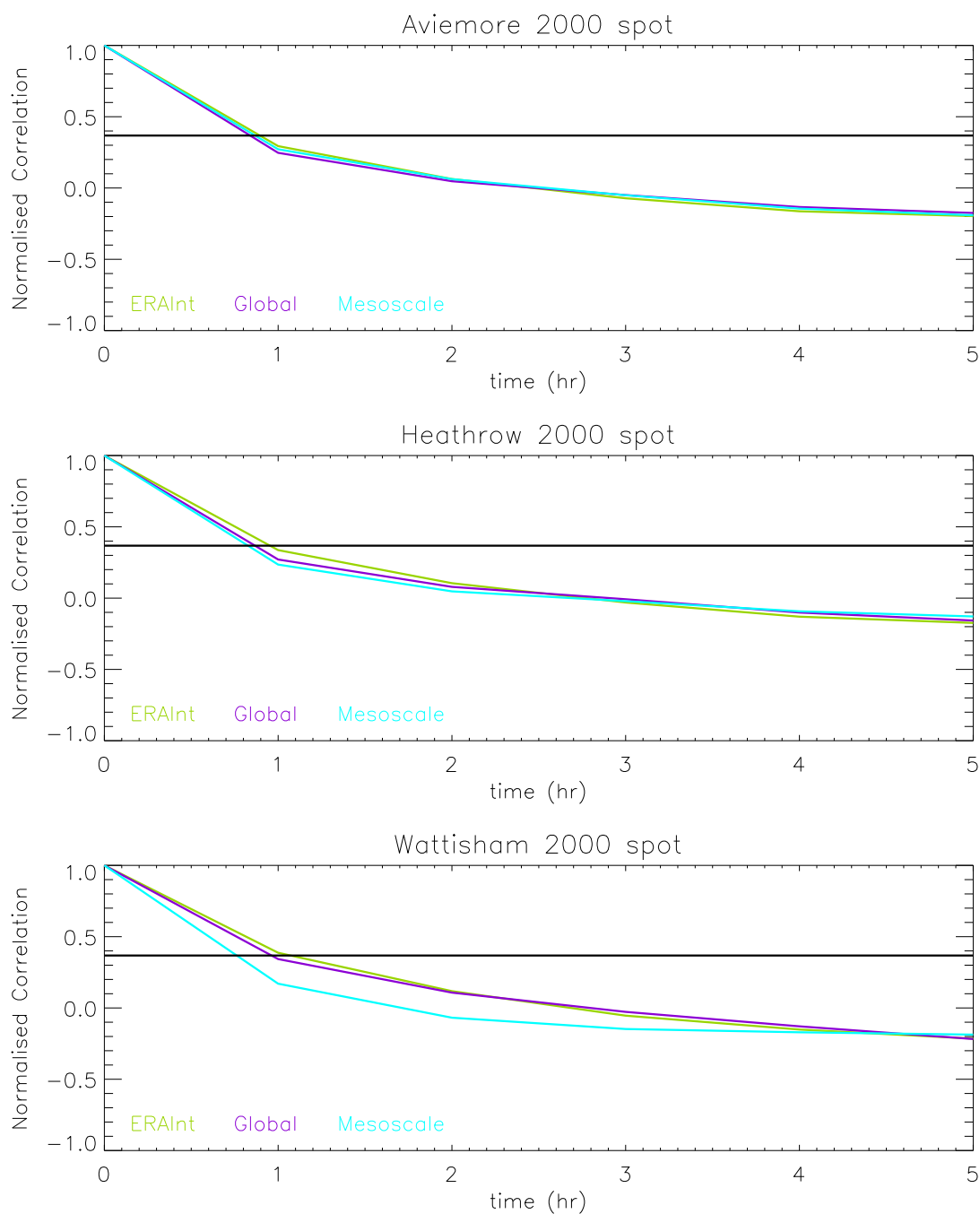


Figure 77: Normalised correlation functions for the unresolved mesoscale motions at a height of 10 m agl at Aviemoire, Heathrow and Wattisham, generated from 2000 observations (hourly spot), MetUM data (global (60 km, 3 hourly) and mesoscale (12 km, 3 hourly)) and ECMWF ERA Interim data (80 km, 3 hourly). The  $1/e$  line (shown in black) is used to determine the timescale.

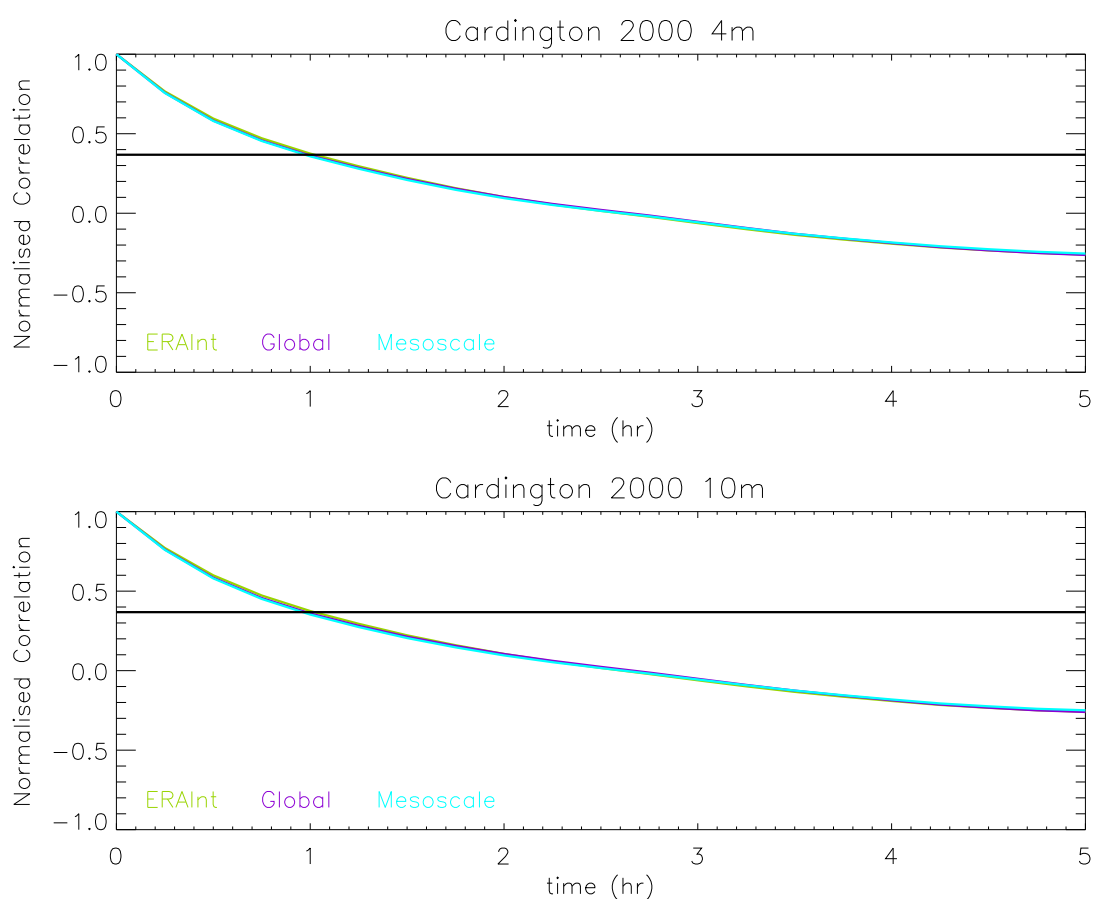


Figure 78: Normalised correlation functions for the unresolved mesoscale motions at heights of 4 m and 10 m agl at Cardington, generated from 2000 observations (17.5 minute), MetUM data (global (60 km, 3 hourly) and mesoscale (12 km, 3 hourly)) and ECMWF ERA Interim data (80 km, 3 hourly). The  $1/e$  line (shown in black) is used to determine the timescale.

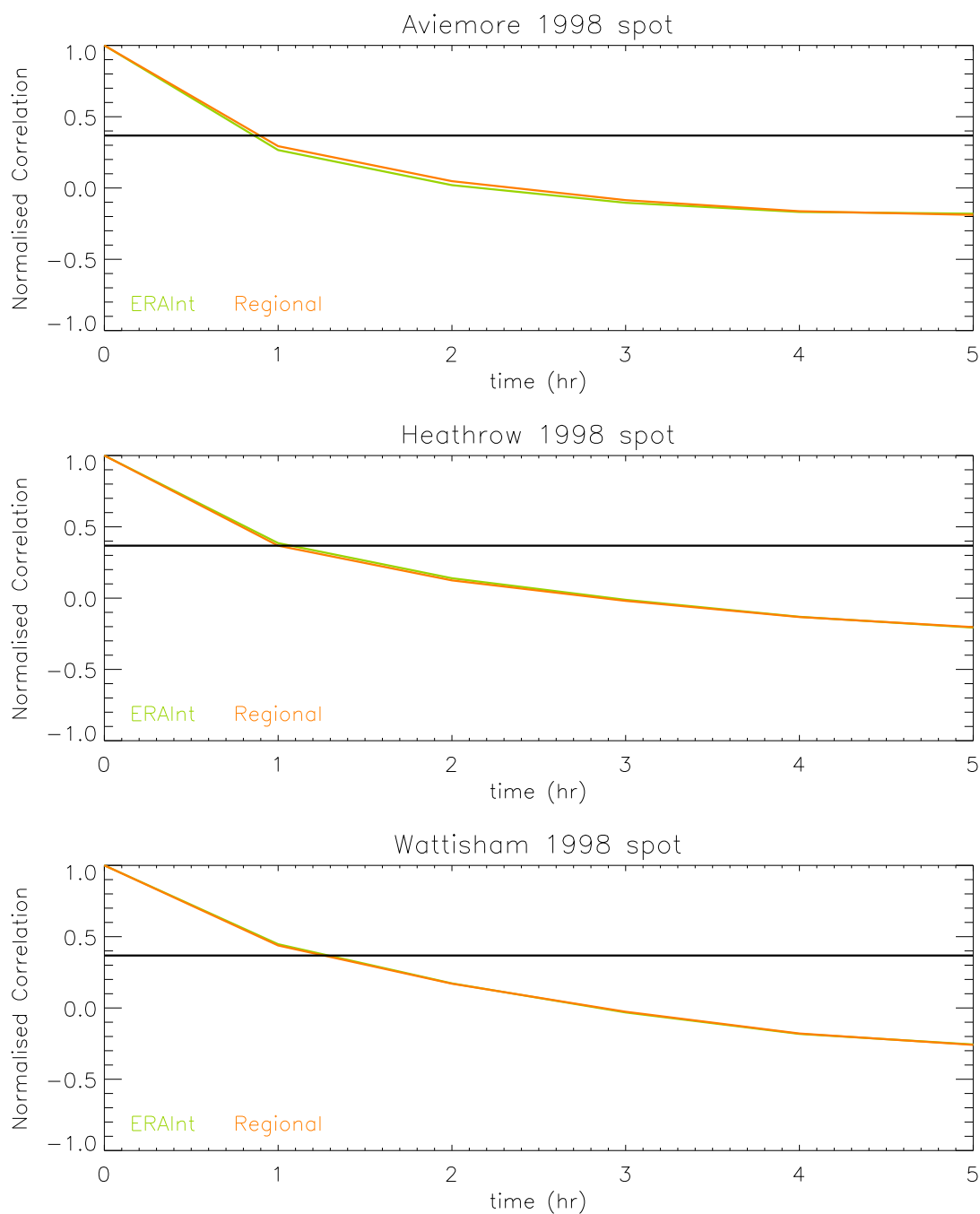


Figure 79: Normalised correlation functions for the unresolved mesoscale motions at a height of 10 m agl at Aviemore, Heathrow and Wattisham, generated from 1998 observations (hourly spot), regional MetUM data (50 km, 3 hourly) and ECMWF ERA Interim data (80 km, 3 hourly). The  $1/e$  line (shown in black) is used to determine the timescale.

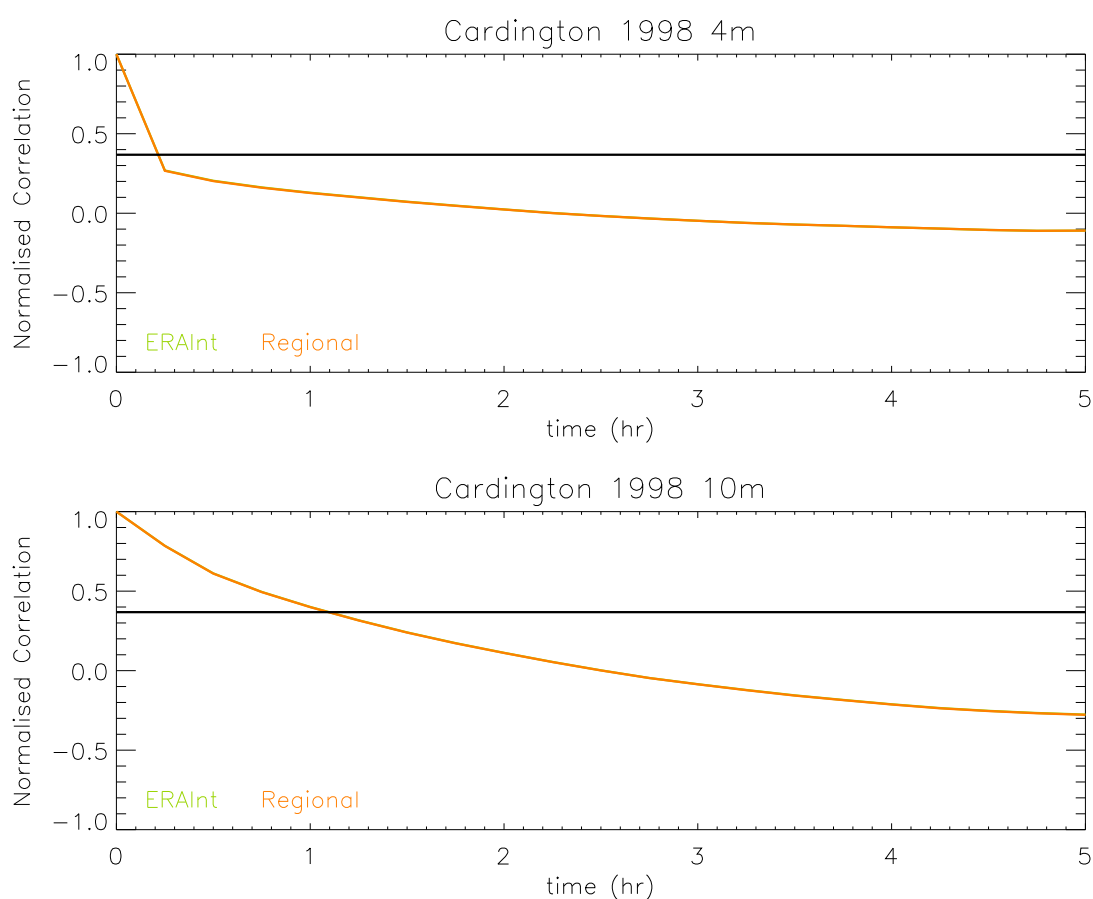


Figure 80: Normalised correlation functions for the unresolved mesoscale motions at heights of 4 m and 10 m agl at Cardington, generated from 1998 observations (17.5 minute), regional MetUM data (50 km, 3 hourly) and ECMWF ERA Interim data (80 km, 3 hourly). The  $1/e$  line (shown in black) is used to determine the timescale.

## F Free tropospheric spectral plots

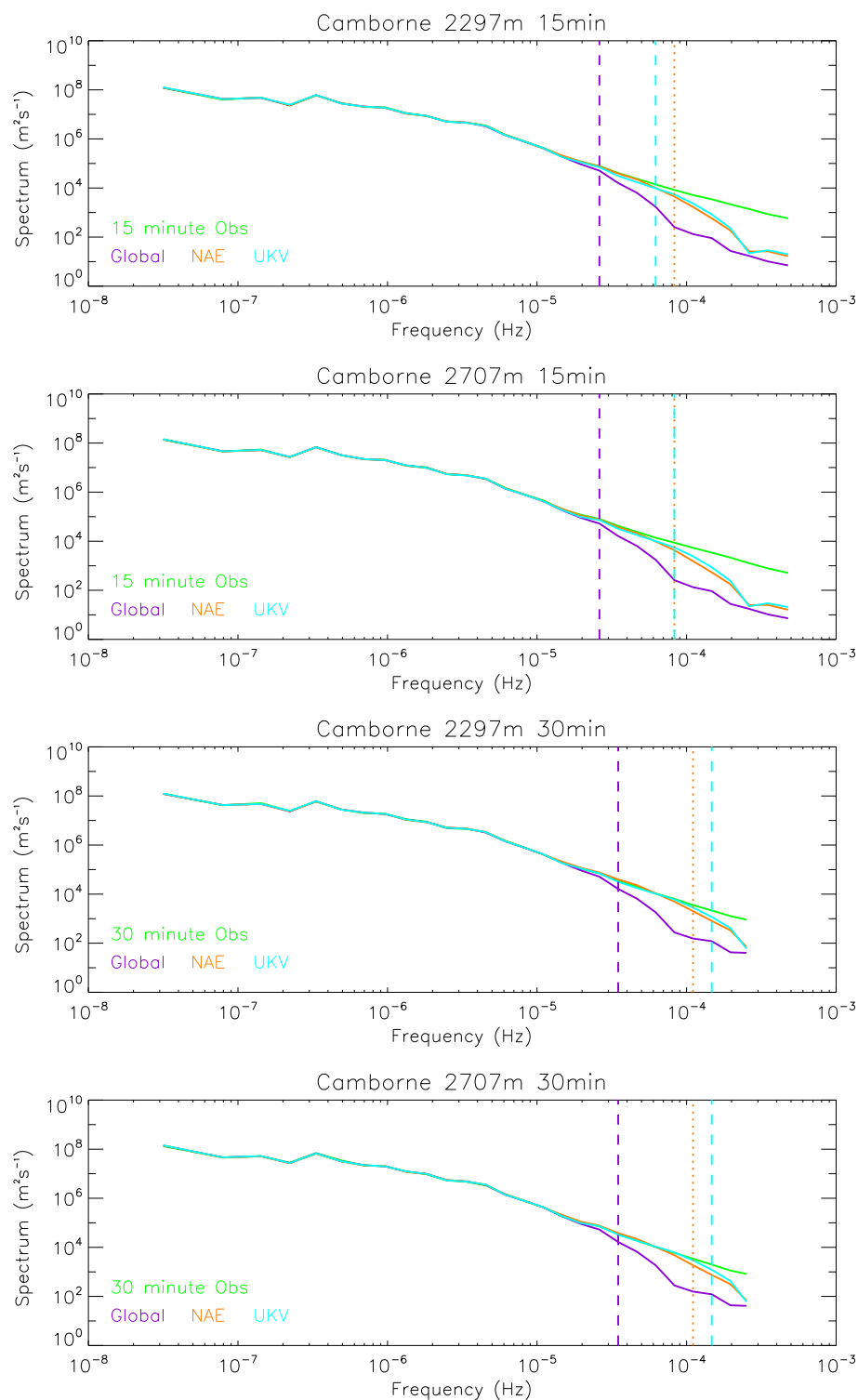


Figure 81: Spectra at Camborne generated from wind profiler observations (15 and 30 minute means) and MetUM data (global (25 km, 3 hourly), NAE (12 km, hourly) and UKV (1.5 km, hourly)).

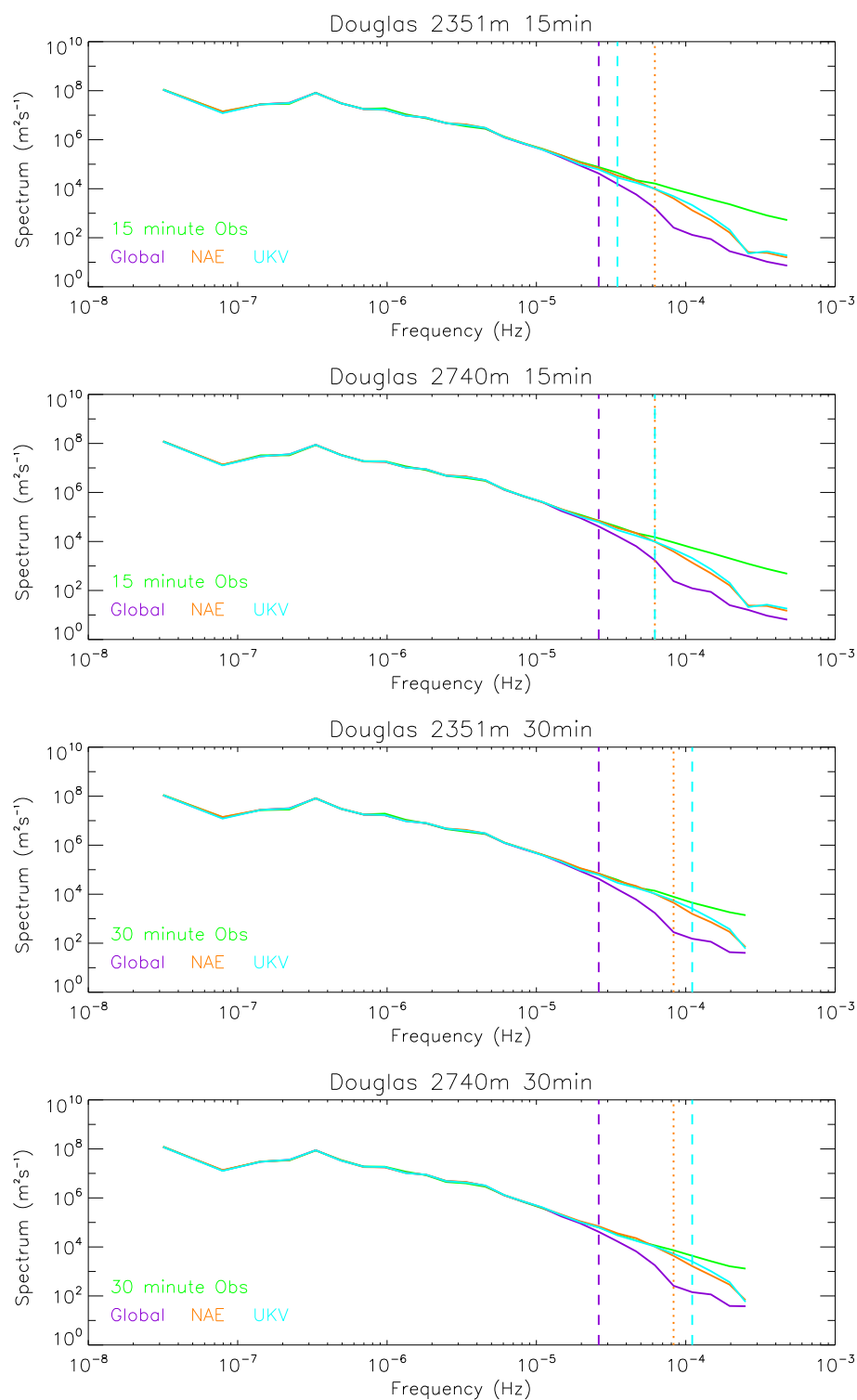


Figure 82: Spectra at Douglas generated from wind profiler observations (15 and 30 minute means) and MetUM data (global (25 km, 3 hourly), NAE (12 km, hourly) and UKV (1.5 km, hourly)).



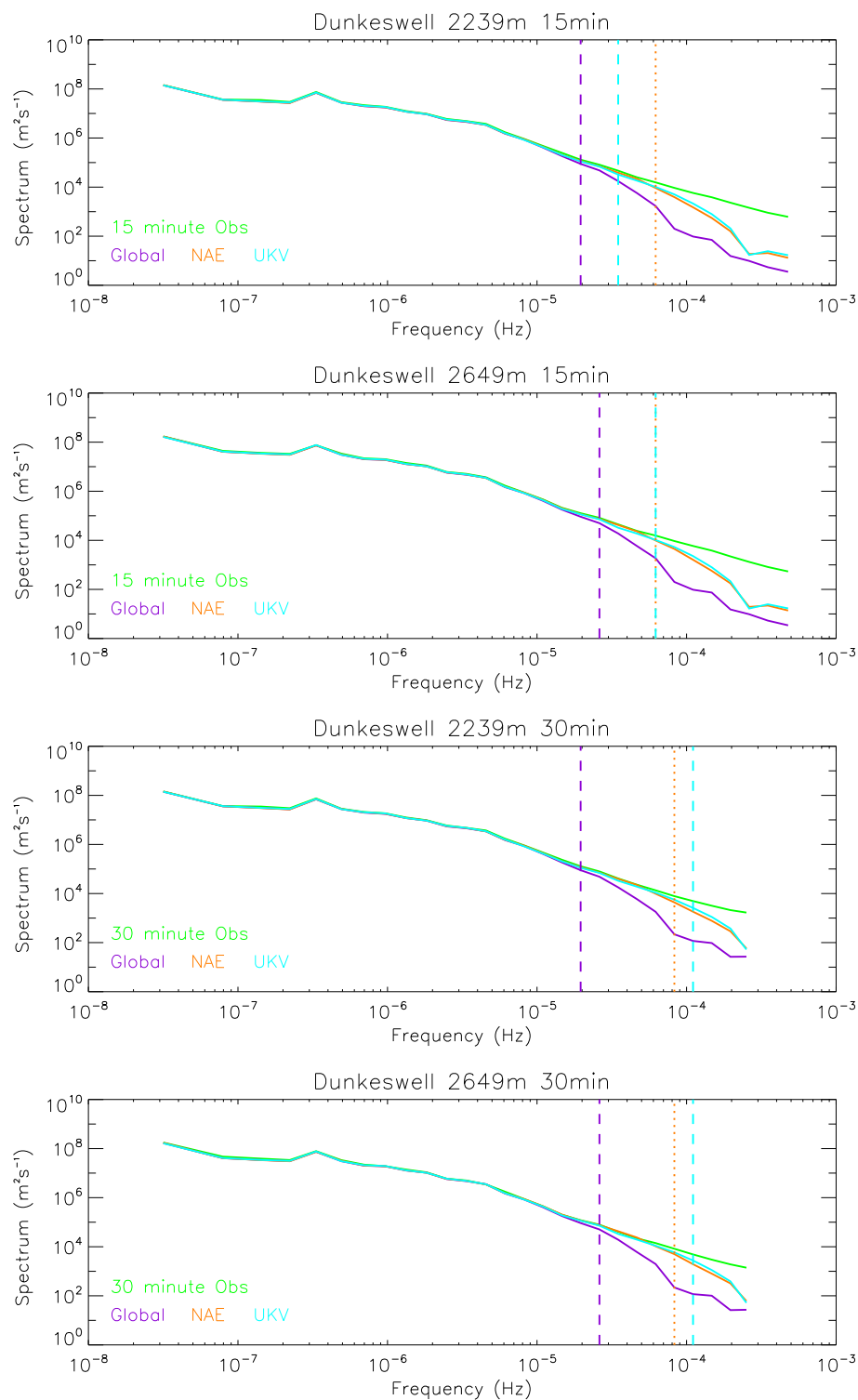


Figure 83: Spectra at Dunkeswell generated from wind profiler observations (15 and 30 minute means) and MetUM data (global (25 km, 3 hourly), NAE (12 km, hourly) and UKV (1.5 km, hourly)).

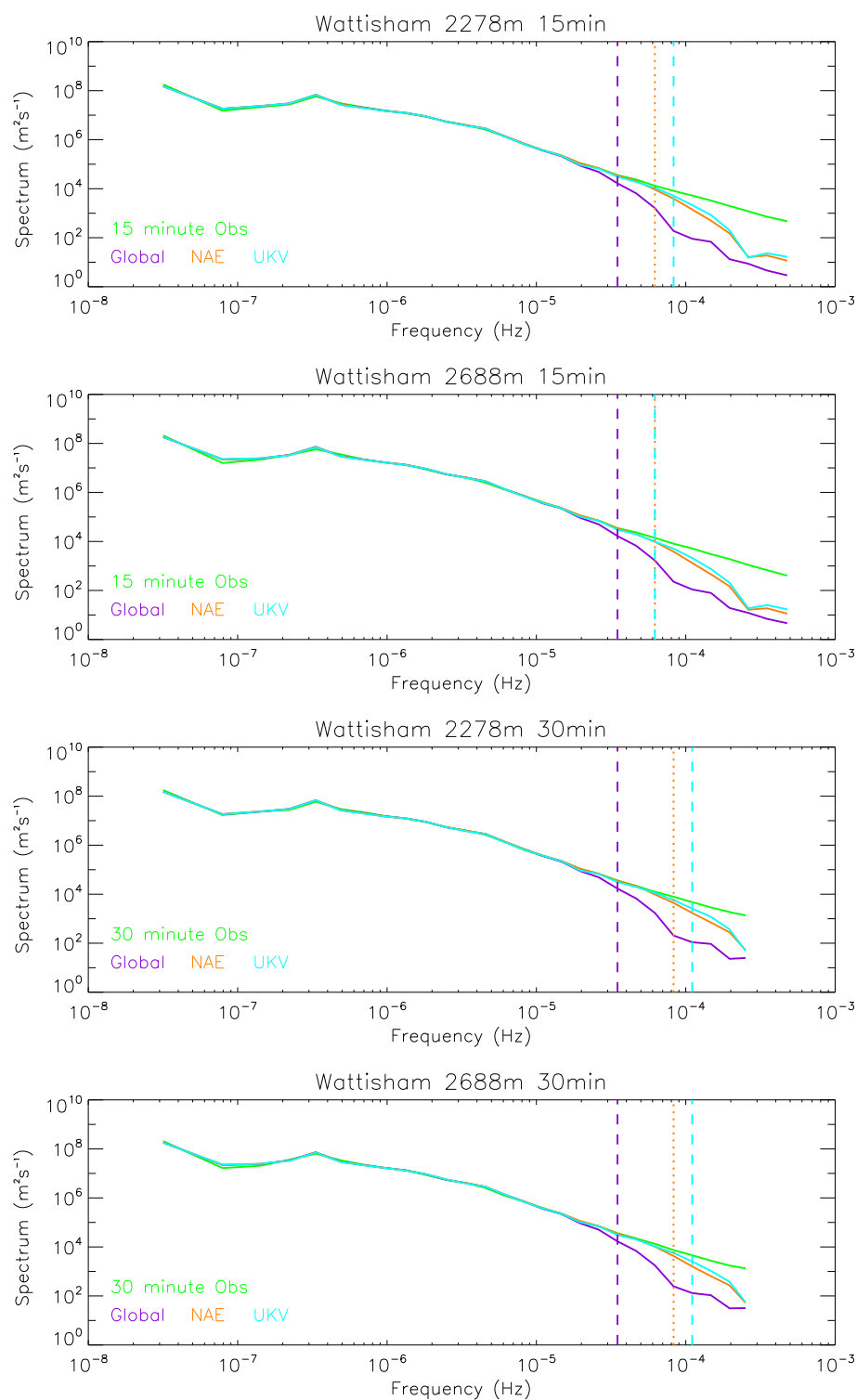


Figure 84: Spectra at Wattisham generated from wind profiler observations (15 and 30 minute means) and MetUM data (global (25 km, 3 hourly), NAE (12 km, hourly) and UKV (1.5 km, hourly)).

## G Free tropospheric fractional difference plots

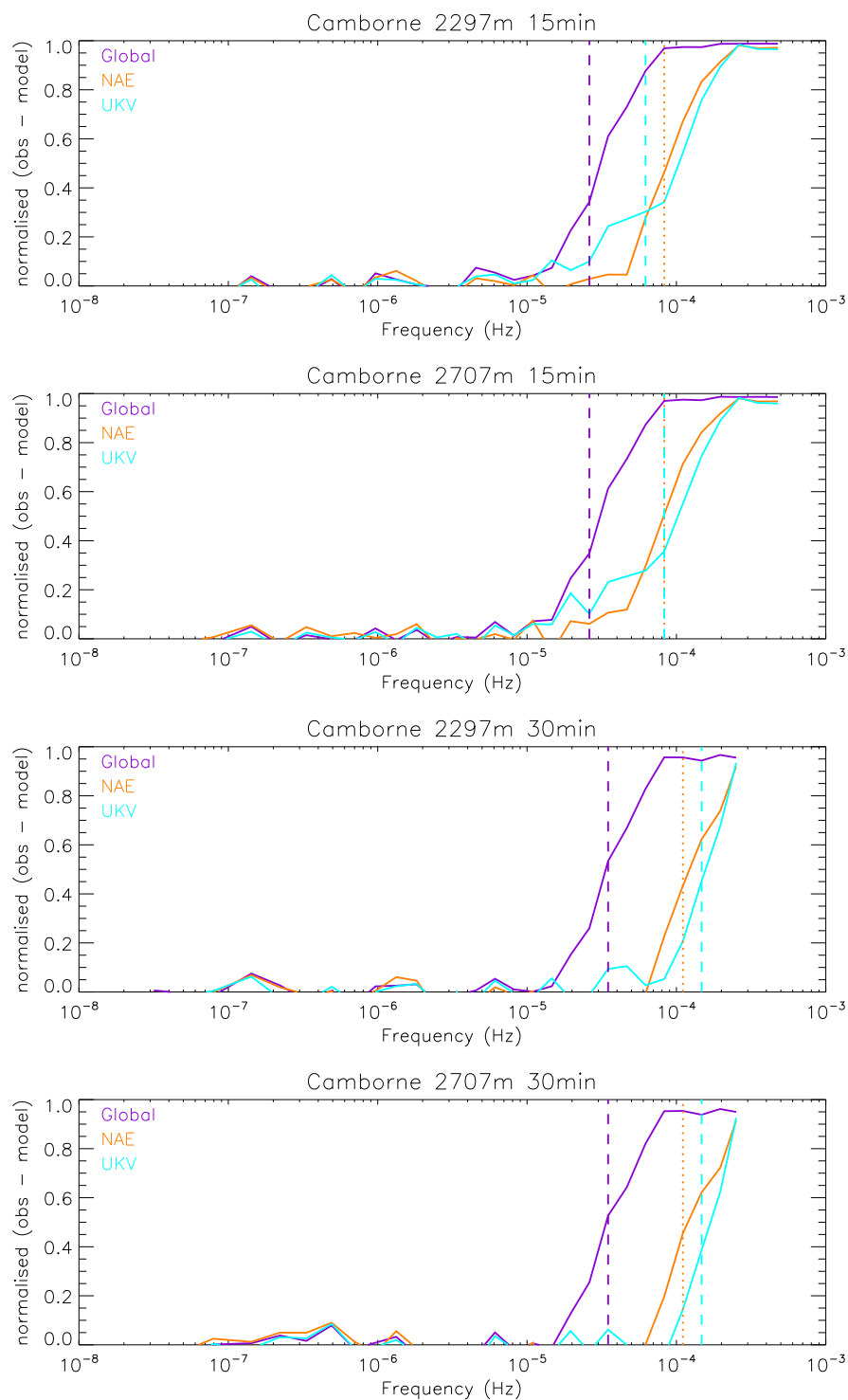


Figure 85: Fractional difference plots at Camborne generated from wind profiler observations (15 and 30 minute means) and MetUM data (global (25 km, 3 hourly), NAE (12 km, hourly) and UKV (1.5 km, hourly)).

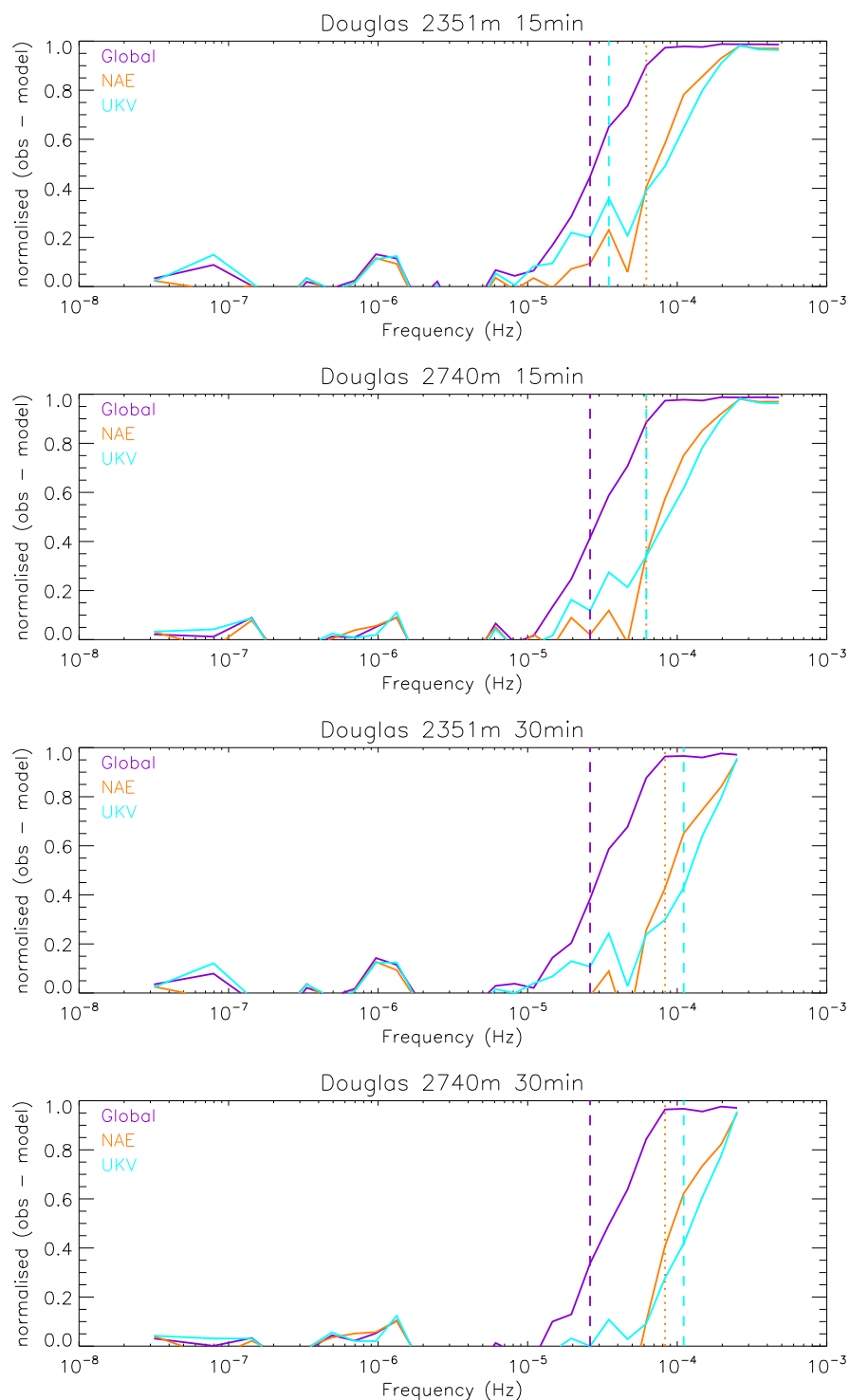


Figure 86: Fractional difference plots at Douglas generated from wind profiler observations (15 and 30 minute means) and MetUM data (global (25 km, 3 hourly), NAE (12 km, hourly) and UKV (1.5 km, hourly)).

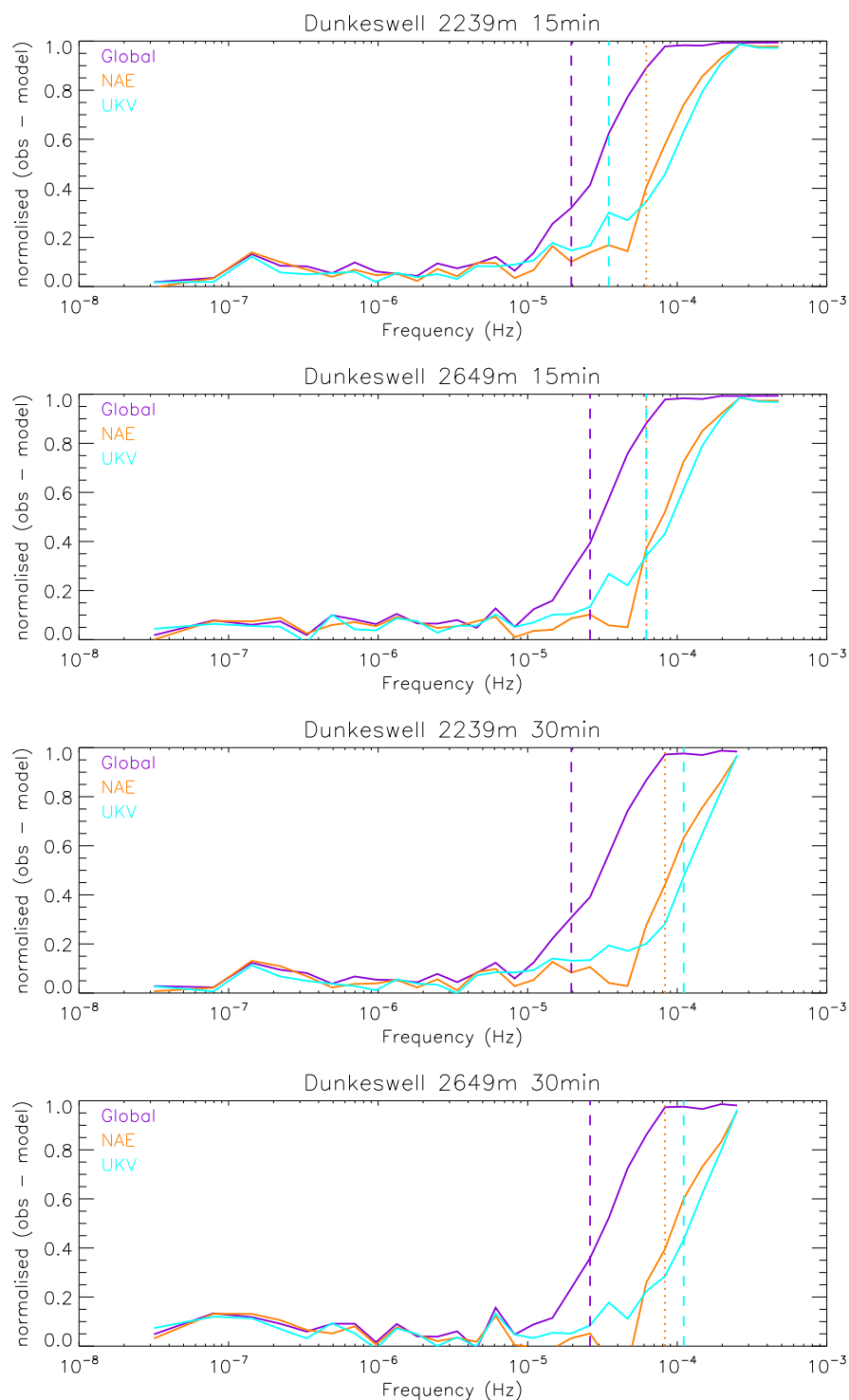


Figure 87: Fractional difference plots at Dunkeswell generated from wind profiler observations (15 and 30 minute means) and MetUM data (global (25 km, 3 hourly), NAE (12 km, hourly) and UKV (1.5 km, hourly)).

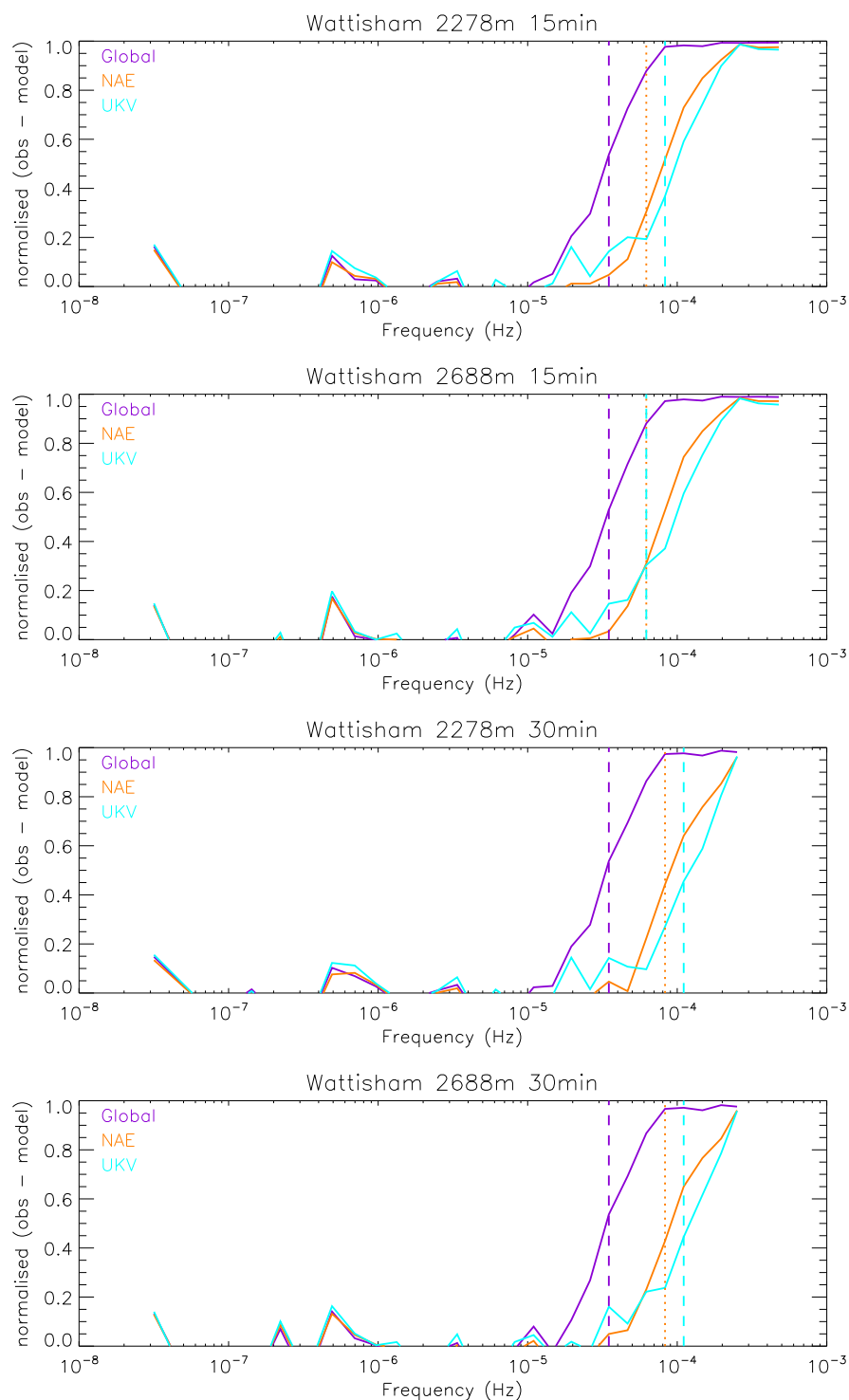


Figure 88: Fractional difference plots at Wattisham generated from wind profiler observations (15 and 30 minute means) and MetUM data (global (25 km, 3 hourly), NAE (12 km, hourly) and UKV (1.5 km, hourly)).

## H Free tropospheric correlation plots

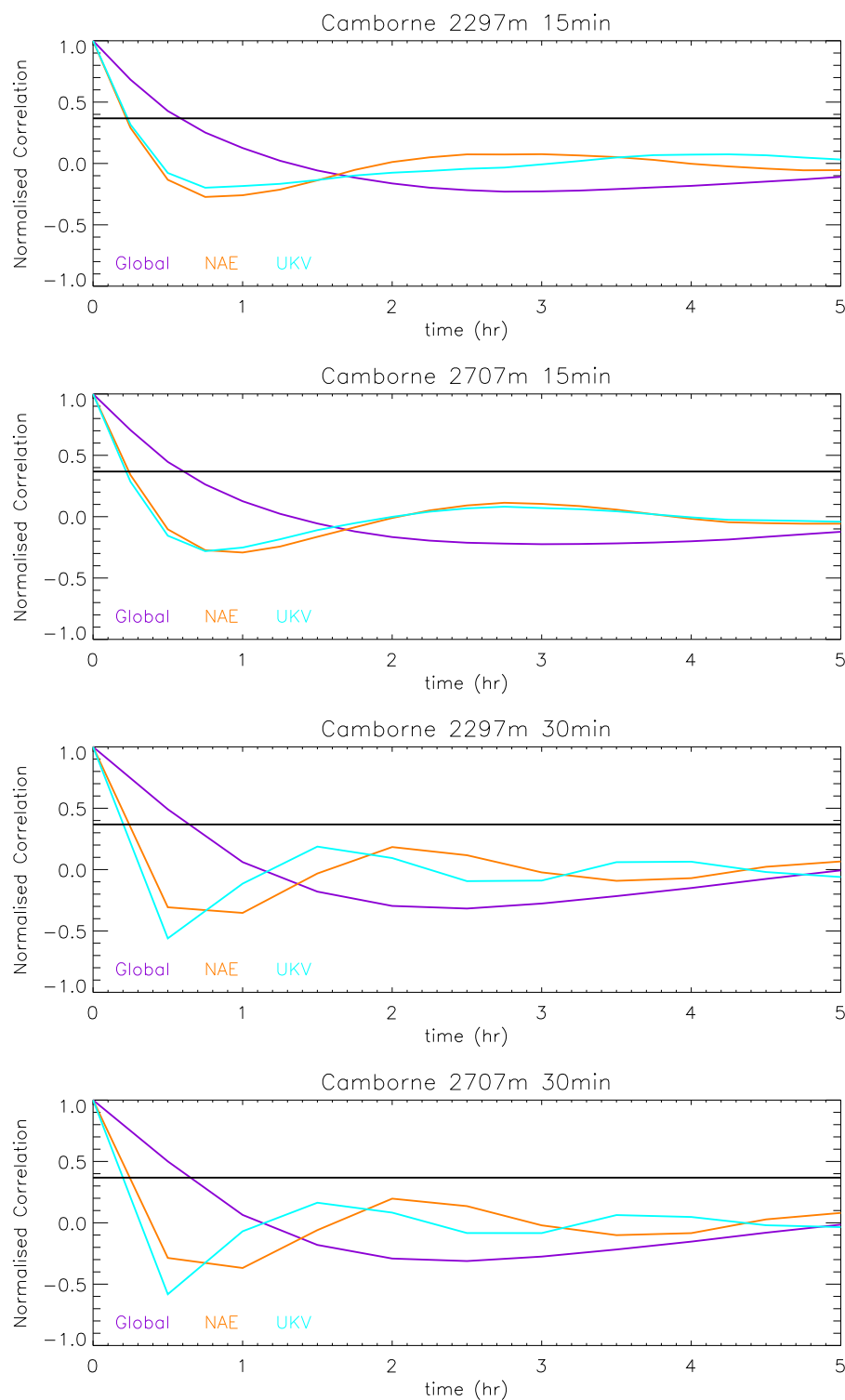


Figure 89: Normalised correlation functions for the unresolved mesoscale motions at Camborne generated from wind profiler observations (15 and 30 minute means) and MetUM data (global (25 km, 3 hourly), NAE (12 km, hourly) and UKV (1.5 km, hourly)). The  $1/e$  line (shown in black) is used to determine the timescale.

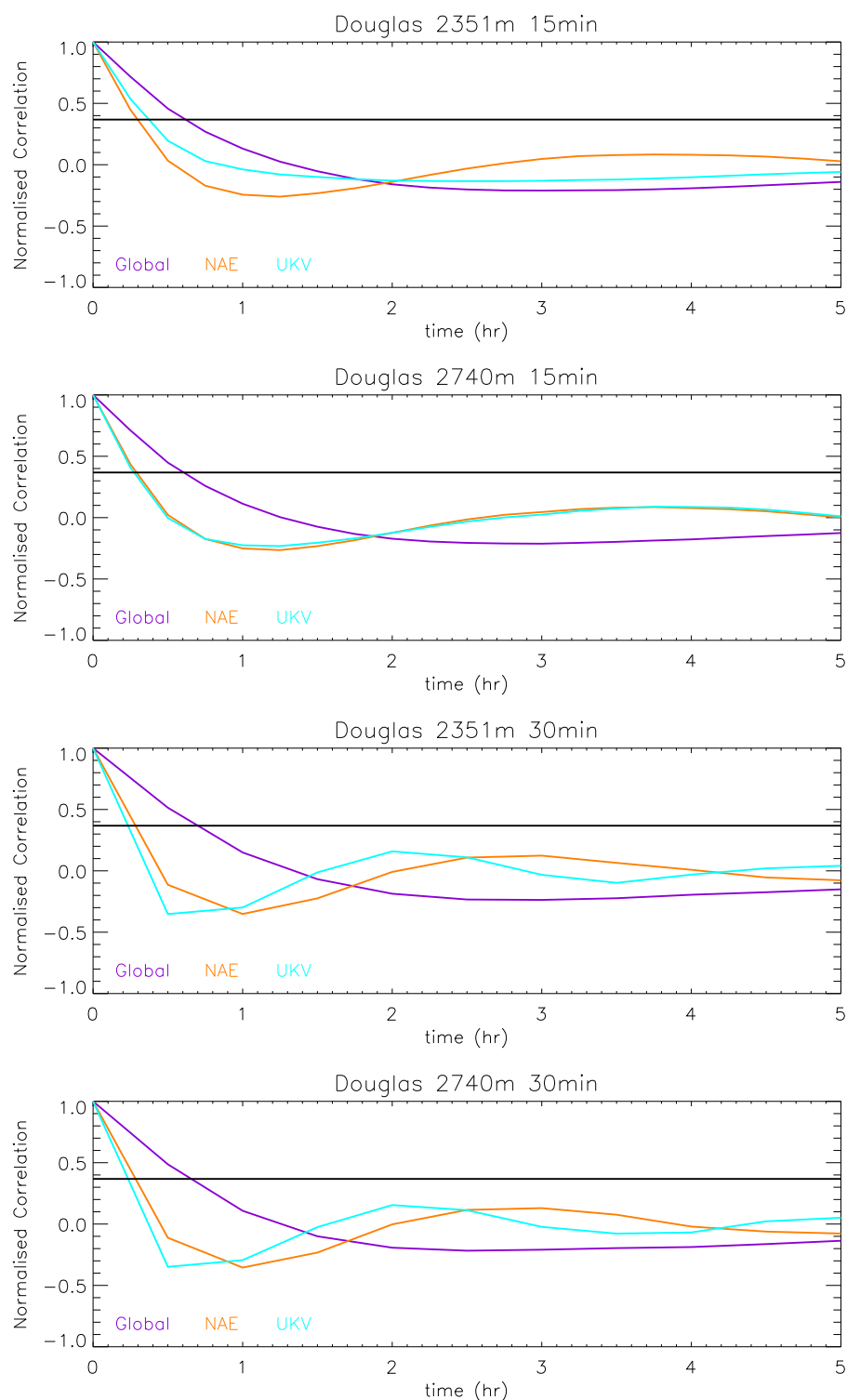


Figure 90: Normalised correlation functions for the unresolved mesoscale motions at Douglas generated from wind profiler observations (15 and 30 minute means) and MetUM data (global (25 km, 3 hourly), NAE (12 km, hourly) and UKV (1.5 km, hourly)). The  $1/e$  line (shown in black) is used to determine the timescale.



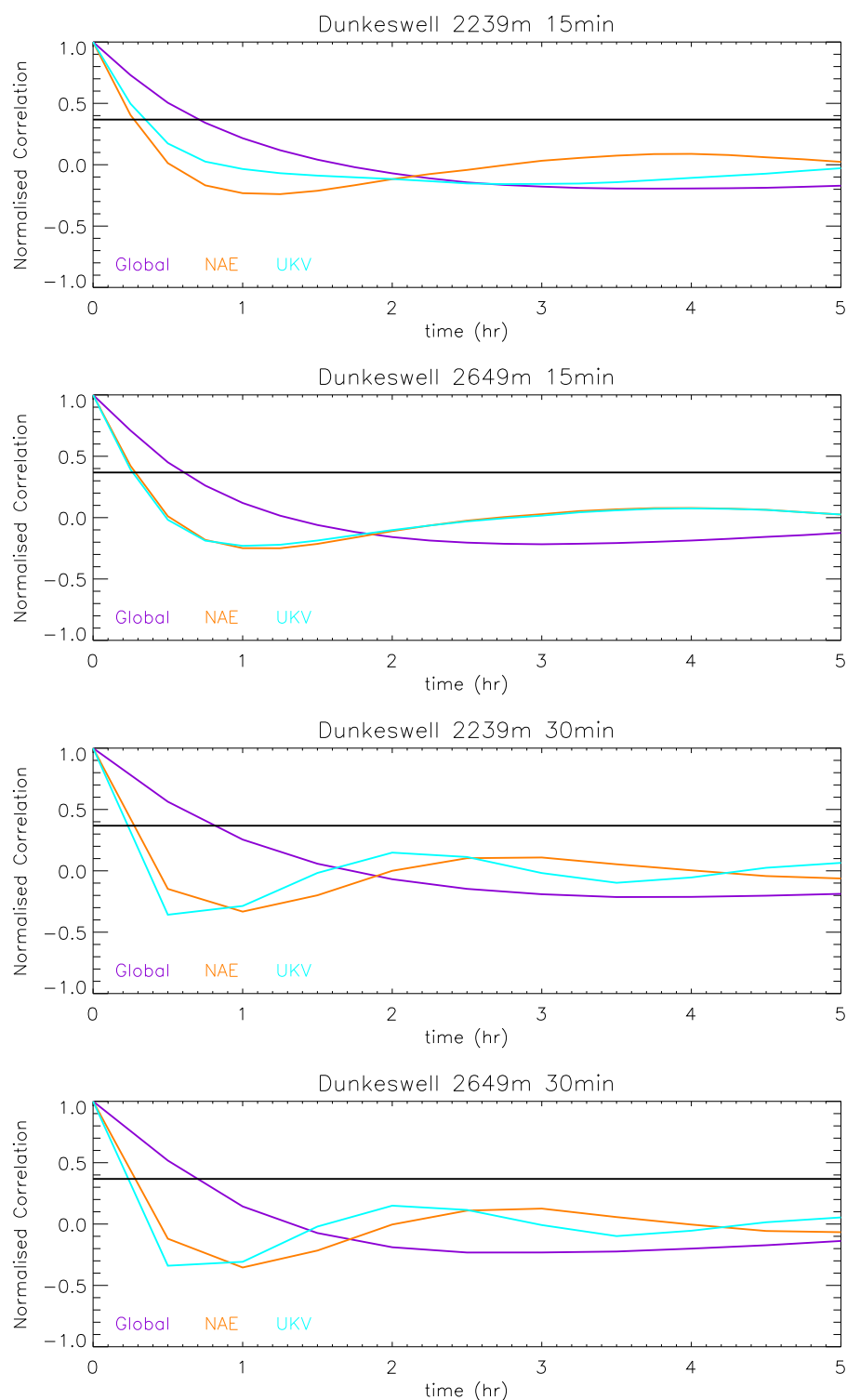


Figure 91: Normalised correlation functions for the unresolved mesoscale motions at Dunkeswell generated from wind profiler observations (15 and 30 minute means) and MetUM data (global (25 km, 3 hourly), NAE (12 km, hourly) and UKV (1.5 km, hourly)). The  $1/e$  line (shown in black) is used to determine the timescale.

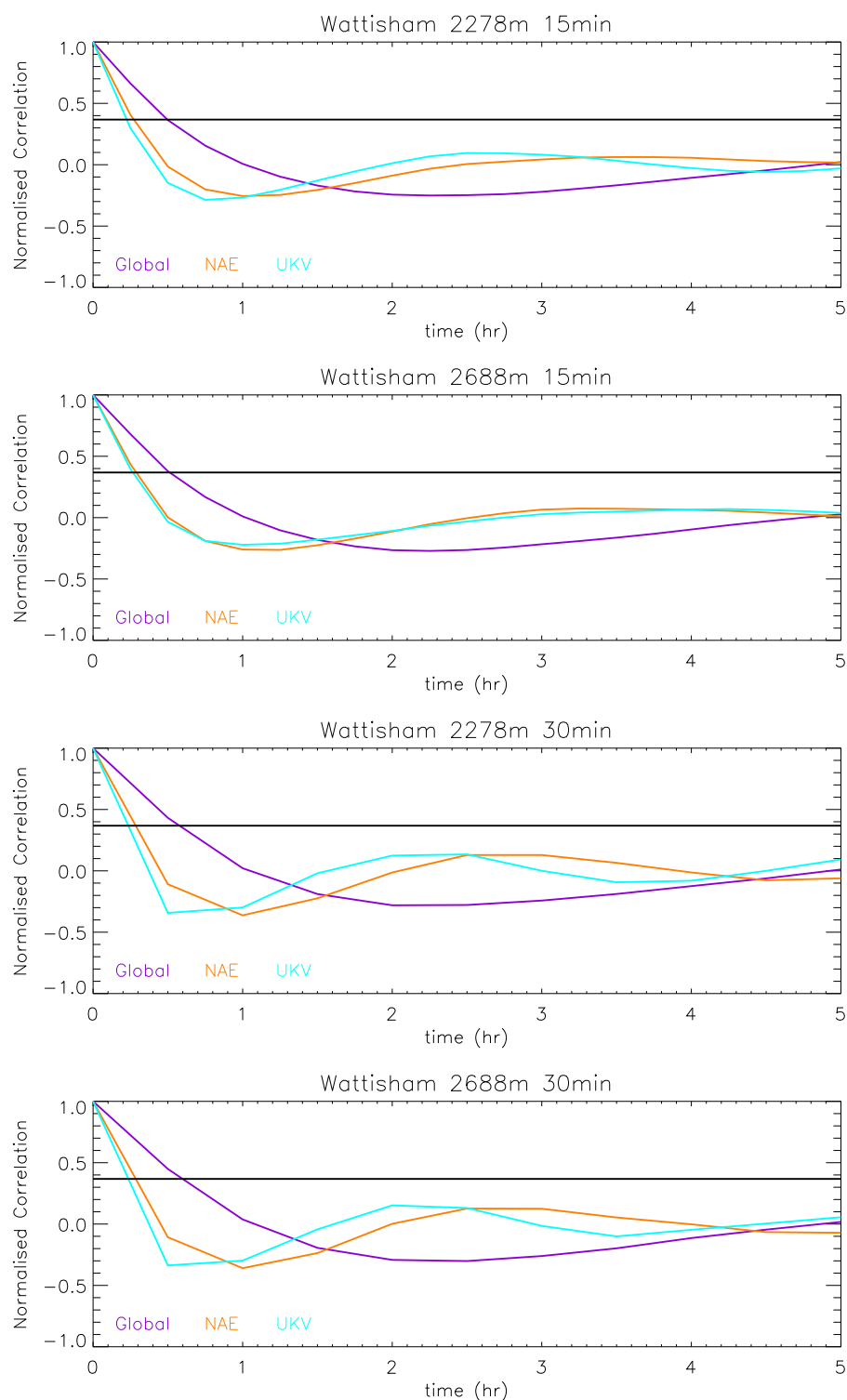


Figure 92: Normalised correlation functions for the unresolved mesoscale motions at Wattisham generated from wind profiler observations (15 and 30 minute means) and MetUM data (global (25 km, 3 hourly), NAE (12 km, hourly) and UKV (1.5 km, hourly)). The  $1/e$  line (shown in black) is used to determine the timescale.

---

## References

- [1] D. Anfossi, D. Oettl, G. Degrazia and A. Goulart. An analysis of sonic anemometer observations in low wind speed conditions. *Bound. Layer Meteor.*, **114**, 179-203 (2005).
- [2] A.R. Brown, R.J. Beare, J.M. Edwards, A.P. Lock, S.J. Keogh, S.F. Milton and D.N. Walters. Upgrades to the boundary-layer scheme in the Met Office numerical weather prediction model. *Bound.-Lay. Meteorol.*, **128**, 117-132 (2008).
- [3] D.J. Carruthers, R.J. Holyroyd, J.C.R. Hunt, W.S. Weng, A.G. Robins, D.D. Apsely, D.J. Thomson and F.B. Smith. UK-ADMS: A new approach to modelling dispersion in the earth's atmospheric boundary layer. *J. Wind Eng. Indust. Aerod.*, **52**, 139-153 (1994).
- [4] CERC. Plume / puff spread and mean concentration module specification. *ADMS 5*, **P10/01X/12** and **P12/01X/12**, CERC, Cambridge, UK, <http://www.cerc.co.uk/environmental-software/technical-specifications.html> (2012).
- [5] R.H. Clarke. A model for short and medium range dispersion of radionuclides released to the atmosphere. *National Radiological Protection Board Report*, **NRPB-R91**, available from National Radiological Protection Board, Harwell, Didcot, Oxon, OX11 0RQ, UK.
- [6] B.M. Davies and D.J. Thomson. Comparisons of some parametrizations of wind direction variability with observations. *Atmos. Environ.*, **33**, 4909-4917 (1999).
- [7] Environmental Protection Agency. Meteorological Monitoring Guidance for Regulatory Modelling Applications. **EPA-454/R-99-005**, Office of Air Quality, Planning and Standards, Research Triangle Park, NC 27711, USA, <http://www.epa.gov/scram001/guidance/met/mmgrma.pdf> (2000).
- [8] D. Etling. On plume meandering under stable stratification. *Atmos. Environ.*, **24**, 1979-1985 (1990).
- [9] S. Gupta, R.T. McNider, M. Trainer, R.J. Zamora, K. Knupp and M.P. Singh. Nocturnal wind structure and plume growth rates due to inertial oscillations. *J. Appl. Meteorol.*, **36**, 1050-1063 (1997).
- [10] S.R. Hanna. Diurnal variation of horizontal wind direction fluctuations  $\sigma_\theta$  in complex terrain at Geysers, CA. *Bound. Layer Meteor.*, **58**, 207-213 (1981).
- [11] S.R. Hanna. Lagrangian and Eulerian time-scale relations in the daytime boundary layer. *J. Appl. Meteorol.*, **20**, 242-249 (1981).
- [12] S.R. Hanna. Lateral turbulence intensity and plume meandering during stable conditions. *J. Clim. Appl. Meteorol.*, **22**, 1424-1430 (1983).

- 
- [13] S.R. Hanna. Lateral dispersion in light wind stable conditions. *Il Nuovo Cimento*, **13C**, 889-894 (1990).
- [14] G.D. Hess and J.R. Garratt. Evaluating models of the neutral barotropic planetary boundary layer using integral measures: Part I. Overview. *Bound-Lay. Meteorol.*, **104**, 333-358 (2002).
- [15] S.M. Joffre and T. Laurila. Standard deviations of wind speed and direction from observations over a smooth surface. *J. Appl. Meteorol.*, **27**, 550-561 (1988).
- [16] L. Kristensen, N.O. Jensen and E.L. Peterson. Lateral dispersion of pollutants in a very stable atmosphere - The effect of meandering. *Atmos. Environ.*, **15**, 837-844 (1981).
- [17] R.H. Maryon. Determining cross-wind variance for low-frequency wind meander. *Turbulence and Diffusion Note*, **236**, (1997).
- [18] R.H. Maryon. Determining cross-wind variance for low frequency wind meander. *Atmos. Environ.*, **32**, 115-121 (1998).
- [19] R.H. Maryon, D.B. Ryall and A.L. Malcolm. The NAME 4 dispersion model: science documentation. *Turbulence and Diffusion Note*, **262**, Met Office, UK.
- [20] D.J. Moore. Observed and calculated magnitudes and distances of maximum ground level concentration of gaseous effluent material downwind of a tall stack. *Adv. Geophys.*, **18**, 201-221 (1974).
- [21] D.J. Moore. Calculation of ground level concentration for different sampling periods and source locations. *Atmospheric Pollution*, Elsevier (1976).
- [22] D. Oetli, A. Goulart, G. Degrazia and D. Anfossi. A new hypothesis on meandering atmospheric flows in low wind speed conditions. *Atmos. Environ.*, **39**, 1739-1748 (2005).
- [23] F. Pasquill. *Atmospheric Diffusion*. 2nd ed., Wiley and Sons, 429 pp (1974).
- [24] *Atmospheric Diffusion*. A study of the dispersion of windborne material from industrial and other sources 3rd ed., Ellis Horwood Limited, Chichester, UK, 437 pp (1983).
- [25] P.M. Pauley, R.L. Creasey, W.L. Clark and G.D. Nastrom. Comparisons of horizontal winds measured by opposing beams with the Flatland ST radar and between Flatland measurements and NMC analyses. *J. Atmos. Oceanic Technol.*, **11**, 256-274 (1994).
- [26] G.S. Raynor and J.V. Hayes. Wind direction meander at a coastal site during onshore flows. *J. Clim. Appl. Met.*, **23**, 967-978 (1984).
- [27] G.E. Schacher, C.W. Fairall and P. Zannetti. Comparison of stability classification methods for parameterizing coastal overwater dispersion. *Proc. First Int. Conf. Meteor. and Air-Sea Interaction of the Coastal Zone*, The Hague, Amer. Meteor. Soc., 91-96 (1982).

- 
- [28] R. Schafer, S.K. Avery and K.S. Gage. A comparison of VHF wind profiler observations and the NCEP-NCAR reanalysis over the tropical Pacific. *J. Appl. Meteorol.*, **42**, 873-889 (2003).
- [29] R.S. Scorer. Theory of airflow over mountains IV. Separation of flow from the surface. *Q. J. R. Met. Soc.*, **81**, 340-350 (1955).
- [30] F.B. Smith and P.F. Abbott. Statistics of lateral gustiness at 16 meters above ground. *Quart. J. Roy. Meteor. Soc.*, **87**, 549-561 (1961).
- [31] A. Stohl. The effect of unresolved mesoscale wind velocity fluctuations on dispersion model results, in *Air Pollution and its Application XIII*: S.E. Gryning and E. Batchvarova (Eds), **13**, 311-320 (2000).
- [32] A. Stohl, H. Sodemann, S. Eckhardt, A. Frank, P. Seibert and G. Wotawa. The Lagrangian particle dispersion model FLEXPART version 8.2. <http://transport.nilu.no/flexpart>, 1-32 (2010).
- [33] H.N. Webster and D.J. Thomson. Parameterising low-frequency meander in atmospheric dispersion models, in *proceedings of the Tenth international conference on harmonisation within atmospheric dispersion modelling for regulatory purposes*: A.N. Skouloudis, P. Kassomenos and J. Bartzis (Eds), 594-598 (2005).
- [34] H.N. Webster, D.J. Thomson, B.T. Johnson, I.P.C. Heard, K. Turnbull, F. Marengo, N.I. Kristiansen, J. Dorsey, A. Minikin, B. Weinzierl, U. Schumann, R.S.J. Sparks, S.C. Loughlin, M.C. Hort, S.J. Leadbetter, B.J. Devenish, A.J. Manning, C.S. Witham, J.M. Haywood and B.W. Golding. Operational prediction of ash concentrations in the distal volcanic cloud from the 2010 Eyjafjallajökull eruption. *J. Geophys. Res.*, doi:10.1029/2011JD016790, **117**, D00U08 (2012).

**Met Office**

FitzRoy Road, Exeter  
Devon, EX1 3PB  
UK

Tel: 0370 900 0100

Fax: 0370 900 5050

[enquiries@metoffice.gov.uk](mailto:enquiries@metoffice.gov.uk)

[www.metoffice.gov.uk](http://www.metoffice.gov.uk)